



**HAL**  
open science

# Coherent imaging of nano-objects with ultra-short X-ray pulses

Anna Luiza Barszczak Sardinha

► **To cite this version:**

Anna Luiza Barszczak Sardinha. Coherent imaging of nano-objects with ultra-short X-ray pulses. Optics [physics.optics]. Université Paris Saclay (COMUE); Universidade técnica (Lisbonne), 2016. English. NNT : 2016SACLX006 . tel-01495628

**HAL Id: tel-01495628**

**<https://pastel.hal.science/tel-01495628>**

Submitted on 25 Mar 2017

**HAL** is a multi-disciplinary open access archive for the deposit and dissemination of scientific research documents, whether they are published or not. The documents may come from teaching and research institutions in France or abroad, or from public or private research centers.

L'archive ouverte pluridisciplinaire **HAL**, est destinée au dépôt et à la diffusion de documents scientifiques de niveau recherche, publiés ou non, émanant des établissements d'enseignement et de recherche français ou étrangers, des laboratoires publics ou privés.

NNT : 2016SACLX006

THESE DE DOCTORAT  
DE  
L'UNIVERSITE PARIS-SACLAY  
PREPAREE A  
"ÉCOLE POLYTECHNIQUE"

ÉCOLE DOCTORALE N° n°572  
EDOM

Spécialité de doctorat : Lasers, molécules, rayonnement atmosphérique

Par

**Mme Anna Barszczak Sardinha Letournel**

Imagerie cohérente de nano-objets avec impulsions ultra-rapides de XUV

**Thèse présentée et soutenue à l'Amphitéâtre CAUCHY École Polytechnique, le 17 mars 2016 :**

**Composition du Jury :**

M, RAX, Jean-Marcel	Professeur, École Polytechnique	Président
M, VELARDE, Pedro	Professeur, Universidad Politécnica de Madrid	Rapporteur
M, ROS, David	Docteur, Laboratoire de Physiques des Gas et Plasmas	Rapporteur
Mme, FAJARDO, Marta	Docteur, Instituto Superior Técnico	Examinatrice
M, MERDJI, Hamed	Docteur, CEA Saclay	Examineur
M, ZEITOUN, Philippe	Docteur, Laboratoire d'Optique Appliquée	Directeur de thèse



# ACKNOWLEDGEMENTS

This thesis is the result of a long collective work between Golp IST/UTL and LOA/Ecole Polytechnique therefore I want to express my gratitude to Professor Marta Fajardo and Professor Philippe Zeitoun for all their help and support. I have really appreciated learning with them more so since I did not arrive from a pure physics background so the learning curve was astonishing and their understanding was outstanding.

All of this work could not have been done either without the help of both Marta's Fajardo GoLP team and Philippe's Zeitoun LOA team.

I would like however to extend my gratitude to all the Golp teams for their help, support, technical support and excellent working environment as well as for the LOA teams even the ones I only met at lunch time or next to the coffee machine.

Very importantly I would like to acknowledge the financial support from IST and FCT Portugal since they were fundamental to the good development of this thesis.

I will take this opportunity to express my gratitude towards Professor Jan Luning and Professor Hamed Merdji for their support and invaluable guidance at LCPMR and CEA. Both teams were extremely friendly and ready to open their own experimental laboratories along with sharing their innovative ideas allowing me to address a larger universe on the course of this thesis.

During this work I have also had the privilege to work with Professor Jens Biegert at ICFO/Barcelona and his team. This opened a new dimension regarding this work since at ICFO I have been introduced to the simulations that could possibly explain the physical phenomena behind our experimental results.

At BESSY-II I have had the pleasure to work with Andreas Gaupp in the early beginning that with his enthusiasm has taught me immensely about magnetism and other fields of physics on long talks while recording data.

At SLAC Stanford I want to express my gratitude to all the teams involved from all over the world as well as for the support night and day from the SLAC home team.

The number of scientists I have come across during this work has been amazing, I am very grateful to have had such an opportunity to learn with them and to give my small contribute.

My time at the Cite Universitaire would have not been the same without all

the people I have met there, from almost all nations and the environment was absolutely amazing for a foreign student.

I could not skip Anh-Tuc Nguyen for being the best friend I could have met in Paris and for her support on both good times and bad times. I am sending all my gratitude to all of the many Parisians or expats I have met and have made my life more colourful during these years, my head is full of good memories from a great number of individuals that made my life even richer.

There is no enough space to cite everyone that has made this period unforgettable so to all of you in France and in Portugal a big Thank you for all the lunches, dinners, breakfasts, trips, experiments.. and the list could go on an on.

Lastly I want to express my deepest gratitude to my family for their invaluable guidance. They stood behind me and given me their unequivocal support throughout, as always, for which my mere expression of thanks likewise does not suffice.

# Contents

<b>Table of contents</b>	<b>vii</b>
<b>List of figures</b>	<b>xx</b>
<b>1 Introduction</b>	<b>1</b>
1.1 Coherent light . . . . .	4
1.2 Synchrotron Radiation Source BESSY-II . . . . .	6
1.3 SLAC Linac Coherent Light Source (LCLS) . . . . .	10
1.4 High Harmonic Radiation . . . . .	13
1.4.1 High Harmonic Generation set-up at LOA . . . . .	15
1.5 Approach to imaging techniques . . . . .	17
1.6 X-Ray microscopy . . . . .	19
1.7 X-ray diffraction . . . . .	21
1.7.1 X-Ray Coherent Diffraction Imaging . . . . .	22
1.8 X-Ray Holography . . . . .	26
1.8.1 In line Holography . . . . .	27
1.8.2 Fourier Transform Holography . . . . .	32
<b>2 Optimisation of a XUV source with 20 nm by laser/matter interaction</b>	<b>40</b>
2.1 High Harmonic Generation . . . . .	43
2.1.1 Optimisation of the High Harmonic Generation process . . . . .	47
2.2 High Harmonic Generation in a two-colour field . . . . .	50
2.2.1 Frequency doubling . . . . .	57
2.2.2 Wavefront and flux optimisation . . . . .	59
2.3 Polarisation of High Order Harmonics . . . . .	64
2.3.1 Two-colour HHG with linearly polarised fundamental a weak orthogonally polarised second harmonic field . . . . .	64
2.4 Conclusion . . . . .	68
<b>3 Polarisation studies of High Harmonics generated in a two-colour field</b>	<b>69</b>
3.1 High Harmonics Generation paths in a two-colour field . . . . .	71
3.1.1 Description of the experimental set-up of the orthogonal two- color scheme for HHG . . . . .	76
3.1.2 Analysis of the measurements . . . . .	80

3.1.3	Conclusions of the first harmonic studies . . . . .	91
3.2	Second polarisation harmonic studies . . . . .	92
3.2.1	Description of the experimental setup of the second HHG polarisation experiment . . . . .	94
3.2.2	Polarisation measurement . . . . .	96
3.2.3	Experimental results of the harmonic polarisation experiment	102
3.2.4	Polarisation of high harmonics in an orthogonal two-colour field . . . . .	108
3.2.5	Matlab data analysis of the harmonic polarisation in an orthogonal two-colour field . . . . .	115
3.3	Polarisation simulations . . . . .	120
3.3.1	Strong field approximation - Bauer . . . . .	121
3.3.2	New theoretical approach . . . . .	129
3.4	Conclusions and Perspectives . . . . .	133
<b>4</b>	<b>Preparation and characterisation of samples containing magnetic nanostructures</b>	<b>137</b>
4.1	Optical Activity and Light Polarisation . . . . .	138
4.1.1	Optical rotation . . . . .	139
4.1.2	Circular Dichroism . . . . .	140
4.1.3	Ellipticity . . . . .	146
4.2	Ultrafast demagnetisation . . . . .	146
4.2.1	Magnetic Optical Kerr Effect (MOKE) . . . . .	147
4.2.2	Magnetic Optical (MO) Faraday Effect . . . . .	149
4.3	Sample design . . . . .	152
4.3.1	Reaching the magnetic behaviour information . . . . .	153
4.4	Measurements at BESSY-II . . . . .	155
4.4.1	BESSY-II End Station . . . . .	156
4.4.2	Experimental Method . . . . .	159
4.4.3	Experimental data - Magnetic properties of the sample . . . . .	161
4.4.4	Conclusions . . . . .	165
4.5	Further developments . . . . .	166
<b>5</b>	<b>Imaging of nanomagnetic structures by diffraction and study of the evolution of the demagnetisation</b>	<b>168</b>
5.1	Magnetisation studies at LOA . . . . .	170
5.1.1	Sample preparation . . . . .	170
5.1.2	Development of the tabletop set-up for the ultrafast demagnetisation experiment . . . . .	172
5.1.3	Ultrafast demagnetisation curves . . . . .	177
5.1.4	Comparison between the HHG source and X-FEL . . . . .	181
5.2	Imaging of nanomagnetic structures by diffraction and study of the evolution of the demagnetisation . . . . .	183
5.3	Linac Coherent Light Source - LCLS . . . . .	184
5.3.1	Single-shot magnetisation dynamic experiment at LCLS . . . . .	184

5.3.2	Single-shot diffraction patterns . . . . .	187
5.3.3	Conclusion . . . . .	192
<b>A</b>	<b>Optical Coherence</b>	<b>196</b>
<b>B</b>	<b>Fourier transform, convolution and correlation: notations and useful properties</b>	<b>202</b>
	<b>Bibliography</b>	<b>210</b>



## List of Figures

1.1	Electromagnetic spectra illustrated with sources for the radiation, its wavelength and its penetration power from <i>Radio waves</i> ; lower energy to <i>Gama radiation</i> ; higher energetic. . . . .	2
1.2	Coherence of a beam a) Spatial coherence scheme. Two distinct points taken from a beam cross section at the same instant will emit two fields that are correlated. b) Temporal coherence scheme. One point taken from a beam cross section at two different instants will emit two fields that are correlated. The temporal coherence length is the given by the propagation distance at which the two waves will show opposite phases. . . . .	5
1.3	BESSY-II at Berlin a) BESSY-II top view. b) Beamline scheme . . . . .	8
1.4	Scheme of principle of a standard synchrotron. . . . .	8
1.5	Free electron laser principle. As the electrons arrive the undulator they present an aleatory phase. The radiation emitted is incoherent. As the electrons interact with the radiation <i>bunching</i> occurs. The train waves emitted are now in phase and the radiation is amplified in a coherent . . . . .	11
1.6	LCLS at Stanford a) LCLS top view. b) Undulator hall, Undulator hall (130 m of undulator to produce photons 9keV) . . . . .	12
1.7	Laser chain installation used. <i>Salle Rouge</i> at LOA . . . . .	14
1.8	Scheme of the principle of installation of an High Harmonic Generation (HHG) line using Neon at <i>salle orange</i> . . . . .	16
1.9	Milestones on imaging techniques. a) Light microscopy; b) Photon imaging. . . . .	18
1.10	Attenuation length of the model cell $H_{230}O_{100}C_{30}N_{10}$ for the wavelengths of 1-10 nanometers. Data from Center for X-ray Optics (CXRO). . . . .	19

1.11	Example of a X-ray microscopy set-up. A zone plate focuses the monochromatised undulator beam onto the object and a micro zone plate objective forms a magnified image on a CCD camera. The phase ring selectively shifts the undiffracted light of the object. . . . .	20
1.12	X-ray Diffraction: a) example of a diffraction pattern. b) its original image [1] . . . . .	23
1.13	Reconstruction of the diffraction pattern represented on figure 1.12 [1] . . . . .	23
1.14	In a tomographic process there is a need to acquire several measurements in different angles in order to reconstruct the tridimensional image. . . . .	24
1.15	Evolution of the sample with irradiation time. With a short pulse of 2 femtoseconds and a long pulse of 50 femtoseconds. [2] . . . . .	25
1.16	Principle of in-line Holography . . . . .	28
1.17	Rayleigh Criterion on the minimum resolvable detail. . . . .	29
1.18	Numerical aperture defined by a) the divergence of the source and b) by the detector . . . . .	30
1.19	Attosecond Holography studies at LOA. a)acquired Hologram, b) cut of the reconstruction presenting a measured FWHM of 840 nm. [3]. .	31
1.20	Fourier Transform Holography a) General set-up b) Image of the mask containing both the object to be imaged and the reference source point on the same plane . . . . .	33
1.21	Fourier Transform Holography. Reconstruction of the object. . . . .	35
2.1	Ultra-fast demagnetisation curve. Beaurepaire et al, retrieve a demagnetisation curve that shows that the process is completed on a ultra-fast time scale. [4] . . . . .	42
2.2	Typical High-Harmonic spectrum where the three zones: <i>Perturbative regime, Plateau</i> and <i>Cut-off</i> , are identified. . . . .	43
2.3	Representative example of HHG . . . . .	44
2.4	Representation of the electronic trajectories in the continuum as a function of the pulse cycle and the position of the electron on the atom	46
2.5	Example of long and short paths trajectories [5] . . . . .	47
2.6	Number of photons of harmonics generated as a function of the length of the media for different lengths of coherence [6] . . . . .	49
2.7	Harmonic spectra for various gases generated with an energy of 6 mJ and a laser of 800 nm [7] . . . . .	50

2.8	Set-up for High harmonic generation with a two-colour field. An intense IR laser pulse is focused onto a gas cell by means of a lens. When the laser pulse passes through the BBO crystal the second colour laser field is generated. The resulting two-colour laser field interact with the noble gas generating high harmonics. A filter is used in order to suppress the two-colour laser field. . . . .	51
2.9	High harmonic generation in a two colour field at LOA . . . . .	52
2.10	High harmonic spectra attained for a single colour field and a two-colour field laser pulse. The conversion efficiency is 25 times higher for Neon in these conditions. It is clear the effect of the doubling of the fundamental frequency: Odd and even harmonics appear. The red shift is also present. . . . .	53
2.11	Comparison between the three models that try to explain the generation of High Harmonics on a two-colour set-up. <i>Corkum, Lewenstein and <math>\delta^3</math></i> . . . . .	54
2.12	Nam's experiment a) Nam's experimental set-up. b) Nam's spectra of results. [8] . . . . .	56
2.13	Nam's second experiment a) Nam's experimental set-up. b) Nam's spectra of results. [9] . . . . .	56
2.14	Scheme of the 2 colour mismatch in the BBO crystal . . . . .	58
2.15	Wavefront principle of actuation . . . . .	61
2.16	Wavefront measurement of an harmonic beam at salle orange . . . .	61
2.17	changes the focusing geometry and cleans the major distortions on the outer part of the beam ( $\omega(L_{cel} = 8mm$ and $P_{Ar} = 30mbar$ ) to $\omega + 2\omega$ ( $L_{cel} = 4mm$ and $P_{Ar} = 16mbar$ [10] . . . . .	62
2.18	Iris clipping: limited decrease of intensity and distortions about $\lambda/17$ RMS . . . . .	63
2.19	High Harmonic footprint vs HH source sizes . . . . .	63
2.20	Single half cycle case. (a) Strong electric field. (b) Electron trajectories defined as $x$ component. (c) Weak second harmonic field with several different phases relative to the strong field by colour. (d) Electron trajectories corresponding to (c) defined as the $y$ component.	66
2.21	Electron velocity as a function of fundamental phase for different trajectories. (red) Cut-off. (blue) Half cut-off, short. (green) Half cut-off, long . . . . .	67

3.1	Linear polarised light wave with the magnetic field $B$ and the electric field $E$ in an perpendicular angle from each other. . . . .	70
3.2	Electronic motion for orthogonally polarised two-colour field. The inset shows the Lissajous diagram. [8] . . . . .	72
3.3	Lissajous diagram for orthogonally polarized two-color field and the influence of the phase. (a) $\phi = 0$ , (b) $\phi = 0.125\pi$ , (c) $\phi = 0.25\pi$ , (d) $\phi = 0.35\pi$ , (e) $\phi = 0.5\pi$ , (f) $\phi = 0.625\pi$ , (g) $\phi = 0.75\pi$ and (h) $\phi = 0.875\pi$ . [11] . . . . .	73
3.4	Lissajous diagram for orthogonally polarised two-color field and the influence of the phase. (a) $\phi = 0$ , (b) $\phi = 0.125\pi$ , (c) $\phi = 0.25\pi$ , (d) $\phi = 0.35\pi$ , (e) $\phi = 0.5\pi$ , (f) $\phi = 0.625\pi$ , (g) $\phi = 0.75\pi$ and (h) $\phi = 0.875\pi$ . [11] . . . . .	74
3.5	Theoretical proposition based on the $\delta^3$ model for the laserlab proposal at Laboratoire d'Optique Applique (LOA). An intense IR laser pulse is focused on a gas cell by means of a lens. The fundamental pulse is on a horizontal axis. When the laser pulse passes through the BBO crystal the second colour laser field is generated. Due to the positioning of the BBO the second-colour pulse will be on an orthogonal axis, in this case the vertical axis. The resulting two-colour laser field interacts with the noble gas generating harmonics. . . . .	77
3.6	Proposed set-up to study the generation of harmonics in a two colour field. The introduction of a multilayer mirror at $45^\circ$ is based on the proposition given by the $\delta^3$ to study generation in this specific regime. . . . .	78
3.7	Multilayer theoretical reflectivity: Mirror reflectivity as a function of the incidence angle for p polarisation (horizontal) and s polarisation (vertical). . . . .	79
3.8	Multilayer theoretical reflectivity: Mirror reflectivity as a function of the wavelength. The mirror is set at $45^\circ$ of incidence. . . . .	79
3.9	Experimental reflectivity for horizontal polarisation and vertical polarisation in function of the harmonic order . . . . .	81
3.10	High harmonic signal registered on the CCD by varying the positioning of the mirror. On the left it is represented the obtained HHG signal at a direct configuration. On the right it is represented the obtained HHG signal at a configuration of $45^\circ$ . . . . .	82
3.11	P polarisation High Harmonic spectre. The full line corresponds to the direct configuration and the dashed line to the $45^\circ$ mirror configuration. . . . .	82

3.12	High harmonic signal registered on the CCD by varying the positioning of the mirror. On the left it is represented the obtained HHG signal at a direct configuration. On the right it is represented the obtained HHG signal at a configuration of 45° . . . . .	83
3.13	S polarisation High Harmonic spectre. The full line corresponds to the direct configuration and the dashed line to the 45° mirror configuration. . . . .	83
3.14	High harmonic signal registered on the CCD by varying the positioning of the mirror. On the left it is represented the obtained HHG signal at a direct configuration. On the right it is represented the obtained HHG signal at a configuration of 45° . . . . .	84
3.15	S polarisation High Harmonic spectre. The full line corresponds to the direct configuration and the dashed line to the 45° mirror configuration. . . . .	84
3.16	Reflectivity of the HHG in the one-colour case as a function of the harmonic order for the s polarisation, p polarisation and the intermediate 45° polarisation. . . . .	85
3.17	High harmonic (odd and even) signal registered on the CCD by varying the positioning of the mirror. On the left it is represented the obtained HHG signal at a direct configuration. On the right it is represented the obtained HHG signal at a configuration of 45° . . . . .	85
3.18	S polarisation High Harmonic odd and even spectre. The full line corresponds to the direct configuration and the dashed line to the 45° mirror configuration. . . . .	86
3.19	High harmonic (odd and even) signal registered on the CCD by varying the positioning of the mirror. On the left it is represented the obtained HHG signal at a direct configuration. On the right it is represented the obtained HHG signal at a configuration of 45° . . . . .	86
3.20	P polarisation High Harmonic odd and even spectre. The full line corresponds to the direct configuration and the dashed line to the 45° mirror configuration. . . . .	87
3.21	High harmonic (odd and even) signal registered on the CCD by varying the positioning of the mirror. On the left it is represented the obtained HHG signal at a direct configuration. On the right it is represented the obtained HHG signal at a configuration of 45° . . . . .	87

3.22	Reflectivity of the HHG in the two-colour case as a function of the harmonic order for the s polarisation, p polarisation and the intermediate $45^\circ$ polarisation. . . . .	88
3.23	High harmonic (odd and even) signal registered on the CCD using a $100\mu\text{m}$ thickness BBO. Using a $250\mu\text{m}$ thickness BBO. The presented intensities on both images are different on order for the spectre to be apparent. . . . .	90
3.24	Experimental results for the influence of the BBO on the generation on the direct configuration. A $100\mu\text{m}$ thickness BBO resulting spectrum is represented in orange and a $250\mu\text{m}$ thickness BBO spectra is represented in blue. . . . .	90
3.25	Experimental results. Spectre attained in direct configuration using a $250\mu\text{m}$ thickness BBO. On light green the horizontal, p polarisation is represented and on darker green the vertical, s polarisation is shown.	91
3.26	For $\alpha = 90^\circ$ and $\beta = 0^\circ$ the fundamental field has Maximum Intensity	95
3.27	Multilayer theoretical reflectivity: Simulated reflectivity for the multilayer used ( <i>IMD</i> ) . . . . .	102
3.28	Multilayer theoretical reflectivity: Transmission function of the set-up in function of the energy for s (blue line) and p (red line) polarisation of light . . . . .	103
3.29	Data images superposed varying the polarisation angle from $-200^\circ$ to $220^\circ$ recorded at the CCD for horizontal polarisation. Set-up of four mirrors coated with Gold. Set-up of four mirrors coated $\text{MoB}_4\text{C}$ .	104
3.30	Experimental data: (a) Harmonic spectrum acquired on the CCD with the polariser for $\alpha = 90^\circ$ and $\beta = 90^\circ$ . Accumulation of 40000 thousand pulses. (b) Cross section of the image with the intensity of each harmonic shown and the distance in pixels between the grating and the CCD. . . . .	105
3.31	Spectra obtained for the harmonic 39 (60 eV) without polariser and with the polariser. The points are the measured data and the line the fit. The intensities are normalised. (a) refers to the configuration with the spectrometer only. The sinusoidals are quite similar. (b) refers to the configuration of spectrometer and polariser. The clear effect of the polariser on the harmonic is shown. . . . .	106

3.32	Table of the harmonics obtained with the polariser. Eight harmonics (31 <sup>st</sup> to 45 <sup>th</sup> ) are visible. For each harmonic the reflectivities $r_p''/2$ and $r_s''/2$ , the phase-shift $\Delta_a''$ , the degree of circular polarisation $P_{Cmax}$ and the circular transmission $T_C$ are shown. The 39 <sup>th</sup> harmonic correspondent to the Co absorption M-edge has a degree of 85% of circular polarisation and a circular transmission of 4.4% . . . . .	107
3.33	Measured BBO crystal generation of second harmonic in joules. . . . .	109
3.34	Set-up for the polarisation of high harmonics in an orthogonal two-colour field experiment. An intense IR laser pulse is focused on a gas cell by means of a lens. The fundamental pulse is on a horizontal axis. When the laser pulse passes through the BBO crystal where the second colour laser field is generated. The BBO is mounted on a rotation stage. The second-colour pulse will be on an orthogonal axis. The resulting two-colour laser field interacts with the noble gas generating harmonics. The laser pulse plus the harmonics will pass through a metallic filter. The harmonic pulse will traverse the spectrometer and the rotating analyser. The image will be collected on a CCD camera. . . . .	110
3.35	Data acquired with an 100 $\mu$ m thickness BBO for a) the maximum generation of second harmonic and b) for the minimum generation of second harmonic. The images were acquired for different rotating stages of the BBO crystal. . . . .	111
3.36	Resulting spectra for the even and odd harmonics and with the influence of the BBO generation. The plots represent the intensity of the generation versus the analyser angle in degrees. On the first row the maximum generation of second harmonic case is portrayed. The first image corresponding to the intensity of even harmonics and the second corresponding to the intensity of odd harmonics. The second row and intermediate case closer to the maximum generation of second harmonic is presented. The third row represents an intermediate case this time closer to the minimum generation of the second harmonic. The fourth and last row represents the minimum second harmonic generation. The plots correspond to the harmonics H34 to H49. . . . .	112

3.37	Acquired data for both BBO crystals. For the maximum generation approximately. The first image corresponds to the maximum generation of energy using the 100 $\mu\text{m}$ thickness BBO. The second corresponds to the maximum generation of energy using the 250 $\mu\text{m}$ thickness BBO. . . . .	113
3.38	Comparison between both BBO crystals. For the maximum generation and for both even and odd harmonics. On the first line the 100 $\mu\text{m}$ thickness BBO is presented. The first image corresponding to the odd harmonics and the second image corresponding to the even harmonics. The second line represents the data for the 250 $\mu\text{m}$ thickness BBO. The first image representing a plot of the odd harmonics and the second a plot of the even harmonics. The plots refer to the different harmonics going from H34 to H49. . . . .	114
3.39	Representation of the elliptic polarisation scheme with the corresponding parameters. . . . .	116
3.40	Intensity representation of the HHG. The first row shows the stronger regimes of generation. The first image represents the maximum generation and the second the intermediate maximum generation. The second row shows the weakest second harmonic generation. The first image the intermediate minimum and the last one the minimum generation of the second harmonic field. . . . .	117
3.41	Representation of the polarisation ellipse for HHG for maximum generation of second harmonic and intermediate maximum. On the x-axis the harmonic order is portrayed. The red line corresponds to the odd harmonics and the blue line to the even harmonics. The first plot shows the semi-major axis of the ellipse. The second plot the ratio minor/major axis of the ellipse and the last plot the angle to the major axis to the x-axis. . . . .	118
3.42	Representation of the polarisation ellipse for HHG for intermediate minimum and minimum of the generation of second harmonic. On the x-axis the harmonic order is portrayed. The red line corresponds to the odd harmonics and the blue line to the even harmonics. The first plot shows the semi-major axis of the ellipse. The second plot the ratio minor/major axis of the ellipse and the last plot the angle to the major axis to the x-axis. . . . .	118

3.43	Representation of the contributions either from the fundamental field or the second harmonic field on the HHG for maximum generation of second harmonic (a), intermediate maximum (b), intermediate minimum (c) and minimum (d). . . . .	120
3.44	Geometry for the SFA simulation studies where the red line corresponds to the fundamental field that is generated over the $xy$ plane and the blue line corresponds to the second harmonic field that is generated orthogonally (BBO type 1) in the $zy$ plane. $\Delta t$ corresponds to the delay time between the two pulses. . . . .	123
3.45	Variation of the fundamental field intensity. In this simulation the fundamental wavelength is blocked at 815 nm and the intensity of the field at $2.6 \times 10^{15} \text{ W/cm}^2$ . The second harmonic field varies its intensity from $2.1 \times 10^{14} \text{ W/cm}^2$ to $2.0 \times 10^{14} \text{ W/cm}^2$ and its wavelength from 407 to 412 nm. The pulse duration varies from is 18.5 to 18.7 fs.	124
3.46	Variation of the second harmonic field intensity. In this simulation the fundamental wavelength is blocked at 815 nm and the intensity of the field varies from its peak intensity $2.6 \times 10^{15} \text{ W/cm}^2$ to $1.8 \times 10^{15} \text{ W/cm}^2$ . The second harmonic field has stationary parameters: Intensity of $2.1 \times 10^{14} \text{ W/cm}^2$ and wavelength of 407 nm. The pulse duration is 18.5 fs. . . . .	125
3.47	Variation of the HH spectra with the phase. Maintaining all the parameters fixed in this simulation. The phase between the two waves will be varied. In blue the waves have no shift. In green the shift corresponds to 0.3 in red the shift corresponds to 0.5 and in light blue the shift corresponds to 1. . . . .	126
3.48	Variation of the second harmonic wavelength maintaining a $\pi$ phase between the fundamental and the second harmonic pulse. The fundamental wavelength is blocked at 815 nm and the intensity of the field at $2.6 \times 10^{15} \text{ W/cm}^2$ . The second harmonic field varies its intensity from $2.1 \times 10^{14} \text{ W/cm}^2$ to $2.0 \times 10^{14} \text{ W/cm}^2$ and its wavelength from 407 to 412 nm. The pulse duration varies from is 19.2 to 19.4 fs.	127
3.49	Simulation for Argon for both the fundamental pulse and the second harmonic pulse. In this simulation the fundamental wavelength is blocked at 815 nm and the intensity of the field at $2.6 \times 10^{15} \text{ W/cm}^2$ . The second harmonic field varies its intensity from $2.1 \times 10^{14} \text{ W/cm}^2$ and its wavelength from 410 nm. The pulse duration is 18.6 fs. . . . .	128

3.50	Phase-match conditions for a BBO type 1 of $100\mu\text{m}$ as a function of the crystal orientation in radians. . . . .	129
3.51	Representation of the elliptic polarisation for a linear horizontal polarisation of the incident fundamental field. . . . .	130
3.52	Normalised intensity of the even and odd harmonics as a function of the $100\mu\text{m}$ thickness BBO crystal. . . . .	131
3.53	Calculated ellipticity of the fundamental field as a function of the $100\mu\text{m}$ thickness BBO crystal. . . . .	131
3.54	Ellipticity of the even (blue) and odd (red) harmonics in function of the BBO rotation. The insets show the calculated polarisations of the fundamental field as a function of the $100\mu\text{m}$ thickness BBO crystal.	132
3.55	Calculated polarisation of the $\omega$ axis, fundamental field as a function of the $100\mu\text{m}$ thickness BBO crystal. . . . .	133
3.56	Experimental axis $\omega$ of polarisation as a function of the $100\mu\text{m}$ thickness BBO crystal. . . . .	133
3.57	Example of a pump-probe experiment that can be used to adjust the delay between both fields and their relative intensity . . . . .	135
4.1	Linearly polarised light upon transmission through a sample with magnetic moment perpendicular to the light direction. The phase difference between the electric field components leads to ellipticity; the dichroism in the absorption leads to an intensity difference and thus to rotation of the polarisation plane after the sample [12] . . . . .	139
4.2	Scheme of circular polarised light. [13] . . . . .	141
4.3	Chiral molecule a) (M)-Hexahelicene. b) Circular Dichroism (CD) Spectrum of (M)-Hexahelicene. . . . .	142
4.4	DNA configurations a) A-DNA b) B-DNA, right hand c) Z-DNA, left hand. . . . .	143
4.5	Electronic transitions in a conventional L-edge x-ray magnetic circular x-ray dichroism illustrated in a one-electron model. The transitions occur from the spin-orbit split 2p core shell to empty conduction band states. By use of circularly polarised x-rays the spin moment and orbital moment can be determined from linear combinations of the dichroic difference intensities A and B, according to other sum rules [12] . . . . .	144

4.6	Example of a set-up of an X-ray polarisation detector based on a multilayer mirror. The polarisation studies are performed rotating the multilayer and the diode in the light axis, that is around the $\gamma$ angle. The incidence is set to the Bragg which is close to the Brewster angle. [12] . . . . .	145
4.7	Example of precessional motion of magnetisation. [14] . . . . .	147
4.8	Survey of X-ray magneto-optical spectroscopy techniques, classified according to three criteria: (i) intensity measurement or polarisation analysis, (ii) using linearly or circularly polarised light, and (iii) dependence on magnetisation, i.e. sensitivity to $M$ or $M^2$ . . . . .	148
4.9	Schematic of MOKE geometry. [15] . . . . .	149
4.10	Scheme of a system showing Faraday rotation. . . . .	150
4.11	SEM image of the integrated mask sample structure patterned with a focused ion beam. This is the final sample structure to be used on further studies. The characterisation studies will only take charge of the magnetic multilayer component. . . . .	152
4.12	Representation of the arrangement of the sample used . . . . .	154
4.13	L-edge for Cobalt measured at BESSY [12] . . . . .	156
4.14	Refractive index shown for the L-edge in Cobalt measured at BESSY [12] . . . . .	157
4.15	APPLE II undulator, schematic. Row 1 and 2 shift in opposite direction (dark arrows, anti-parallel shift, $s_1=-s_2$ ) which controls the inclination of the polarisation ellipse. Row 3 and 4 shift in the same direction (light arrows, parallel shift, $s_3=s_4$ ) which changes the ellipticity of the polarisation ellipse. [16] . . . . .	158
4.16	Optical layout of the beam line UE112 -PGM1 (schematic). . . . .	160
4.17	Source characteristics. Photon flux at UE112. Focal spot for 100 microns exit slit . . . . .	161
4.18	Examples of transmission of a foil of 0.2 microns of Aluminium (blue) and a foil of 0.2 microns Beryllium (red) . . . . .	162
4.19	Calibration of the system for the different radiation polarisations, Linear (blue), circular positive (red), circular negative (green) . . . . .	162
4.20	XMCD measurements on the Co(40nm)/Al(5nm)/SiN(50nm) sample. The angle of incidence was 30 degrees and the maximum signal can be seen at 60 eV as expected corresponding to the M-edge of Cobalt . . . . .	163
4.21	Signal in function of the polarisation of the incident beam (from s to p at an energy of 60 eV) . . . . .	163

4.22	Raw data showing the hysteresis on the Co(100nm)/Al(5nm) sample using the T-MOKE geometry. . . . .	164
4.23	Longitudinal MOKE . . . . .	165
4.24	Measured dispersive ( $\Delta\beta$ ) and absorptive ( $\Delta\delta$ ) components of the refractive indices for Cobalt . . . . .	166
5.1	Magnetic force micrograph of the magnetic structures of the sample composed by Cobalt and Palladium. The magnetic domains presented are in aligned stripes alternating the up and down magnetic domains. The domains are in the same direction with an out-of-plane magnetisation. . . . .	171
5.2	Cross-section of the beam spectrally filtered to keep only of the harmonic 39 in Neon corresponding to 60 eV . . . . .	171
5.3	Pump probe setup. An intense IR laser pulse is split by a beam splitter resulting on a pump beam and a probe beam. The probe beam is focused by a lens onto a gas cell resulting in high harmonic generation. The IR is filtered and the remaining beam is reflected on a focusing mirror onto a monochromator onto the sample. The pump is directed onto the sample and focused by means of a lens. A CCD camera records the data. . . . .	173
5.4	Image of pump-probe set-up at salle orange. The intense IR beam is split in two at the beginning of the table. The non covered beam is the pump and the probe will be in vacuum. When the probe beam crosses the first chamber containing the gas cell harmonics are generated here portrayed in light blue. The IR will be filtered by a metallic filter and the probe will be mainly XUV radiation. . . . .	174
5.5	Set-up of HHG at LOA tuned to cover the M-edge of transition metals.	175
5.6	Interior of the interaction chamber. The probe of XUV radiation is portrayed in light blue. The pump of IR radiation is portrayed in red.	175
5.7	Magnetic scattering and domain size . . . . .	177
5.8	Resonant magnetic scattering patterns and radial integration of the intensity . . . . .	178
5.9	Demagnetisation curve obtained at salle orange (LOA). For a fluence given in $\text{mJ}/\text{cm}^2$ of 4 (represented in red), 6 (represented in green), 7.5 (represented in cyan) and 9 (represented in purple). . . . .	180
5.10	Femto-slicing measurements at BESSY-II [17] . . . . .	182

5.11	Experimental set-up (a) 15-reference gold holography mask. Aperture and references, (b) Spectro-holography: A CCD camera located 490 nm with a numerical aperture of 0.028 records in the far field, (c) reconstruction of the initial magnetic states. . . . .	186
5.12	(a) Single shot reconstruction of the nanoscale ferromagnetic ordering with a 80 femtosecond pulse, (b) and (c), the strategic placement of the references produces well-separated images of the spin-resolved electronic structure in the autocorrelation after the Fourier inversion.	188
5.13	Shot fluence . . . . .	189
5.14	Fluence thresholds on single-shot images with 360 femtosecond pulses (a) fluence plot for a single-shot sequence, (b)-(c) average reconstruction from the shots 12 to 23 and reconstruction of the shot 24, (d)-(e) average reconstruction from the shots 25 to 31 and reconstruction of the shot 33 . . . . .	191
A.1	Coherence and interferences . . . . .	199
A.2	Principle of the Young slits experiment . . . . .	200

---

**Introduction**

---

---

**Contents**

---

<b>1.1 Coherent light . . . . .</b>	<b>4</b>
<b>1.2 Synchrotron Radiation Source BESSY-II . . . . .</b>	<b>6</b>
<b>1.3 SLAC Linac Coherent Light Source (LCLS) . . . . .</b>	<b>10</b>
<b>1.4 High Harmonic Radiation . . . . .</b>	<b>13</b>
1.4.1 High Harmonic Generation set-up at LOA . . . . .	15
<b>1.5 Approach to imaging techniques . . . . .</b>	<b>17</b>
<b>1.6 X-Ray microscopy . . . . .</b>	<b>19</b>
<b>1.7 X-ray diffraction . . . . .</b>	<b>21</b>
1.7.1 X-Ray Coherent Diffraction Imaging . . . . .	22
<b>1.8 X-Ray Holography . . . . .</b>	<b>26</b>
1.8.1 In line Holography . . . . .	27
1.8.2 Fourier Transform Holography . . . . .	32

---

The quest for pushing the boundaries of our knowledge of the world leads us to explore it with different tools. Being able to observe smaller objects with a faster time range will play a major role in our times. Technologies allowing imaging of cells with unprecedented space and time resolution, with applications not only in structural biology but also in bio-material science, with the measurement of forces and motions of nanomachines etc., are among the most promising. The infrared domain reaches its limits. Nowadays ultrashort impulsions can be generated with only on optical cycle [18] and their spatial resolution is only limited by the wavelength used. The electromagnetic spectra is the basis of representation to all the types of known radiation in function of their energy or wavelength. An example is represented on Figure 1.1. The discovery of the high harmonic generation (HHG) process in the late 1980 pushed the boundaries further allowing to reach new axis of research and development.

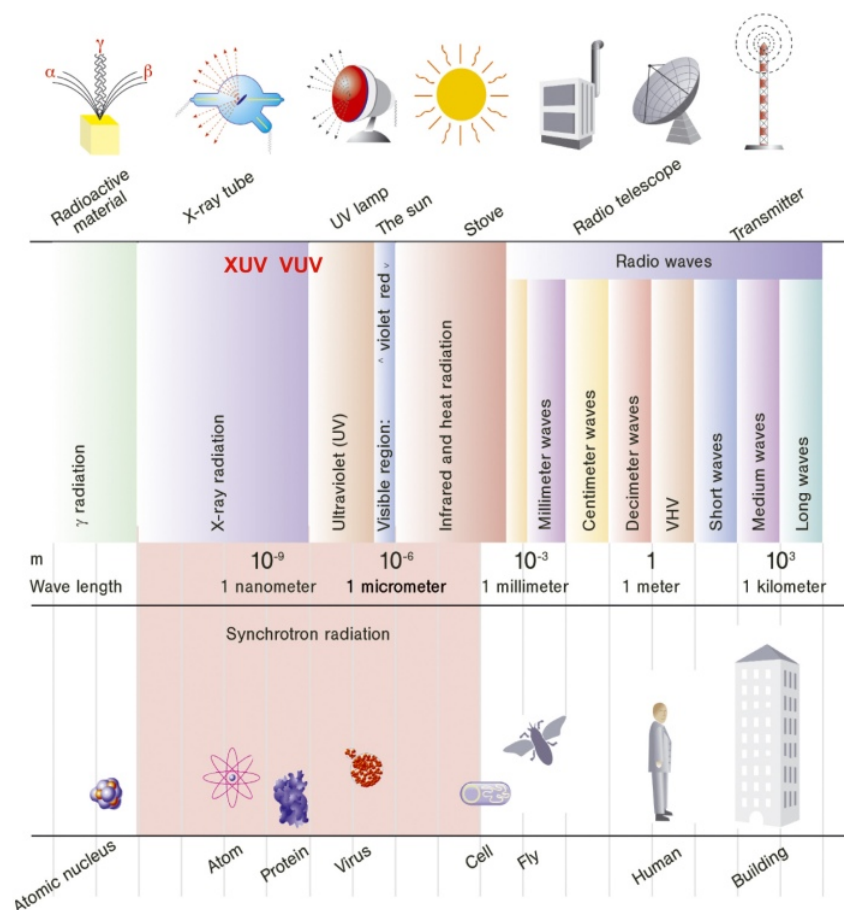


Figure 1.1: Electromagnetic spectra illustrated with sources for the radiation, its wavelength and its penetration power from *Radio waves*; lower energy to *Gamma radiation*; higher energetic.

The soft-X-ray (XUV) range has a tremendous potential for imaging, not yet fully explored. Bridging the resolution gap between optical and electron microscopy and its nondestructive qualities will allow real-time imaging. New tabletop XUV coherent sources rely on the interaction with a visible or infrared, ultra-short laser pulse at modest intensities ( $10^{14} \text{ W/cm}^2$ ) with noble gases, producing a cascade of correlated high harmonics of the fundamental laser with efficiency up to  $10^{-4}$  in the 30nm range exhibiting a high degree of coherence. Attosecond (1as =  $10^{-18}$ s) XUV sources predicted in the early 90s are already demonstrated, measured, characterised and used for applications [19].

Coherent XUV radiation allows to attain good resolution which is required for imaging. Its characteristic short wavelength offers the possibility to focus the pulse on small dimensions. Thus it opens the door to explore new divisions of particle physics not yet reached. Nevertheless this technique requires in general a high photon flux. Work in this field is still to be improved and a substantial axis of the current research is focusing on this problematic. Another important axis is the search for coherent radiation with even shorter wavelengths. Extending the source to the X-ray radiation spectra, ideally to the wavelengths of 2 nanometers (nm) to 4.4 nm, the so called *water window*, would immediately open the door to biological imaging. Being that the K absorption edge of oxygen is placed at 2.34 nm and the K absorption edge of Carbon is placed at 4.4 nm this is an area where water will be totally invisible. The *water window* would allow the study of the other absorbing chemical elements present in the biological samples.

Two techniques take advantage of the coherence of the source: diffraction imaging and holography. Diffraction imaging in the XUV has been revolutionised by Miao *et al* when the concept was extended to non-crystalline samples [20]. The feasibility of this technique was demonstrated with FELs in a single-shot [1] and more recently with table-top harmonics [21]. XUV holography also takes benefit of the spatial coherence of the HHG beam. Holography has the additional benefit of 2D imaging with depth of field (3D-like). In a study lead by LOA in collaboration with the IST group, a digital in-line holographic microscopy experiment attained a resolution of 600 nm with a HHG beam at 32nm [3]. Most recently, single-shot XUV holography has been demonstrated at DESY with the FLASH Free Electron Laser [22]. Single shot holographic imaging with a tabletop source such as High Order Harmonics has yet to be demonstrated.

## 1.1 Coherent light

Images can be formed either by coherent light or by incoherent light and have different properties depending on the way they were acquired. Coherent illumination is particularly sensible to the imperfections that might exist along the path followed by the light until reaching the detector. All the dusts on optics or defects on a filter or mirror can result in a diffraction figure that will superimpose to the actual image. For everyday imaging coherent imaging does not bring any ameliorations where its speckles can even result on a poor image. Coherent imaging is important when it can be used to treat images on the frequency domain due to the treatments made on optical elements.

Coherent radiation is widely used in research as well as on industrial applications. There are two types of coherence: spatial coherence (or transverse) and temporal coherence (or longitudinal). Figure 1.2 represents this two types of coherence in a scheme. It is understood as *coherence of a beam* the correlation between electromagnetic fields emitted on two spots of a luminous source that are apart on space or time. The *coherence of a beam* is observed by the means of the interference when covering them in an interferometric system.

The phase relation, characteristic of the coherent radiation, allows to focus on the diffraction-limit since it determines the angular limit of diffraction. This enables us to record interference images by means of interferometry or holography. Coherent beams are accessible and are already used for visible optics. The aim is to reach shorter wavelengths to meet the need for progress. As an example of applications where spatial resolution is needed we have *Lithography*, as a technique for printing and *Microscopy* as a technique to see systems. Since these applications are dependent on the wavelength of the beam, reaching shorter wavelengths will optimise the results. Synchrotrons are a reliable source of XUV radiation however they present two big limitations, its costs and its accessibility. Namely the light source can be incoherent so there is a real need to filter spatially which results in lower flux values. In alternative small sources, the so called "table top" are being developed based on the process of emission of hot plasmas that present a temperature and density sufficient to generate XUV radiation. This hot dense plasmas are created when a big amount of energy is deposited on short times. That can be easily done by the use of ultrafast lasers or electrical discharges. When emitting

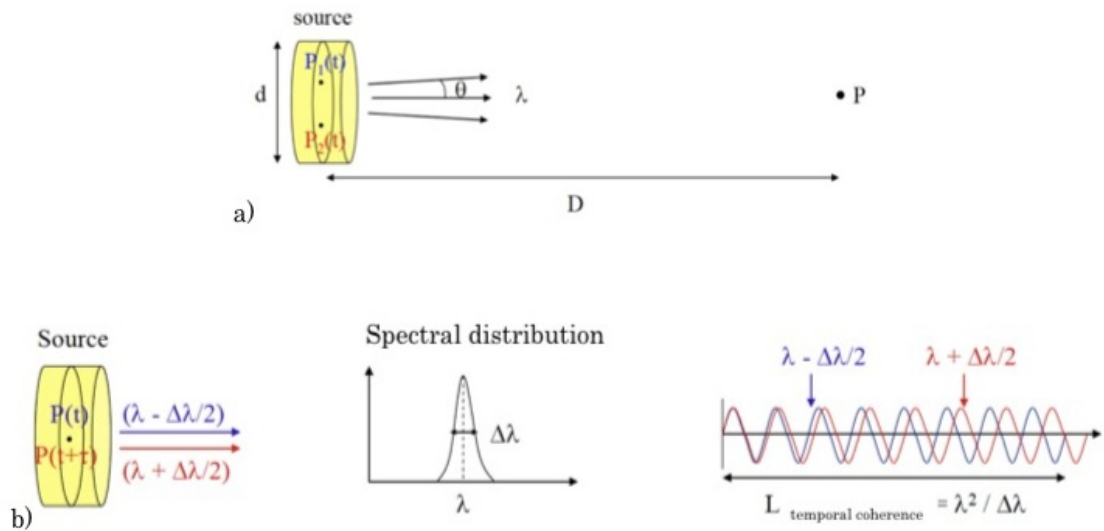


Figure 1.2: Coherence of a beam a) Spatial coherence scheme. Two distinct points taken from a beam cross section at the same instant will emit two fields that are correlated. b) Temporal coherence scheme. One point taken from a beam cross section at two different instants will emit two fields that are correlated. The temporal coherence length is the given by the propagation distance at which the two waves will show opposite phases.

the hot plasma ions can be excited to produce emission lines and when certain conditions are met an inversion of population can be produced giving birth to a laser with different wavelength than the original pulse thus creating a soft X-ray laser. High harmonic generation arrives therefore in force prompted by researchers looking for different ways to generate XUV radiation. Progresses have been made on the infrared pump used as the fundamental field. The optimisation of the high harmonic generation process itself allows it to be used as a laboratorial process to generate XUV radiation. Its intrinsically laser-like property of phase coherence surpasses the problem of filtering the radiation therefore maintaining its flux.

The applications require as well a complete set-up of optics that will allow to manipulate the beam such as collecting, transporting, focusing bearing in mind that we are dealing with coherent radiation. The materials commonly used, as an example the lenses made of  $MgF_2$  are not adequate for this wavelengths that have a bigger penetration depth. In the XUV region there are no such materials as lenses. Even the metallic materials so *in vogue* in our laboratories are relatively transparent to certain wavelengths and their refraction indexes are so close to the unity that no important refraction occurs. This refraction index close to 1 induces

in every interface the occurrence of a small reflexion. Specific XUV optics were developed in the last decades and nowadays common refractive lenses can be replaced by diffractive optics of the type of Fresnel lens, and metallic mirrors can be replaced by multilayer mirrors. Those advances have been fundamental in the development of optic systems operating at this spectral range. Going further to the hard X rays, the lack of optics is even more felt due to the enormous penetration power of this type of radiation. Therefore the quality of images obtained from this domain is limited. Until now the highest spatial resolution has been obtained with an XUV microscope.

The XUV spectral bandwidth we will tackle in this thesis englobes radiations from 10 nm to 40 nm that in terms of energy correspond to an energy range of 30 eV to 150 eV. In this introduction chapter the main sources of coherent XUV radiation will be presented. They were all used for this work in different facilities. High harmonic generation radiation was used at Laboratoire d'Optique Appliquée (LOA), synchrotron radiation was used at the synchrotron radiation source BESSY-II and free electron laser radiation was used at SLAC Linac Coherent Light Source (LCLS). The principle of the sources will be explained on the next sections. In this range the most used and reliable source nowadays is the synchrotron.

## 1.2 Synchrotron Radiation Source BESSY-II

The most commonly used source of XUV radiation is the synchrotron radiation. The physical process of generating radiation starts on an accelerator ring where an accelerated charged particle bunch, most commonly a relativistic electron accelerated in a magnetic field. This particle reaching a velocity close to the light velocity  $c$  emits radiation in a cone that is tangent to the trajectory of the particle. Due to the velocity of the electrons a Doppler shift is induced therefore the radiation emitted presents a large spectra that can be extended until the hard X-rays. As magnetic structures we can find, bending magnets, undulators and wigglers. Synchrotron facilities have been built all over the world for its power for research and its range of short wavelengths of the electromagnetic spectra. They are however not a coherent source. Additional filtering must be added at the exit of the beam. The very large average flux of photons allows a very strong spatial filtering so that the radiation provided is diffraction limited.

Electrons are relatively easy to accelerate due to their high electric charge and their small mass. These electrons can then be accelerated by means of an electric potential (voltage). At BESSY-II electrons can be accelerated until 1.7 GeV (X-ray regime) reaching a velocity of almost  $3 \times 10^8$  m/s, the velocity of light.

For synchrotron radiation the speed of the electrons is important. The time in which they reach their velocity is less important. The electrons at BESSY-II reach the maximum possible velocity since particles with mass can come close to the velocity of light but can never actually reach it. If one approaches light-velocity, the energy that normally is used for the acceleration, is converted into mass. The mass increase is expressed with the Lorentz factor gamma. The Lorentz factor  $\gamma$  is important for the properties of synchrotron radiation and it can be written as:

$$\gamma = \frac{1}{(1 - \sqrt{\frac{v^2}{c^2}})^{1/2}} \quad (1.1)$$

where  $v$  is the velocity of the particle and  $c$  the velocity of light.

In normal life it is impossible to notice the relativistic effect. But at BESSY-II the electrons, however, approach the velocity of light. Hence, the effect is strong.

BESSY II has a circumference of 240m, providing 46 beam lines, and offers a multi-faceted mixture of experimental opportunities (undulator, wiggler and dipole sources) with excellent energy resolution. The combination of brightness and time resolution enables both femtosecond time *femtoslicing* and picometer spatial resolutions. Figure 1.3 presents an air view of BESSY-II as well as the scheme of its beam-lines.

BESSY-II generates a 70 kV electron beam. Before injection in the main storage-ring the beam is accelerated over a microtron and a synchrotron to its final energy of 1.7 GeV. The microtron enables to provide high-energy electron beams with a low beam emittance (no radiation equilibrium) and a high repetition rate (equal to the operation frequency of the linac). Microtrons are designed to operate at constant field frequency and magnetic field in the ultra-relativistic limit. Thus they are especially suited for very light elementary particles, namely electrons. Particles in a classic microtron get emitted from a source and accelerated once per turn,

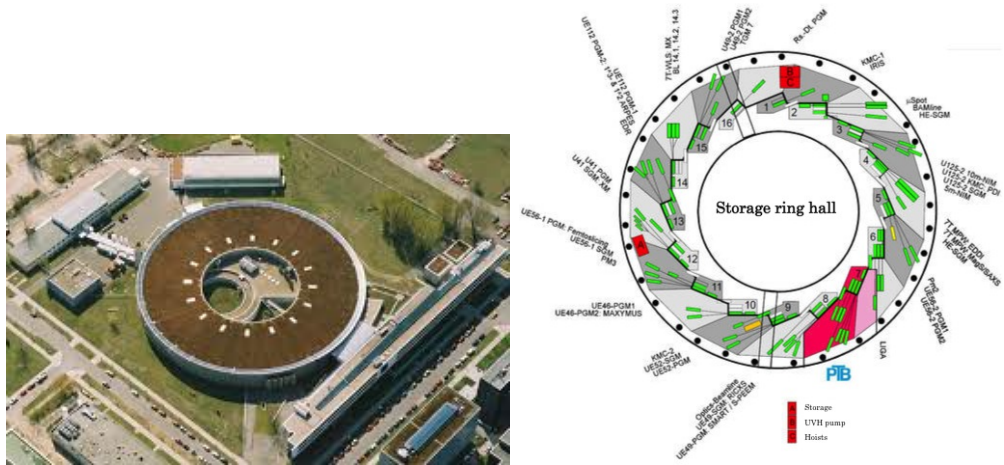


Figure 1.3: BESSY-II at Berlin a) BESSY-II top view. b) Beamline scheme

increasing their path radius until ejection. The synchrotron is a particular type of a cyclic particle accelerator on which the particles are bent by a guiding magnetic field that is time-dependent and synchronised in order to form a particle beam of increasing kinetic energy. Bending, beam focusing and acceleration are separated into different components such it is a large-scale facility. A scheme of a standard synchrotron is presented on the Figure 1.4.



Figure 1.4: Scheme of principle of a standard synchrotron.

The accelerating process takes  $50\text{ms}$  and can be repeated with a repetition rate of  $10\text{Hz}$  or higher. The total current in the storage ring of  $100\text{mA}$  or higher can be obtained by successive injection of electrons, accelerated in multiple accelerating

cycles.

Due to the high voltage at BESSY-II an electrostatic acceleration is not practical. As an alternative it employs micro-waves or, more accurately, radio-frequency *rf* waves. The *rf* – waves are stored in a *rf* – cavity. Electrons entering this cavity at the correct moment feel an accelerating force. Electrons can only be accelerated, however, when they enter at the maximum of the beam. They can thus only be accelerated at specific periods in time. The *rf* – accelerated electron-beam is therefore not continuous but consists of a train of short pulses. However for the major part of the detector used (CCD cameras for instance) this radiation is considered as continuum. The beam obtained can be polarised linearly or circularly.

There are several accelerator types. For low accelerating voltage, e.g., for TV's or X-ray tubes, the electrostatic accelerator is the most economic. In the linear accelerator a lot of *rf* – cavities are put after each other such that an electron bunch may be accelerated successively in each cavity. Linear accelerators have the advantage that they can accelerate a lot of current to very high energy. At high energy they become very costly, though. Alternative to the linear accelerator one may also bend the electron back to the entrance of the accelerator.

Energy losses inherent to the emission of synchrotron radiation are compensated at the level of the storage ring by *rf* – cavities. The storage ring is the largest component at BESSY II. Other components are important for the accelerating process. Magnets ensure that the electrons may circle in the storage ring. The main components are the dipoles (32x), the quadrupoles (144x) and the sextupoles (112x). The dipoles enable the circular orbit of the electrons. The quadrupoles compensate the natural behaviour of electrons to drift apart. Sextupoles make small corrections on the quadrupoles and are important for storing the beam over a longer period of time.

Electrons may scatter on atoms in the air. To avoid this the electrons are kept in a draining pipe. Inside this pipe the regime is the ultra-high vacuum with a pressure of about  $10^{-9}$  mbar.

The amount of synchrotron radiation is proportional to the stored beam current. In order to keep the current high there is a need to reduce the loss of electrons.

This can be compensated using radiation with a large life-time. At BESSY-II the design allows to reach a life-time of eight to ten hours followed by breaks for injection of around one hour.

### 1.3 SLAC Linac Coherent Light Source (LCLS)

For harder radiation the most emblematic and innovator X-ray source nowadays is the X-ray free electron laser LCLS [23] (Linac Coherent Light Source) in California that started operating on 2009. It has the ability to reach the *hard X-ray* region maintaining its short pulses. It is capable to deliver photons of energies between 540 eV and 9 keV translated on a range of wavelengths from 2.3 nm to 1.4 Å. It provides an impulsion of 3mJ maximum in some femtoseconds with a repetition rate of 60Hz. Other free electron lasers (FEL) in the X-ray domain are being built such as: European XFEL [24] in Germany and the SCSS [25] in Japan.

Free electron lasers are based on synchrotron radiation that is emitted by a relativistic electron bunch when following a circular trajectory. Its principle of actuation is to make the synchrotron radiation coherent by means of an interaction of an electron beam stored in the source in a magnetic structure denominated undulator, such is shown on figure 1.5.

An undulator is a constituent that forces the electrons to oscillate in a transversal way therefore creating electromagnetic radiation. The first theoretical works on the spontaneous emission of such a system date back to 1950 [26] such as the first observation of incoherent radiation at visible and millimetric wavelengths [27]. It has been only on the 1970s that the interest of the scientific community on the use of an undulator started once a thin gain regime was predicted due to the interaction between the electron beam and the radiation emitted by it [28]. The first observation for a laser effect on the infrared domain was demonstrated some years later [29].

The first FEL were constituted of an unique undulator placed in an optical cavity. Their capabilities of extension to the XUV and X regime are limited by the fact that there aren't much available optics for this electromagnetic regime. However the use of higher electromagnetic currents and electronic beams of poor emittance allows to reach a strong gain regime on which the power of the radiation emitted

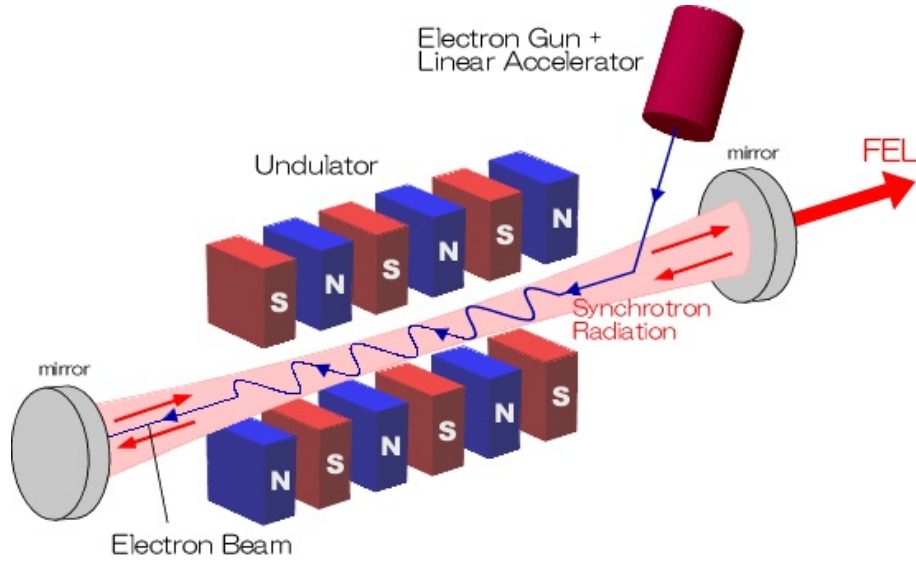


Figure 1.5: Free electron laser principle. As the electrons arrive the undulator they present an aleatory phase. The radiation emitted is incoherent. As the electrons interact with the radiation *bunching* occurs. The train waves emitted are now in phase and the radiation is amplified in a coherent

increases exponentially with the distance travelled by the electron beam and the wave. FEL amplification is therefore accomplished in a simple passage through several undulators. This regime of functioning is called SASE as in *Self-Amplified Spontaneous Emission* as a reference to traditional lasers [30].

The FEL gain is a positive retroaction process. The electrons emit a radiation that affects their speed and the whole effect is in fact a modulation of the electronic density in the direction of the beam. The electrons will emit an *in phase* radiation that becomes more intense and coherent. While the synchrotron radiation spectra is relatively large only certain wavelengths interfere constructively and can therefore be amplified in a FEL. This wavelength  $\lambda_p$  are given by:

$$\lambda_p = \frac{\lambda_0}{2p\gamma_0^2} \left( 1 + \frac{K^2}{2} \right) \quad (1.2)$$

where  $\lambda_0$  is the undulator period,  $\gamma_0$  the energy of the electron beam normalised to the fundamental and  $K$  is a parameter of the undulator, function of the applied magnetic field and its spatial period. The fundamental wavelength corresponds to  $p = 1$  and represents the highest gain. For  $p > 1$ , the wavelengths are called non-linear harmonics and are irradiated with several order of magnitude less than

the fundamental.

The SASE radiation provides an intense photon beam and with good transverse coherence quality but its temporal coherence properties are limited. Indeed the generation of synchrotron radiation noise induces packets that intervene randomly at different positions of the packet. The temporal and spacial profiles of the emitted radiation are then composed with structures called *spikes* that are translated on important statistic fluctuations.

In the XUV domain we can cite FLASH [31] in Germany, that can deliver pulses of several hundreds of  $\mu\text{J}$  in some tenths of  $fs$  at a wavelength that can reach the  $3nm$ . For larger wavelengths ( $50nm$ ) the SCSS Test Accelerator in Japan, delivers pulses of some  $\mu\text{J}$  in some hundreds of  $fs$ . In the VUV regime ( $160nm$ ) there is SPARC [32] in Italy that delivers impulsions comparable to those of the SCSS.

Reaching such outstanding performances this installations are necessarily of a large scale. The need of an linear accelerator plus the undulatory is translated in to several kilometres of space as it can be viewed on the figure 1.6 that represents an air view of the LCLS site in Stanford and a view of the LCLS hall of ondulators.

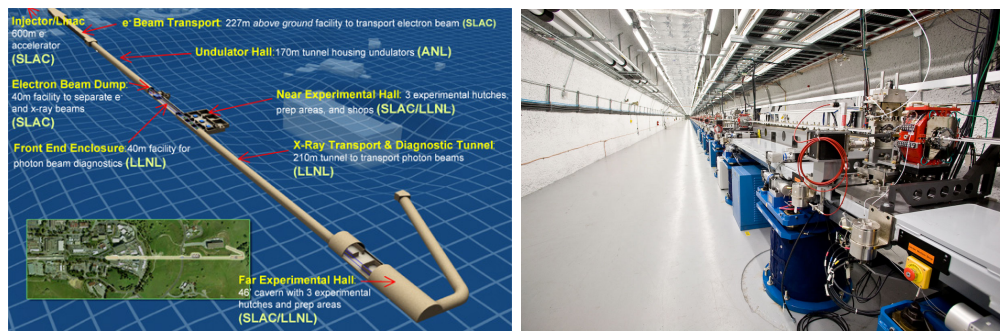


Figure 1.6: LCLS at Stanford a) LCLS top view. b) Undulator hall, Undulator hall (130 m of undulator to produce photons  $9keV$ )

Several studies are being performed with the aim of using a total wavelength smaller in order to obtain the same number of photons, that is to saturate the system earlier and to change radically the temporal and spectral structure of the radiation emitted. This is so called harmonic injection technique [33]. The only FEL in service being injected by harmonics are the SCSS Test Accelerator, the SPARC and the FERMI.

## 1.4 High Harmonic Radiation

Overall it becomes clear that a coherent XUV source in a femtosecond time duration and with a table-top set-up opens a vast area for new applications and will allow a better diffusion of this technique in small laboratories worldwide outside synchrotrons. High Harmonics as a XUV source is also of importance when dealing with pump-probe set-ups since it is jitter free and aberration free [10].

The radiation source present at LOA delivering energy pulses for high harmonic generation on gases is based at *salle rouge*. It is a system entirely based on a sapphire crystal doped on titanium (Ti:Sa) and uses the technique of chirped pulse amplification as a way to amplify its frequencies. It delivers  $45\text{fs}$  pulses at a wavelength of around 815 nanometers with a cadence of  $1\text{kHz}$ . This repetition rate is particularly well adjusted to the high harmonic generation. At  $35\text{fs}$  few millijoules are enough to generate effectively harmonics thus allowing high repetition rates. The average harmonic flux per second is then increased in a simple way in relation to sources with a lower repetition rate. In our experimental set-ups the energy per pulse has varied from 4 to 7 mJ and the beam diameter, measured in parallel at the beam exit and measured in the sense of the gaussian beam ( $1/e^2$  of the maximum intensity) is of  $22\text{mm}$ , thus a brilliance of around  $2\text{mJ}/\text{cm}^2$ . In this case the laser intensities are fair enough to allow us to work in the air, therefore making easier possible modifications.

The technological choices done in the laser chain have consequences on the efficacy of high harmonic generation. For starters the one saying that a highly non linear effect is very sensible to the intensity created reached by the impulsion, intensity that is inversely proportional to the duration of the fixed energy impulsion. We have also seen that the importance of the quality of the contrast of the laser impulse, measured between the principal peak and the background of the impulsion. Indeed parasite impulsions of enough energy can provoke a partial ionisation of the gaseous media, without however generate efficiently harmonics. They can induce complex propagation effects and perturb the phase match at the passing of the principal impulsion. The brightness except at the focus of the laser is highly dependent on the regularity of the spatial wavefront of the beam.

On the figure ?? a scheme of the installation of the various parts constituting

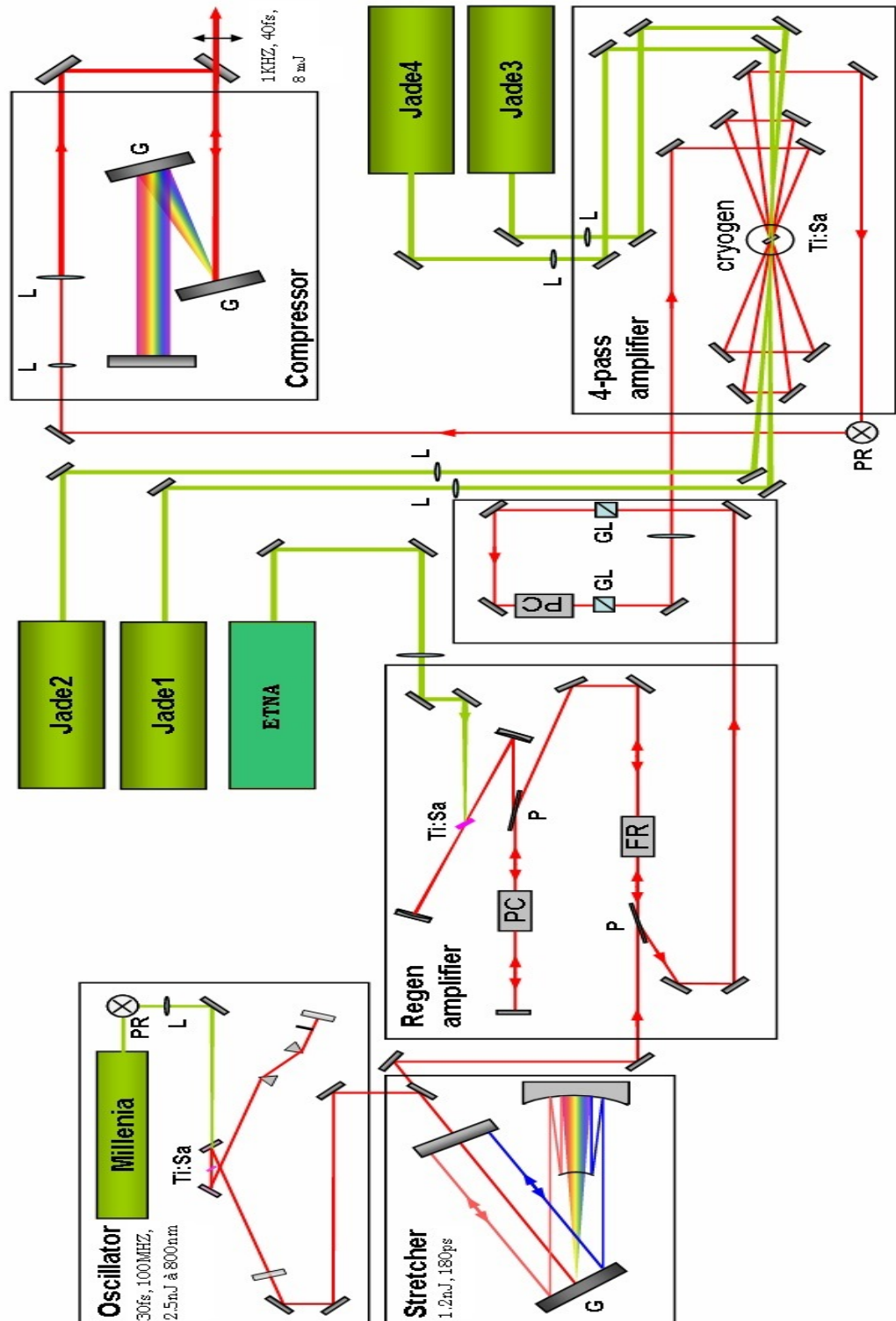


Figure 1.7: Laser chain installation used. Salle Rouge at LOA

the laser of the salle rouge is represented.

The first element of the laser chain is the oscillator, that delivers a train of pulses of some nJ at a duration of 15 femtoseconds at very high repetition rate (100 MHz).

Before amplification the pulse is stretched until 100 picoseconds in a stretcher based in the principle of an Offner triplet. The interest of the Chirped Pulse Amplification (CPA) technique is of stretching in a perfectly controlled way the femtosecond pulses to allow the amplification without the creation of non-linear effects due to the intensities achieved, or even a deterioration of the different optical elements composing the laser chain (gratings, mirrors, crystals, etc [34]. It is sufficient then in the end of the chain to compress the pulse to a duration of a few tens of femtoseconds by the inverse process of stretching.

The compressor situated in the end of the chain is constituted by two diffraction gratings. Their high reflectivity allow to limit the absorption of energy therefore to diminish the thermal effects that can induce a temporal and spatial deformation of the pulse.

#### 1.4.1 High Harmonic Generation set-up at LOA

There are different kinds of harmonic installations. Either one of them has specific characteristics that have to be met.

The high harmonic generation method can be either, in a cell, a capillary, a jet or in a solid target. It is the result of an highly non-linear interaction between an intense laser field and the atoms of a target. This radiation is constituted as its name indicates by several frequencies multiples of the frequency of the wave of the generating laser. The detection or its further application implies precise technological choices. The object of our studies is also a determinant factor. If we want to use all the harmonics in a packet or only a single one in which case we use diffraction gratings or multilayer mirrors or monochromators to enable the selection. If there is a need to maximise the flux the chosen instrumentation will be different as well.

In this work the harmonic generation device is a gas cell, that can be used with different noble gases. There are different kinds of spectrometers, in transmission

or in reflection and the detection is chosen as a function of the wavelength in study.

A big problem is exactly the wavelength that can reach the detector. Since, if non subtracted, the infrared radiation will reach the detector and therefore damage it. There is a need to eliminate the IR radiation from the propagation axis of the harmonics. Different ways can be implemented, in our experimental room *salle orange* due to our experimental conditions such as the optical table layout the choice was the use of metallic filters. One other alternative would be the use of Micro-channel-plates (MCP) that is insensitive to IR radiation but sensitive to harmonic wavelengths however it represents a higher cost.

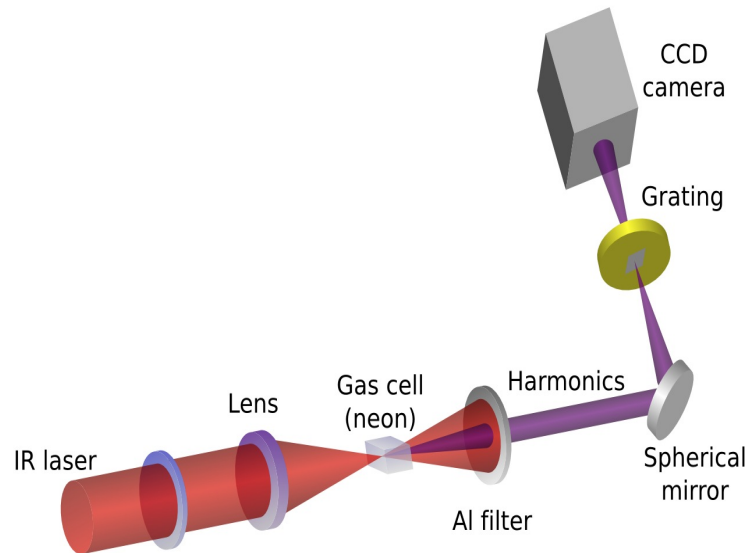


Figure 1.8: Scheme of the principle of installation of an High Harmonic Generation (HHG) line using Neon at *salle orange*

A general High harmonic generation experimental set-up is presented in the figure 1.8. The laser arrives from *salle rouge* and enters *salle orange* propagating in the air. At the beginning of the set-up a diaphragm is placed on the laser path in order to adjust the energy or the geometry of the focus. Later the beam is focalised using a 1.5 meter  $MgF_2$  lens, material that prevents eventual non linear effects of the Kerr type. The focus of the laser is located in the proximity of the gas cell, slightly after, and the gas cell is placed under vacuum. Harmonics are then generated in the cell and are emitted collinearly to the infrared beam and propagate under vacuum. The filters are placed as further as possible to avoid the deterioration effects of the IR laser intensities. A analysis device is then placed, such as a spectrometer or another experiment that will use the harmonics obtained

as a XUV source. The detector can be either an XUV CCD camera, a photo-diode or even a MPC.

## 1.5 Approach to imaging techniques

The creation of visual representations of objects, for the purpose of medical diagnosis or data collection, using any of a variety of usually computerised techniques is denominated *Imaging*. The imaging chain is the foundation of imaging science. A conceptual model describing all of the factors which must be considered when developing a system for creating images. In general, an imaging chain includes the human visual system; the subject of imaging; the capture device; the processor and the display. The subject of image will be the limitative asset on the choice of the capture device. On the history of mankind two big fields were developed in view of progress on the understanding, by imaging, of the world named *Light microscopy* and *Photon microscopy*. Figure 1.9 shows the most important milestones on light microscopy and photon imaging. Light microscopy was born 500 years ago however photonics imaging, by means of holography or laser technology, had its outcome in the 1950s-1960s. In about one tenth of the time the photonic technique has evolved and even surpassed the light microscopy technique as a result of its good resolution. Light microscopy is now studying ways to respond. Presented in Milestone 21 *Stimulated Emission Depletion Microscopy (STED)* fluorescent dyes are used to overcome the resolution limit and therefore keep up the pace with its "competitor".

Physically a system's resolution is limited by its operating wavelength. Therefore working on the XUV domain allows automatically a better spatial resolution. Its penetration power is also bigger what opens the door to observing whole samples without the need to cut them in thin slices and therefore evolve to a most simple and fast way to retrieve images.

One of the biggest targets in this field of interest, as said before, is to reach the *water window*. The water window is of extreme importance on biological applications due to the fact that in this window, so to say, water is invisible it absorbs less than carbon, the main constituent of biological material. Figure 1.10 shows the attenuation length in microns of an average cell. The cell composition can be

Biological Milestones Timeline		Photon Milestones Timeline	
1595	Invention of the microscope (M1)	1600s-1800s	Debate on the character of light (M1)
1858	First histological stain (M2)	1861	Maxwell's equations (M2)
1871	Synthesis of fluorescein (M2)	1900	Planck's theory of black-body radiation (M3)
1873	Diffraction limit theory (M3)	1905	Special relativity (M4)
1911	First fluorescence microscopy (M4)	1923	Compton effect (M5)
1929	First epifluorescence microscope (M4)	1947	Quantum electrodynamics (M6)
1935	Phase contrast microscopy (M5)	1948	Holograms (M7)
1939	Polarisation microscopy (M6)	1954	Solar cells (M8)
1942	Immunofluorescence (M7)	1960	The laser (M9)
1955	Differential interference contrast (M8)	1961	Nonlinear optics (M10)
1961	Concept of confocal microscopy (M9)	1963	Quantum optics (M11)
1967	The dichroic mirror (M4)	1964	Bell inequality (M12)
1972	Fluorescence correlation spectroscopy (M10)	1966	Optical fibres (M13)
1976	FRAP (M10) FRET (M11)	1970	CCD cameras (M14) Semiconductor lasers (M15)
1980	Calcium probes (M12)	1981	High-resolution laser spectroscopy and frequency metrology (M16)
1981	Video-enhancement differential interference contrast (M8) TIRF microscopy (M13)	1982-1985	Quantum information (M17)
1983	Deconvolution microscopy (M14)	1987	Photonic crystals (M18)
1987	Realisation of confocal microscopy (M14)	1993	Blue light-emitting diodes (M19)
1990	Two-photon microscopy (M15)	1998	Plasmonics (M20)
1993	Light sheet microscopy (M16) Single molecule microscopy (M17)	2000	Metamaterials (M21)
1994	GFP (M18)	2001	Attosecond science (M22)
1997	Fluorescent protein-based biosensors (M19)	2006	Cavity optomechanics (M23)
1999	Red fluorescent proteins (M20)		
2000	Breaking the diffraction limit: STED (M21)		
2002	Photoactivatable fluorescent proteins (M20)		
2006	Breaking the diffraction limit: PALM/STORM (M21)		

Figure 1.9: Milestones on imaging techniques. a) Light microscopy; b) Photon imaging.

estimated as  $H_{230}O_{100}C_{30}N_{10}P_{<1}S_{<1}$  with the water content of the cell being around 70%. It can be seen that it is a rich area for biological contrasts. Biological imaging in this wavelengths will be even more within reach.

XUV imaging can be reached using either light microscopy or photon imaging. In terms of imaging techniques new horizons are being reached such as XUV holography, XUV diffraction, XUV interferometry and micro-focussing. The demand on the source is pushed even further with the pump-probe set-ups required. In the following sections of this introduction some of this techniques will be presented as well as its pertinence to the overall goal of this work.

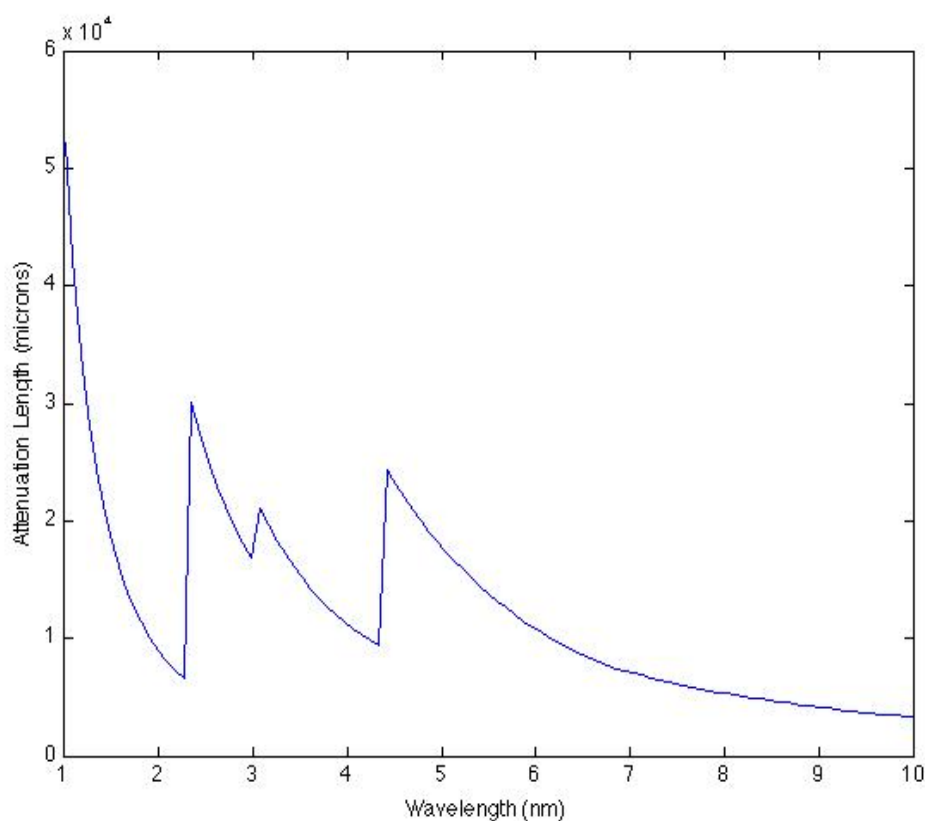


Figure 1.10: Attenuation length of the model cell  $H_{230}O_{100}C_{30}N_{10}$  for the wavelengths of 1-10 nanometers. Data from Center for X-ray Optics (CXRO).

## 1.6 X-Ray microscopy

High resolution X-Ray imaging of general nonperiodical structures is an area in which much progress has been made in recent years. In terms of specimen size and imaging resolution, X-ray microscopy lies between electron and light microscopy, and is thus suited to image extremely large and complex structures. In addition, it demands little or no specimen preparation since while electron microscopy is widely used to obtain images with nanometer level resolution the samples have to be chemically fixed, dehydrated and embedded in resin, then prepared in ultra thin slices. Therefore the relatively thick living cell cannot be observed. X-ray microscopy can also be used to observe local composition and chemical state as well as structure. It has an advantage over conventional electron microscopy in that it can view biological samples in their natural state. Thus X-rays, which have played the leading role in imaging crystallisable materials, may also prove to be

highly valuable in the imaging of very large non-crystalline structures. Throughout this chapter, attention is paid to the relationships connecting the subject with X-ray crystallography, as it has emerged in recent years, in relation to the established imaging methods.

With regard to the techniques by which imaging is accomplished, it will be noted that X-ray crystallography uses diffraction analysis as its central imaging methodology, while electron and light microscopies use focusing optics as their principal technique.

Sources of soft X-rays suitable for microscopy, such as synchrotron radiation sources, have fairly low brightness for the required wavelengths so an alternative method of image formation is a scanning transmission soft X-ray microscopy. The X-rays are focused to a point and the sample is mechanically scanned through the produced focal spot. At each point the transmitted X-rays are recorded with a detector such as a proportional counter or an avalanche photodiode. This technique is called Scanning Transmission X-ray Microscope (STXM). A scheme of a set-up of X-ray microscopy is presented on figure 1.11.

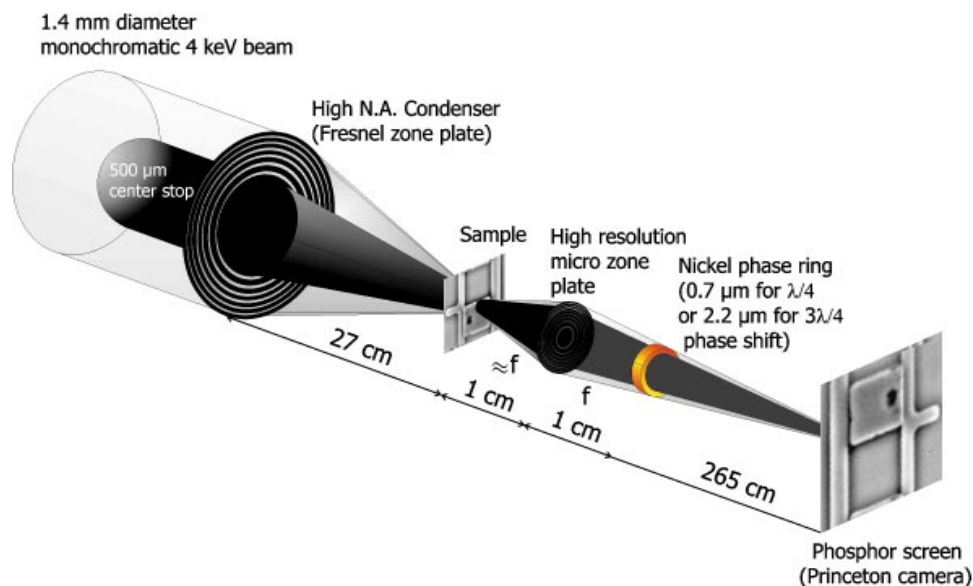


Figure 1.11: Example of a X-ray microscopy set-up. A zone plate focuses the monochromatised undulator beam onto the object and a micro zone plate objective forms a magnified image on a CCD camera. The phase ring selectively shifts the undiffracted light of the object.

This technique has the advantage of a 3D image reconstruction since several images corresponding to several angles can be taken. A computerised reconstruc-

tion can be done in order to recreate the tridimensional visual of the object. Until now, resolutions of 30 nanometer were possible using the Fresnel zone plate lens which forms the image using soft x-rays emitted from a synchrotron. However Fresnel zone plates come at high costs limiting the use of this technique. X-ray microscopy was not used directly in the course of this work.

Recently, the use of soft x-rays emitted from laser-produced plasmas rather than synchrotron radiation is becoming more popular.

## 1.7 X-ray diffraction

Diffraction occurs as waves interact with a regular structure whose repeat distance is about the same as the wavelength. The phenomenon is common in the natural world, and occurs across a broad range of scales. One of the advantages of imaging by diffraction is that the image given corresponds to the complex transmittance of the object.

X-Diffraction will be used on the course of this work on nanometric samples therefore on the *Fraunhofer regime*. Fraunhofer diffraction deals with the limiting cases where the light approaching the diffracting object is parallel and monochromatic, and where the image plane is at a distance large compared to the size of the diffracting object. This far-field diffraction is described quantitatively by the formula:

$$z \gg \frac{a^2}{\lambda} \quad (1.3)$$

where  $z$  is the distance to the diffraction point;  $a$  is the characteristic dimension of the object and  $\lambda$  is the wavelength of the illuminating wave.

Diffraction happens when a propagating wave encounters small obstacles resulting in a spreading out of waves past small openings. Its effects are generally most pronounced for waves where the wavelength is roughly similar to the dimensions of the diffracting objects. If the obstructing object provides multiple, closely

spaced openings, a complex pattern of varying intensity can result. This is due to the superposition, or *interference* therefore an highly coherent beam is required. This coherent beam is generated at the source, such as a synchrotron, FEL or high harmonic generation since it has to maintain its coherence properties until diffraction.

On *X-ray coherent diffraction imaging* each dot in the diffraction pattern corresponds to the coherence interference of scattered X-ray passing through the obstacle.

### 1.7.1 X-Ray Coherent Diffraction Imaging

The X-ray coherent diffraction technique is a so called *lensless* technique. Its principle of function relies on the interference of a coherent beam with an object, giving birth to a scattered beam that will produce a diffraction pattern on a detector. This recorded pattern is then used to reconstruct an image via an iterative feedback algorithm. The advantage in using no lenses is that the final image is aberration-free and so the resolution is only due to diffraction and it is dose limited (dependent on wavelength, aperture size and exposure). A simple Fourier transform retrieves only the intensity information but not the phase therefore being insufficient to create an image directly from the diffraction pattern. The retrieval of the phase presents a problem.

As said before there are two relevant parameters for diffracted waves: amplitude and phase. When a diffraction pattern is collected, the data is described in terms of absolute counts of photons or electrons, a measurement which describes amplitudes but loses phase information. The diffraction pattern can give us the information on the *dimensions of the object*: the angular spacing of the features in the diffraction pattern is inversely proportional to the dimensions of the object causing the diffraction; and its *periodicity*: When the diffracting object has a periodic structure, for example in a diffraction grating, the features generally become sharper. As an example the diffraction pattern of a perfect crystal is symmetric so the inverse Fourier transform of that pattern is entirely real valued which makes the reconstruction easier.

An example of a diffraction pattern and the original image from which it was

retrieved is presented on Figure 1.12.

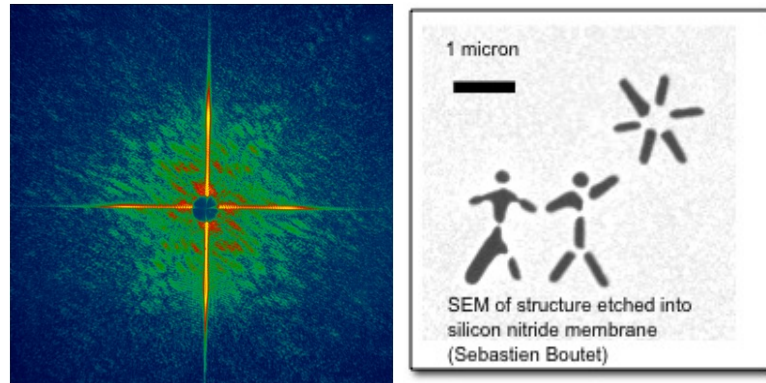


Figure 1.12: X-ray Diffraction: a) example of a diffraction pattern. b) its original image [1]

The diffraction pattern on Figure 1.12 can be reconstructed into an image retrieving the information of the phase by iterative algorithms. However retrieving a 2D image by X-ray diffraction is not an immediate process. For instance it requires a mask, meaning that we need to know beforehand the object we are imaging and several images and a minimum of 10000 shots. If we take a image each second we will need seven hours to be able to reconstruct the object. A way to ameliorate damage tolerance may be to extend it to new limits with extremely intense photon pulses with ultra-short durations. in the way that the energy is deposited fast and efficiently enough to extract the information.



Figure 1.13: Reconstruction of the diffraction pattern represented on figure 1.12 [1]

However there is still the problem of the *phase recovery*. Two solutions were so far presented: the first retrieval algorithms were demonstrated in 1999 by Miao [35] and secondly tomographic studies that were already performed.

*Phase recovery algorithms:* In order to reconstruct an image the first step is to generate random phases and combine them with the amplitude information from the reciprocal space pattern. Then a Fourier transform is applied back and forth to move between real space and reciprocal space with the modulus squared of the diffracted wave field set equal to the measured diffraction intensities in each cycle. By applying various constraints, by means of a mask that depends on the experimental setup and the sample to be imaged the pattern evolves into an image after hundreds or thousands of iteration cycles since diffraction patterns must be recorded under oversampling conditions to be able to solve the phase problem. The object to be imaged has to be isolated and can be initially assumed to reside in a region no larger than roughly the beam size. In most cases the support constraint imposed is *a priori* in that it is modified by the researcher based on the evolving image. In theory this is not necessarily required and algorithms have been developed [36] imposing an evolving support based on the image alone using an auto-correlation function. This eliminates the need for a secondary image (support) thus making the reconstruction autonomic.

*Tomography:* This procedure uses X-rays to produce tomographic images or *slices* of the object in study. Digital geometry processing is used to generate a three-dimensional image of the inside of an object from a large series of two-dimensional X-ray images taken around a single axis of rotation. Figure 1.14 shows an example of the steps involved in a tomographic reconstruction.

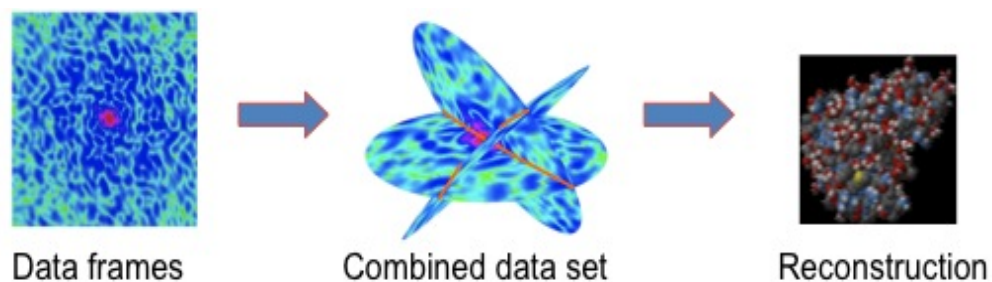


Figure 1.14: In a tomographic process there is a need to acquire several measurements in different angles in order to reconstruct the tridimensional image.

There are several steps involved in a tomographic set-up: X-ray slice data is generated using an X-ray source that rotates around the object; X-ray sensors are positioned on the opposite side of the circle from the X-ray source to collect the data. Many data scans are progressively taken as the object is gradually passed through the gantry. Once the scan data has been acquired, the data must be pro-

cessed using a form of tomographic reconstruction, which produces a series of cross-sectional images. An internal model of the scanner's physical properties and of the physical laws of X-ray interactions is used in order to retrieve information the result is images with improved resolution, reduced noise and fewer artefacts, as well as the ability to greatly reduce the radiation dose in certain circumstances. The disadvantage is a very high computational requirement, which is at the limits of practicality for current scan protocols and the amount of radiation deposited on the sample. In order to have high resolution imaging a higher number of acquisitions have to be made which can lead to the death of a biological material when used. In general the diffraction pattern will be modified by the radiation. Induced radiation damages of the XFEL utilisation can be seen at figure 1.15 [2] using as a biological material a lysozyme. This study has been performed using as source a beam of  $3 \times 10^{12}$  photons at  $12 \text{keV}$  and in a 100 nanometers focus. The sample shows clear degradation ending up to be totally destroyed over time. Cooling may slow the sample deterioration but cannot hold the damages the required time to perform a measurement.

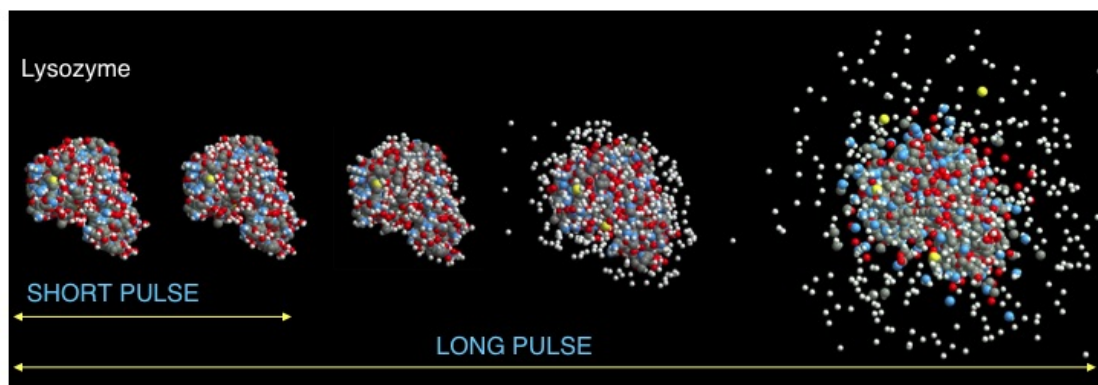


Figure 1.15: Evolution of the sample with irradiation time. With a short pulse of 2 femtoseconds and a long pulse of 50 femtoseconds. [2]

In general the resolution of a lensless system is *diffraction limited* that is by the numerical aperture and the propagating wave wavelength. In more practical terms the biggest limitation is the signal engraved as a diffraction pattern and the ability to recover this information. Since it is the inversion of the pattern of diffraction that allows to retrieve the information. The resolution can be then taken as the maximum diffraction angle to which the signal to noise ratio (SNR) allows to extract the information necessary to the reconstruction.

The second path allowing to retrieve phase information is the Fourier Trans-

form Holography (FTH) where a punctual source superimposed to the object allows to encode the phase information by interference on the diffraction figure, creating an hologram. In holography, the reconstruction of the scattered complex-valued object wave is directly provided by a well-defined reference wave that must cover the entire detector area which often is an experimental challenge. With the phase information available, the condition of oversampling of diffraction patterns becomes obsolete, and the phase problem can be solved in a fast and unambiguous way.

## 1.8 X-Ray Holography

In 1948, Dennis Gabor proposed a new procedure for imaging on two steps based on lensless imaging [37]. The physical principle was of superimposing a coherent light as a reference suitable to the light diffracted by an object, information concerning the amplitude and phase of the diffracted wave can be recorded even if the photographic film can only "see" the intensities. It is demonstrated that such an interference diagram most commonly called *hologram* can be used to obtain an image of the original object. This technique for image formation called most commonly *holography* has a large field of applications being of first importance nowadays in the theory of image formation.

Holography enables three-dimensional images to be made. It involves the use of a laser, focusing, interference, diffraction, light intensity recording and suitable illumination of the recording. The first stage of holography consists in recording a fringe pattern coming from the interference between a reference wave and the beam scattered by the sample. If the differential path between the two waves is larger than the temporal coherence length, then there is a loss of the fringe contrast that in turn degrades the spatial resolution. The far field diffraction of the object is recorded. The image is less sensitive to aberrations provoked by optical elements. When a hologram is illuminated by a proper light source, the exact amplitude and phase is reconstructed and the original light field recreated. Since the observer has the whole light field available, the genuine three dimensional sensation is achieved. The image changes as the position and orientation of the viewing system changes in exactly the same way as if the object were still present, thus making the image appear three-dimensional. The holographic record-

ing itself is not an image; it consists of an apparently random structure of either varying intensity, density or profile. It is important to emphasise the fact that the reconstructed light field is part of some more complex light field. Finding ways of separating the wanted part of diffracted light field from the unwanted is one of the research branch on its own in holography. One of the most common solution is capturing a hologram using the off-axis configuration.

Thanks to their exceptional temporal properties only sources based on high harmonic generation (HHG) demonstrated so far a train of attosecond pulses and recently single a 130 as pulse. However attosecond holography has to face a serious problem that is the large spectrum of such ultra-fast source. Indeed all holography experiments achieved so far with HHG were spectrally filtering the beam such as to keep only one harmonic, with the drawback of loosing the attosecond duration. The first attempt to perform holographic studies present was by using the in line holography technique.

### 1.8.1 In line Holography

The first hologram capturing was done using *in line holography*. Because the light source, captured object and the hologram plate are aligned in one line this set up is called *in line hologram*. It is the simplest but also the least performing setup. In line holography places some restrictions on the object to be analysed. The majority of the incoming light has to get through in order to act like a reference beam. The minor part will be therefore scattered on the object. Figure 1.16 represents a scheme of the principle of the in-line holography with all the required participants. The low quality of images reproduced from in line holograms is caused by the fact that the reconstructed virtual image fully overlaps with the directly transmitted reference beam and with the blurred real image. This fact was the reason for the low interest on holography at the beginning.

One of the limitations of this kind of set-up is the inherent formation of a pair of intertwined images. When in presence of the real image a virtual blurred image will be accompanying it. There are several ways to cope with this problem one of which is the *Leith and Upatnieks Holography* [3]. The main difference is that in this type of set-up the recording stage is accompanied with a separated reference wave that is independent of the wave that is illuminating the object. This reference

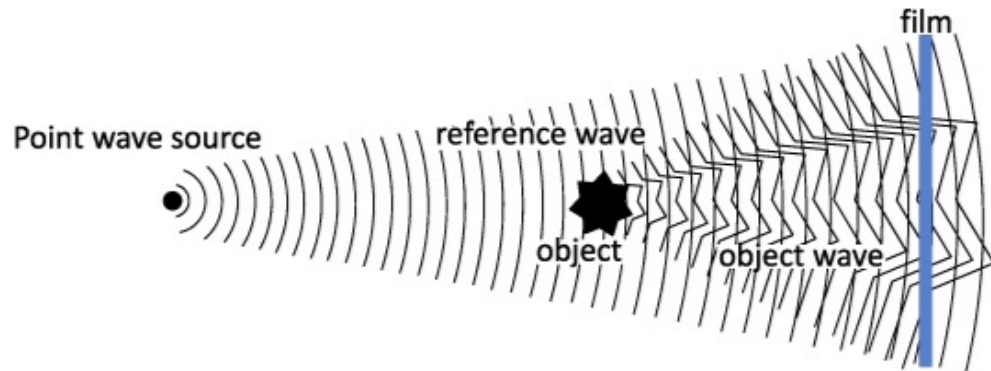


Figure 1.16: Principle of in-line Holography

wave has an angle in relation to the axis object-film. In this case the wave resulting of the interference of the illuminating wave with the object and the blurred twin image are separated.

At the Laboratoire d'Optique Appliquée (LOA) a first approach to holographic studies was conducted by Anne-Sophie Morlens during her PhD thesis. Attosecond holography in a table-top set-up using as coherent source High harmonic generation was demonstrated for the first time in 2003 [3].

While Leith-Upatnieks Holography is very useful to avoid the blurred twin wave it requires a separated reference wave. For a High Harmonic source this is not a limitation, two sources can be generated of the beam that could be split using a beam splitter. However the actual set-up would be much more complex. Another way to overcome this problem is to have a digital reconstruction of the recorded interference pattern by numerical reconstructions. These were developed by Goodman et Lawrence [38] and by Yaroslavskii, Merzlyakov et Kronrod [39]. The hologram was acquired on a photographic film, was optically magnified and recorded on a video camera. This digitalised hologram is then reconstructed numerically by algorithms improved to fit the measurement of particles by Onural et Scott [40]. A great improvement was due to the direct recording of the Fresnel Holograms thanks to the use of Charged Coupled Devices (CCDs) by Schnars et Jptner [41]. This method allowed to digitalise both the recording step and the reconstruction step.

When using a CCD to record a hologram one should take in consideration its minimum resolution. The pixel size of a Gabor hologram using a plane wave of the

reconstructed object will equal the pixel size of the Hologram. The smallest step on a commercial XUV CCD is of  $13.5 \mu\text{m}$  that is superior to the resolution expected. There is a need to expand the hologram. This can be reached by using XUV optics that have the disadvantage of being expensive and complex or by a reference spherical wave placed next to the object resulting on a simple magnification by homothety.

The resolution of this system can be explained by the Rayleigh criterion that states that two incoherent points are resolved by a diffraction limited system when the centre of the Airy disk produced by one of the two sources is coincident with the first zero of the Airy disk on the second source. A representation of the Rayleigh Criterion is presented on Figure 1.17.

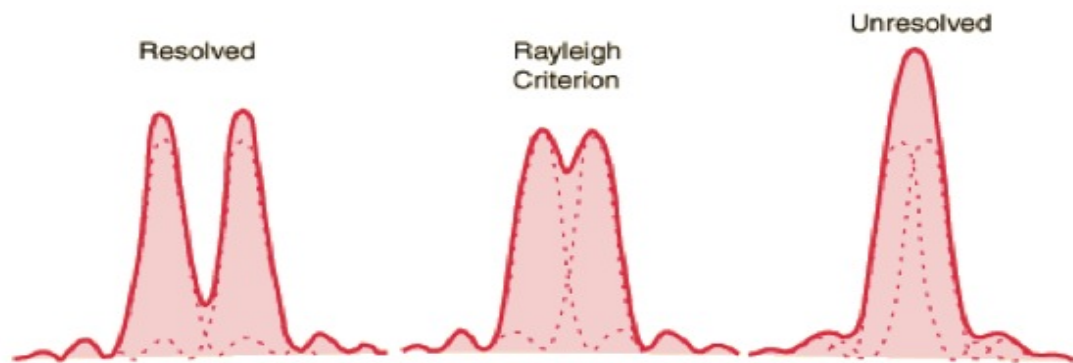


Figure 1.17: Rayleigh Criterion on the minimum resolvable detail.

The minimal resolvable distance indicated as  $\delta$  of geometrical images is therefore:

$$\delta = 0.61 \frac{\lambda}{NA} \quad (1.4)$$

where  $\lambda$  is the wavelength of the radiation source and  $NA$  represents the *Numerical Aperture* of the system. This corresponds to approximately the Full-width at Half Maximum of the Airy Disk.

The Numerical Aperture ( $NA$ ) is a number that describes the amount of light coming from one source and it can be written as:

$$NA = \sin\theta \quad (1.5)$$

where  $\theta$  is the half-angle of aperture of the beam coming from the source. It can be limited by the divergence of the source or by the size  $W$  of the detector.

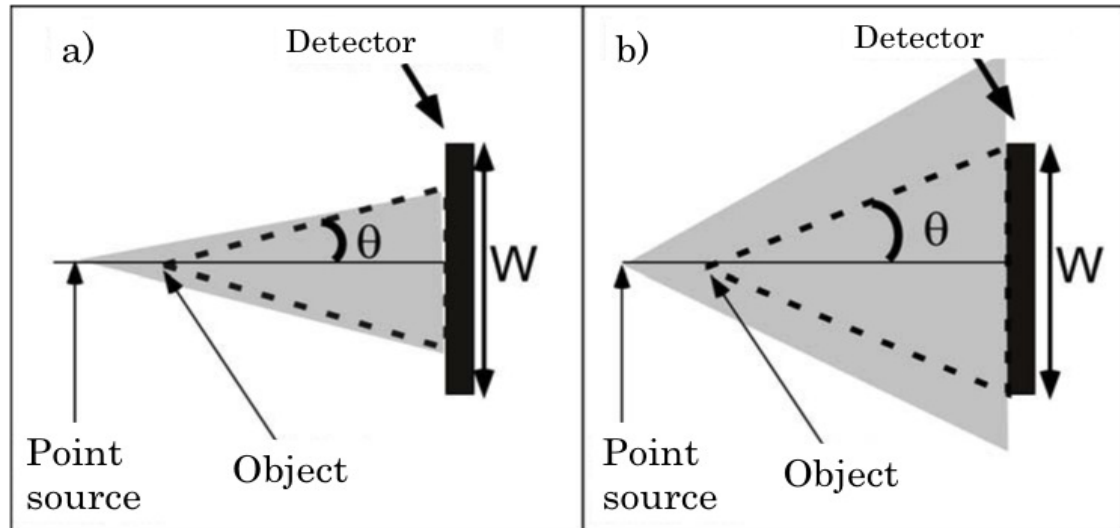


Figure 1.18: Numerical aperture defined by a) the divergence of the source and b) by the detector

The two kind of limitation of the  $NA$  are represented on Figure 1.18. Harmonics present a low divergence, between 1 mrad and 2 mrad therefore the resolution will be limited by the  $NA$  of the object in relation to the CCD. In such a coherent set-up this small divergence will also have to be compensated with adequate optics.

The modes used for the determination of the resolution are founded on the principle that a punctual object is similar to a Fresnel lens this was demonstrated by Rogers [42]. It was demonstrated that holograms of complex objects can be looked as a superposition of Fresnel lens therefore the formulas used on them can be transposed to give a calculation of the transversal and longitudinal formulas [43] as shown in Equation 1.6 and Equation 1.7 respectively.

$$|\vec{r}_2 - \vec{r}_1| \geq \frac{\lambda}{NA} \quad (1.6)$$

$$|\vec{r}_2 - \vec{r}_1| \geq 0.61 \frac{\lambda}{NA^2} \quad (1.7)$$

All these advances on High Harmonic Generation (HHG) sources and in-line

holography lead to the development of a Digital In line Holographic Microscopy set-up at *salle orange* by Anne-Sophie Morlens. The set-up was constituted on a first level with a harmonic source and two aluminium filters that protect the CCD from unwanted IR radiation. An off-axis parabola is covered with a multilayer composed of two periods and each period is constituted of  $B_4C/Mo/B_4C/Si$  that enlarges the bandwidth from 26 nm to 41 nm which is theoretically translated in to 6 harmonics. In practical a resolution inferior to 850 was obtained with 4 harmonics as shown in Figure 1.19. Simulations were made in order to estimate the impulsion duration of the harmonics and a value of 400 to 500 as was indicated [3].

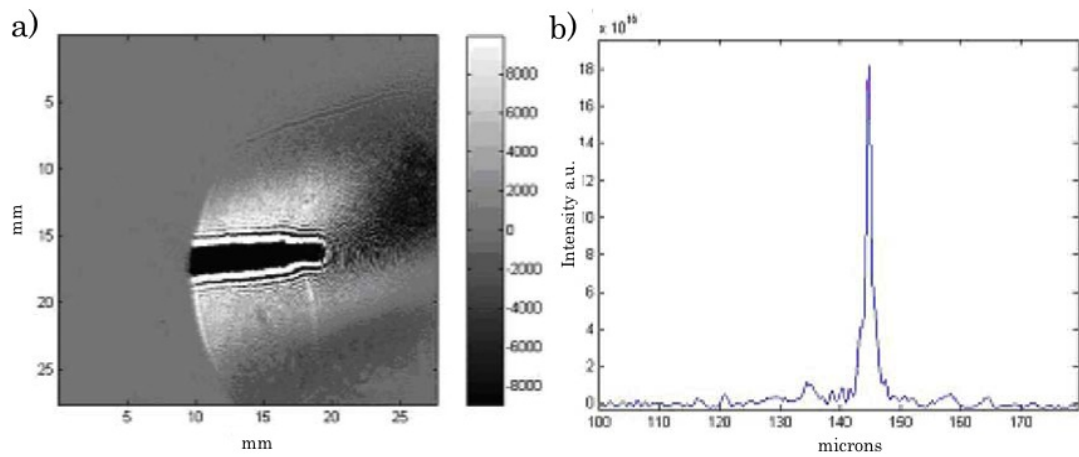


Figure 1.19: Attosecond Holography studies at LOA. a)acquired Hologram, b) cut of the reconstruction presenting a measured FWHM of 840 nm. [3].

This experiment demonstrated the feasibility of Holography using harmonics in a table-top set-up. The amplitude and phase informations were recorded allowing a tridimensional reconstruction with a single hologram. The use of a CCD is very important to perform this technique with a smaller flux of photons due to the use of High Harmonics. Digital in-line XUV Holography has also been studied by Anne L'Huillier in Lund, Sweden [44]

There are some improvements to develop on the Holography domain. The biggest limitation is the low spatial resolution. This can be ameliorated with the use of higher harmonics. If the 4nm wavelength is reached the resolution is expected to increase by a factor of 10 [3]. It can also be achieved by playing with the Numerical Aperture however new optics would have to be put in place.

In order to further advance in the knowledge of our world different objects

must be studied. In in-line holography only thin wires have been so far used. It is of major interest to expand this technique in order to approach other kinds of objects to be imaged. Structure of objects can be viewed by a different technique named *Off Axis Holography* that it is introduced in the following section. This technique introduces a new feature, a reference hole close to the sample. When in an off-axis holography set-up the point source of the reference wave is placed at an appropriate distance from the object. This will allow to illuminate either the object as well as the reference hole. In this case a simple Fourier Transform of the resulting hologram will be enough to have the reconstruction of the object. And as explained in the next section this presents another way to improve the resolution. This technique is called *Fourier Transformed Holography*

### 1.8.2 Fourier Transform Holography

Fourier Transform Holography (FTH) is a imaging lensless technique that presents a high spatial resolution. It is attractive in numerous applications due to its simplicity and direct reconstruction [45]. In order to perform it a point source must be placed in the vicinity of the object. One of the approaches is the use of a perforated mask in the plane of the object. The same source can therefore illuminate both the object and the reference hole giving birth to two patterns. The immediate interaction of this two waves allows the formation of the hologram. The image resolution given by FTH will be given by the size of the punctual source. An illustration of this set-up is presented on Figure 1.20 where it can be seen a representation of a set up and the actual mask containing the reference hole and the sample. This true imaging technique has already been performed on the soft-X-ray and as well for a wavelength of 3.4 nm in 1991 by McNulty [46].

A Fourier hologram is one in which the complex amplitudes of the waves that interfere at the hologram are the Fourier transforms of the complex amplitudes to the original object and reference waves. This implies an object that lies in a single plane or is of limited thickness.

Considering the transmission function  $t$  of the sample constituted by the object  $o$  and the reference  $r$  we have:

$$t = o + r \quad (1.8)$$

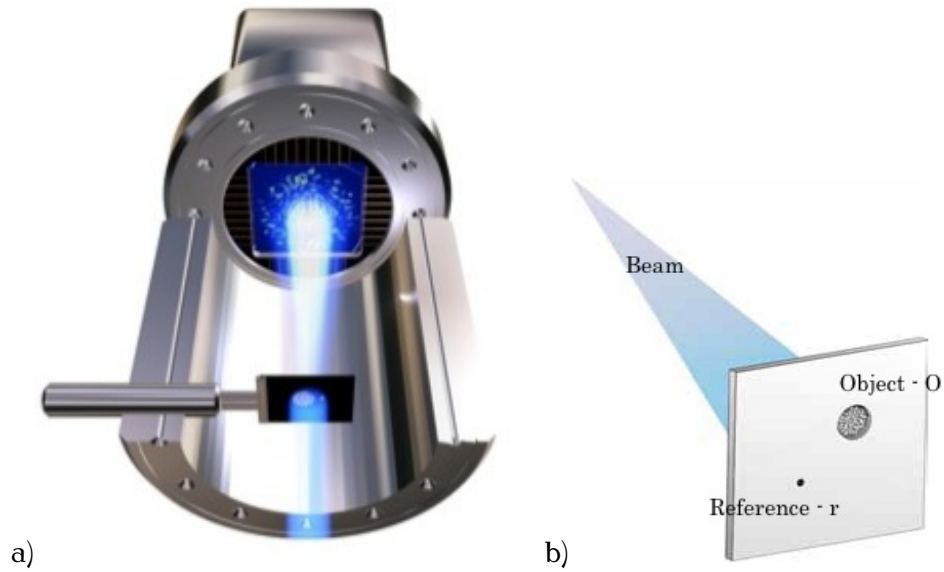


Figure 1.20: Fourier Transform Holography a) General set-up b) Image of the mask containing both the object to be imaged and the reference source point on the same plane

in the far field diffraction regime with a narrow numerical aperture, *paraxial approximation*, we have on the detection plane the figure of diffraction or hologram.

$$H = | \mathcal{F} \{ t \} |^2 = | T |^2 \quad (1.9)$$

With the Fourier Transformations of the object  $\mathcal{F} \{ o \} = O$  and the reference  $\mathcal{F} \{ r \} = R$  we have:

$$| T |^2 = | O + R |^2 \quad (1.10)$$

The hologram is then detected and sampled by the CCD. Any analysis that follows the recording of the hologram is performed on discrete signals using computer tools. An analytical description is sufficient for the description of the principle of reconstruction. The reconstruction is obtained by the Fourier transform (inverse) of the hologram:

$$\mathcal{F}^{-1} \{ H \} = \mathcal{F}^{-1} \{ | \mathcal{F} \{ t \} |^2 \} = t \otimes t \quad (1.11)$$

The Fourier transform of the hologram corresponds to the autocorrelation of

the transmittance of the sample. In developing the transmittance, we get:

$$t \otimes t = o \otimes o + r \otimes r + o \otimes r + r \otimes o \quad (1.12)$$

The last two terms in this expression correspond to the holographic reconstruction. The two complex conjugates of each other, represent the product of the correlation between the object (complex) and the reference: the resolution is limited by the dimensions of the reference. A holographic reconstruction can be written as the convolution of the object by reference, the latter playing a role equivalent to that of the point spread function *PSF* of an optical system.

In *off-axis holography* it is possible to separate the terms of equation 1.12. Reducing the problem to one spatial dimension the transmittance of the object is written as follow:

$$t(x) = o(x) + r(x - x_0) \quad (1.13)$$

the distance  $x_0$  represents the distance between the object and the reference. Which translates into:

$$H = | O(k) + R(k)e^{-ikx_0} |^2 = | O(k) |^2 + | R(k) |^2 + O^*(k)R(k)e^{-ikx_0} + O(k)R^*(k)e^{ikx_0} \quad (1.14)$$

where  $O(k)$  and  $R(k)$  are complex, with:

$$O(k) = | O(k) | e^{i\varphi_O(k)} \quad (1.15)$$

and

$$R(k) = | R(k) | e^{i\varphi_R(k)} \quad (1.16)$$

From where we have:

$$H = | O(k) |^2 + | R(k) |^2 + 2 | O(k) | | R(k) | \cos(\varphi_O(k) - \varphi_R(k) - kx_0) \quad (1.17)$$

The last term (term heterodyne) of this expression is at the origin of the interference between the object and the reference. It represents the coding of the amplitude and the phase of the object (and the reference) in the modulation of the

hologram. By applying the transformation

$$k = \frac{rk_0}{z} \quad (1.18)$$

with  $k$  reciprocal space and  $r$  detection space. Modulations of the hologram have a periodicity of

$$\frac{\lambda z}{x_0} \quad (1.19)$$

The reconstruction of this hologram gives:

$$\mathcal{F}^{-1}\{H\}[\mathbf{o} \otimes \mathbf{o}](x) + [\mathbf{r} \otimes \mathbf{r}](x) + [\mathbf{o} \otimes \mathbf{r}](x - x_0) + [\mathbf{r} \otimes \mathbf{o}](x + x_0) \quad (1.20)$$

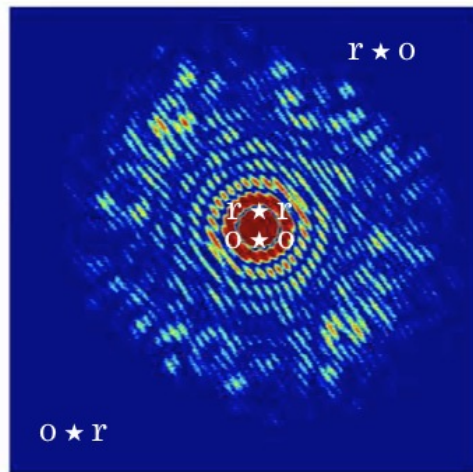


Figure 1.21: Fourier Transform Holography. Reconstruction of the object.

While the "core terms" are centred at the origin, the two images are located on either side of the origin at a distance  $x_0$ . There is an holographic separation (with a reference point) if this distance is superior 1.5 times to the dimensions of the object. This is represented on figure 1.21 taken during our beam-time at LCLS.

In sum FTH is a true imaging technique with wavelength limited spatial resolution. It has a good image quality and is able to record multiple images with a single pulse in a simple and affordable set-up that is basically insensitive to vibrations or thermal drifts. It is ideal for *in-situ* studies and sample arrays since no alignment or focusing is required. Its wide applicability allows samples to grown or placed in aperture or on back of mask or placed separately behind it. Reflection geometry may be possible.

The ability of this technique relates primarily to the quantity and quality of the signal recorded. This justifies the strong motivation to develop sources of ultra-short X-UV delivering an important stream of coherent photons as is the case for free electron lasers. However these machines are few and therefore remain inaccessible to the scientific community motivating the development of an alternative XUV source suitable for imaging applications with or without lens. To reach the infinite small at ultra-fast time duration this work focuses on the development of a table-top source based High Harmonic Generation (HHG).

The present thesis is focused on the thematic of tabletop imaging of the nanometer range with XUV radiation by ultra short impulsions in the order of the femtosecond time scale. The main constraints in this field are the difficulties of generating a source on the femtosecond regime and the challenge of making it work in a tabletop set-up directed to imaging. Another difficulty is the pertinence of the study object. The main negative consequences are that imaging in the ultra short time scale can be performed only in the main facilities like the synchrotrons with the penalty that it only reach the pico-nanosecond ( $10^{12} - 10^9$ ). Therefore it is not easily accessible to study interesting phenomena occurring in the femtosecond regime like for example the process of magnetisation/demagnetisation of a given sample since it can only be done at at very few large facilities. Table top XUV imaging can be reached in the femtosecond regime by three different techniques: *X-ray diffraction*, *X-ray tomography*, *X-ray microscopy* and finally by *X-ray holography*. XUV diffraction was already performed at CEA by Merdji et al [47] with good resolution in a simple tabletop set-up and in a femtosecond time range. However the acquisition time is long. In order to have the information to reconstruct the image which can cause an interference the main constraint is that we need to know in advance the shape of the object. To retrieve the object we need intensive computation with complicated algorithms and without it we can retrieve only the size of the object and not a real 2D image. X-ray tomography was performed at FLASH already allowing us to have a 3D image however the way to reach it is to do several plans of accumulation of images leading to an even longer exposure time. X-ray microscopy is a good method that allows us to have a good 3D image in a rather fast way. Its inconvenient is that it is an expensive set-up. Which leads us to the X-ray holography. X-ray holography was already achieved at Laboratoire d'Optique Applique (LOA) in 2005 by Anne-Sophie Morlens [3] in a femtosecond time scale and attaining a 3D image retrieval. This was performed using a High Harmonic Generation (HHG) source which is very useful since it also allows us to reach better the problematic of a pump-probe experiment. The set-up was replicated later by Lund. The main inconvenient is the lateral resolution which is given by the wavelength  $10^{-2}$ . One solution to this problem is the off axis holography, already achieved by J. Lunning for synchrotron use, this technique allows us to reach small lateral resolutions of the size of the reference hole. One of the main conclusions of the AS Morlens was that X holography is reachable but however there is a need to have a plausible study object since the images retrieved where with a test object.

That is what brings us to the goal of this thesis. This study is based on the de-

velopment of a tabletop imaging system in three dimensions in the XUV range with polarisation control of the electromagnetic impulsions. Which will allow to further explore the phenomena of excitement of samples with magnetic nanostructures that occur in a femtosecond time scale and therefore unseen so far.

The work was conducted at a first level on optimising an XUV source at 20 nm by laser matter interaction. Our goal was to have a strong signal 20 nm radiation with a femtosecond duration and coherent in order to allow the making of images. For this we have put in place a High harmonic Generation set-up and tuned our parameters in order to reach the 20 nm. The 20 nm point corresponds to the M edge of Cobalt and it is chosen since it presents a good dichroic contrast. In order to achieve it Neon was used since it is known to generate HHG in smaller wavelengths. Generation parameters have been optimised, like the gas cell length, the pressure and the focal lens was changed to a larger focal lens in order to have a longer region of generation and therefore more signal in the end. The chirp of the laser was slightly changed since it has an effect in the wavelength of the harmonic generated in order to adjust the harmonic wavelength to the M edge of Cobalt. Using Neon to produce harmonic radiation, a two-colour scheme was put in place to increase the conversion efficiency. Imaging requires a high photon count and this is one of the limitations of the HHG. Using a two-colour field set-up and optimising the latter is a way to increase the conversion efficiency (Chapter 2).

In the following chapter the source previously optimised was put in place to study the polarisation of the high harmonics generated in a two-colour field. The overall goal was to understand the process of polarisation of the HHG radiation and be able to replicate it since most of the available XUV sources have polarisation control together with the other light parameters. In order to achieve this a system with the purpose of measuring the polarisation was conceived. Based on the stokes vector and representing it on a rotation axis to have a way of measuring the polarisation of the radiation experimentally, that set-up represents a break-through step for table-top sources. The next step was to install the two-colour HHG set-up with the purpose to generate odd and even harmonics. A rotation axis was also installed of the type 1 Beta Borate (BBO) crystal in order to study the generation on various regimes. Simulations were conducted in order to find a model to verify the experimental results. At the large infrastructures such as a synchrotron and SLAC (Stanford) the polarisation control of the radiation is already possible. In our study a polariser chamber was constructed in order to have a fixed element

that will allow to change the polarisation of the w radiation centred in the 20 nm wavelength to be easily controlled and turned to circular. Being therefore adapted to our table-top setup and suited to interact with the magnetic domains of the M edge of the cobalt (Chapter 3).

Having a source that is tuned to give the brightest radiation at the wavelength desired the samples containing the magnetic nanostructures were built and characterised at BESSY-II. The M-edge was studied for its dichroic characteristics to estimate the performance in our lab with the previously optimised source (Chapter 4). XMCD effects and Magneto Optical effects were measured at its potential was analysed. The several studies performed at FLASH and SOLEIL and BESSY-II allowed us to know the response of the materials and gave us a solid base for comparison.

The samples developed were then used for the purpose of imaging its magnetic nanostructures by magnetic diffraction and in order to perform magnetisation studies. In this point our source and the samples are compatible and allow us to retrieve the information we look for. Holographic and diffraction imaging were performed at LCLS with the goal to see the magnetic nanostructures and take snap-shots of its magnetic evolution behaviour in order to study the punctual differences of shape. A set-up of magnetic diffraction was built in order to allow the acquisition of signal. A monochromator was installed in order to have only the wanted radiation as a measure of safety not to surcharge the system of image acquisition and heat the structure. A pump-probe set-up was installed at LOA to allow the study of the evolution of the magnetisation of the magnetic nanostructures (Chapter 5). In this chapter an overall comparison of the different sources used is made to analyse the pertinence of the results.

Finally a conclusion and perspectives on the achieved work are presented.

**Optimisation of a XUV source with 20 nm by laser/matter interaction**

---



---

**Contents**

---

<b>2.1 High Harmonic Generation . . . . .</b>	<b>43</b>
2.1.1 Optimisation of the High Harmonic Generation process . . .	47
<b>2.2 High Harmonic Generation in a two-colour field . . . . .</b>	<b>50</b>
2.2.1 Frequency doubling . . . . .	57
2.2.2 Wavefront and flux optimisation . . . . .	59
<b>2.3 Polarisation of High Order Harmonics . . . . .</b>	<b>64</b>
2.3.1 Two-colour HHG with linearly polarised fundamental a weak orthogonally polarised second harmonic field . . . . .	64
<b>2.4 Conclusion . . . . .</b>	<b>68</b>

---

Imaging ultra-fast phenomena occurring in the nanometer scale requires intense soft X-ray beams with an ultra short pulse duration. The quality of this radiation source should attain the diffraction limit but still be accessible and easy to manipulate. The goal of this thesis is to develop a table-top source that allows to reach the very small in an ultra fast time regime. As a first application of this source the study about femto-magnetism is presented focusing mainly on the electronic movement. The temporal domain of the electron movement is on the femtosecond or attosecond range ( $10^{15} - 10^{18}$  seconds). Then direct access will be provided to the deeper understanding of the magnetic properties of matter. Larger facilities such as LCLS, FLASH and BESSY-II are reaching this regime. To study the underlying magnetic properties the source has to be tuned to be able to reach wavelengths on the X or XUV range of the spectre that can reach the absorption edges K,L or M of the magnetic samples. As seen on the previous chapter this range is spread roughly from 1 nm to 100 nm. These are the regions where magnetic dichroism can be observed and recorded. In the Laboratoire d'Optique Appliquée (LOA) the source will be tuned to the M-edge or Cobalt whilst compared to the K-edge of the LCLS, BESSY-II and other synchrotrons. A very good spatial resolution close to the diffraction limit and given by the following equation where  $NA$  is the numerical aperture as seen on the previous chapter.

$$Resolution = 0.62\lambda/NA \quad (2.1)$$

The beam has to be coherent in order to be able to use diffraction or holography techniques which have the great advantage of getting rid-off large numerical aperture (NA) XUV optics that are extremely costly and difficult to manufacture. And last but not least the source has to be ultrafast to be able to follow the elementary processes implied on the demagnetisation of a material after an ultrafast infra-red (IR) laser excitation as it was shown on a study conducted by Beaurepaire whose demagnetisation curve is represented on the Figure 2.1.

With the recent progress of the infrared lasers used for generating harmonics and the optimisation of the process, harmonics appear as a reliable approach for laboratorial research. High Harmonics have as well the interest of being a compact coherent source with good phase properties and requiring a medium energy laser. The table-top systems in use nowadays to reach this working conditions are fem-

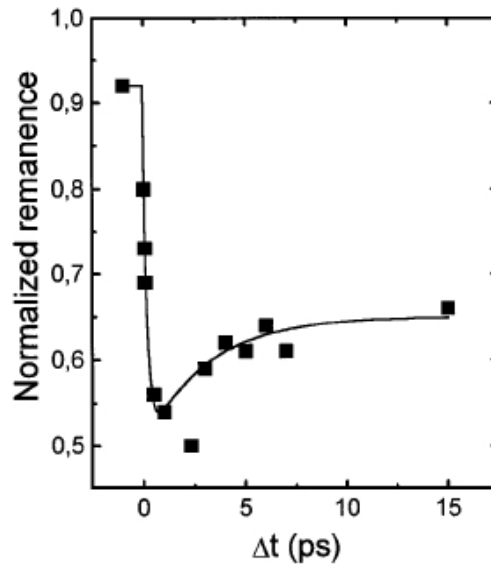


Figure 2.1: Ultra-fast demagnetisation curve. Beaurepaire et al, retrieve a demagnetisation curve that shows that the process is completed on a ultra-fast time scale. [4]

to second Ti-Sa lasers with wavelengths centred at 800 nm with reaching  $2.7\text{fs}$ . This time range corresponds to the duration of one optical cycle [48] which states the record of ultra-fast lasers nowadays. This kind of lasers are rare and highly used for the production of coherent XUV sources called high harmonic generation that are the atomic response to the excitation by an intense and often ultrashort laser field. This results in intense, coherent and ultrashort bursts of radiation obtained in table top set-ups. A high harmonic generation spectra contains various harmonics which means various energies and therefore various wavelengths involved in the XUV range. In this case the this system has been optimised for a wavelength of 20.7 nm (60 eV) corresponding to the M-edge of the Cobalt.

The overall goal of this chapter is to develop a coherent XUV table-top source that gives a strong signal at the wavelengths of 20 nm in a femtosecond time scale and which will be accessible to a larger number of users. *High Harmonic generation* is therefore presented as the XUV source with laser-like properties in conditions to answer this problematic.

## 2.1 High Harmonic Generation

High Harmonic generation is a highly non-linear process resulting of the interaction of an intense laser field in the order of  $10^{14} \text{ W/cm}^2$  or above and typically the atoms of a noble gas. The result is the emission of radiation in the XUV domain that propagates in the same direction as the incident laser. This radiation has a periodical spectral structure constituted of odd harmonics ( $2n+1$ ,  $n$  being an integer) of the fundamental frequency until really high integer multiples of the original laser frequency otherwise named *orders* [49]. The spectrum obtained presents a characteristic structure that can be divided into three distinct zones and an example is represented on figure 2.2.

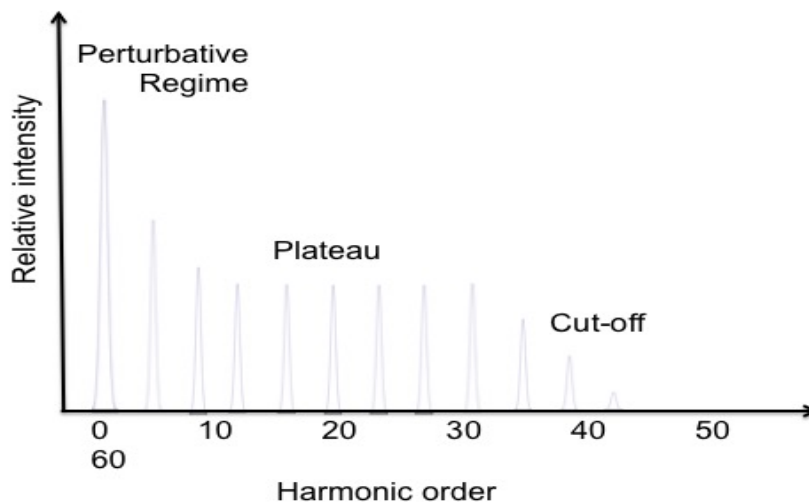


Figure 2.2: Typical High-Harmonic spectrum where the three zones: *Perturbative regime*, *Plateau* and *Cut-off*, are identified.

For the lower order harmonics a fast decrease of the conversion efficiency is observed with the increase of harmonic order. This behaviour is explained by the theory of perturbations in non-linear optics and it is therefore called *perturbative regime*. The following area presents close-to constant conversion efficiencies therefore it is named *plateau*. In this intermediate orders the amplitude of the spectra is a function of the noble gas used and the illumination of the fundamental laser. The final part of the spectra is called *cut-off* where the conversion efficiency drops rapidly corresponding to higher order harmonics and defining the maximum energy of the generated photons. In 1992 Krause [50] proposed the *cut-off law* given by:

$$h\nu_{max} = I_p + 3.2U_p \quad (2.2)$$

with  $I_p$  as the ionisation potential of the atom,  $U_p = e^2E^2/4m\omega^2$  or  $U_p \propto I_{Laser}\lambda_{Laser}^2$  that corresponds to the mean kinetic energy of a free electron acquired in the laser field also called *ponderomotive energy*. Only odd harmonics  $(2n + 1)\omega$  are emitted where  $\omega$  is the angular frequency given by:  $\omega = 2\pi f$  and  $f$  is the frequency. The exact model for the interaction leading to HHG needs the time-dependent Schrödinger equation to solve the atomic system. This is an equation with no analytical solutions therefore only the models that are based on approximations allow to describe approximately the processes that intervene in the generation of this kind of radiation.

When an intense laser interacts with the atoms of a gas three direct ionisation mechanisms can take place. The multi-photon ionisation, the tunnel ionisation and the ionisation by suppression of the potential barrier. The HHG in noble gases in the XUV range can be described mainly by *tunnel ionisation*. Tunnel ionisation can be obtained for intensities from  $10^{13}W/cm^2$  to  $10^{16}W/cm^2$  depending on the element. Such a laser field is strong enough to modify the atomic structure of the atom. One of the models used to explain the HHG is the semi-classical model in three steps [51]. The first has a quantic approach, the second a classical and finally the last a quantic approach again. A representation of this model is shown on figure 2.3.

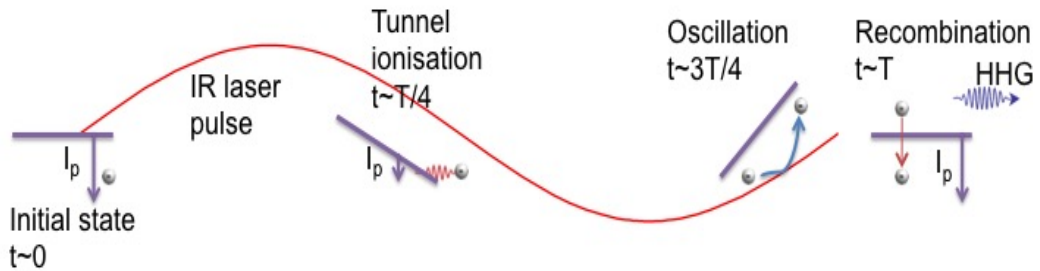


Figure 2.3: Representative example of HHG

The first step represented on figure 2.3 as *tunnel ionisation* occurs when the Keldysh parameter  $\gamma$  that relates the characteristic time of crossing the barrier of potential of the atom and the period of the oscillation of the laser field is inferior

to one [52].

$$\gamma = \sqrt{\frac{I_p}{2U_p}} < 1 \quad (2.3)$$

The atom is ionised by tunnel effect. There is a deformation of the barrier of potential leading to an increased probability of the release of an electron over it. This tunnelling process is specially effective at the peak of the laser electric field. The simple atom response varies with the square of the inverse of the period of the laser. Therefore is more efficient as the wavelength is smaller and as shorter the impulse.

The second step is represented on figure 2.3 as *acceleration in the laser field*. In function of the instant of ionisation the rejected electron or the electronic wave packet accelerates in the laser field freely. The potential of Coulomb being neglected, it can gain kinetic energy. During the first semi-period of the laser pulse the electrons are accelerated far from the atom. On the second semi-period a change of direction of the electric field of the laser pulse occurs and the electrons are accelerated this time onto the parent ion. This is a purely classical model having the classical trajectory of the electron in an electric field. Quantum mechanical models also deal with the electron motion in the field but cannot resolve other types of trajectories.

The third and last step is represented on figure 2.3 as *radiating recombination*. The electron or electron wave packet can recombine radiatively with the parent ion emitting an ultrashort pulse in the order of the attoseconds of XUV radiation. The energy of the emitted photon is the sum of  $I_p$  and the acquired kinetic energy per electron that changes depending on the phase of the electric cycle when it was released, being equal or inferior to  $3.2U_p$ . The maximum efficiency that corresponds to a phase of  $17^\circ$  which is the peak of the electric field oscillation. This phenomena is repeated at every period of the exciting laser. The interference between the different attosecond bunches of X-rays builds up the final spectrum as measured. Translated in frequencies it results in a wave of a multiple frequency of the fundamental - *harmonic*. When the wavelengths are smaller the HHG efficiency is increased due to the simple fact that there are more electrons close to the core able to recombine more easily. If the generation is done using higher intensities the cut-off can be extended until a certain point. Above that energy the generation will suffer the effects of plasma defocusing and alterations of the medium refraction

index. The pulse profile will change on the time and space domain. Also when the intensity of the incident electric field is very high the electron can acquire near speed of light velocities starting to go under the influence of a magnetic field whose force can get comparable to the one of the electric field. The electron will describe a quantum path in the shape of a bow-tie and as a consequence it will have less probability of interaction with the core and the obtained spectra will show less harmonics. In this regime the relativistic forces of the electron can also start to push it to lower energies.

In the plateau region of the harmonic spectra (see figure 2.2) the harmonics are generated essentially by two trajectories that are the main contributors to the generation: the *long path* and the *short path*. A representation of the electron trajectory in the continuum is shown on figure 2.4. The two sets of trajectories are visible as well as the chirp represented by the colours of the electronic paths.

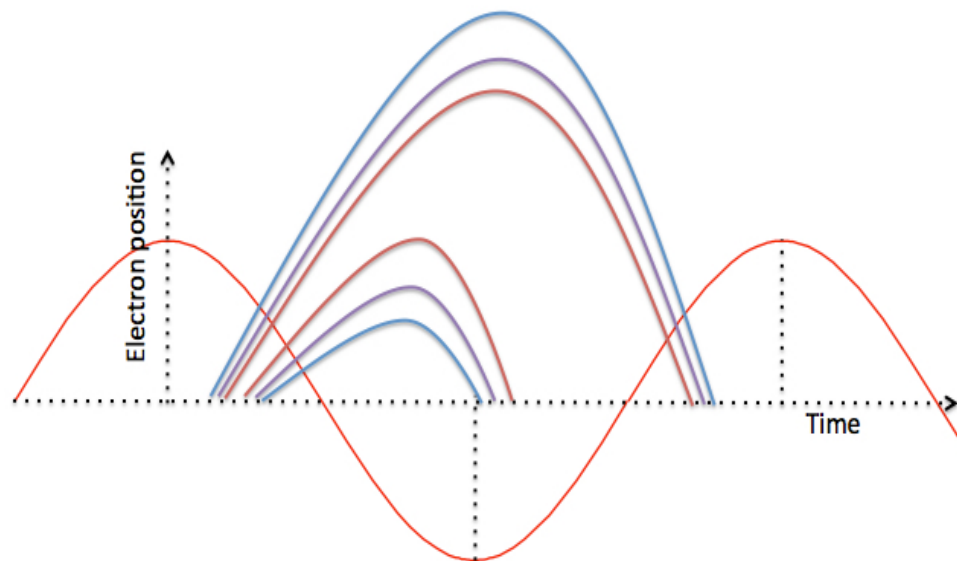


Figure 2.4: Representation of the electronic trajectories in the continuum as a function of the pulse cycle and the position of the electron on the atom

The short path trajectory has a brief lifetime while the long path trajectory has a longer one that corresponds approximately to a period. Both will superimpose and result in a larger spectral peak. Figure 2.5 shows an example of two quantum paths for the same harmonic emission. In the cut-off region both are merged in a single trajectory.

As high harmonics are dependent on the intensity of the incident laser it can

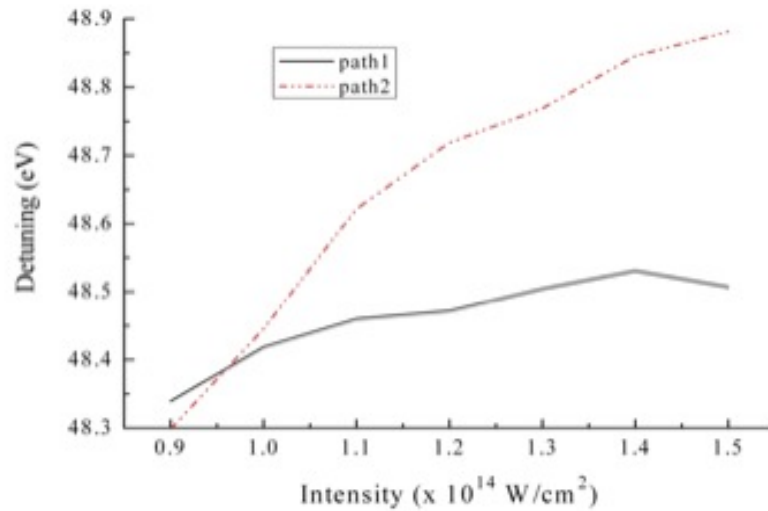


Figure 2.5: Example of long and short paths trajectories [5]

occur a division on the harmonic peak due to the imposed blueshift on the longer trajectory.

### 2.1.1 Optimisation of the High Harmonic Generation process

The high spatial quality of the High Harmonic Source is translated into a source with great potential for micro-focusing. However when compared to a synchrotron source this sources present a small photon flux. The optimisation of the generation conditions should in a short time allow to multiply the photon flux by at least a factor of ten. Since the 1990s various studies have tried to optimise the High Harmonic Generation radiation [5], [8], [9]. In order to increase the number of photons a maximisation of the capability of the generation has to be put to place. Various changes can be performed, the geometry of the cell, the type of gas, the focus spot of the IR laser and the use of a diaphragm to clean the profile of the IR beam.

To improve the total number of photons emitted by the media the macroscopical response of the system must be taken into account. To optimise the transfer of energy between the laser field and the media a quasi-phase matching condition must be met. The source and the harmonic fields should propagate at the same phase velocity leading to the constructive interference of the harmonic fields emitted by the dipoles, resulting on a macroscopically coherent field exiting the media.

However this condition is hard to be met experimentally which prompts us to use the parameter of the coherent length defined as:

$$L_{coh} = \frac{\pi}{\Delta k_q} \quad (2.4)$$

which is the length at which the harmonic field and the non-linear polarisation are approximately *in phase*. It depends also on the ionisation. Or in other words the limit of length for an effective construction of the harmonic radiation. The length of the media  $L_{med}$  must preferably be of the order of the coherence length. The harmonic field can be destroyed by the interferences but also by the absorption of the radiation by the media itself. This parameter is defined as:

$$L_{abs} = \frac{1}{\omega_q N_{at}(r, z, t)} \quad (2.5)$$

where  $\omega_q$  is the effective section for photo-absorption of the atomic media to the frequency  $q$ . At  $L_{abs}$  the field is attenuated of a factor  $1/e$ .

Constant et al [6] related these parameters in writing an equation for the number of photons  $N_q$  generated at a frequency  $q$ :

$$N_q \propto \frac{4L_{abs}^2}{1 + 4\pi^2 \left(\frac{L_{abs}^2}{L_{coh}^2}\right)} \left[1 + \exp\left(-\frac{L_{med}}{L_{abs}}\right) - 2\cos\left(\pi \frac{L_{med}}{L_{coh}}\right) \exp(-L_{med} 2L_{abs})\right] \quad (2.6)$$

To maximise harmonic generation it is required that the signal is at least equal to half of the maximum theoretical signal the following conditions are then defined:

$$L_{med} > 3L_{abs} \quad (2.7)$$

$$L_{coh} > 5L_{abs} \quad (2.8)$$

Different lengths of coherence influence the generation of harmonics such is shown on figure 2.6. The optimisation of this length can be done experimentally using a long focal lens that determines homogeneous condition for phase-matching and a large transverse section of the volume of interaction in the focal region. The focalisation should maintain a level of intensity close to the  $I_{sat}$ . This illumination shouldn't become superior otherwise it will destroy the harmonic beam.

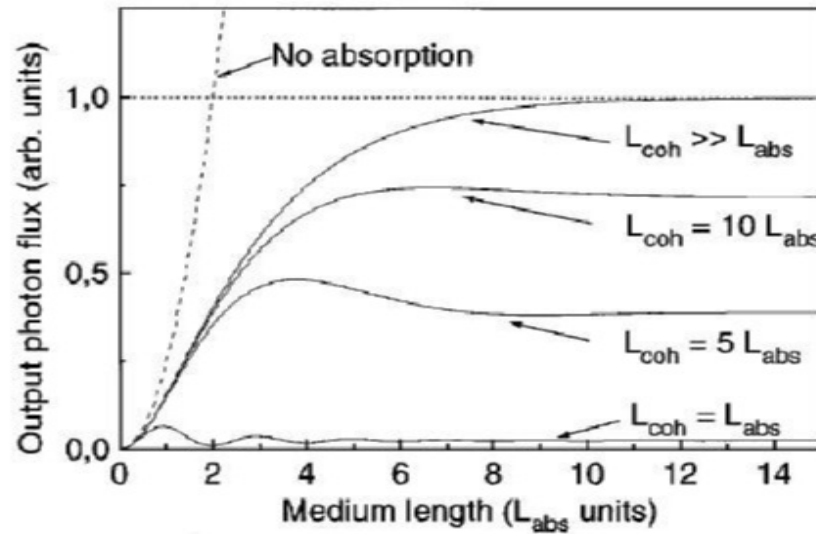


Figure 2.6: Number of photons of harmonics generated as a function of the length of the media for different lengths of coherence [6]

Another important point for the optimal generation of harmonics is the high atomic density that should be however compatible with the phase matching condition. It determines the level of reabsorption of the harmonic radiation in the media. This is presented in this thesis by changing the pressure in the gas cell.

In this manuscript a High harmonic generation set-up was developed and the radiation tuned in order to reach the 20 nm, which is the M edge of Cobalt this means that at this energy Cobalt presents a good dichroic contrast. This is a short wavelength therefore the conditions of the generation have to be improved. As seen in equation 2.2 the *cut-off* of the harmonics is given by the potential of the barrier and the ionisation potential of each atom. Therefore with a smallest atomic number gas the generation of harmonics will reach higher energies until the cut-off. Figure 2.7 shows the envelope of the harmonic spectra obtained at *salle orange* in 2009. It can be seen that for 20nm the better conversion efficiency corresponds to Neon. The generation parameters have been optimised, like the gas cell length, the pressure and a larger focal lens was put in place in order to have a longer volume of generation. The chirp of the laser was slightly changed since it has an effect in the wavelength of the harmonic generated in order to adjust the harmonic wavelength.

It can be seen from figure 2.7 that Neon even though has a good conversion

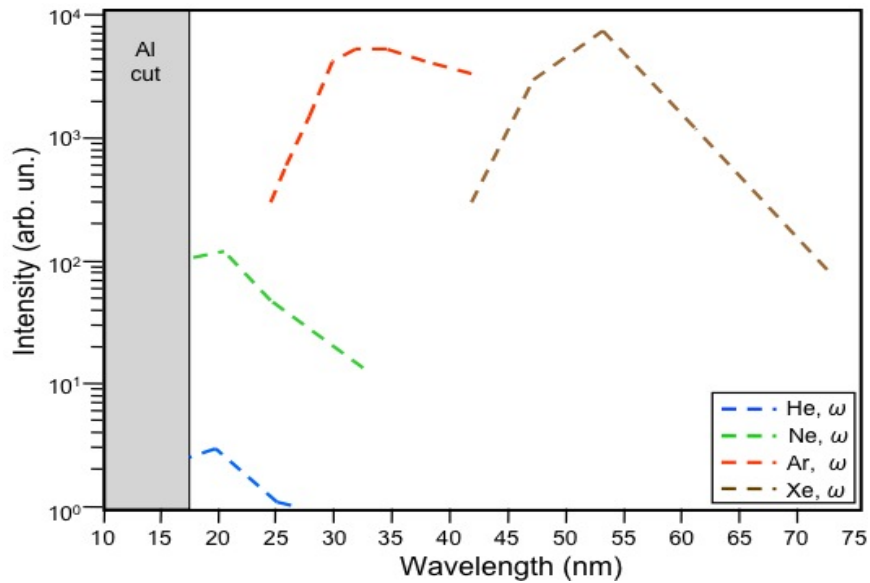


Figure 2.7: Harmonic spectra for various gases generated with an energy of 6 mJ and a laser of 800 nm [7]

efficiency around the required wavelength has a small conversion efficiency overall for imaging experiments. To increase its conversion efficiency the path chosen was a *two-colour scheme* as presented in the following section.

## 2.2 High Harmonic Generation in a two-colour field

Nowadays efforts are made to enhance the HHG conversion efficiencies in order to make it a useful source of coherent extreme ultraviolet (XUV) light. There is a real need to control the HH spectra as a source for new applications. *Beta barium borate or BBO crystal* converts a fraction of the fundamental laser into a second-harmonic residual fundamental laser pulse. High Harmonic Generation that is a highly non-linear process has its conversion efficiencies enhanced when generated in a two-colour field. In a two-colour field all integer-order harmonics are generated (instead of only the odd harmonics) due to the breaking of inversion symmetry. The harmonics are generated with enhanced signal depending on the two field laser configuration and a reduction of the attosecond harmonic pulse can be achieved [8]. Generating harmonics with a shorter wavelength and with significant control of the intensities of specific harmonics of the resultant spectra requires an optimisation of the gas pressure, the length of the generating medium

and the intensity of both components.

To try to understand this phenomenon there is a need to go down to the atomic scale to the physical phenomena of the generation of harmonics. Enhancement is even more striking on high harmonics generated in an orthogonal two-colour field as it will be presented on the next chapter. With this technique better signal is obtained however there is a shift of the HHG cut-off towards lower energy (higher wavelengths) the so called *redshift*. That is to lower orders translating in an increase of the wavelengths. This effect has to be taken into consideration when choosing the desired resultant XUV source. In this region the number of photons starts to decrease fast. To explain the general behaviour the generating laser beam has to be seen as a mixed beam of the fundamental (red) and the second harmonic (blue) beam. When following the equation 2.2 it is clear the relation between the wavelength of the generating laser and the energy of the last harmonic obtained. The intensity and the wavelength are then balanced by the ratio  $\frac{I_{2\omega}}{I_{\omega}}$ . The redshift is clearly dependent on this relation. The bigger the  $\frac{I_{2\omega}}{I_{\omega}}$  the longer the wavelength at which the cut-off occurs.

This explains the so called redshift of the cut-off observed when using this technique.

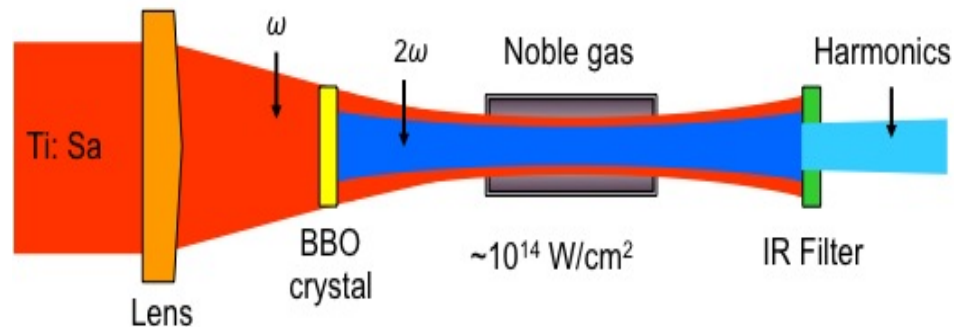


Figure 2.8: Set-up for High harmonic generation with a two-colour field. An intense IR laser pulse is focused onto a gas cell by means of a lens. When the laser pulse passes through the BBO crystal the second colour laser field is generated. The resulting two-colour laser field interact with the noble gas generating high harmonics. A filter is used in order to suppress the two-colour laser field.

At LOA this method has already been studied in order to have a general idea of the behaviour of the harmonics. A lens is used to focus the IR laser. The BBO is placed in the path of the laser, now called fundamental laser, doubling the frequency according to its conversion efficiency. A noble gas is placed in a container located in

the beam path at the focus of the IR it will work as the medium for the generation of the harmonics. Lastly a metallic filter is used to block the non-converted IR laser radiation. Figure 3.34 shows the high harmonic general installation on a two colour field. Figure 2.9 shows the experimental results of the generation of high harmonics at *salle orange*. A spectra of the envelope of harmonics is represented. The experiment was conducted at first for the optimisation of shorter wavelengths as we can see by the signal increase factor of 100 for He and 25 for Ne. In the same conditions the generation of harmonics on heavier atoms was not that perfect, reflecting on a decrease of 0.5 in Argon and Xenon. The enhancement of the signal is therefore dependent on the gas. The lower the ionisation rate in the HHG the stronger the enhancement factor (represented in the Helium and Neon) For efficient gases such as Argon an Xenon, using this method can eventually lead to a decrease of the HH signal. Nonetheless the spectra is doubled so the energy is conserved. The possibility to increase the signal demonstrated at LOA by varying the optimisation parameters is an example of how the optimisation parameters are vital for the success of this method and how much this technique can be useful to the brilliance of this types of sources.

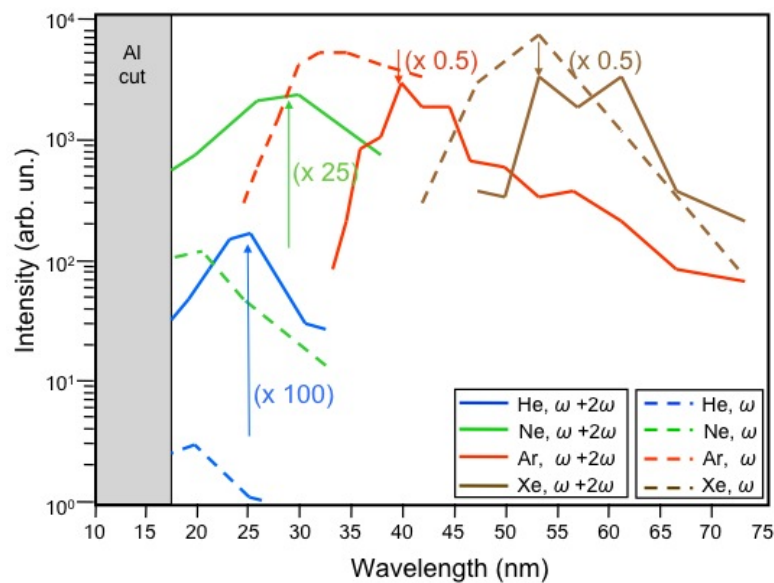


Figure 2.9: High harmonic generation in a two colour field at LOA

While standard HHG generates only odd harmonics with this technique both even and odd harmonics are generated by two independent electric laser fields. The two colour field induces a selection of the short electron quantum path for which the specific moment when the electrons are released from the atom corresponds to 10 times higher ionisation rate than with the single colour field. When an electric

field of second harmonic is added to the HHG the harmonic content will still take into consideration the  $2n + 1$  also called *odd harmonics* from  $\omega$  but the spectra reveals *even harmonics* as well that are separated in two different categories: the  $2(2n + 1)$  even harmonics generated mainly from  $2\omega$  and the  $2(2n)$  harmonics that are a result of the mixing both fields. Figure 2.10 shows the attained spectra at LOA for Neon.

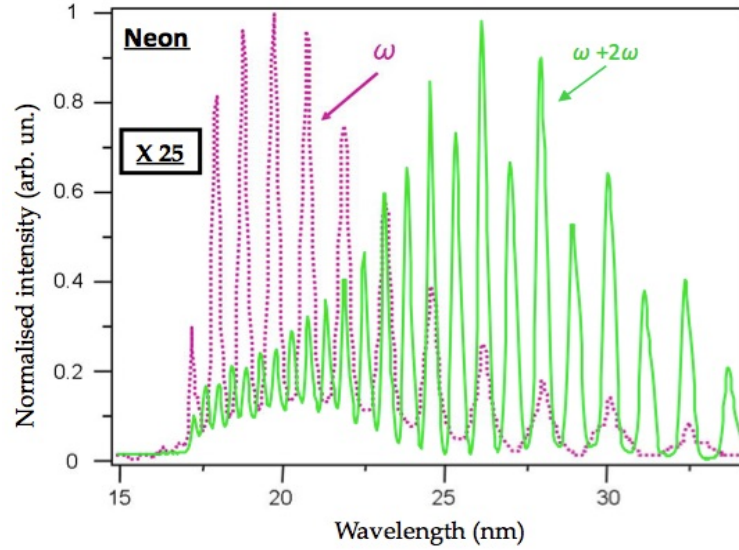


Figure 2.10: High harmonic spectra attained for a single colour field and a two-colour field laser pulse. The conversion efficiency is 25 times higher for Neon in these conditions. It is clear the effect of the doubling of the fundamental frequency: Odd and even harmonics appear. The red shift is also present.

As referred before  $U_p \propto I_{Laser} \lambda_{Laser}^2$  therefore there is a redshift and an increase on the number of photons coupled to this generation set-up. In the Neon case the signal is increased on the 20-30 nanometer range where other HHG have negligible intensity. The application of this technique is then adjusted to the problematic of this work covering the energy range since the aluminium (present in the filters to protect the CCD) cuts out radiation below 17 nm. Having the Harmonic spectra in the desired range harmonics can be adjusted to specific wavelengths. Such technique is called *tuneability* and it is easily performed by chirping the fundamental laser [53, 54] and frequency mixing [55]. When reaching really high orders however the spectra starts to approach the continuum. This leads to a decrease of the conversion efficiency due to quantum diffusion effects that dominate to a great extent the impact of the trajectories with multiple returns [56].

The exact generation procedure is not yet fully known. There are three impor-

tant models that try to explain this generation method, three different theoretical models of the high harmonic generation on a mixed field: *Corkum*, *Lewenstein* and the  $\delta^3$  model. Each model has its own unique features. *Corkum* is basically a semi-classical model while *Lewenstein* and  $\delta^3$  are quantum mechanical. All models assume the same ionisation rate calculation and in all only the ground state contributes to the evolution of the system. The ground state does not verify any depletion meaning that there are always enough electrons to be ionised. In the continuum the electrons do not feel the effect of the atomic potential. *Corkum* and *Lewenstein* are the most popular ones. All the models result in the typical high harmonic spectra. They are exemplified on figure 2.11.

Corkum	Lewenstein	$\delta^3$
Treats the motion of the electron in the field classically. Therefore its a semi classical treatment of the problem and not quantum mechanical	Fully quantum mechanical	Fully quantum mechanical
Assumes that only the electrons that appear in the continuum with zero velocity contribute to the calculation		
Can be used with any type of potential	Can be used with any type of potential	Only has 1 bound state Atomic potential has spherical symmetry but is not finite
Can be used with any type of electric field	Can be used with any type of electric field	Can be used with any type of electric field
Gives accurate results and provides a simple interpretation of the physics behind HHG	Gives the best results but is also extremely "heavy" to use both in direct calculations and simulations	Is an extremely simple model that gives accurate qualitative results and is very friendly to use for complex (multicolor) electric fields
Provides an intuitive picture of HHG phenomenon that is always very useful	The most solid model because it assumes little and can be used to explain allot	Allows for an interesting alternative interpretation of HHG

Figure 2.11: Comparison between the three models that try to explain the generation of High Harmonics on a two-colour set-up. *Corkum*, *Lewenstein* and  $\delta^3$

In this work the  $\delta^3$  model is used due to its rather simplistic approach comparing to *Lewenstein* and *Corkum* that need a computer code to be interpreted.

In particular in this model it is stated that even harmonics are generated by the second-harmonic field and odd harmonics by the fundamental field and that both have the same propagation properties as their ordinary electric field. In the case of the two-fields linear polarised with an orthogonal geometry the  $\delta^3$  model takes form of a simple equation that can be immediately interpreted. *In this case and only in this case is the polarization of the emitted harmonic photon identical to the polarization of that incident field from which an odd number of photons was absorbed* [57].

This is the simplest regime to start to understand the mechanism of generation of harmonics in a two colour field. According to the theory when the polarisation of the two-colour combining laser fields is parallel it is predicted an enhancement of the harmonic signal by a factor of 2 orders of magnitude of the generation with only the fundamental field. In 2005 Nam's group in Korea generated high harmonics in He using an orthogonally polarised two colour laser field and obtained an extremely high conversion efficiency ( $5 \times 10^{-5}$  for the 38<sup>th</sup> harmonic at 21.6nm) [8]. In Figure 2.12 the set-up developed for this experiment is represented where we can see the presence of a special quartz wave-plate that acts like a half wave plate for the fundamental and a full wave-plate for the Second Harmonic field in this way a rotation of the fundamental polarisation can be obtained. The obtained spectra is presented on the right where it can be seen the effect of the two-colour field HHG. This technique enhanced the harmonics obtained by a factor of more than 50. In this experiment however the surprise was that the harmonics generated with the orthogonal two-colour field configuration were much more enhanced than the ones generated with the parallel two-colour field configuration. Harmonic generation in this situations is unexpected by the  $\delta^3$  model. The signal increased by a factor of 2 for the 38th and 42nd harmonics. In this case all the harmonics generated at the  $2(2n + 1)$ th orders were stronger than their neighbours. Overall this configuration enhanced the harmonic signal by a factor of 100 quite unexpectedly.

In 2008 the same group repeated the experiment only focusing on the intensity of the harmonics generated on a two colour laser field. All parameters were therefore optimised and as a result strong harmonics were obtained using an orthogonally polarised two-colour field. Unprecedented conversions efficiencies were obtained ( $2 \times 10^{-4}$ ) for the range of 21.6 nm. On Figure 2.13 it is represented the set-up used for this experiment and the resulting spectra obtained. By adjusting all the parameters they were able to reach the optimum harmonic generation. In this

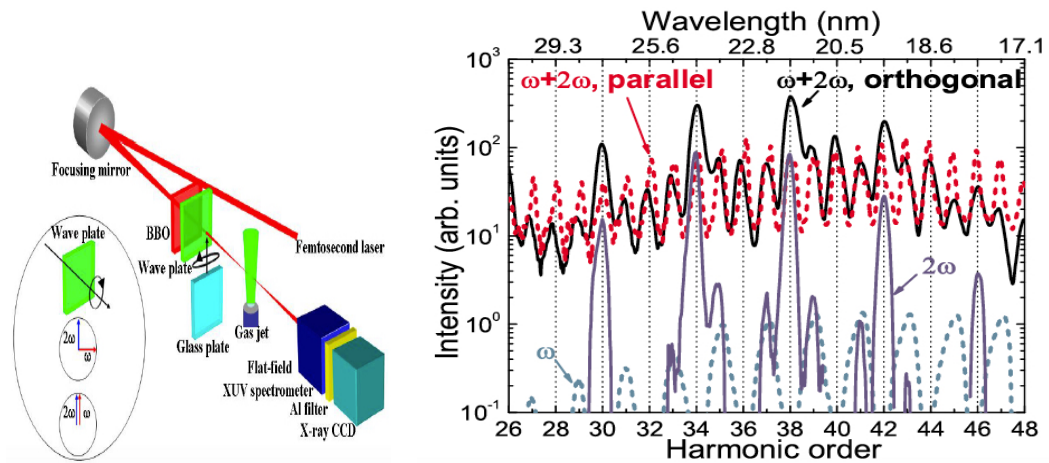


Figure 2.12: Nam's experiment a) Nam's experimental set-up. b) Nam's spectra of results. [8]

experiment a clear dominance of the  $2(2n+1)$ th orders was observed being much stronger than the  $2(2n)$ th and the  $(2n+1)$ th. One of the conclusions of this study is that with further increase of the laser energy the enhancement of the HHG in a two-colour scheme can be pushed to even shorter wavelengths [9]. The two-colour laser field induces a selection of the short electron quantum path, for which the specific moments when the electron is released from the atom corresponds to a ten times higher ionisation rate than with the single colour field [58].

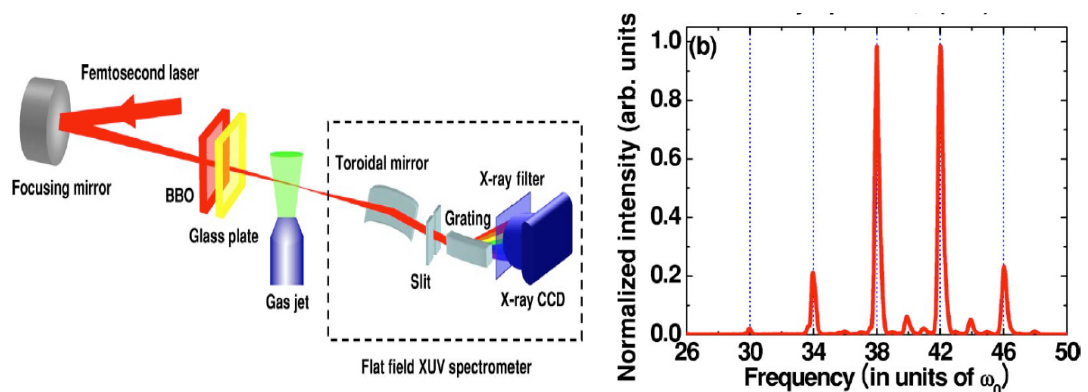


Figure 2.13: Nam's second experiment a) Nam's experimental set-up. b) Nam's spectra of results. [9]

Nam's papers renewed the interest on two colour field harmonics and its physical phenomena. It showed that the generation of harmonics with  $\omega + 2\omega$  in a parallel field has a lower signal than the  $\omega + 2\omega$  in an orthogonal field. As it can be seen the conversion efficiency was higher for the orthogonal set-up which is highly

unexpected. To explain the results obtained by the Korean group both *Lewenstein* and *Corkum* models have been applied. As a conclusion it turns out that the great enhancements of the conversion efficiency observed in the parallel case can be explained by the existing single atom response theories. However the enhancement in the orthogonal case cannot. This might be due to propagation effects therefore a collective response model that takes into account propagation effects has to be developed in order to solve the problem. To calculate propagation effects the usefulness of a simpler model becomes important, the *Lewenstein* is extremely heavy. When used in a two-colour set-up the  $\delta^3$  model can become very helpful. It gives a simpler analytical expression for the harmonic emission which is computed lightly. In the view of the formula the atom can be pictured at a system that absorbs an  $x$  number of photons and produces a photons whose energy is the sum of the energies of the absorption according to the energy conservation rule.

The physical phenomenon is not yet fully understood and needs therefore a more intensive analysis. The  $\delta^3$  model will be used in the development of this work in order to see if it is possible to extract more exact predictions about the HHG spectrum. It is known for being a very simplified model and uses the single atom response. HHG in a two-color field is not very popular. It will be observed in the next chapter if the predictions of the  $\delta^3$  model correspond to the reality thus examining its validity.

### 2.2.1 Frequency doubling

The Barium Borate (BBO) crystal:  $BaB_2O_4$  is a nonlinear optical material which is transparent in the range of 190 to 3300 nm. Second-harmonic generation or the so called *frequency doubling* is performed when at the input of the system there is a pump wave (our fundamental wave) that crosses the *non-linear* crystal exiting a residual pump wave and the second harmonic wave. This is due to the strong negative uniaxial birefringence of the Barium Borate. This crystal can be phase-matched for second harmonic generation from 409.6 to 3500 nm (type I). The type I corresponds to the configuration for which the efficiency of the HHG is known to be the highest one. In this case the  $2\omega$  component is obtained with a linear polarisation and in an orthogonal geometry in relation to the fundamental. The temperature sensitivity of the indices of refraction is low, leading to an unusually large (55°C) temperature phase-matching bandwidth.

Due to the group velocity mismatch between  $\omega$  and  $2\omega$  in the non-linear crystal the IR beam is delayed (about  $18,5fs$  for  $100\mu m$  BBO) compared to blue beam. The duration of the blue component can be calculated using the following formula:

$$S_B = \sqrt{\delta_R^2 + \frac{\Delta t^2}{2}} \quad (2.9)$$

where  $S_B$  is the duration of the blue component, the  $\delta_R$  represents the duration of the fundamental (red) wave and the  $\Delta t$  is the mismatch induced by the BBO crystal. The later is given by the manufacturer. In general the thicker the crystal the higher the intensity of the  $2\omega$  component nevertheless its temporal overlap is reduced. In our experiments the BBO thickness is reduced to  $250\mu m$ . BBO thickness thus play an important role. For a given thickness of  $100\mu m$  the corresponding time mismatch will be of  $18.5fs$  enlarging the time duration of the second field from  $40$  fs to  $42$  fs. Energy is conserved therefore the amplitude decreases. If we are in the presence of a  $250\mu m$  BBO the duration of the second pulse will increase to:  $18.5 \times 2.5 = 46.25fs$ . As stated before the energy is conserved the amplitude decreasing even more. As a perfectly gaussian beam the the second harmonic beam is proportional to the intensity profile of the  $800$  nm or fundamental one. The  $2\omega$  divergence decreases as a consequence. The focal spot size of the second field is  $1.414$  times smaller than the fundamental one  $\sqrt{\frac{800}{400}}$ .

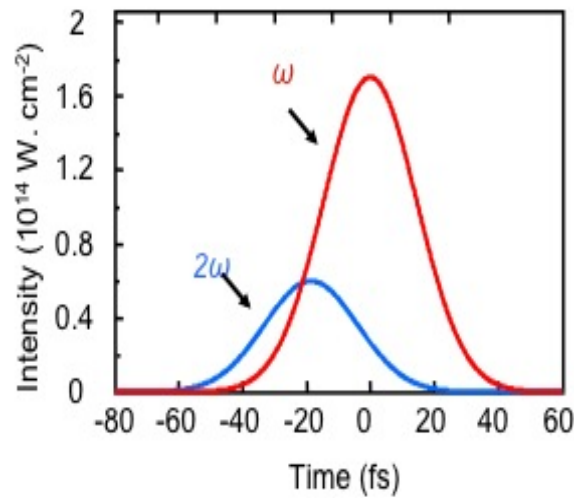


Figure 2.14: Scheme of the 2 colour mismatch in the BBO crystal

As we can see in figure 2.14 for a 100  $\mu$  m BBO the pulse duration remains close to the fundamental ( $\approx 40$ fs). Another important aspect of the generation is that the blue component generated arrives first to the generation medium, the first harmonics will be generated as this field presents enough energy to move the potential of the atom. This is mostly in the region where both are superposed. For a 100  $\mu$ m BBO at presented in the figure 2.14 corresponds to the focusing region of the blue. The generation efficiency of the BBO is given by the manufacturer and it is around the following values: for a 100  $\mu$ m BBO it is on 25%; as for a 250  $\mu$ m BBO is around 35%.

To understand the intensity and polarisation of High Harmonics (HHs) a correlation with the intensity and polarisation of the  $\omega$  (800nm) and  $2\omega$  (400nm) field is necessary. The intensity of the  $2\omega$  field can be calculated in a simplified model for the second harmonic generation (SHG) as follows:

$$I(2\omega, l) = \frac{2\omega^2 d_{eff}^2 l^2}{n_{2\omega} n_{\omega}^2 c_0^3} \left( \frac{\sin(\frac{\Delta kl}{2})}{\frac{\Delta kl}{2}} \right)^2 I^2(\omega) \quad (2.10)$$

where  $l$  is the length of the crystal,  $d_{eff}$  the cross area,  $n_{\omega}$  the refractive index of the fundamental field and  $I(\omega)$  the intensity of the fundamental field.

The next step of this technique is to focus this two fields on the gas cell and induce the laser-matter non-linear interaction that will give birth to High Harmonics. For that we will need to optimise the beam profile.

### 2.2.2 Wavefront and flux optimisation

Since the laser beam and the harmonic beam are coherent, we can speak of their wave fronts and possibly measure them. Recall that the wavefront is the set of points of the beam of the same phase. The measurement of the wavefront beam has long been confined to the study of beams in the spectral range the near infrared to VUV. Nevertheless, the capacity of a beam to be focused to sizes close to the diffraction limit is related among others to the quality of the wavefront therefore the study of the wavefront in the XUV becomes indispensable. It may be noted that for 32.8 nm in a beam diameter of 5 mm focussed at F/20, the diffraction limit is

800 nm. Due to the complexity of the methods used to measure it in the XUV field relatively little work has been undertaken in this spectral range. Transposition there few years in the field of sensor type XUV Hartmann highly prevalent in other spectral ranges [59] that has been very effective in characterising harmonics [10, 60].

The sensor we used was developed in collaboration with the company Imagine Optic, and its principle is illustrated in Figure 2.15. The incident beam is sampled by a matrix of holes (51 x 51) into a plurality of sub-beams. According to the Huygens-Fresnel principle the wave vector of each sub-beam is the wave vector of local (normal to the curvature of wavefront) of the incident beam at the hole. A sub-beam can be assimilated to a ray propagating in a direction given by the initial wave vector. Note that the holes are square, and inclined relative to each other by an angle of  $22.5^\circ$  to minimise the interferences between adjacent holes. Each beamlet is projected and recorded onto a CCD camera located at a distance, here  $L = 20$  cm, of the grid. A measure of the position of the spot originating from each radius relative to the reference positions can build a map of local slopes of the wavefront, thus derived from the local phase. We can then deduce by integrating gradually in local areas of the pupil. This method is called zonal reconstruction. The reference wave is actually not flat but spherical. Calibration of the sensor has been carried out by allowing an harmonic beam diffracted by a 10 microns in diameter hole located 50 cm from the source [3]. Given this calibration the accuracy of measurements presented here is  $0.04\lambda$  RMS or  $\frac{\lambda}{25}$  at 32.8 nm.

What we call wavefront then is the difference between the real wavefront measured and the reference wavefront, assumed to be ideal, in each point of the surface phase. The phase of the wave at a given point in the plane of the sensor can be written as:

$$\varphi(x, y) = \frac{\pi}{\lambda} \left[ \frac{x^2 + y^2}{z_H^2} + 2\delta x, y \right] \quad (2.11)$$

It is expressed in microns, or more commonly as a function of the wavelength  $\lambda = 32.8\text{nm}$ . The quantities characterising its distortions are aberrant standard deviation  $\Delta\lambda_{RMS}$  (for root-mean-square), expressed as  $\lambda$  or sometimes the maximum deviation obtained over the entire surface  $\Delta\lambda_{p-v}$ (peak to valley), also expressed in  $\lambda$ .

In gases that can be easily ionised like Argon it has been noted that the harmonic

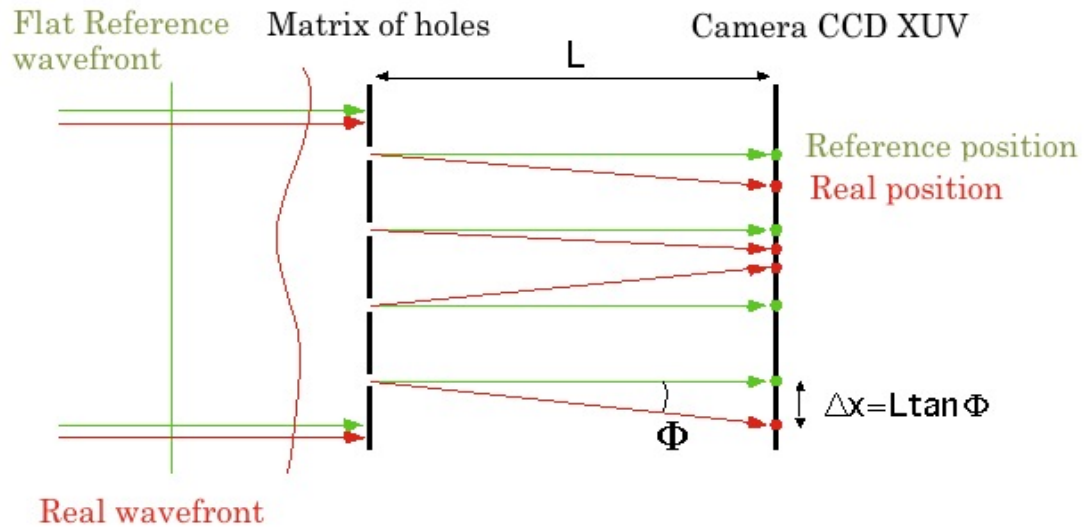


Figure 2.15: Wavefront principle of actuation

yield can be maximised by clipping the IR beam. Clipping the beam with an iris changes both the energy and the waist of the beam [61]. There is a need to establish a compromise. For small apertures the focal geometry and the ionisation, for large apertures the harmonic dipole amplitude and phase. Nevertheless the *iris clipping* technique is very used and useful to avoid distortions that change the focusing geometry and to clean major distortions on the outer part of the beam:  $\lambda$  to  $\lambda/6$  RMS. An image of an harmonic obtained in the *salle orange* is represented in figure 2.16. A spectrometer was put in place in order to focus on the optimisation parameters for one harmonic. Some of the flexible parameters are the length of the gas cell, gas pressure, focalising lens, aperture and chirp as presented before.

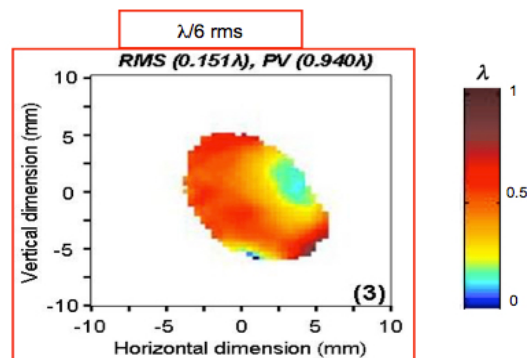


Figure 2.16: Wavefront measurement of an harmonic beam at salle orange

In this case we are in the presence of a flat spectrum that is a spectrum having

the same intensity level for odd and even harmonics. A very high increase of the intensity of the even harmonics are to due with the strong blue component generated from the IR. An example can be seen in figure 2.17.

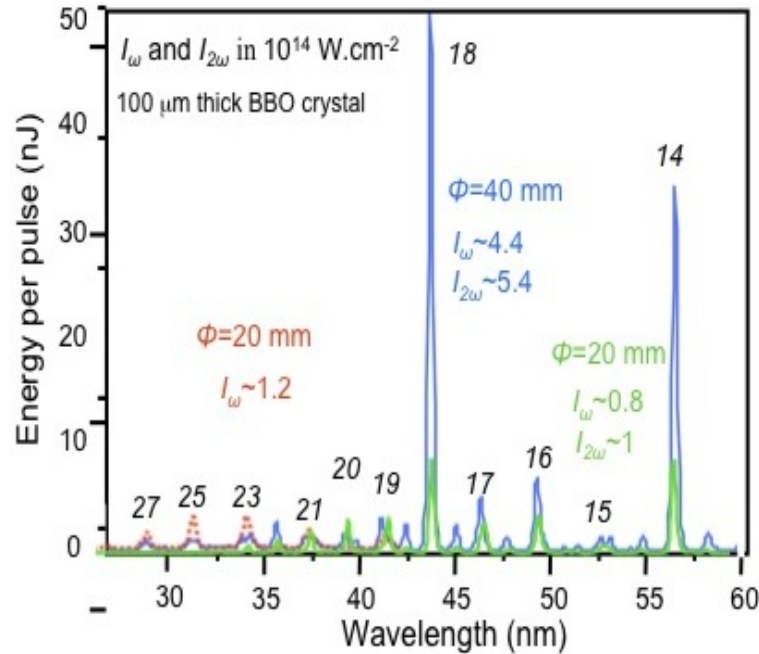


Figure 2.17: changes the focusing geometry and cleans the major distortions on the outer part of the beam  $\omega$  ( $L_{cel} = 8\text{mm}$  and  $P_{Ar} = 30\text{mbar}$ ) to  $\omega + 2\omega$  ( $L_{cel} = 4\text{mm}$  and  $P_{Ar} = 16\text{mbar}$ ) [10]

The intensification of the harmonic signal essentially takes place on the blue generated harmonics  $2(2n + 1)$  while the complementary components saturate the purely mixed field harmonics  $2(2n)$ . It can be seen the effect of the BBO in the shift to lower orders of the harmonics generated on the two-color field as discussed before.

The clipping is cutting the deformities of the laser to 20 mm. At this diameter it is safe to say that the IR beam is essentially free from aberration and residual deformations. On figure 2.18 a clipping was performed in the single field HHG and a RMS of  $\lambda/6$  was obtained. For the generation of harmonics in a two-color field without the iris on, that is with the full 40 mm beam, it was obtained a RMS of  $\lambda/5$  or three times the diffraction limit. Reducing the iris to a 20 mm a beam totally free from aberrations was obtained with a RMS of  $\lambda/17$ .

The first aberration-free high harmonic beam is obtained. Presented in fig-

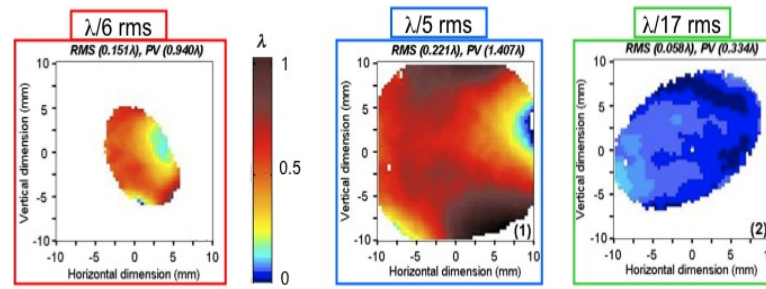


Figure 2.18: Iris clipping: limited decrease of intensity and distortions about  $\lambda/17$  RMS

Figure 2.19 is the reconstruction of the source size obtained with retro-propagation calculations. In a clipped two color configuration the astigmatism is negligible.

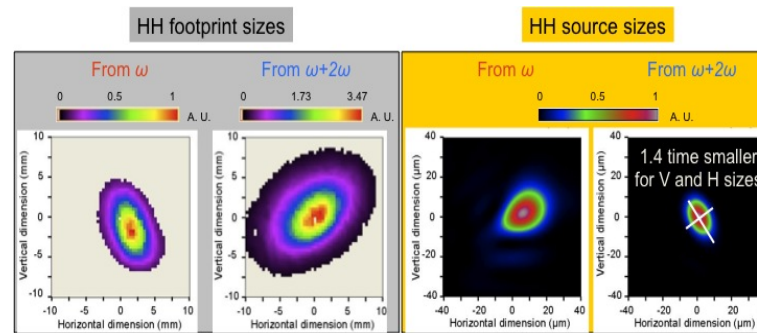


Figure 2.19: High Harmonic footprint vs HH source sizes

The result of this optimisation techniques is the good optical quality of the laser-like source HHG. Being smaller and more intense it will allow to reach higher intensities required to explore imaging in the nanometric and ultra-fast world.

The HHG XUV operational source is ready for use in the 60 eV range with under 40 femtoseconds pulse duration and fully coherent. Its high repetition rate and energy in the range of 5 mJ is perfect to give intensities at short wavelengths. The wavefront of the beam is diffraction limited and is built upon a simple system. In order to reach our goal of 20 nm this source provides enough tuneability for both odd and even harmonics. The generation of high harmonics in the two-colour case raises questions about how the generation process works when two fields are concerned. The simplified model in use was shown not to be in agreement with the first results obtained by Nam. Thus the optimisation of the source is not complete until the polarisation control studies of the source are achieved. A theoretical approach is presented in the next section.

## 2.3 Polarisation of High Order Harmonics

When establishing a parallel with the High Harmonic XUV source and the other available XUV sources a lack on its manipulation is found: the *polarisation control*. This useful tool is still to be fully understood and implemented. This step is fundamental in order to advance the attosecond science and fundamental studies of dichroic materials. XUV harmonic sources when reaching this level can be taken to the level of seeding X-FELs. With such a source the nanoscale ultrafast magnetic dynamics can be reached by means of the Magnetic Circular Dichroism [62], [4]. Some biological systems also present dichroism therefore its nanoscale dynamics could as well be reached using this type of source [62]. Another application is to use FELs or laser plasmas and the so called *seeding*. A way to attain amplified circular polarised light. [63].

One of the goals of today's attosecond science is to produce intense attosecond bursts. A theoretical study by Marangos [64] shows that by using two pulses of radiation one can have control on the exiting attosecond pulse train. A control over the polarisation was obtained for a orthogonal two-color field. This prompted us to use this geometry in order to achieve control of our XUV harmonic source.

This relatively compact source can therefore be transformed into a easier reach platform to perform this types of studies since nowadays the structures that can do it have limited reach and are only in few places worldwide.

### 2.3.1 Two-colour HHG with linearly polarised fundamental a weak orthogonally polarised second harmonic field

The first approach regarding high-harmonic generation (HHG) presented in this manuscript is the case where the fundamental field is strong and linearly polarised and the second field is weaker (up to 10% of the fundamental [65]) and orthogonally polarised. This means we will treat the second harmonic field as a perturbation on the system hence we will apply the perturbative regime. The simulations were done in partnership with the *icfo* in Barcelona.

The three-step model isn't identical at every step. Conditions such as the half-

cycles, envelope of the pulse, depletion of the ground state and dephasing cause by ionisation can interfere at the atomic level on the generation. However this fact can be overlooked considering that the harmonic spectrum presents discrete harmonics so the effects are negligible and apparently periodic. The total single-atom response is written as a sum of the responses of all the three-step processes. Since we are adding all the processes the relative phase is crucial in shaping the harmonic spectrum. For odd harmonics all the terms have a phase differing by an integer as seen before. This translates onto a phase of  $2\pi$  hence adding up in phase.

Classically superposing a second field to the fundamental would actually make the electron miss the atom on the recombination stage. However when dealing with electrons we always deal with electron wavepackets therefore even if it isn't the same precise point emission will still occur. The emission will however be attenuated since the amplitude of the wavepacket is variable.

Regarding even harmonics looking closer at the phase it is possible to see that on the case of HH generation on a fundamental field the phase differing is set to  $\pi$  leading to a destructive interference. However when a second field is added the relevant quantities such as birth time, return time and action can undergo a shift regarding the perturbative approach. Changing the birth time means that the electric field will be different at birth therefore a change in the ionisation rate corresponding to the amplitude of the emission is to be expected. Also a small fraction of a change on the phase leads to different interferences on the atomic system. We can see it as two independent electron motions: the first one, dominant, due to the fundamental strong field and the other one, weaker, due to the second field. The action is changed by their dot product integrated over time.

On orthogonally polarised fields however these two independent electron motions will evaluate to zero since they are perpendicular. We have established that in the orthogonal weak field starting with a single half-cycle the first-order changes in the birth and return times, and the momentum component along the strong field axis are all identically zero. What does change is the momentum along the weak field axis. The electron seems to be born with exactly the right z-component such that a recollision occurs with the core. The electron velocity at recollision determines the polarisation of the emitted radiation at that instant. One can see that different trajectories: distinguished by their return kinetic energy and whether they

are long or short: exhibit different behaviour, but in all cases the electron velocity at the recombination time varies sinusoidally with the phase of the fundamental field. Figure 3.51 portrays these behaviours on the different cases.

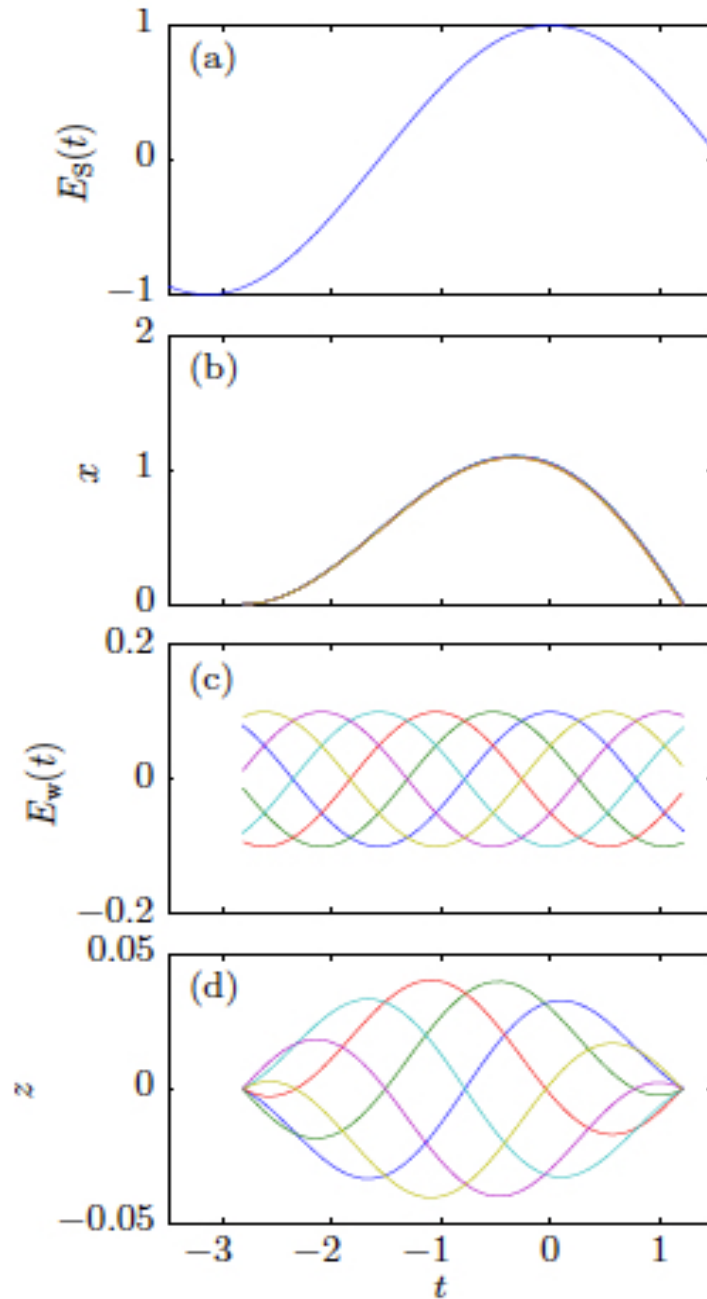


Figure 2.20: Single half cycle case. (a) Strong electric field. (b) Electron trajectories defined as  $x$  component. (c) Weak second harmonic field with several different phases relative to the strong field by colour. (d) Electron trajectories corresponding to (c) defined as the  $y$  component.

The  $x$  component of the response undergoes no first-order change in action or return velocity being constant. The  $z$  component has an amplitude which depends on the relative phase of the strong and weak fields. Using these observations, one can now predict how the spectrum will be changed by the weak orthogonally-polarised field.

Upgrading the system too many half cycles there will be different frequencies and the relative frequency between the strong and weak fields phase changes each half-cycle by an amount of:

$$\Delta\phi_w = \pi(\omega_w - 1) \quad (2.12)$$

when  $\omega_w = 2$  the phase slip is  $\Delta\phi_w = \pi$ . The return velocity depends sinusoidally on  $\phi_w$ , this corresponds to a  $\pi$  phase flip with respect to the motion in the  $x$  direction. This the  $x$  motion has a  $\pi$  flip every half-cycle, this additional flip cancels it out, so that the  $z$  motion is perfectly periodic every half-cycle leading to the production of even harmonics. Figure 2.21 shows this sinusoidal dependence.

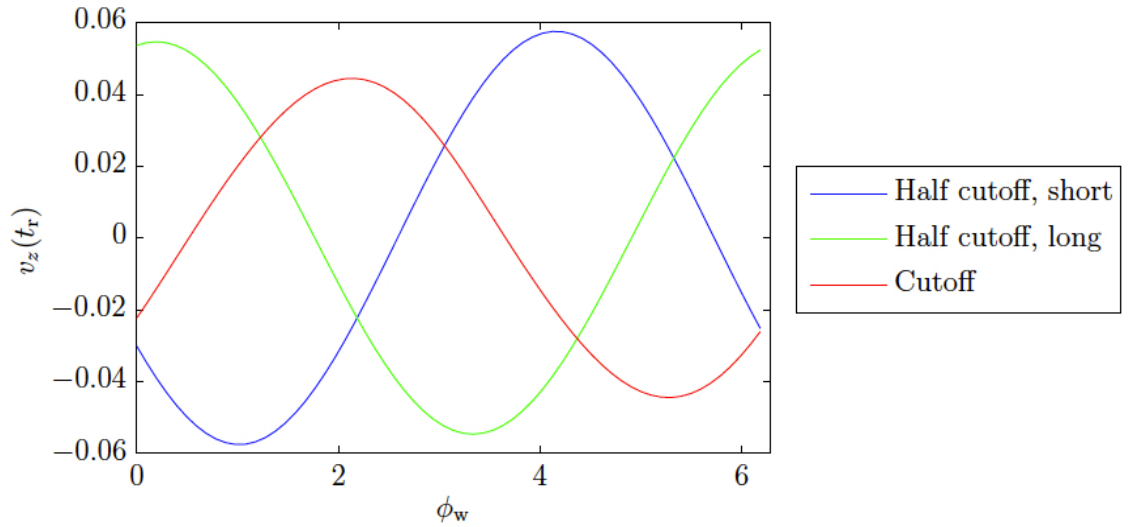


Figure 2.21: Electron velocity as a function of fundamental phase for different trajectories. (red) Cut-off. (blue) Half cut-off, short. (green) Half cut-off, long

Another way to look at this is to realize that a half-cycle advance of the fundamental is a full cycle advance of the second harmonic. Therefore, the motion along the  $z$  direction repeats exactly every half-cycle of the strong field. For a weak orthogonal second-harmonic field, the radiation polarised along the  $x$  axis should be odd harmonics and independent of the weak field, whilst the radiation

polarised along  $z$  axis should be even harmonics. They should be proportional to the weak field strength, and vary sinusoidally with the relative phase of the weak and strong fields. The phase for maximum intensity depends on the trajectory.

## 2.4 Conclusion

In this point an optimised coherent XUV table-top source with 20 nm attained by laser/matter interaction in the form of high harmonic generation is ready at the LOA. The development of a more robust source is nowadays an exigency in various fields of science. The search for understanding the smaller, shorter or just improving imaging techniques is a real goal aiming to be reached by the scientific community. Fields like Biology, high XUV fields, plasma physics and femtochemistry demand strong energy in the milijoule range, short pulse durations in the femtosecond or attosecond range, high repetition rates, shorter wavelengths, high spatial coherence and good wavefront and *polarisation control*. As practically all the requirements are being met at the moment at *salle orange* the next section of this manuscript will be focused on the polarisation studies of the HHG source obtained using a two-colour set-up and the attempt to increase further the knowledge of its physical phenomena by recurring to simulations.

---

## Polarisation studies of High Harmonics generated in a two-colour field

---

### Contents

---

<b>3.1 High Harmonics Generation paths in a two-colour field . . . .</b>	<b>71</b>
3.1.1 Description of the experimental set-up of the orthogonal two-color scheme for HHG . . . . .	76
3.1.2 Analysis of the measurements . . . . .	80
3.1.3 Conclusions of the first harmonic studies . . . . .	91
<b>3.2 Second polarisation harmonic studies . . . . .</b>	<b>92</b>
3.2.1 Description of the experimental setup of the second HHG polarisation experiment . . . . .	94
3.2.2 Polarisation measurement . . . . .	96
3.2.3 Experimental results of the harmonic polarisation experiment	102
3.2.4 Polarisation of high harmonics in an orthogonal two-colour field . . . . .	108
3.2.5 Matlab data analysis of the harmonic polarisation in an orthogonal two-colour field . . . . .	115
<b>3.3 Polarisation simulations . . . . .</b>	<b>120</b>
3.3.1 Strong field approximation - Bauer . . . . .	121
3.3.2 New theoretical approach . . . . .	129
<b>3.4 Conclusions and Perspectives . . . . .</b>	<b>133</b>

---

In the last chapter the optimisation steps in order to develop a table top source of wavelength  $20\text{ nm}$  and femtosecond pulse duration with application on the magnetic imaging of nano-domains in a Cobalt sample and therefore study its magnetisation phenomenon were presented. It was seen that one of the ways to increase the High Harmonic signal is by using a set-up of a two-colour field and generate harmonics from both a fundamental  $\omega$  field and a second harmonic  $2\omega$  field. During the two-colour optimisation process a point was made on the discordance between theory and experiments. The very relevant question of the polarisation of the source was presented which prompted the study the physical phenomena behind the two-colour field HHG. An hypothesis is made: the resulting high harmonics follow the respective generating fields as predicted in the  $\sigma^3$  model. This chapter describes the polarisation studies made in order to understand furthermore the phenomenon.

Polarisation is a property of vector waves such as light, that describes the orientation of their oscillations. The fact that these waves are characterised by vectors differs from other types of waves such as sound waves, and involves the phenomenon of polarisation. The simplest manifestation of polarisation is that of a plane wave, which is a good approximation of most light waves. As any electromagnetic wave that propagates, it consists of an electric field and a magnetic field perpendicular to both the direction of propagation as shown in figure 3.1.

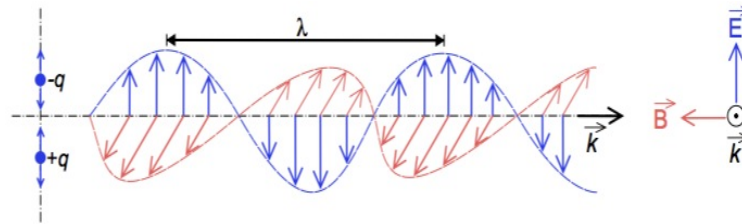


Figure 3.1: Linear polarised light wave with the magnetic field  $B$  and the electric field  $E$  in an perpendicular angle from each other.

The electric field of a plane wave which is a good approximation of most light waves has the following shape:

$$E(r, t) = (A_x \cos(kz - \omega t), A_y \cos(kz - \omega t + \phi), 0) \quad (3.1)$$

where  $A_x$  and  $A_y$  are the amplitudes of the  $x$  and  $y$  directions and  $\phi$  is the relative phase between both components.

In terms of polarisation control not many optical elements equivalent to the half-waveplates and so on are available in the XUV range. This control has therefore to be established during the harmonic generation process. Milosevic and Becker [66] proposed the use of perpendicular fields to control the polarisation angle of the resulting high harmonic radiation generated.

### 3.1 High Harmonics Generation paths in a two-colour field

The generation of High Harmonics in a two-colour laser fields gained some interest due to the introduction of new degrees of freedom in the generating step. Harmonics have been used for the last decades for many applications including holography, precision spectroscopy, understanding of atomic ionisation and now also play a major role in attosecond science and more recently in seeded free-electron lasers [67]. Limitations of this technique mainly weak tuneability and low number of photons at short wavelengths, prompted the development of new harmonic sources such as from a solid target, ions and still from a gas medium with more elaborated techniques: either with very long interaction region or two-colour laser fields. In this latter, both linearly polarised fundamental  $\omega$  and second harmonic  $2\omega$  generated from a nonlinear crystal, are recombined in the gas target. First, due to the  $2\omega$  field, the symmetry of the atoms is broken; the harmonic content is doubled with the presence of the even components. Second, with two-colour fields in an orthogonally polarised geometry, and on very specific conditions a single attosecond pulse can be isolated and the highest harmonic generation efficiency is obtained. Yet, while the polarisation of harmonics in single-colour follows the linear polarisation of the laser, in this perpendicularly polarised arrangement the resulting polarisation of the harmonics has only been predicted by calculations but not measured.

The use of the mixed field, that is with the first harmonic  $\omega$  and the second harmonic  $2\omega$  has the purpose of controlling the electron wave packet from its formation until the recombination and generation of the harmonic radiation. By controlling the wave packet one can substantially modify the quantum electron trajectory. Actually, HH theory in a two-colour field is challenging in the sense that the calculations are extremely complex and can not give a general idea of the physical mechanisms used. As explained in the last chapter the available models

that explain high harmonic generation are very heavy to compute and fail to explain some geometries of the generation. In this work the hypothesis of the  $\delta^3$  model is explored. The reason to use this model is the conviction that many properties are governed by the propagation of the free electrons in the continuum subjected to the driving fields rather than by the structure of the atom. For instance, the Lissajous diagram, representing the spatial mean trajectories of returning electrons, follows a bow-tie shape allowing only short electron paths to be formed. Since the time evolution of the electric fields vector flips by half optical cycles, the polarisation of the emitted pulses also flips. This is why, using HH classically generated from multiple laser cycles and in which recollision energies vary, strongly complicates the global HH polarisation estimation. An example of a Lissajous diagram for an orthogonally polarised two-colour field is represented on Figure 3.2.

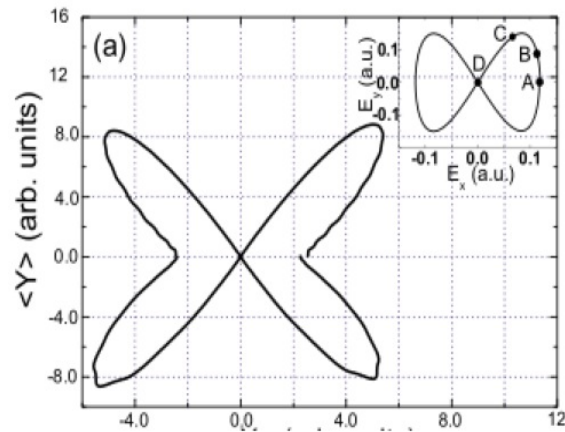


Figure 3.2: Electronic motion for orthogonally polarised two-colour field. The inset shows the Lissajous diagram. [8]

Control over the emitted radiation can be achieved by manipulating the free electron trajectories leading to the HHG [64].

Two-colour HHG results in a broadly tuneable XUV radiation with unprecedented conversion efficiencies as presented in the last chapter. The enhancement effect is a result of the modified electron trajectories produced in the two-colour laser field. The constructive interference between multiple quantum paths allows the selection of specific harmonics and the consequent increase of the conversion efficiency. The XUV radiation can be, if controlled, enhanced selectively in the XUV region. This is also true for the destructive interference case. Some harmonics can result in very low levels of signal due to the multiple quantum paths available can cancel each other. In conclusion the XUV HHG spectra can be modulated

selectively according to our needs [68].

Considering a single field generating harmonics the formation of quantum paths can be explained as follows. In an atom the quantum paths available after ionisation can be split in two main groups: the short trajectory path and the long trajectory path. The recombination and ionisation times is what differentiates them. Figure 3.3 shows that the short path starts between  $0.05T$  and  $0.25T$ , where  $T$  is the period, when the electron leaves the atom and recombines before the sign of the driving field reverses again. The total traveling time in the medium is  $0.65T$ . In a long path the electron leaves the atom between the peak of the field,  $0.00T$  and  $0.05T$  the traveling time is longer than  $0.65T$ . The *border* between the two regimes is the *cut-off path* that presents a total time of  $0.65T$ . It is formed at  $0.05T$  and the electron recombines at  $0.7T$ . Between  $0.25T-0.5T$  and  $0.75T-T$  the ionised electrons have to chance of recombination with the parent ion. The electron paths that emerge between  $0.5T$  and  $0.75T$  have the opposite sign and are phase shifted but nonetheless contribute to the same harmonics. Quantum deformation effects eliminate to a great extent the impact of trajectories with multiple returns [11].

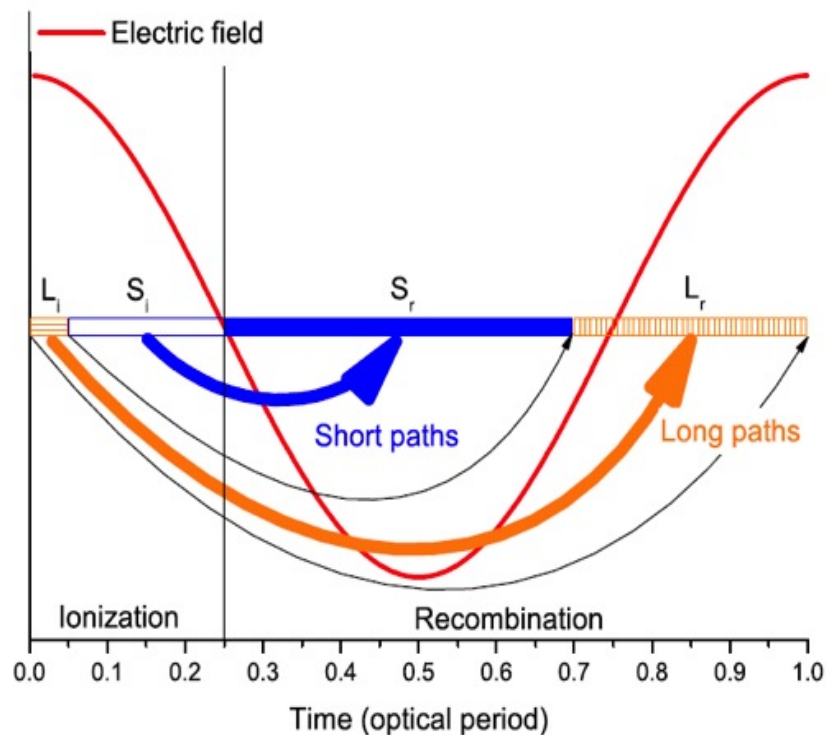


Figure 3.3: Lissajous diagram for orthogonally polarized two-color field and the influence of the phase. (a)  $\phi = 0$ , (b)  $\phi = 0.125\pi$ , (c)  $\phi = 0.25\pi$ , (d)  $\phi = 0.35\pi$ , (e)  $\phi = 0.5\pi$ , (f)  $\phi = 0.625\pi$ , (g)  $\phi = 0.75\pi$  and (h)  $\phi = 0.875\pi$ . [11]

Long paths are more affected by the medium. Since the traveling time is longer the wave packet is denser and more subjected to quantum diffusion. Spreading the electron wave packet in the continuum leads to a strong decrease in the emission efficiency. In terms of intensity sensitivity these paths are more dependent on the laser intensity as they travel more time in the medium. The use of short pulses can reduce the loss of energy due to depletion. Depletion does not change the cut-off. Short paths are more robust to the laser intensities and tend to provide a clean harmonic spectra with well defined harmonic peaks.

The addition of the second colour field  $2\omega$  adds new degrees of freedom. Controlling the pulses is then possible selecting the electron paths contributing to the process of generation. The motion of a free electron can be easily adjusted by changing the shape of the applied field. Considering the fundamental field with an intensity of  $I_1$  and the second harmonic field with an intensity of  $I_2$ . The return times of the electrons in the media are dependent of the ration between the two intensities,  $\beta = \frac{I_2}{I_1}$ . Its relative phase is also an important parameter according to Eichmann [55] and Frolov [69] since the recombination is affected by both fields and is sensitive to its parameters. In the specific case of an orthogonal two-colour field the harmonics generated varying the phase between the pulses gives something similar to the figure 3.4. Here the phase,  $\phi$  varies between 0 and  $0.875\pi$  and the correspondent Lissajous diagram for the electronic motion is represented.

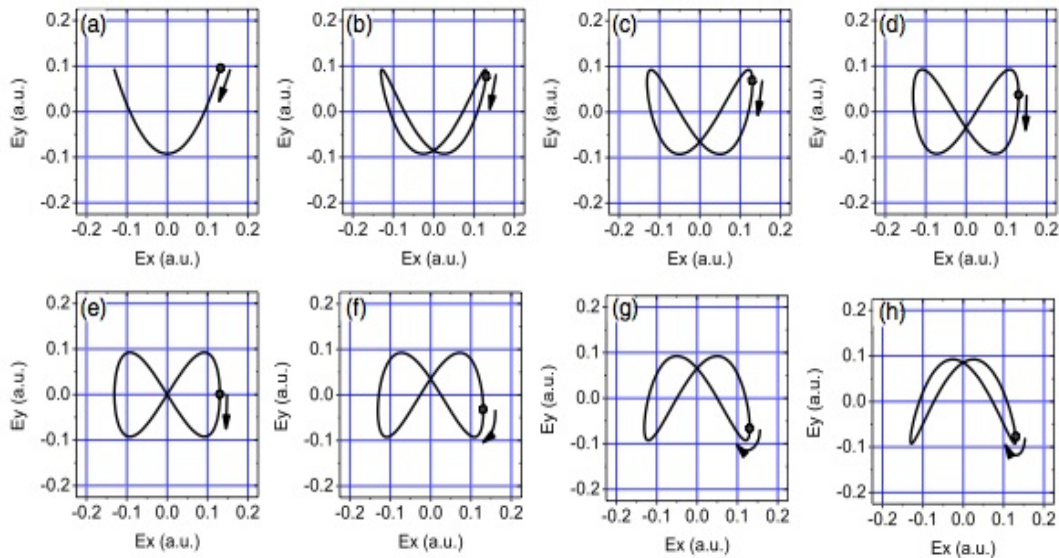


Figure 3.4: Lissajous diagram for orthogonally polarised two-colour field and the influence of the phase. (a)  $\phi = 0$ , (b)  $\phi = 0.125\pi$ , (c)  $\phi = 0.25\pi$ , (d)  $\phi = 0.35\pi$ , (e)  $\phi = 0.5\pi$ , (f)  $\phi = 0.625\pi$ , (g)  $\phi = 0.75\pi$  and (h)  $\phi = 0.875\pi$ . [11]

For  $\phi = 0$  the traveling time of the electron is higher than  $0.7T$  leading to the formation of long paths exclusively. From the diagram 3.4 (a) it can be seen that the two components of the field the  $x$ -axis and the  $y$ -axis never cross zero simultaneously leading to no formation of harmonics originating from short paths. At a relative phase of  $\phi = 0.5\pi$  only short paths are formed, with traveling time shorter than  $0.4T$ . The Lissanjous diagram has the form of a perfect bow-tie and both linear regions around zero resemble figure 3.2 that represents the one colour field generation scheme. This selection of paths is maintained for any value of intensity of the fundamental and second harmonic field. If these change the variations observed in the Lissanjous diagram are mostly of elongating or compressing its shape according to the relative force of the fields [9]. From here the main conclusion is that the selection of quantum paths can be done mainly with varying the relative phase between both fields and leaving the intensity variable alone if they are of comparable intensities. However when there is a difference of more than one order of magnitude between both fields the quantum paths associated with the electrons can be affected although the path formation remains rather unchanged.

If the case is of a non-orthogonal polarisation of the two-colour field the path formation will depend on both fields and its relative magnitude. This case will not be study in this manuscript.

A particular case of harmonic polarisation is the case of the generation over elliptical laser fields. Harmonics are generated when the electrons return to the core and considering the simple classic model as soon as the polarisation is no longer linear the electrons will generally never return to the core. The electrons that contribute to the HHG must have a closed trajectory meaning that they have to return to the core. Following the laser field, electrons emerge in the continuum with a transverse velocity that compensates the lateral difference acquired. The trajectory is therefore not linear and a certain angle is added with respect to the main axis of the laser. With the increase of ellipticity no electronic trajectories passing by zero (the nucleus) are predicted. Even small ellipticities can induce slight changes in the recollision angle resulting on a very dependent of the field strength and ellipticity recollision step. For higher Intensities of the driving laser field the ellipticity and the rotation angle induced on the generated harmonics vary fast exhibiting quantum inference effects [70]. Simulations done by Ph. Antoine *et al.* suggest that the trajectories corresponding to long return times are dominant in HHG with special focus on the higher orders. Also in this case the laser intensity

doesn't play a influential role. Harmonic generation is predicted to decrease with the increase of ellipticity of the field.

The  $\delta^3$  model, which is a simplified model of the atom using a 3D Dirac delta function to represent the atomic potential maintaining the symmetry of the central potential, nevertheless proposes a solution. In that model, the possible bound states are reduced to one and the harmonic properties are governed by the possible trajectories of the free electrons, allowing exact qualitative predictions. In the case of an orthogonally polarised two-colour fields scheme, the general formula takes a very simple form that can be immediately interpreted; the odd harmonics have the polarisation of the fundamental field while the even harmonics have the polarisation of the  $2\omega$  field.

The first proposal submitted to take place at LOA was based on the  $\delta^3$  model for an orthogonal two-colour field. Figure 3.5 is a scheme representing the harmonic polarisation hypothesis when generated in a two-colour orthogonal field. A relatively simple set-up is proposed, allowing to quantify precisely the polarisation angles of the odd and even HH fields (respectively  $2n + 1$  and  $2n$ ). It combines the production of HH in orthogonally polarised two-colour configuration from a laser with a variable linear polarisation (polariser), and the HH measurement of polarisations with a soft X-ray optical system (analyser).

In order to verify this theory some measurements were obtained in early experiments at LOA.

### 3.1.1 Description of the experimental set-up of the orthogonal two-color scheme for HHG

A detailed experimental study of the  $\omega$ ,  $2\omega$  harmonic generation model was performed at the Laboratoire d'Optique Appliquee at *salle orange* with a kHz Ti:Sa laser system. The pulse central wavelength is located at 800 nm with an output energy of 5 mJ. Its time duration is of 35 fs in Full Width Half Maximum. Frequency doubling is achieved by the insertion of a BBO Beta Barium Borate crystal in the path of the fundamental IR laser resulting in two beams, the doubled frequency beam at a wavelength of 400 nm and the fundamental beam that has not been converted. The doubling efficiency of the radiation is given by the manufacturer

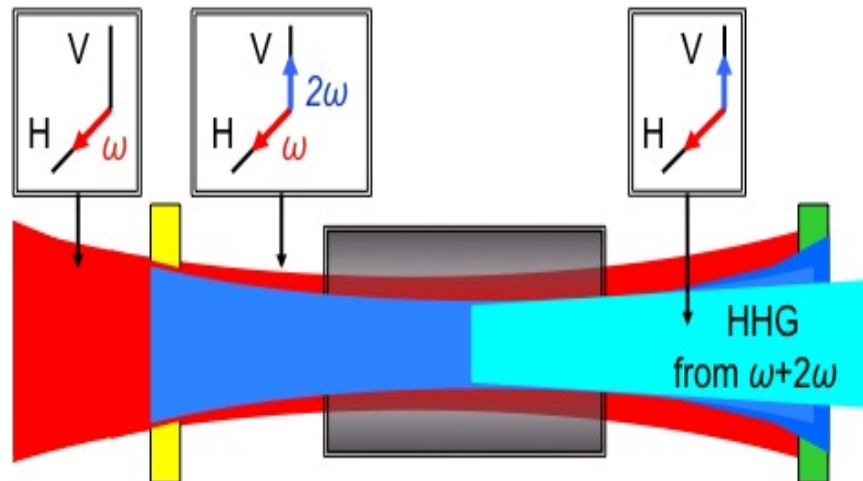


Figure 3.5: Theoretical proposition based on the  $\delta^3$  model for the laserlab proposal at Laboratoire d'Optique Appliquée (LOA). An intense IR laser pulse is focused on a gas cell by means of a lens. The fundamental pulse is on a horizontal axis. When the laser pulse passes through the BBO crystal the second colour laser field is generated. Due to the positioning of the BBO the second-colour pulse will be on an orthogonal axis, in this case the vertical axis. The resulting two-colour laser field interacts with the noble gas generating harmonics.

of the BBO and it is a characteristic of the type used. In our experiment a BBO type 1 was used, this configuration generates the the second harmonic generation at 400 nm beam orthogonally to the fundamental one. In the Korean's case [9] a silicate plate was introduced to compensate the delay between the two pulses. In our set-up no silicate plate was added. The fact that it has to be placed between the BBO and the gas cell was a determinant factor since the focused energy in addition to the repetition rate could lead to laser damage. Since no correction was made choosing the adequate thickness for the BBO crystal is of great importance. In the case of  $100 \mu\text{m}$  the  $2\omega$  field component can be generated rather efficiently (15% giving  $0.6 \times 10^{14} \text{W.cm}^2$  for  $2\omega$  compared to  $10^{14} \text{W.cm}^2$  for inside the generation medium). Due to the lack of temporal pulse correction a  $100 \mu\text{m}$  BBO is adequate since it keeps a relatively small induced delay (18.5 fs) between both field pulses and short pulse duration for the  $2\omega$  beam that is approximately about 35 fs, for maintaining a correct temporal overlap. In this configuration of generation due to the slight delay the maxima, both envelopes are not in phase. The temporal window is given by the intensity ratio of  $\omega/2\omega$  relating to one generated burst of harmonics photons.

In this experiment the incident laser polarisation was set to be variable. To

change the polarisation of a beam is possible recurring to a  $MgF_2$  plate with the birefringence axis perpendicular to the surface. This optical component is known as a waveplate. By defining a tilt on the plate the polarisation of the fundamental laser wave will be continuously changed from  $p$  to  $s$  passing by the intermediate polarisations. In any case of incident polarisation wave the BBO exits a second harmonic beam that is orthogonal to the fundamental. Its conversion efficiency can however be different for the various incident polarisations. This can however lead to different efficiencies for the generation of the  $2\omega$  field.

The BBO crystal was placed about 30 mm before the gas cell (20 mm long), in which both  $\omega$  and  $2\omega$  fields are focused, ensuring a natural spatial overlap.

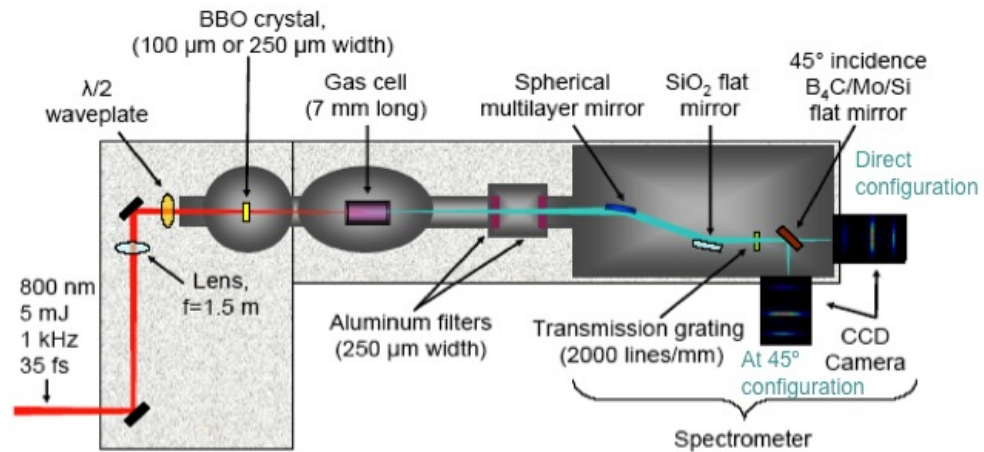


Figure 3.6: Proposed set-up to study the generation of harmonics in a two colour field. The introduction of a multilayer mirror at  $45^\circ$  is based on the proposition given by the  $\delta^3$  to study generation in this specific regime.

This experiment is represented on Figure 3.6. In this figure the representation of the hypothesis for the harmonics generated follow the  $\delta^3$  model.

Harmonics are detected in a system based in a spectrometer and two similar CCD Cameras (Princeton,  $1340 \times 400$  pixels,  $20 \mu m^2$ ) placed as shown on fig ?? one to perceive the direct radiation, that is in the axis of propagation and the other on a 45 degree angle in order to retrieve the harmonic content at this position. The detection system is protected by two thin aluminum filters (200 nm thickness each) for suppressing the strong residual IR laser beam not converted in HHG in the gas cell. The spectrometer is more precisely composed by a spherical mirror

at grazing incidence with a 800 nm anti-reflection coating ( $ZrO_2/Si$  multilayer deposit) and a transmission grating (2000 lines/mm with the diffraction efficiency as function of the wavelength in the presented spectral range). From the recorded pictures (vertical position as a function of the wavelength), spectra are obtained by lineouts in the horizontal plan and by the integration of this lineout over the vertical dimension.

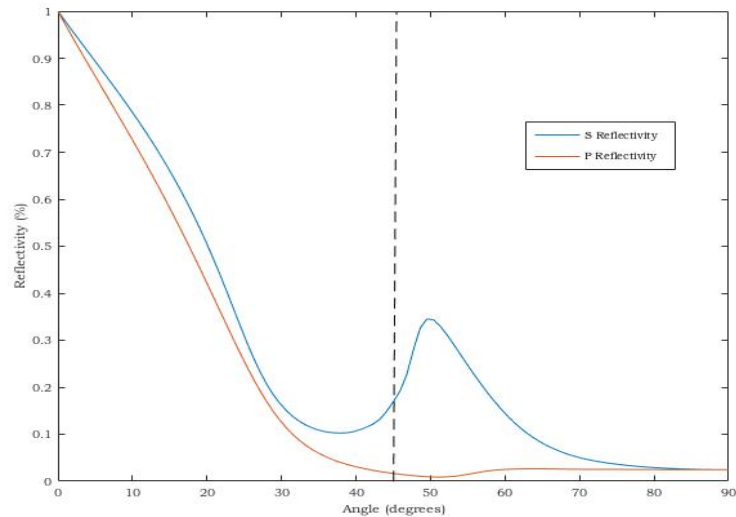


Figure 3.7: Multilayer theoretical reflectivity: Mirror reflectivity as a function of the incidence angle for p polarisation (horizontal) and s polarisation (vertical).

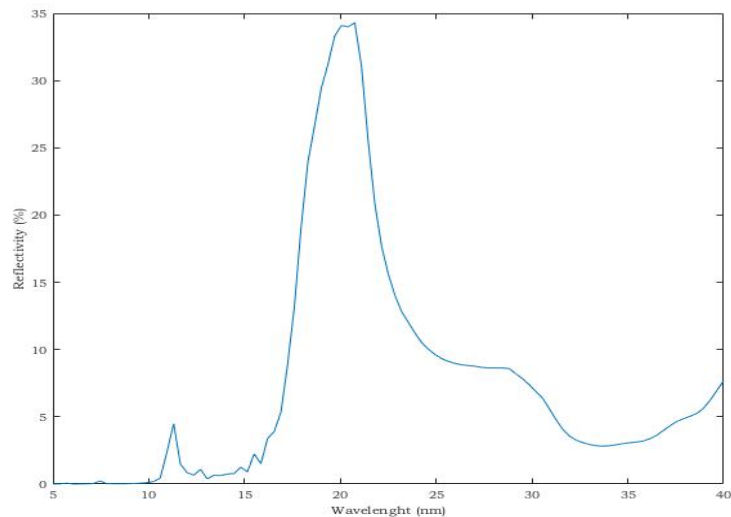


Figure 3.8: Multilayer theoretical reflectivity: Mirror reflectivity as a function of the wavelength. The mirror is set at  $45^\circ$  of incidence.

The objective of this first experiment is to analyse the output polarisations of

the generated harmonics. This is achieved by a polarised multilayer mirror placed at a  $45^\circ$  angle from the axis of propagation of the harmonics. This  $B_4C/Mo/Si$  mirror is visible in the figure ?? and it is retractable. That means that it conditions the harmonic content retrieval. When it is out the harmonics are measured on the "direct" CCD. However when on, it blocks the direct configuration and its multilayer nature allows the reflection of the harmonics onto the " $45^\circ$  configuration" CCD. Therefore each CCD retrieves a different but complementary information. The multilayer in use to reflect the radiation presents the following theoretical reflectivities shown on figure 3.7 and figure 3.8 .

The reflectivity of the multilayer for each harmonic is then achieved by dividing the harmonic intensity profile measured in reflection on straight. The mirror is placed at  $45^\circ$  of incidence, close to the Brewster angle, in order to strongly reduce the horizontal component of the reflectivity (p) and as a consequence even small variations of polarisation can be observed. In the figure 3.8 a theoretical reflectivity of the chosen multilayer is plotted in which the desired enhancement of the 20 nanometer wavelength is seen.

### 3.1.2 Analysis of the measurements

In order to evaluate the optical system used to collect the data the reflectivity of the multilayer has been measured for both its vertical (s) and horizontal (p) components using Argon to generate HHG in the soft-X-ray region. HHG was performed using a one-colour laser field focused in the gas cell full of Argon. In this case harmonics of higher wavelength are obtained due to the cut-off law of around 30 nm. In figure 3.7 it is shown the reflectivity of the multilayer mirror in function of the incident energy. It is visible then even the harmonics from Argon are not in the optimal 20 nm range they can still present an acceptable reflectivity signal. The reflectivity of a multilayer changes with the wavelength. Figure 3.7 presented in the previous section shows the theoretical reflectivity as a function of the energy and the polarisation of light. The best contrast for the polarisation is at  $50^\circ$  however this configuration was complicated in terms of set-up. The best experimental contrast for the polarisation is at  $45^\circ$  where the multilayer strongly marks the reflectivity of the vertical polarisation (or s) and the horizontal polarisation (or p). At  $45^\circ$  the s component is rather high compared to the p component making it easier to difference both types of polarisation.

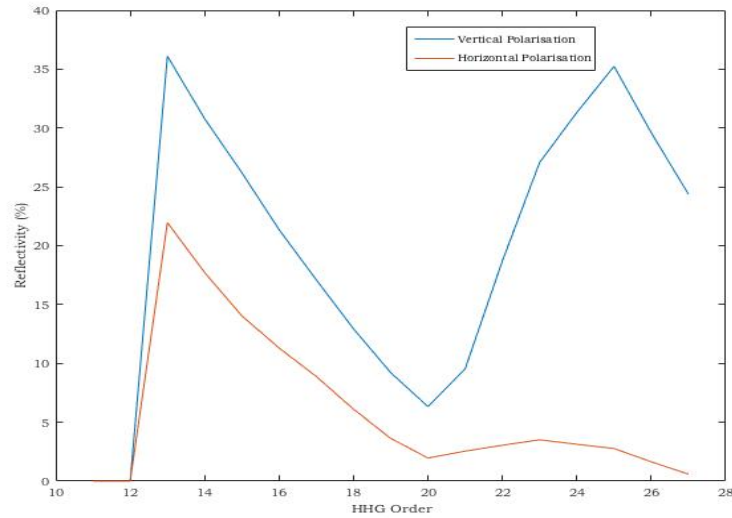


Figure 3.9: Experimental reflectivity for horizontal polarisation and vertical polarisation in function of the harmonic order

Figure 3.9 portrays the experimental results concerning the reflectivity of various harmonic orders. Both the vertical and the horizontal polarisations are analysed. The harmonic order goes from the 11<sup>th</sup> to the 27<sup>th</sup> to which corresponds a wavelength range of ] 30, 72 [ nanometers. This data will allow to know exactly how much each harmonic is attenuated.

The following figure 3.10 shows the experimental spectra attained with a direct configuration and a 45° configuration of the multilayer mirror.

The represented polarisation corresponds to the horizontal, p polarisation.

The harmonic signal is clearly higher on using a direct configuration, that is without the multilayer, as shown on the figure 3.11.

The represented polarisation corresponds to the vertical, s polarisation as presented on figure 3.12.

The harmonic signal is clearly higher on using a direct configuration as the spectre shows on figure 3.13.

The represented polarisation corresponds to the intermediate, 45° polarisation

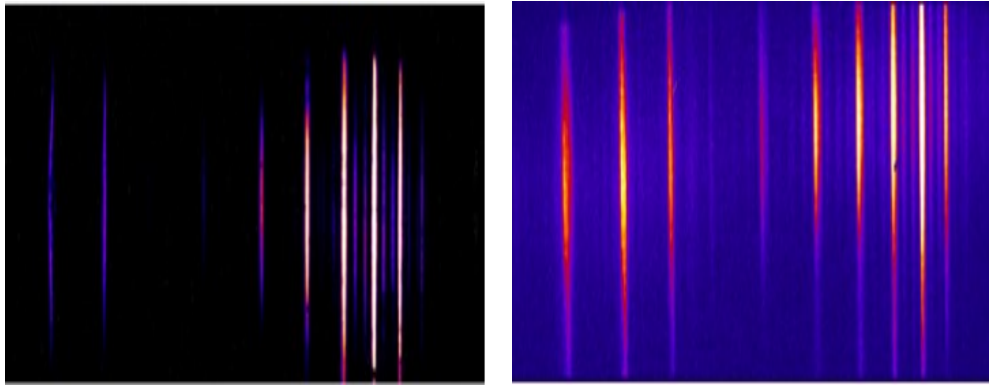


Figure 3.10: High harmonic signal registered on the CCD by varying the positioning of the mirror. On the left it is represented the obtained HHG signal at a direct configuration. On the right it is represented the obtained HHG signal at a configuration of  $45^\circ$ .

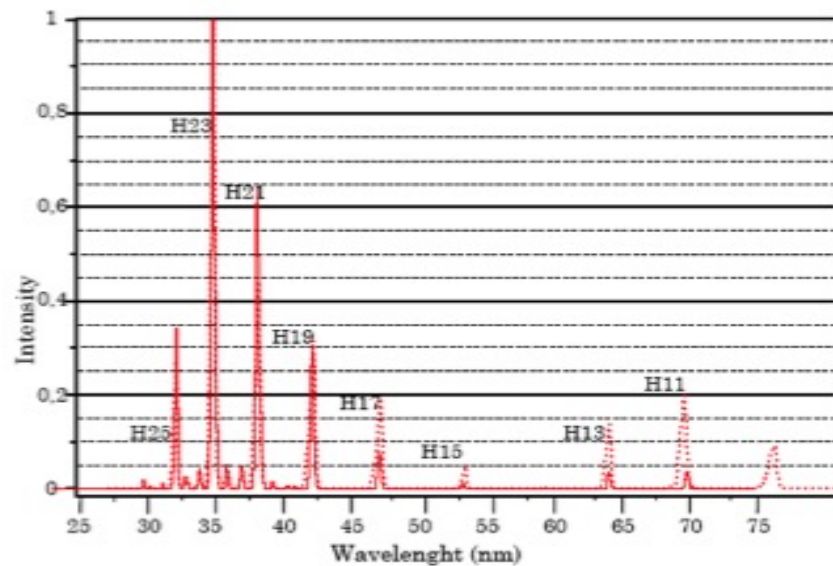


Figure 3.11: P polarisation High Harmonic spectre. The full line corresponds to the direct configuration and the dashed line to the  $45^\circ$  mirror configuration.

as shown of figure 3.14.

The harmonic signal is clearly higher on using a direct configuration as the spectre shows on figure 3.15.

Experimentally the reflectivity as a function of the harmonic order is shown on figure 3.16. As it can be seen the experimental reflectivity of the intermediate polarisation appears to be correct in between the horizontal polarisation and the

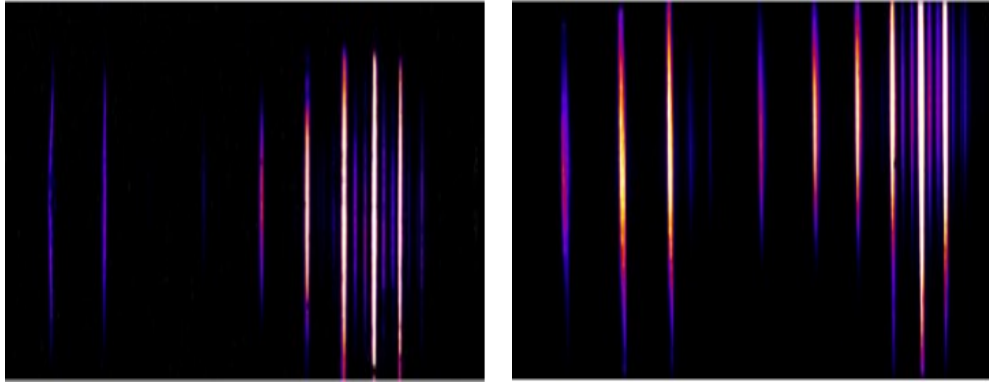


Figure 3.12: High harmonic signal registered on the CCD by varying the positioning of the mirror. On the left it is represented the obtained HHG signal at a direct configuration. On the right it is represented the obtained HHG signal at a configuration of  $45^\circ$ .

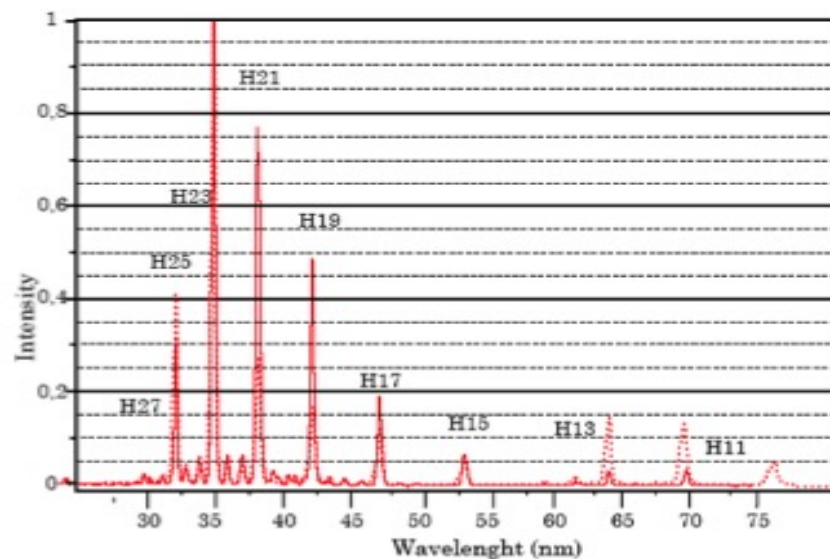


Figure 3.13: S polarisation High Harmonic spectre. The full line corresponds to the direct configuration and the dashed line to the  $45^\circ$  mirror configuration.

vertical polarisation at all orders.

From the  $\delta^3$  model it is expected that the odd harmonic will follow the  $\omega$  polarisation and the even harmonic the second field  $2\omega$  polarisation. Being both orthogonal there is an easy way to retrieve this information. The CCD only gives information about magnitude so there is a need to play with the s and p components and their projected value. At this configuration the odd and even harmonics should be mathematically equal in magnitude. The odd and even harmonics spaced by  $90^\circ$

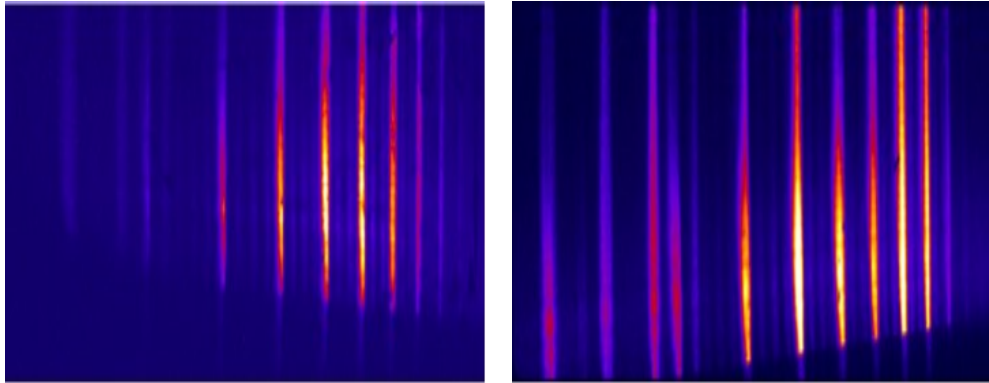


Figure 3.14: High harmonic signal registered on the CCD by varying the positioning of the mirror. On the left it is represented the obtained HHG signal at a direct configuration. On the right it is represented the obtained HHG signal at a configuration of  $45^\circ$ .

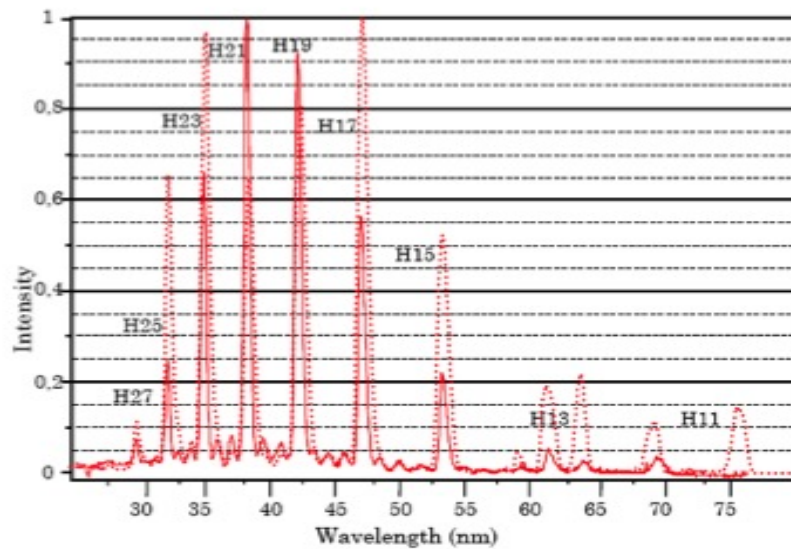


Figure 3.15: S polarisation High Harmonic spectre. The full line corresponds to the direct configuration and the dashed line to the  $45^\circ$  mirror configuration.

should project the same horizontal and vertical components leading to a similar reflection from the multilayer. Figure ?? shows the obtained CCD image data and the correspondent spectra.

The represented polarisation corresponds to the horizontal, p polarisation as represented on figure 3.17..

The harmonic signal is clearly higher on using a direct configuration as the

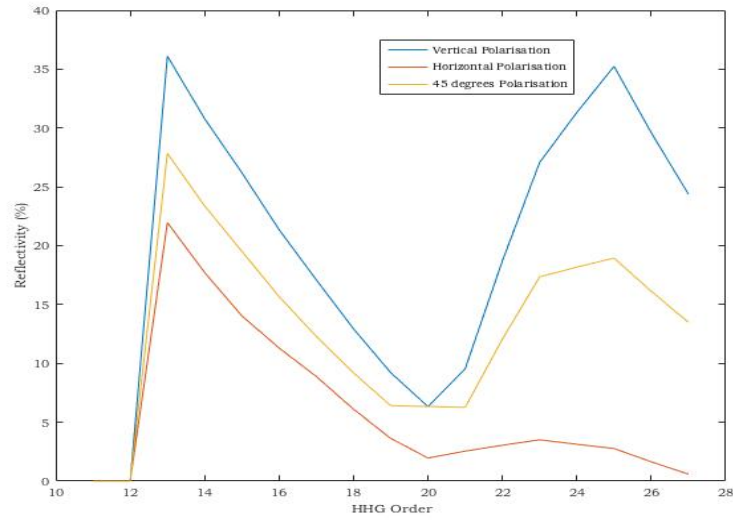


Figure 3.16: Reflectivity of the HHG in the one-colour case as a function of the harmonic order for the s polarisation, p polarisation and the intermediate  $45^\circ$  polarisation.

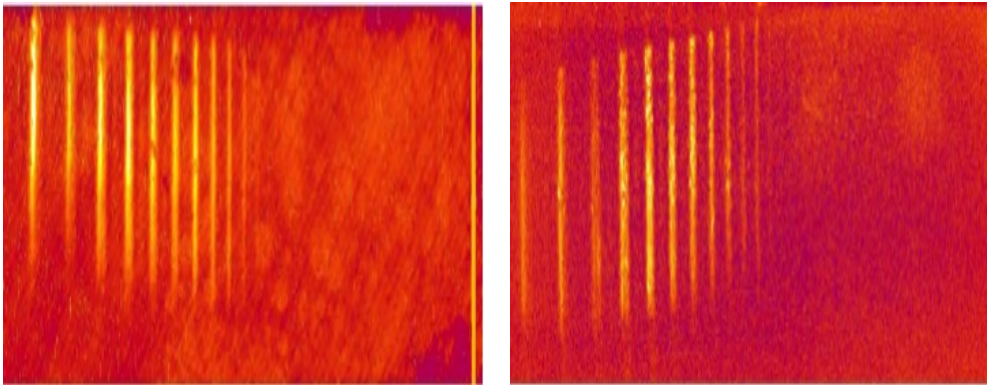


Figure 3.17: High harmonic (odd and even) signal registered on the CCD by varying the positioning of the mirror. On the left it is represented the obtained HHG signal at a direct configuration. On the right it is represented the obtained HHG signal at a configuration of  $45^\circ$ .

spectre shows on figure 3.18.

The represented polarisation corresponds to the vertical, s polarisation as represented on figure 3.19.

The harmonic signal is clearly higher on using a direct configuration as the spectre shows on figure ??.

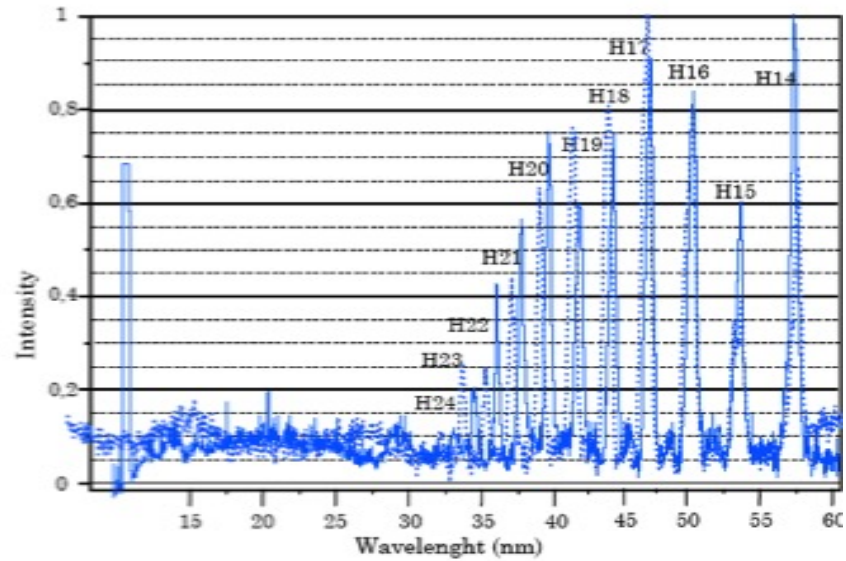


Figure 3.18: S polarisation High Harmonic odd and even spectre. The full line corresponds to the direct configuration and the dashed line to the  $45^\circ$  mirror configuration.

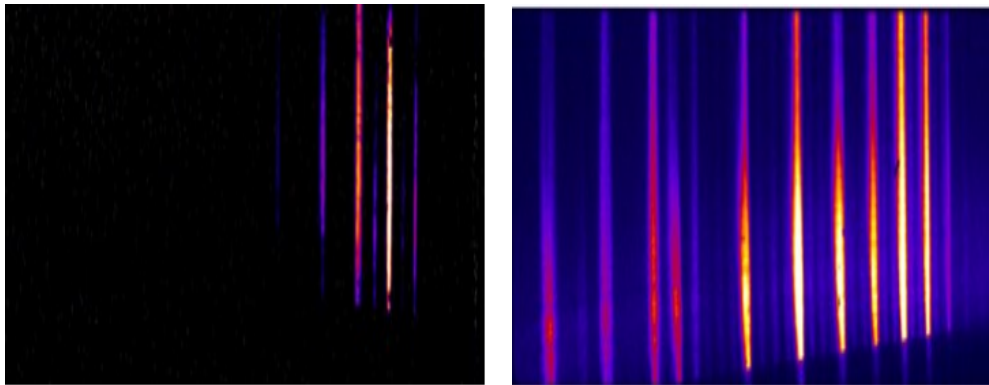


Figure 3.19: High harmonic (odd and even) signal registered on the CCD by varying the positioning of the mirror. On the left it is represented the obtained HHG signal at a direct configuration. On the right it is represented the obtained HHG signal at a configuration of  $45^\circ$ .

The represented polarisation corresponds to the intermediate,  $45^\circ$  polarisation represented on figure 3.21.

It can be seen that that the reflectivity of the harmonics is not the same as the *Direct configuration* harmonic data shows. Indeed, while for low orders ( $13^{th}$  to  $20^{th}$ ), the vertical component is about 1.5 higher than the horizontal one, for high orders ( $21^{st}$  to  $27^{th}$ ) the ratio strongly varies and increases to almost 10 for the

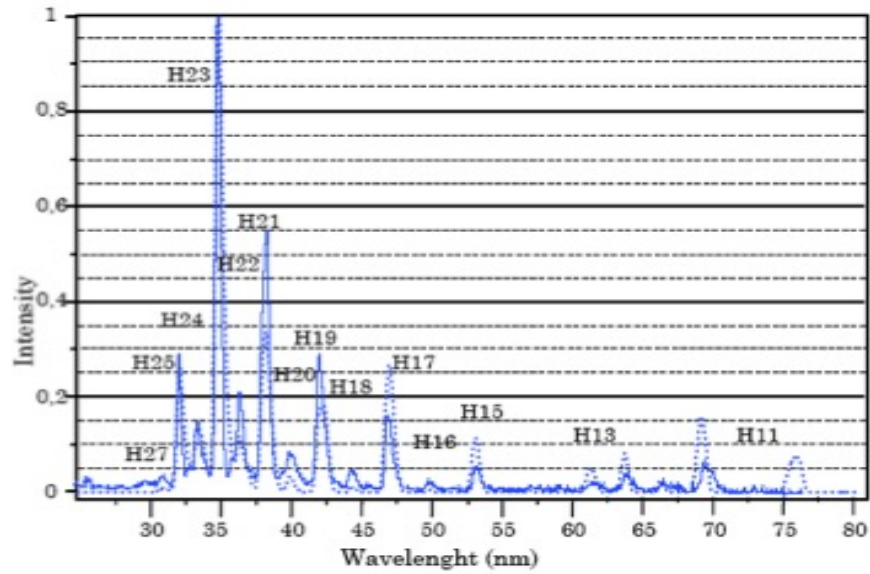


Figure 3.20: P polarisation High Harmonic odd and even spectre. The full line corresponds to the direct configuration and the dashed line to the  $45^\circ$  mirror configuration.

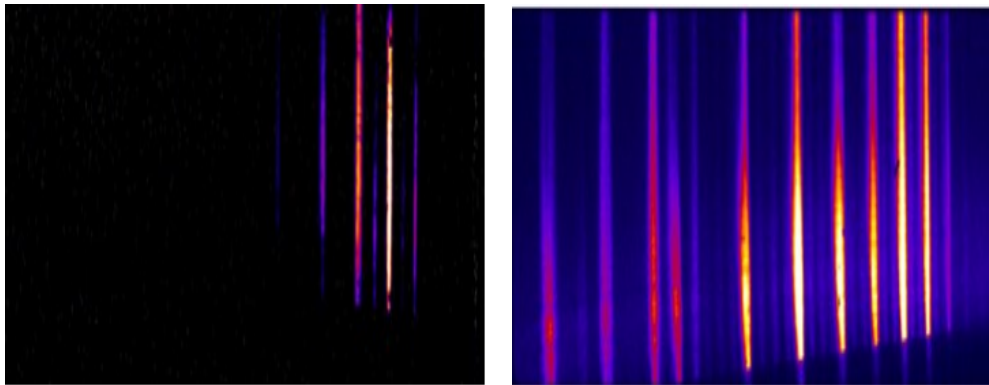


Figure 3.21: High harmonic (odd and even) signal registered on the CCD by varying the positioning of the mirror. On the left it is represented the obtained HHG signal at a direct configuration. On the right it is represented the obtained HHG signal at a configuration of  $45^\circ$ .

$25^{th}$  harmonic.

Another phenomena to take into account is the reflectivity of the multilayer. Since the measure used is the s and p magnitudes the multilayer with its selective reflection should clearly separate both components. Using either an horizontal or a vertical polarised beam a strong variation of reflectivity between odd and even harmonics, should be observed (especially in the high order range).

Figure 3.22 shows the reflectivity obtained for the harmonics generated either with a simple one colour field and the two colour field and for three different fundamental laser polarisations. In the simple  $\omega$  case the envelope of harmonics seems to be in concordance with the multilayer reflectivity shown in figure 3.7 a).

In the  $\omega/2\omega$  case the results are unexpected. The oscillations seen to be smaller in the high order spectral range, for which the difference of mirror reflectivity between the horizontal and vertical components is stronger. For each fundamental laser polarisation, either horizontal, vertical or at  $45^\circ$  a clear oscillation between consecutive odd and even harmonics is obtained. The strength of this oscillations is higher for low orders. The horizontal field presents an overall lower reflection with less harmonic orders reflected and only in the optimal multilayer range, in this case there are oscillations with the odd harmonics presenting a higher reflectivity value, since the ratio between  $I_{2\omega}/I_\omega$  is small this is a result that can be expected. In the vertical fundamental polarisation the oscillations between consecutive harmonics are in the opposite direction but with a quite reduced strength in the high order range. In the  $45^\circ$  case a big oscillation can be observed although they tend to fade for higher orders as well as the overall reflectivity.

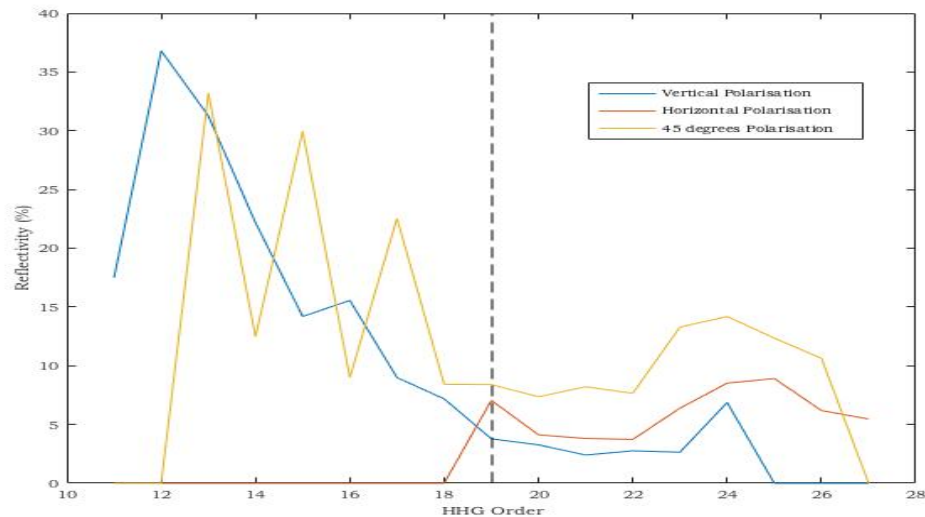


Figure 3.22: Reflectivity of the HHG in the two-colour case as a function of the harmonic order for the s polarisation, p polarisation and the intermediate  $45^\circ$  polarisation.

It is clearly shown here that the expectations from the  $\delta^3$  model are not met. Indeed with the  $45^\circ$  polarised  $\omega$  beam, oscillations of reflectivity and as a consequence of polarisation are observed with higher vertical component for odd har-

monics compared to even ones. Besides, these variations seem to be dependent of the order. Two distinct behaviours seem to appear. One on the left of the 19<sup>th</sup> harmonic, the low harmonic order regime and another one on the right the high harmonic order regime.

At this point it becomes safe to say that the polarisation of the harmonics generated in a two colour scheme don't seem to follow the polarisation of the fields from where they were generated. It is then more accurate to try to understand the variation of the polarisation by vectorial schemes. For the different cases vectorial schemes of the harmonic fields can be deduced. The total polarisation can then be known simply adding the two vectors of both fields. The oscillations between odd and even harmonics are a sign that the polarisation system clearly evolves. For instance, for the 45 degree polarised  $\omega$  case, while the polarisation of even harmonics seems to be on the order of 45 degree in the whole spectral range, the odd harmonic has a straight evolution from vertically polarised for low orders to 45 degree polarised for high orders. In the vertically polarised  $\omega$  field however both odd and even vertical components are significantly reduced with the increase of the harmonic number even if stronger for even harmonics. In other words, either  $2n, 2n + 1$  or both of them are dependent on the harmonic order.

The new hypothesis for the polarisation of the harmonics is that they might come out elliptically polarised. The polarisation of odd harmonics is closer to the one of the  $2\omega$  field while in opposite the polarisation of even harmonics is closer to the one of the  $\omega$  field. In addition, as the oscillation is opposite for vertically polarised beam and as the reflectivity of odd harmonics is very high in the 45 polarised  $\omega$  beam,  $2n + 1$  can not be too much higher or smaller than 45. This gives a more precise idea of the general evolution of polarisation. Be the case when the exiting harmonics are elliptical polarised.

In this studies the influence of the BBO that generates the second harmonic was also tested. Being an important asset to the success of the experiment the BBO crystal can regulate the generation of the harmonics. The larger the crystal the more intensity can be expected of the second harmonic. In the other hand the time delay between both pulses also increases leading to a less effective generation. The goal, since no time delay correction was used, is to wisely balance this two parameters. The BBO chosen was as explained before the  $100\mu\text{m}$  thickness BBO however some measurements were also taken with the  $250\mu\text{m}$  thickness BBO in

order to see the effect. Figure 3.23 shows images attained on the CCD related to the generation of harmonics with both thicknesses of BBO.

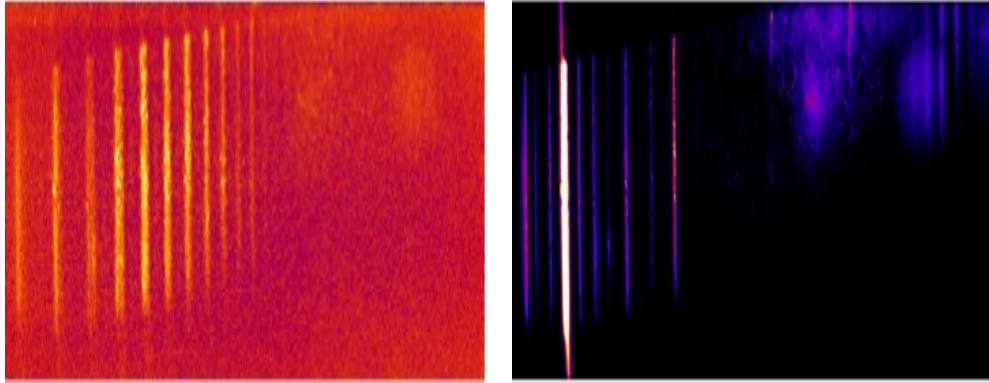


Figure 3.23: High harmonic (odd and even) signal registered on the CCD using a  $100\mu\text{m}$  thickness BBO. Using a  $250\mu\text{m}$  thickness BBO. The presented intensities on both images are different on order for the spectre to be apparent.

Analysing this images the following spectra is attained, show on figure 3.24

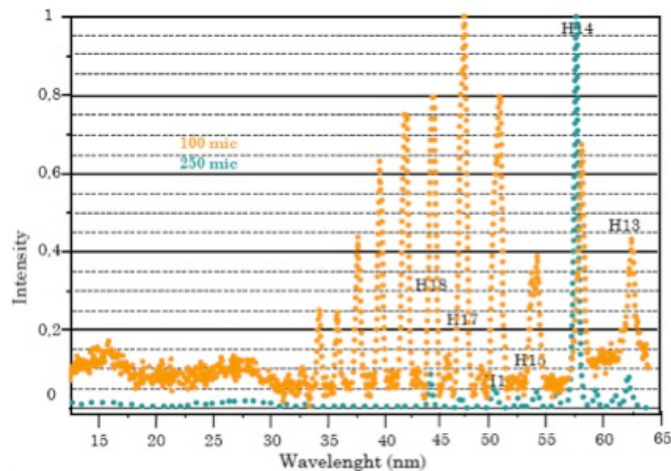


Figure 3.24: Experimental results for the influence of the BBO on the generation on the direct configuration. A  $100\mu\text{m}$  thickness BBO resulting spectrum is represented in orange and a  $250\mu\text{m}$  thickness BBO spectra is represented in blue.

It can be seen that the larger BBO has more of a differential generation of harmonics. The higher value corresponds to the H14 followed by H18. These are all even ( $2(2n+1)$ ) harmonics, therefore generated by the second harmonic field. The result is compatible with the findings of Nam [9] where the  $2(2n+1)$  harmonics were related to be the strongest. This confirms the more important efficiency on generating this field. However since the fundamental and the second harmonic fields are less overlapped the importance of the fundamental field and the mixed

field in the generation is lower leading to smaller intensities on odd harmonics and harmonics that are generated by the mixed field being in a latter approach less effective in terms of total envelope intensity.

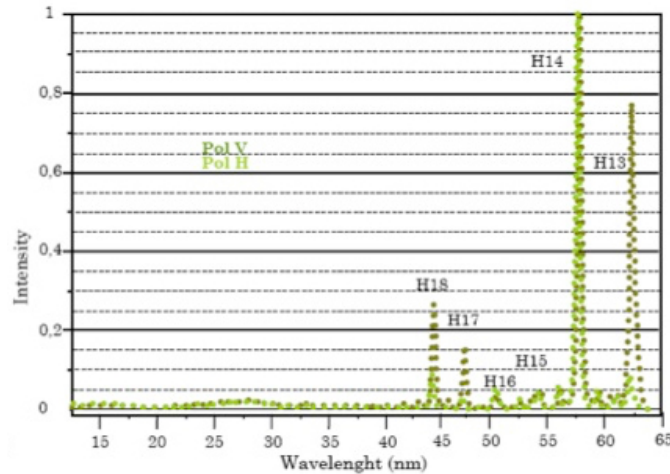


Figure 3.25: Experimental results. Spectre attained in direct configuration using a  $250\mu\text{m}$  thickness BBO. On light green the horizontal, p polarisation is represented and on darker green the vertical, s polarisation is shown.

Figure 3.25 shows the difference in generation when generating in a fundamental vertical polarisation and fundamental horizontal polarisation. The H14 is still the most enhanced harmonic but there is a change in measurement ratios of the other harmonics, H13 and H17 appear stronger on the vertical polarisation measurement which is due to the favourable multilayer reflectivity.

### 3.1.3 Conclusions of the first harmonic studies

This first work was very important in the way that opened the opportunity to develop high harmonic polarisation generated in a two colour field models. The models in use didn't explain the results obtained in the laboratory therefore new hypothesis were made. A whole new problematic has raised in terms of how to explain the polarisation of harmonics. The linear polarisations of harmonics in an orthogonally polarised two-colour arrangement do not follow neither the polarisation of the fundamental nor the second harmonic fields, but correspond to intermediary polarisations, which evolve with the harmonic number. Indeed, the polarisation of even and odd harmonics can drastically vary in the full spectral range of generation. The harmonic order plays a major role in the polarisation

scheme such as will do the overlapping of both fundamental and second harmonic beam and the relative intensity of both. All these components have to be evaluated for a precise study of the polarisation. Actually, the real and precise evolution of the polarisation is very complex to determine and is probably a direct consequence of no less complex electronic phenomena encountering compared to single colour configuration.

The results were however consistent for the  $250\mu\text{m}$  thickness BBO with the actual experimental literature.

A polarisation controlled system is highly recommended in order to further search the polarisation states of the harmonic generated with an orthogonal two-colour field. Leading to the second experiment of polarisation studies performed at LOA, France.

### 3.2 Second polarisation harmonic studies

Previous results obtained at the LOA strengthened the need to come up with a model to explain the polarisation of harmonics in generated in a two-colour field. While harmonics generated in a simple one colour field follow the polarisation of the fundamental field the polarisation of harmonics generated in a mixed field is still a work in progress. The generation phenomenon itself is still to be fully understood.

In this second round of experiments performed at LOA the focus is the polarisation study. Light in the XUV region is hardly manipulated, the penetration depth of the radiation makes it hard to orientate. In order to change the polarisation an interaction with the light's components has to occur. In the visible and near UV region of the electro-magnetic spectrum circularly polarising a linearly polarised light beam is easily done using quarter-wave plates. However when reaching the XUV region almost all materials become transparent. This is the reign of coated mirrors and multilayers. These components present artificial dichroism, meaning they have a range of reflection depending on the energy of the incident XUV radiation. To produce circularly polarised light from linearly polarised light, a phase-shift of  $\frac{\pi}{2}$  must be introduced. Since the phase-shift introduced by a mirror ranges from 0,

at grazing incidence, to  $\pi$ , at normal incidence, one can always find an incidence angle for which the phase shift is  $\frac{\pi}{2}$  [71].

A multiple mirror design is proposed in order to mend the limitation regarding the low reflectivity of the p component. Since the phase-shift per mirror is divided by the number of mirrors, a smaller glancing angle can be used [72]. This will increase the efficiency of the polariser system. Hochst *et al.* are responsible for describing the four mirror circular polariser for use in synchrotron facilities. The quadruple reflector scheme will be mounted at LOA. It consists of two pairs mirrors. The light will be directed parallel to the axis of the first pair mirrors and the second pair will deflect the light to its original on-axis direction. The advantage of this system is that the beam position on the sample will stay the same allowing the rotation of the polariser. Considering that all the angles of incidence are equal with this geometry the total amplitudes of reflection are given by:

$$r_s = [r_{s1}]^4 \quad (3.2)$$

and

$$r_p = [r_{p1}]^4 \quad (3.3)$$

Each mirror will introduce a phase-shift between the s and p component of the electromagnetic wave and the total phase shift is then given by:

$$\Delta_{tot} = 4\Delta_1 \quad (3.4)$$

This phase-shift between the vertical and horizontal polarisations will ensure that the linear polarised light that enters the polariser exits elliptically polarised. The angle of incidence is then adjusted and circular polarised light will then be obtained after reflection when the s and p components are equal. As seen in the last section the s and the p polarisations don't reflect with the same efficiency. The p component is always lower than the one of the s component the angle between

the electric field and the p direction must be chosen between  $0^\circ$  and  $45^\circ$ . In the XUV region, the incidence angle which gives a phase-shift of  $\frac{\pi}{2}$  is in general close to the Brewster angle. The light can exit as left-handed polarised or right-handed polarised.

The polariser was optimised to circularly polarised XUV radiation at the working wavelength of 20.7 nm, at the absorption M-edge of Co, using calculations performed with the optical constants of the IMD software package [73]. At this wavelength, the polariser should yield a phase-shift of  $\frac{\pi}{2}$  for a glancing angle of about 23.4 degrees. To obtain circularly polarised light an angle of  $32^\circ$  is needed. Positive and negative helicity can be obtained using  $32^\circ$  or  $-32^\circ$ . The theoretical transmission should be 8%, much higher than the 0.6% of a gold coated four reflectors phase-shifter [72].

### 3.2.1 Description of the experimental setup of the second HHG polarisation experiment

A detailed experimental study was performed at the Laboratoire d'Optique Appliquée at *salle orange* with a kHz Ti:Sapphire laser system. The pulse central wavelength is placed at 815 nm with an output energy of 5 mJ. Its time duration is of 35 fs in Full Width Half Maximum. The harmonics are generated on a gas cell in Neon with a pressure of 25 mbar. These harmonics span a wide wavelength range between 16 and 31 nm. The harmonics are linearly polarised and their direction of polarisation is the same as the incoming infrared laser (i. e. horizontal, p-polarised). By rotating the direction of polarisation of the infrared laser with a half-wave plate by an angle  $\alpha$ , the direction of polarisation of the harmonics can be rotated by the same angle.

The second group on the set-up is the polariser. It consists in four mirrors coated with 35 nm of molybdenum capped with 5 nm of  $B_4C$  to prevent oxidation. In the earlier stage four mirrors capped with gold were used to verify the system and to take the first data. Gold is usually used in this range but doesn't have the same reflectivity power as molybdenum. Molybdenum has a high reflectivity efficiency and high phase-shift in the XUV range. The polarisation step is slightly different from what was proposed by Hochst [72] since the mirrors are fixed while the plane of polarisation of the incoming light can be rotated. In terms of materials

it was also the first time that molybdenum mirrors are used for this purpose.

IR radiation that was not transformed on to XUV by HHG is blocked after the polariser but adding two 150 nm thick aluminium foils to protect the detection system. Harmonics go through and are focused and dispersed by a platinum coated toroidal mirror working in conjunction with a 120 grooves per millimetre reflection grating. The harmonics are then reflected by a *Mo/Si* multilayer mirror set at an incidence angle of  $45^\circ$  and recorded by a PI-MTE CCD camera (Princeton Instrument). The mirror presents a period of 16 nm, a ratio of Mo and Si thicknesses of 0.6 and 20 repetitions. This mirror acts as an analyser since the ratio of the s and p reflectivity ranges from 6 to 16 for the brightest harmonics between 18 and 27 nm ( $31^{st}$  to  $45^{th}$  harmonics). The multilayer mirror and the CCD camera can be rotated around the optical axis. A complete scheme of the set-up is presented on figure 3.26. In this figure two main angles are to be changed during the experimental time: the  $\alpha$  representing the angle of the fundamental laser, and the  $\beta$  representing the angle of collection of the data, or in other words the angle of the analyser.

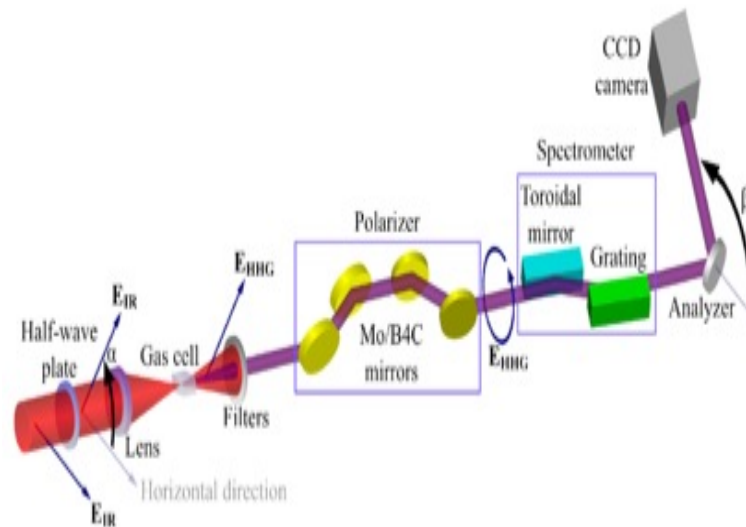


Figure 3.26: For  $\alpha = 90^\circ$  and  $\beta = 0^\circ$  the fundamental field has Maximum Intensity

The CCD camera records the intensity of each harmonic. A typical measurement consists of an accumulation of 40,000 pulses (i. e. 40 s). The intensities obtained for different  $\alpha$  and  $\beta$  angles are dependent on the characteristics (reflectivity and phase-shift) of the different optical elements present in the setup. It is possible to retrieve these characteristics and to obtain the performance of the polariser by

fitting the intensities recorded on the CCD camera with a model describing the optical system.

### 3.2.2 Polarisation measurement

In our current set-ups we are able to measure only the intensity of the signal. The intensity of the polarisation of the field is projected on a referential therefore there is a need to change the way data is acquired in order to be able to measure the polarisation of light.

Considering a beam of light traveling along the  $z$  direction and the coordinate system given by three unitary vectors  $z$ ,  $e_p$  and  $e_s$ . The electric field of the light  $E$  can be described by two complex numbers  $E_p$  and  $E_s$  :

An electric field can be described by:

$$E(z, t) = (E_p e_p + E_s e_s) \exp(-i(\omega t - kz)) \quad (3.5)$$

The polarisation state of the beam can be described by the Stokes vector,  $S$  which is defined as follows:

$$\begin{pmatrix} S_0 \\ S_1 \\ S_2 \\ S_3 \end{pmatrix} = \begin{pmatrix} \frac{(|E_p|^2 + |E_s|^2)}{2} \\ \frac{(|E_p|^2 - |E_s|^2)}{2} \\ \Re(E_p E_s^*) \\ \Im(E_p E_s^*) \end{pmatrix} \quad (3.6)$$

With  $S_0$  proportional to the intensity of the beam while the degree of linear polarisation,  $P_L$ , and the degree of circular polarisation,  $P_C$ , are related to the Stokes vector by the following equations:

$$P_L = \frac{(S_1^2 + S_2^2)}{S_0^2} \quad (3.7)$$

$$P_C = \left(\frac{S_3}{S_0}\right)^2 \quad (3.8)$$

In a rotation of an  $\phi$  angle, around the  $z$  axis is described by the rotation matrix  $R(\phi)$ :

$$R(\phi) = \begin{bmatrix} 1 & 0 & 0 & 0 \\ 0 & \cos(2\phi) & \sin(2\phi) & 0 \\ 0 & -\sin(2\phi) & \cos(2\phi) & 0 \\ 0 & 0 & 0 & 1 \end{bmatrix} \quad (3.9)$$

The related Stokes vector being  $R(\phi)S$ .

The interaction of the light with an optical element can be described by the Mueller matrix  $M_x$  of this optical element. After the interaction, the Stokes vector becomes  $M_x S$ . In the case of a reflective element with complex reflective coefficients  $r_{px} = r_{px} \exp(i\delta_{px})$  and  $r_{sx} = r_{sx} \exp(i\delta_{sx})$  we have:

$$M_x = \frac{1}{2}(r_{px}^2 + r_{sx}^2) \begin{bmatrix} 1 & -\cos(2\Psi_x) & 0 & 0 \\ -\cos(2\Psi_x) & 1 & 0 & 0 \\ 0 & 0 & \sin(2\Psi_x) \cos(\Delta_x) & \sin(2\Psi_x) \sin(\Delta_x) \\ 0 & 0 & -\sin(2\Psi_x) \sin(\Delta_x) & \sin(2\Psi_x) \cos(\Delta_x) \end{bmatrix} \quad (3.10)$$

where  $\tan(\Psi_x) = \frac{r_{px}}{r_{sx}}$  and  $\Delta_x = \delta_{px} - \delta_{sx}$ .  $\Delta_x$  represents the phase-shift induced by the optical element. A rotation, of an angle  $\phi$  of the optical element implies a coordinate transformation given by the rotation matrix  $R(\phi)$ , the resulting Muller matrix being  $R(-\phi)MR(\phi)$ .

Considering one harmonic in a coordinate system such that the vector  $e_p$  and  $e_s$  are respectively chosen to be parallel and perpendicular to the plane of incidence of the circular polariser, that is the horizontal plane. The harmonic being linearly polarised with its polarisation plane rotated by an angle  $\alpha$  compared to  $e_p$ , the electric field of this harmonic is written:

$$E(z, t) = (E_0 \cos(\alpha)e_p + E_0 \sin(\alpha)e_s) \exp(-i(\omega t - kz)) \quad (3.11)$$

the corresponding Stokes vector being:

$$S_i = I_0 \begin{pmatrix} 1 \\ \cos(2\alpha) \\ \sin(2\alpha) \\ 0 \end{pmatrix} \quad (3.12)$$

where

$$I_0 = \frac{|E_0|^2}{2} \quad (3.13)$$

is proportional to the intensity of the harmonic.

Let us divide the optical elements of our setup in two blocks. The first block is composed of the circular polariser and the spectrometer (the toroidal mirror and the grating). This block is describe by a Muller matrix  $M_a$ , its parts being fixed compared to the coordinate system, no coordinate transformation is needed. Passing through this block, the Stokes vector is transformed into:

$$S_a = M_a S_i \quad (3.14)$$

from which the degree of circular polarisation can be retrieved:

$$P_C = \left( \frac{S_{a3}}{S_{a0}} \right)^2 = \frac{\sin^2(2\Psi_a) \sin^2(2\alpha) \sin^2(\Delta_a)}{(\cos(2\Psi_a) \cos(2\alpha) - 1)^2} \quad (3.15)$$

This equation shows that obtaining circular polarisation,  $P_C = 1$ , requires a phase-shift,  $\Delta_a$ , of  $\frac{\pi}{2}$ . Furthermore, the value of the angle  $\alpha$  which maximises  $P_C$  is  $\Psi_a$ . When the latter condition is met the degree of circular polarisation and the circular transmission are respectively:

$$P_C^{Max} = \sin^2(\Delta_a) \quad (3.16)$$

and:

$$T_C = \frac{S_{a0} P_C^{Max}}{I_0} = \frac{(r_{pa}^2 + r_{sa}^2 \sin^2(2\Psi_a) \sin^2(\Delta_a))}{2} \quad (3.17)$$

The circular transmission  $T_C$  can be seen as the ratio between the number of photons circularly polarised after the first block and the number of incident photons. The second block is composed of the rotating analyser and the CCD camera. This analyser is described by a Muller matrix  $M_b$ . To take into account the orientation of the polariser, angle  $\beta$ , we need to proceed to a coordinate transformation. After this block, the Stokes vector becomes:

$$S_b = R(-\beta)M_bR(\beta)M_aS_i \quad (3.18)$$

The CCD camera is sensitive to the intensity of the harmonics the first component of the Stokes vector. In our case the CCD camera records:

$$S_{b0} = \frac{1}{4}I_0(r_{pa}^2 + r_{sa}^2)(r_{pb}^2 + r_{sb}^2) \begin{pmatrix} 1 \\ -\cos(\alpha)\cos(2\Psi_a) + \cos(2\beta)\cos(2\Psi_b) \\ -\sin(2\alpha)\sin(2\beta)\sin(2\Psi_a)\cos(2\Psi_b)\cos(\Delta_a) \\ \cos(2\beta)\cos(2\Psi_a)\cos(2\Psi_b) \end{pmatrix}$$

equation)

By varying  $\alpha$  and  $\beta$  independently, and by fitting the measured data the values of  $\Psi_a$ ,  $\Delta_a$ ,  $\Psi_b$  and

$$I_f = \frac{1}{4}I_0(r_{pa}^2 + r_{sa}^2)(r_{pb}^2 + r_{sb}^2) \quad (3.20)$$

can be retrieved.

It must be noted that the parameters  $\Psi_a$  and  $\Delta_a$  describe a composite optical element which include the polariser and the spectrometer. To calculate the performance of the polariser only, we have to separate the contribution of the spectrometer, which reflection coefficient are:

$$\vec{r}'_{(p,s)a} = r'_{(p,s)a} \exp(i\delta'_{(p,s)a}) \quad (3.21)$$

from the contribution of the polariser, which reflection coefficient are

$$\vec{r}''_{(p,s)a} = r''_{(p,s)a} \exp(i\delta''_{(p,s)a}) \quad (3.22)$$

This is done by removing the polariser and recording a new set of data. From this new measurements

$$\Psi'_a = \arctan\left(\frac{r'_{pa}}{r'_{sa}}\right) \quad (3.23)$$

$$\Delta'_a = \delta'_{pa} - \delta'_{sa} \quad (3.24)$$

and

$$I'_f = \frac{1}{4} I_0 (r'^2_{pa} + r'^2_{sa}) (r'^2_{pb} + r'^2_{sb}) \quad (3.25)$$

can be retrieved.

Remarking that

$$\vec{r}_{s,pa} = \vec{r}'_{s,pa} \vec{r}''_{s,pa} \quad (3.26)$$

and

$$\frac{I_f}{I'_f} = \frac{r_{pa}^2 + r_{sa}^2}{r_{pa}'^2 + r_{sa}'^2} \quad (3.27)$$

one can deduce:

$$\Delta_a'' = \Delta_a - \Delta_a' \quad (3.28)$$

$$r_{sa}'' = \sqrt{\frac{I_f}{I'_f} \frac{1 + \tan^2(\Psi_a')}{1 + \tan^2(\Psi_a)}} \quad (3.29)$$

$$r_{pa}'' = r_{sa}'' \frac{\tan^2(\Psi_a)}{\tan(\Psi_a')} \quad (3.30)$$

where  $P_C^{Max}$  and  $T_C$  can be calculated using  $r_{pa}''$ ,  $r_{sa}''$ ,  $\Delta_a''$  and

$$\Psi_a' = \arctan\left(\frac{r_{pa}''}{r_{sa}''}\right) \quad (3.31)$$

In our case the theoretical results for the 39th harmonic (20.7 nm) of the degree of circular polarisation is 100 % and the circular transmission is of 7.9%.

The intensity of each harmonic was recorded on the CCD camera for different  $\alpha$  and  $\beta$  angles. Polarisation angles ranging from  $-200^\circ$  to  $220^\circ$ , and for four different analyser angles  $0^\circ$ ,  $45^\circ$ ,  $90^\circ$  and  $135^\circ$ , were used. Two sets of data were recorded, with and without the polariser. The space between two successive harmonics can be measured from the cross section. Knowing the characteristics of the grating (120 grooves/mm) and the distance between the grating and the CCD camera, the order of each harmonic has been determined. This calibration is checked using the aluminium L-edge at 17.1 nm.

### 3.2.3 Experimental results of the harmonic polarisation experiment

This section presents the analysis of the performance of a four mirror system used to circularly polarise the XUV pulses produced by an HHG source. In order to study the Magnetic Circular Dichroism effect at the cobalt M-edge, this system has been optimised by simulation for a wavelength of 20.7 nm (60 eV). The performance of the polariser has been measured using a rotating analyser consisting of a multilayer mirror set at an incidence angle of  $45^\circ$ .

The use of multilayer optics can provide reflection of the radiation until up to 70% of incident XUV light: Each layer pair is designed to have a thickness equal to half the wavelength of light to be reflected. The multilayer used:  $B_4C/Mo/B_4C/a - Si$ . On Figure 3.27 a simulated curve of the multilayer is presented. The curve was drawn on the program IDM.

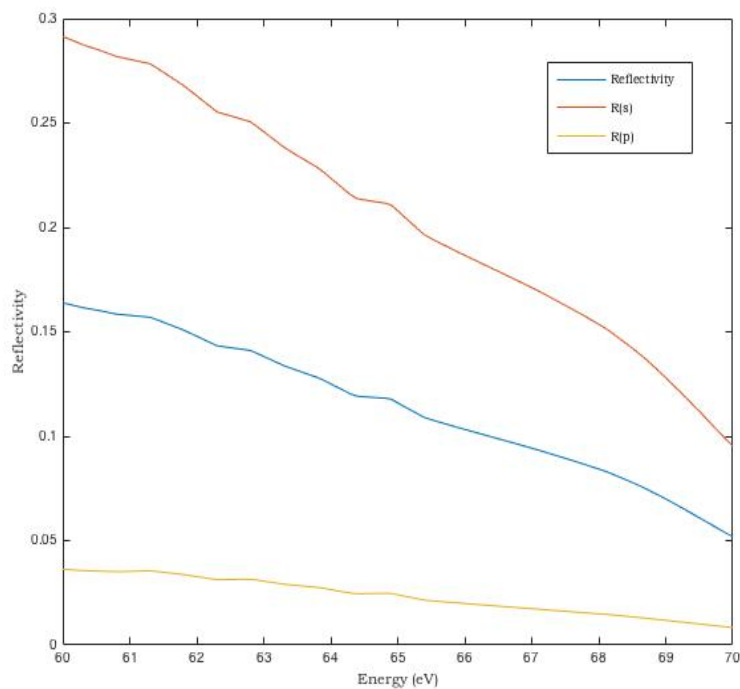


Figure 3.27: Multilayer theoretical reflectivity: Simulated reflectivity for the multilayer used (*IMD*)

In order to access the transmission function of the developed system. It was taken into account the transmission of the multilayer and the aluminium filters. The corresponding curve is presented on Figure 3.28. The two curves correspond

to the transmission of the system in terms of the polarisation of light and the energy.

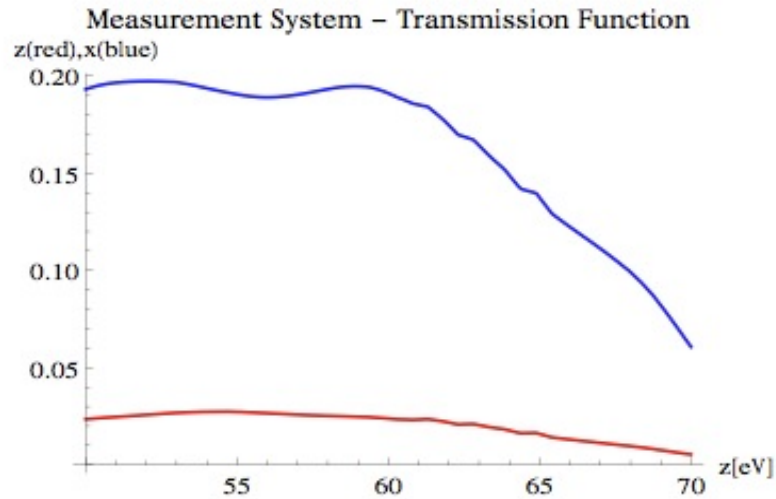


Figure 3.28: Multilayer theoretical reflectivity: Transmission function of the set-up in function of the energy for s (blue line) and p (red line) polarisation of light

Using this function it is now possible to deduce the real harmonic signal obtained during the experiment.

Firstly the harmonics have to be differentiated using a spectrometer. The polarisation can then be measured by acquiring the intensity while rotating the analyser. This will give typical sinusoidal evolution with periodicity of 180 degrees. The contrast being directly linked to the ellipticity and the position corresponding to the maximum of intensity giving the axis of polarisation. Figure 3.29 shows three sets of data. These sets are a superposition from  $-200^\circ$  to  $220^\circ$  from where we take the circular feature for fundamental horizontal polarisation translated as the analyser angle of  $0^\circ$ . The first set of data is taken with no polarising mirror set-up remaining as a calibration image. Analysing this picture it can be seen that the intensity display is modulated when following the circle this corresponds to the modulations of the electric field. The centre is aligned on the 41<sup>th</sup> harmonic. The second picture represents the data obtained with the four gold coated mirrors. This corresponds to the preliminary study done with gold. In this image a smaller modulation of the intensity is observed if compared to the previous one. This indicates that the electric field components are being modulated into more similar values, the signature of the ellipticity of the field polarisation. The last image shows the resulting

data set superposition of the four mirrors coated  $MoB_4C$ . In this last figure it is clear that the intensity has reached an almost identical value for each angle of polarisation. Almost all the harmonics have the same intensity shade indicating that the components of the electric field didn't change with the polarisation angle. Both s and p have approximately the same intensity being sure to say here that the circular polarisation of the harmonics was reached.

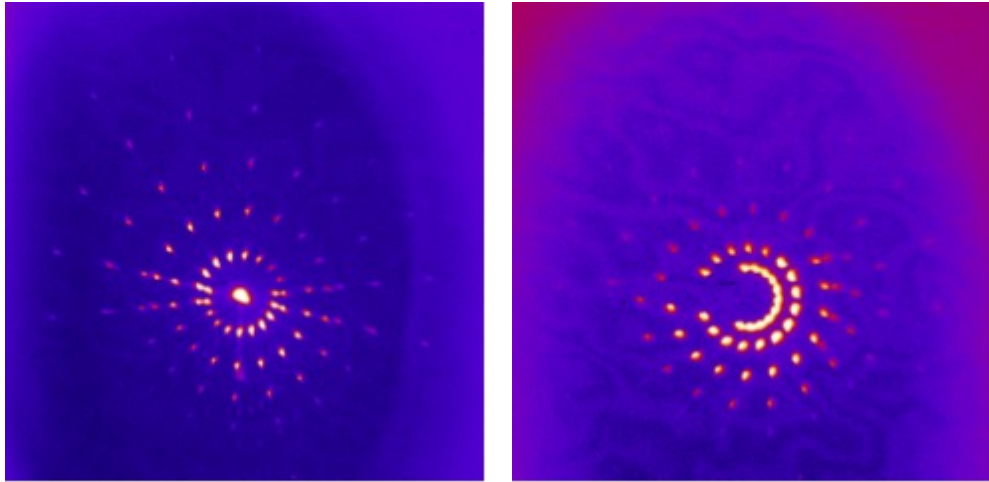


Figure 3.29: Data images superposed varying the polarisation angle from  $-200^\circ$  to  $220^\circ$  recorded at the CCD for horizontal polarisation. Set-up of four mirrors coated with Gold. Set-up of four mirrors coated  $MoB_4C$ .

Each row of the circle corresponds to a polarisation angle acquired over 40 seconds which at a rate of 1 kHz corresponds to 40 000 shots.

Figure 3.30 represents a spectra of the acquired data for a polariser angle of  $0^\circ$  and an analyser angle of  $90^\circ$ . The area below a peak gives the intensity of the corresponding harmonic. In this case integrated counts (HHG) indicate  $4.10^7$  photons/HHG/s for Harmonic 39 in Neon (20.7 nm).

The intensity of each harmonic is then plotted as a function of  $\alpha$  for the four  $\beta$  angles. The results are obtained for the  $39^{th}$  harmonic (20.9 nm). Before a quantitative analysis we shall examine these results qualitatively. Without the polariser, four sinusoids of approximately the same amplitude with a  $45^\circ$  shift between them are observed. This behaviour is expected if the phase-shift induced by the spectrometer is zero and the ratio of its p and s reflectivity is close to 1. This means that the spectrometer has only a little effect on the polarisation of the  $39^{th}$  harmonic. A similar behaviour has been observed for all the harmonics.

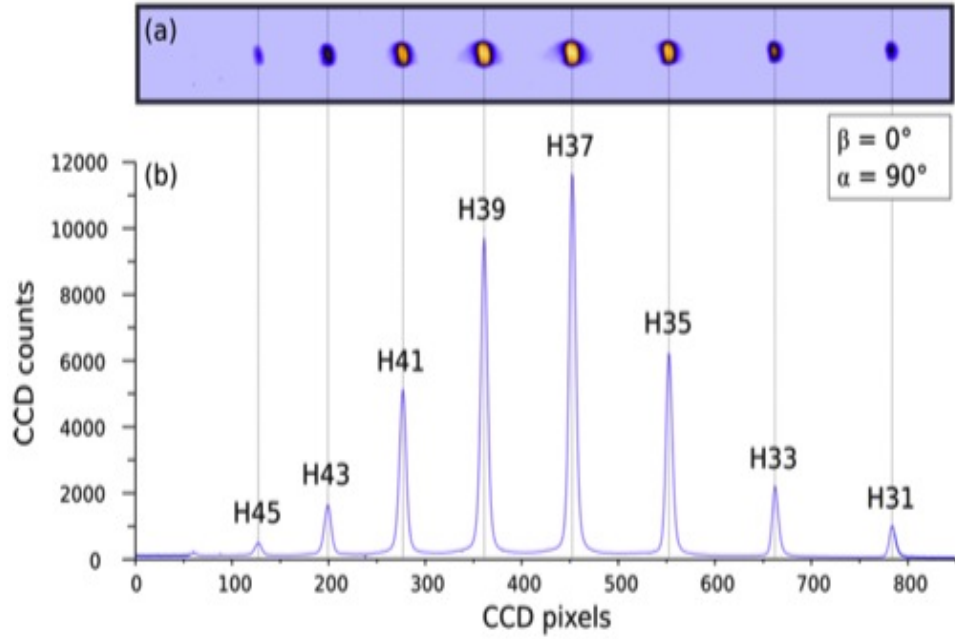


Figure 3.30: Experimental data: (a) Harmonic spectrum acquired on the CCD with the polariser for  $\alpha = 90^\circ$  and  $\beta = 90^\circ$ . Accumulation of 40000 thousand pulses. (b) Cross section of the image with the intensity of each harmonic shown and the distance in pixels between the grating and the CCD.

As expected, with the polariser, the curves obtained are still sinusoids but look very different than without the polariser. The shift between them and their amplitude have changed. The fact that the curves obtained for  $\beta = 45^\circ$  and  $135^\circ$  are almost in phase indicates that the phase-shift induced by the polariser is close to  $\frac{\pi}{2}$ . To extract more information, the data must be fitted.

Figure 3.31 shows the fits performed for each case represented as solid lines. From these obtained curves the values of  $\Psi_a$ ,  $\Delta_a$ ,  $\Psi'_a$ ,  $\Delta'_a$ ,  $I_f$ ,  $I'_f$  and  $\Psi_b$  can be extracted. From here the parameters  $r''_{pa}$ ,  $r''_{sa}$ ,  $\Psi''_a$  and  $\Delta''_a$  are calculated. From here  $P_{Max}C$  and  $T_C$  can be calculated. The curves represented have been normalised divided by  $I'_f$  and  $I_f$ . This normalised intensity can vary only between 0 and 4.

Table 3.32 summarises the results obtained for each harmonic. First, some general trends can be observed. The reflectivities  $r_{pa}$  and  $r_{sa}$  increase with harmonic order while the phase-shift decreases. This behaviour is expected theoretically for molybdenum mirrors at glancing angles smaller than  $30^\circ$  and at wavelengths between 18 and 27 nm. As a result, the degree of circular polarisation,  $P_{Max}C$ , decreases with harmonic order. The circular transmission,  $T_C$ , follows an op-

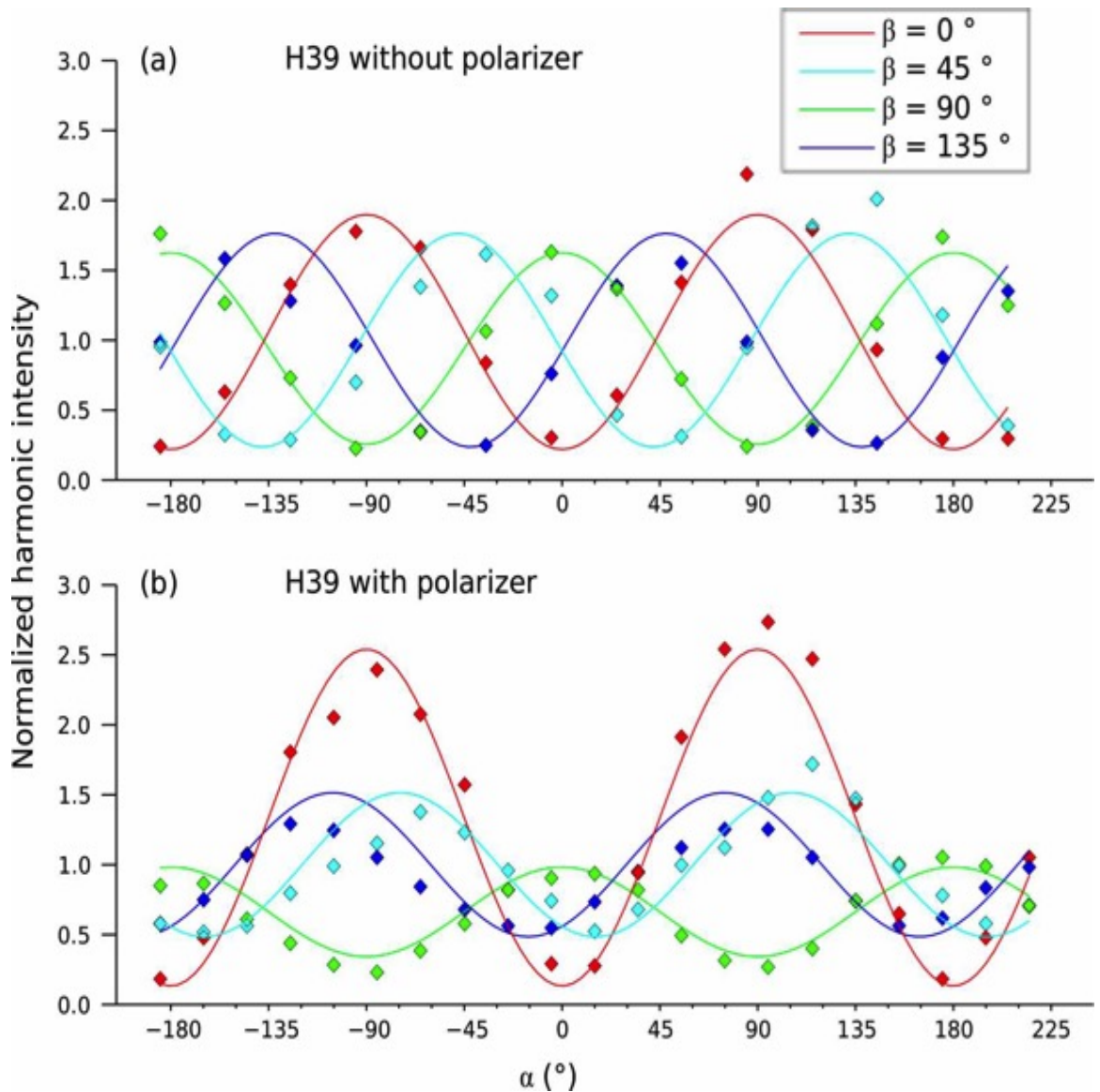


Figure 3.31: Spectra obtained for the harmonic 39 (60 eV) without polariser and with the polariser. The points are the measured data and the line the fit. The intensities are normalised. (a) refers to the configuration with the spectrometer only. The sinusoidals are quite similar. (b) refers to the configuration of spectrometer and polariser. The clear effect of the polariser on the harmonic is shown.

posite trend up to the 39<sup>th</sup> harmonic. For higher order harmonics the s and p reflectivities are superior but the angles are smaller resulting in a reduced circular transmission compare to the 39<sup>th</sup> harmonic.

The 39<sup>th</sup> harmonic, at 20.9 nm, is the closest to the cobalt resonance at 20.7 nm. For this harmonic, the degree of circular polarisation is 85 % and the circular transmission is 4.4 %. The theoretical values are 100 % and 7.9 % respectively.

Harmonic Order	31 <sup>st</sup>	33 <sup>rd</sup>	35 <sup>th</sup>	37 <sup>th</sup>	<b>39<sup>th</sup></b>	41 <sup>th</sup>	43 <sup>th</sup>	45 <sup>th</sup>
$\lambda$ (nm)	26.3	24.7	23.3	22	<b>20.9</b>	19.9	19	18.1
$r''^2_{pa}$ (%)	1.5	1.6	2.5	2.7	<b>3.8</b>	4.3	4.5	4.5
$r''^2_{sa}$ (%)	7.8	7.4	7.6	7.8	<b>8.3</b>	8.5	9.3	9.6
$\Delta''_a$ (°)	87.6	85.2	80.5	72.3	<b>67.2</b>	60.4	54.4	51.1
$P_{Cmax}$ (%)	100	100	97	91	<b>85</b>	76	66	61
$T_C$ (%)	2.6	2.7	3.7	3.6	<b>4.4</b>	4.3	4.0	3.7

Figure 3.32: Table of the harmonics obtained with the polariser. Eight harmonics (31<sup>st</sup> to 45<sup>th</sup>) are visible. For each harmonic the reflectivities  $r''^2_{pa}$  and  $r''^2_{sa}$ , the phase-shift  $\Delta''_a$ , the degree of circular polarisation  $P_{Cmax}$  and the circular transmission  $T_C$  are shown. The 39<sup>th</sup> harmonic correspondent to the Co absorption M-edge has a degree of 85% of circular polarisation and a circular transmission of 4.4% .

Imperfections of the mirrors (e. g. roughness, oxidation . . . ) and small errors on the incidence angle of the polariser could be responsible for these discrepancies. Indeed, a reduction of the reflectivity per mirror of 15 % would lead to a drop in transmission of the four mirror system of 50 %. Nevertheless, this is a very good achievement. For example, with these characteristics it will be possible to measure the MCD effect at the cobalt M-edge. Indeed, using previous measurements for the generation of harmonics in two-colour fields ( $> 0.65$  nJ at 20.9 nm, [33]), our polariser could yield up to 30 pJ per impulsion or 30 nJ per second for the 39th harmonic at 20.9 nm with a very high degree of circular polarisation. With such a power it would be easy to measure the transmission of a 40 nm thick cobalt layer at the cobalt M-edge (transmission  $> 1$  %) very accurately. Doing so for both light helicity would give a measure of the MCD effect. The results obtained for harmonics other than the 39th are also very impressive. For the 31st and 33rd harmonics the degree of circular polarisation even reaches 100 %. All this results have taken into account the CCD quantum efficiency, the efficiency of the multilayer and other optics and the Al filter transmission.

At this stage circularly polarised XUV radiation is accomplished being this the first report of circularly polarised high order harmonics. The transmission of the polariser for these 2 harmonics is superior to 2.5 %. The degree of circular

polarisation for the 35<sup>th</sup> harmonic is still very high at 97 % and the transmission is close to 4 %. This opens the door to the magnetic studies possibilities since the 35<sup>th</sup> harmonic is situated at the absorption M-edge of iron. In this regard, it has to be noted that the degree of circular polarisation of the 41<sup>st</sup>, 43<sup>rd</sup> and 45<sup>th</sup> harmonics and their circular transmission are still high. Then, It will be possible to probe the MCD effect at the absorption M-edge of nickel around 18.5 nm after further signal optimisation.

The quest for higher intensities brings up the subject of the polarisation of the harmonics generated by a two colour field. To study the polarisation of the two-colour case a frequency doubling crystal and the analyser were used. The same basic set-up was used taking out the four mirror system since its validity was already proven.

#### 3.2.4 Polarisation of high harmonics in an orthogonal two-colour field

The set-up used for this experiment was very similar to the set-up used in the previous study. The experimental study of the  $\omega$ ,  $2\omega$  harmonic generation model was performed at the Laboratoire d'Optique Appliquee at *salle orange* with a kHz Ti:Sapphire laser system with 815 nm central wavelength giving 5 mJ in 40 fs. Harmonics are generated on a gas cell in Neon.

Frequency doubling is achieved inserting a BBO Beta Barium Borate crystal in the path of the fundamental IR laser resulting in two beams, the doubled frequency beam at a wavelength of 407 nm and the fundamental beam that has not been converted. A 100 $\mu$ m BBO type 1 was used generating the second harmonic orthogonally to the fundamental laser beam. Due to the small delay between both pulses no compensation such as silicate plate was added. The high repetition rate and the fact that it had to be placed next to the focus constitutes a risk of damage. By mounting the BBO on a rotational support rotating the efficiency curve of the formation of the second harmonic is retrieved. Figure 3.33 represents the obtained curve simply measured with a photo-diode. This gives us the maximum and minimum energy of the second harmonic pulse. The curve presented on the figure already takes into account the extraction of the fundamental wave and the noise system.

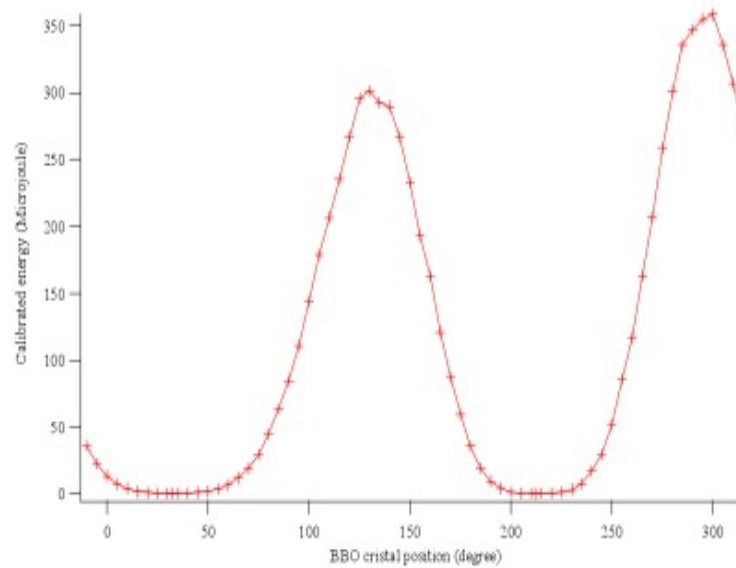


Figure 3.33: Measured BBO crystal generation of second harmonic in joules.

This radiation is focused on the gas cell generating harmonics. The IR residual pulse is blocked by the use of two 150 nm thick aluminium foils to protect the detection system. The next step is to analyse the generated harmonic radiation. Harmonics go through and are focused and dispersed by a platinum coated toroidal mirror working in conjunction with a 120 grooves per millimetre reflection grating. The harmonics are then reflected by a *Mo/Si* multilayer mirror set at an incidence angle of  $45^\circ$  and recorded by a PI-MTE CCD camera (Princeton Instrument). The mirror presents a period of 16 nm, a ratio of Mo and Si thicknesses of 0.6 and 20 repetitions. This mirror acts as an analyser since the ratio of the s and p reflectivity ranges from 6 to 16 for the brightest harmonics between 18 and 27 nm (31<sup>st</sup> to 45<sup>th</sup> harmonics). The multilayer mirror and the CCD camera can be rotated around the optical axis. The  $\beta$  angle still representing the angle of collection of the data or in order words the angle of the analyser. This analyser has the advantage of being already tested in the former experience. The set-up is presented on figure 3.34.

Four sets of data where obtained. The maximum generation of second harmonic and the minimum generation of second harmonic and two points in between them. The first intermediate case is closer to the maximum of the SH generation and the second intermedium is closer to the minimum of generation. These sets where taken as complementary results to analyse all the steps of generation. The data obtained is presented on figure 3.35 for the two main sets of data, the maximum generation of second harmonic (SH) and the minimum generation of the

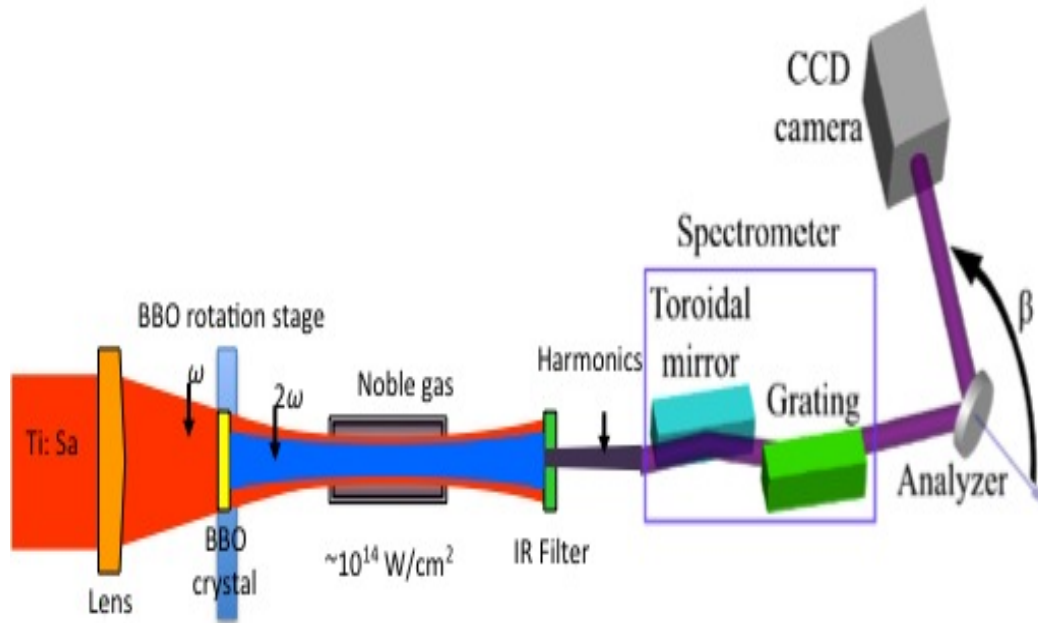


Figure 3.34: Set-up for the polarisation of high harmonics in an orthogonal two-colour field experiment. An intense IR laser pulse is focused on a gas cell by means of a lens. The fundamental pulse is on a horizontal axis. When the laser pulse passes through the BBO crystal where the second colour laser field is generated. The BBO is mounted on a rotation stage. The second-colour pulse will be on an orthogonal axis. The resulting two-colour laser field interacts with the noble gas generating harmonics. The laser pulse plus the harmonics will pass through a metallic filter. The harmonic pulse will traverse the spectrometer and the rotating analyser. The image will be collected on a CCD camera.

SH.

It can be seen that the difference between the intensity of the even harmonics (the weaker, smallest ones) is very important. Some even harmonics are more visible than others. For each line (analyzer position) spectra was obtained. Figure 3.36 represents all the spectra for each analyzer angle measured.

The set of data presented corresponds to the normalised intensity of the harmonics for each intensity of second harmonic pulse. From the most intense  $2\omega$  to the least intense. The first conclusion that meets the eye is that the behaviour of even and odd harmonics is different depending of the second pulse intensity. The odd and the even harmonics are then represented in different graphs. In the first case, the maximum SH generation the odd harmonics seem to follow a linear behaviour, their intensity in function of the analyser angle is close to a gaussian peak.

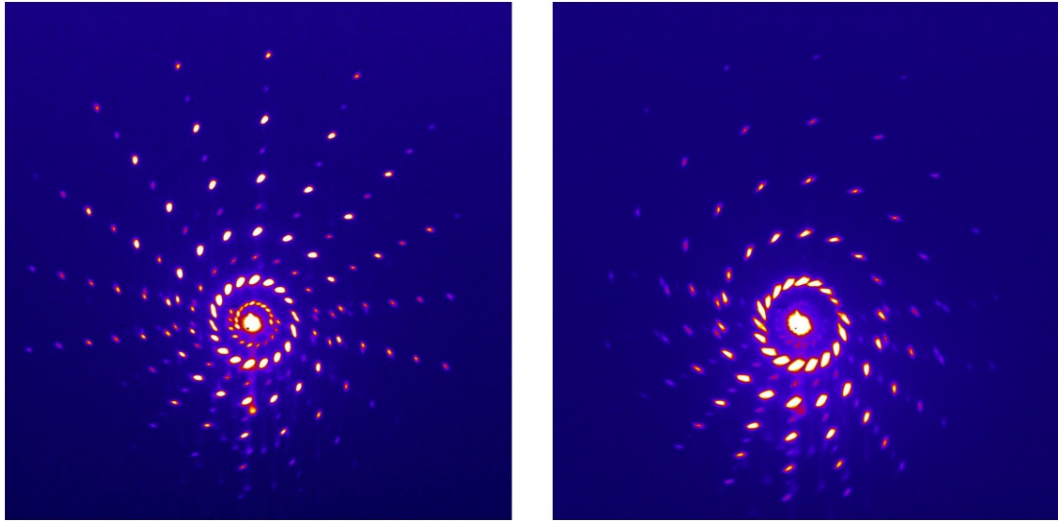


Figure 3.35: Data acquired with an  $100\mu\text{m}$  thickness BBO for a) the maximum generation of second harmonic and b) for the minimum generation of second harmonic. The images were acquired for different rotating stages of the BBO crystal.

The even harmonic case however is very disturbed suggesting that the intensity of this harmonics are quickly changing for some analyser angles and that stabilise for others suggesting ellipticity. For the second case, where the second harmonic intensity is intermediate but still closer to the maximum harmonic intensity both even and odd harmonics have a similar behaviour. Some present a marked peak suggesting a linear polarisation as the others have more or less stable intensities suggesting ellipticity. For the third case, the intermediate closer to the minimum of generation of the second harmonic both even and odd harmonics look different but the behaviour for each case looks still looks elliptic but closer to the linear polarisation. In the final case, the minimum generation of the second harmonic both peaks look similar. Linearity looks to rule in this situation. For the even case the second harmonic generation only influences the width of the peak and the odd harmonics look fairly linear polarised. In this case as explained before the second harmonic pulse only shifts a little the peak of generation, being the generation clearly dictated by the fundamental pulse.

Another study was taken in order to see the influence of the thickness of the BBO in the generation of high harmonics. This study is presented in figure 3.38. The influence of the two types of BBO, the  $100\mu\text{m}$  and the  $250\mu\text{m}$  is studied. As stated before the increase of the thickness of the BBO in the generation process increases the intensity of the second harmonic field  $I_{2\omega}$ . The intensity ratio between

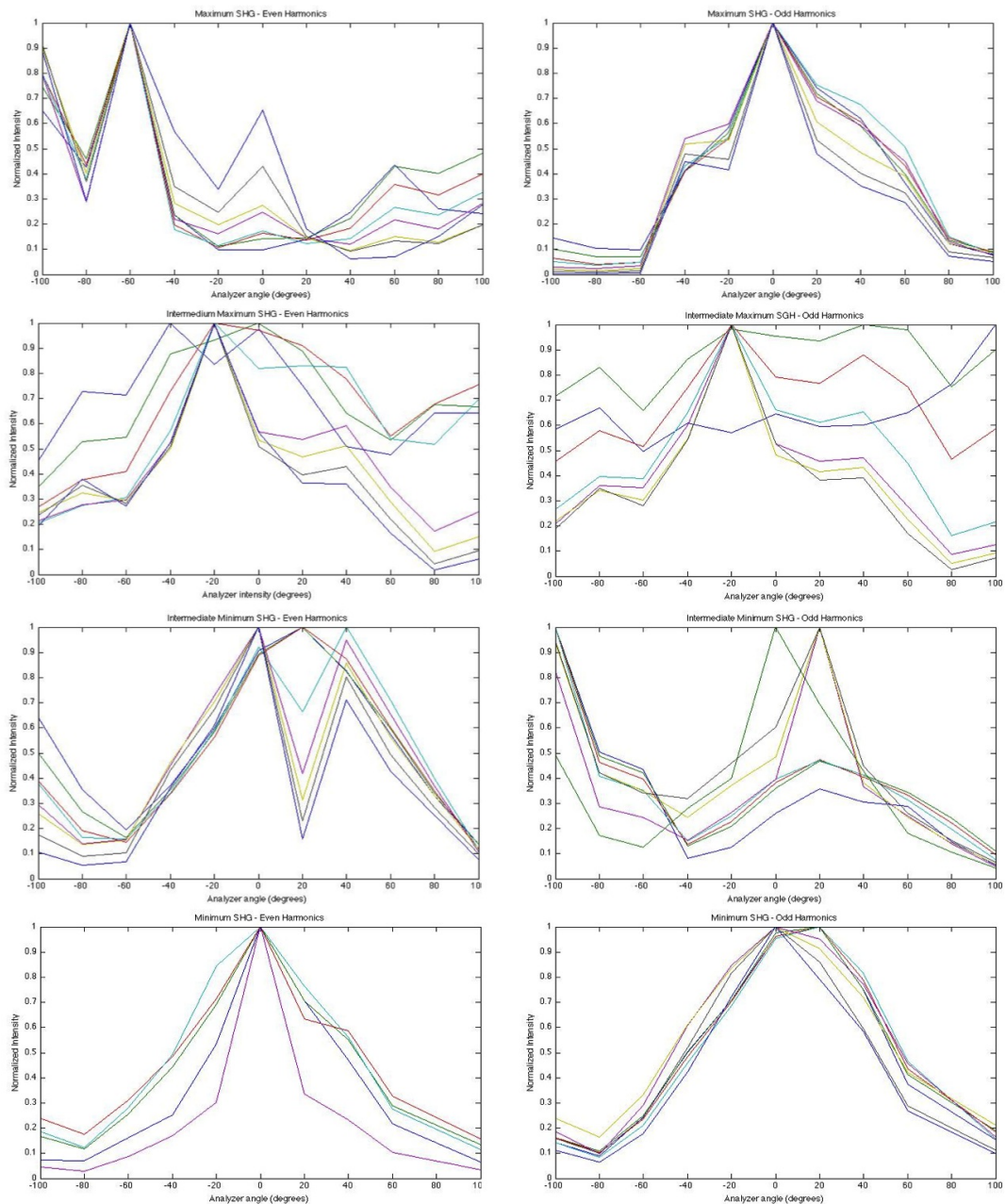


Figure 3.36: Resulting spectra for the even and odd harmonics and with the influence of the BBO generation. The plots represent the intensity of the generation versus the analyser angle in degrees. On the first row the maximum generation of second harmonic case is portrayed. The first image corresponding to the intensity of even harmonics and the second corresponding to the intensity of odd harmonics. The second row and intermediate case closer to the maximum generation of second harmonic is presented. The third row represents an intermediate case this time closer to the minimum generation of the second harmonic. The fourth and last row represents the minimum second harmonic generation. The plots correspond to the harmonics H34 to H49.

both second harmonic field and fundamental field  $I_{2\omega/\omega}$  is closely related to the generation of even harmonics and of the harmonic resulting of the mixing.

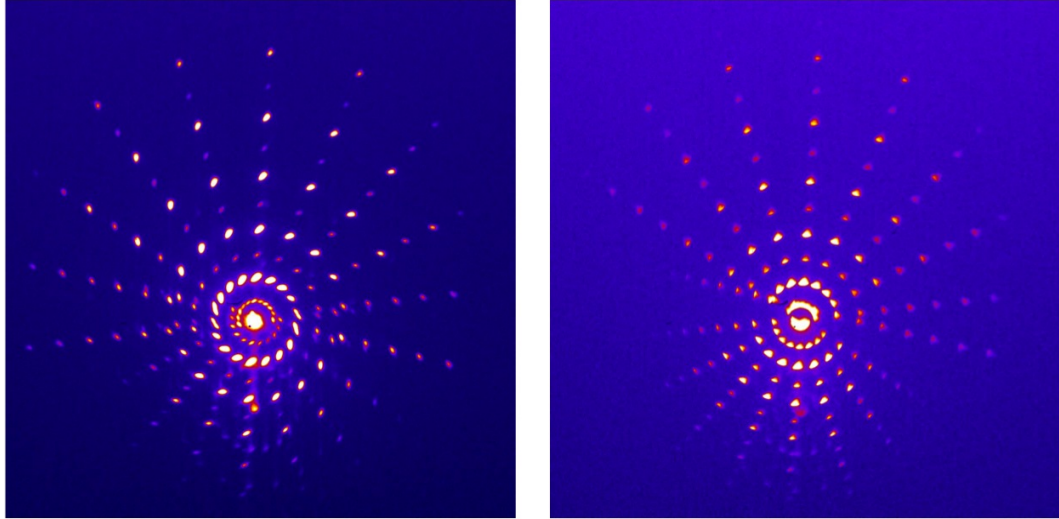


Figure 3.37: Acquired data for both BBO crystals. For the maximum generation approximately. The first image corresponds to the maximum generation of energy using the  $100\mu\text{m}$  thickness BBO. The second corresponds to the maximum generation of energy using the  $250\mu\text{m}$  thickness BBO.

For the case of the  $250\mu\text{m}$  BBO the intensity of the  $2\omega$  and the  $\omega$  is given by the relation (60:40). This is translated onto a wider second harmonic peak. The wider the pulse lower its amplitude which can affect the generation in the case that the energy amplitude reveals itself too low to reach the generation conditions. For the case of the  $100\mu\text{m}$  BBO the  $2\omega$  field is weaker, the pulse is sharper. The overall probability to generate more harmonics is higher. An image of the obtained data is presented on figure 3.37. As expected the  $100\mu\text{m}$  thickness case shows bigger contrast between the odd and even harmonics than the  $250\mu\text{m}$  that normally has a bigger efficiency for generating the second harmonic.

In this figure 3.38 we can see that the behaviour of the polarisation of the harmonics are close for both thicknesses of BBO. In the case of the odd harmonics no flagrant change is marked. It can be only seen that with the increasing thickness the width of the peak is enlarged. In the case of even harmonics however the change is more pronounced. As for the relative intensity of the harmonics as a function of the analyser angle, or the ellipticity of the radiation it can be seen that there is an inflection point at about  $40^\circ$  where the relative intensity of the harmonics from the higher harmonic until the lowest order is inverted. After this point the higher relative intensity becomes confusing. However from the analyser angle

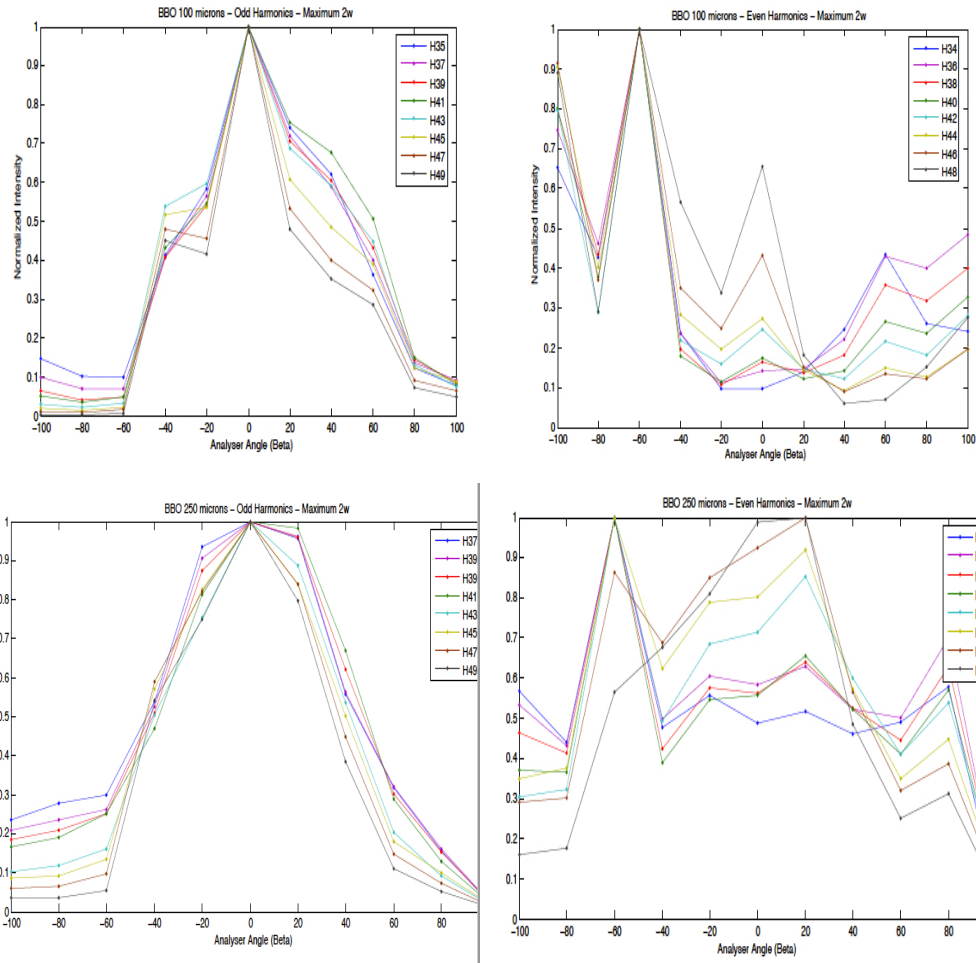


Figure 3.38: Comparison between both BBO crystals. For the maximum generation and for both even and odd harmonics. On the first line the  $100\mu\text{m}$  thickness BBO is presented. The first image corresponding to the odd harmonics and the second image corresponding to the even harmonics. The second line represents the data for the  $250\mu\text{m}$  thickness BBO. The first image representing a plot of the odd harmonics and the second a plot of the even harmonics. The plots refer to the different harmonics going from H34 to H49.

$-20^\circ$  the oscillations decrease indicating a smaller linearity of the harmonics and consequently increase of their ellipticity. For the odd harmonic spectra it can be seen that the increase of the thickness of the BBO seems to increase their linearity.

This raw results obtained are still very hard to interpret due to the complex behaviour that they are illustrating. The control of the second harmonic field over the harmonic generation is still to be studied, the intensities of the field produced by the fundamental and the second harmonic and its relation and the gap between

the generation of the two types of radiation has to be studied deeper. At this point there is a need to connect these results to theoretical models in order to withdraw more consistent conclusions. The first step into realising a fully theoretical study is to rewrite this obtained results in physical comparable measure units. A Matlab routine was implemented and it explained in the next section.

### 3.2.5 Matlab data analysis of the harmonic polarisation in an orthogonal two-colour field

In order to be able to link this results to the simulation codes developed and presented in the previous chapter a Matlab routine was developed to transform the data obtained on projections over the  $x$  and  $z$  axis.

Using the Stokes parameters to study the polarisation of the experimental data we have

$$S = \begin{pmatrix} S_0 \\ S_1 \\ S_2 \\ S_3 \end{pmatrix} = \begin{pmatrix} I \\ Q \\ U \\ V \end{pmatrix} \quad (3.32)$$

Rewriting the stokes parameters are rewriting them in the form of a polarisation ellipse we have

$$I_p = A^2 + B^2 \quad (3.33)$$

$$Q = (A^2 - B^2) \cos(2\theta) \quad (3.34)$$

$$U = (A^2 - B^2) \sin(2\theta) \quad (3.35)$$

$$V = 2ABh \quad (3.36)$$

where  $A$  is the major axis of the ellipse,  $B$  the minor axis of the ellipse,  $\theta$  the angle in relation to the  $x$  axis and  $h$  the sense of rotation of the ellipse.

An example of the polarisation ellipse is given on figure 3.51 with all the physical constants represented.

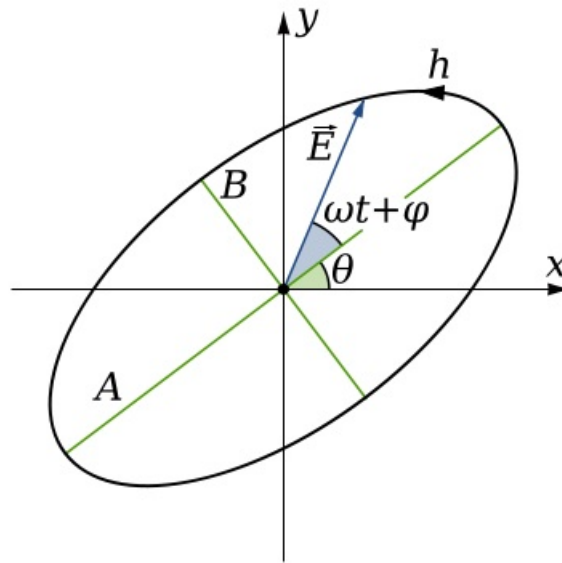


Figure 3.39: Representation of the elliptic polarisation scheme with the corresponding parameters.

Rewriting these equations using the linear and circular polarisation motions. Where  $|L|$  corresponds to the intensity of linear polarisation and can be written as  $L = |L|e^{i(2\theta)}$  or  $L = Q + iU$  and  $|V|$  is the intensity of circular polarisation. The total intensity of the polarisation is represented by  $I_p$  and is given by  $\sqrt{L^2 + V^2}$ . Using the previous equations the result is:

$$A = \sqrt{\frac{1}{2}(I_p + |L|)} \quad (3.37)$$

$$B = \sqrt{\frac{1}{2}(I_p - |L|)} \quad (3.38)$$

$$\theta = \frac{1}{2} \arg(L) \quad (3.39)$$

$$h = (V) \quad (3.40)$$

In order to visualise the harmonic intensity to help visually the following image was plotted 3.40.

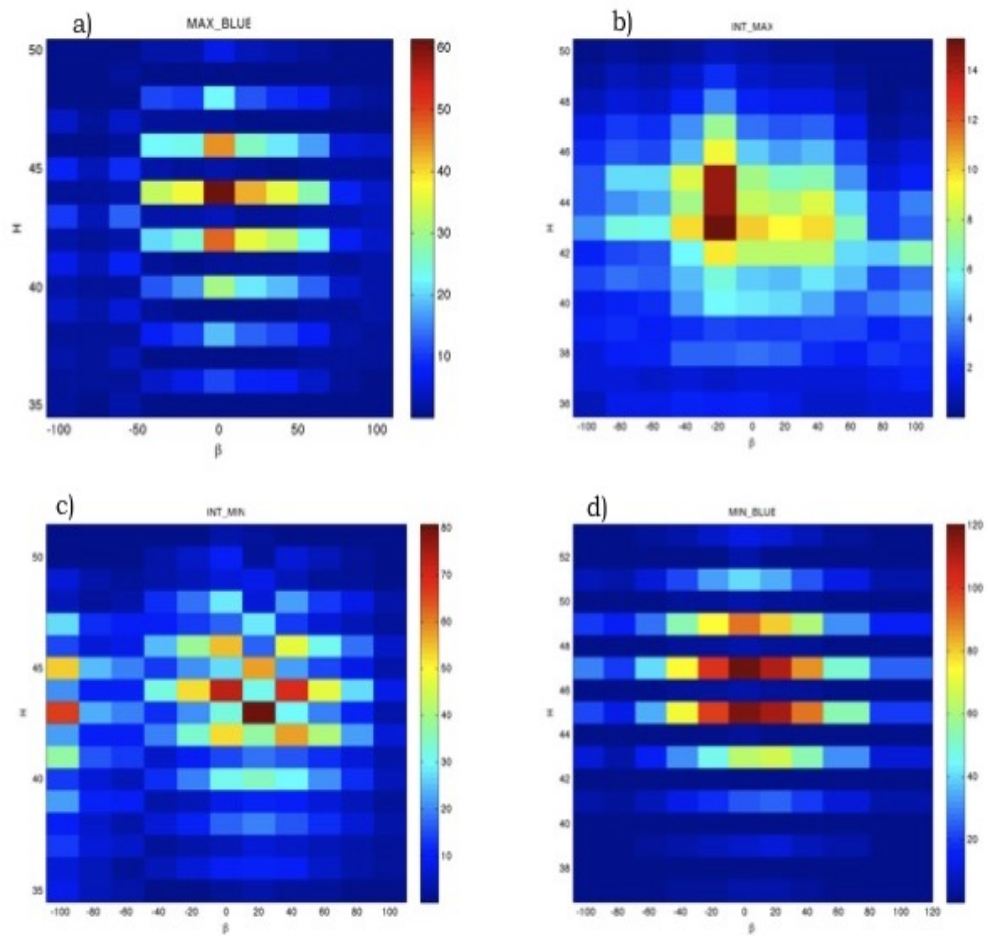


Figure 3.40: Intensity representation of the HHG. The first row shows the stronger regimes of generation. The first image represents the maximum generation and the second the intermediate maximum generation. The second row shows the weakest second harmonic generation. the first image the intermediate minimum and the last one the minimum generation of the second harmonic field.

In this image the four sets of data are represented. The maximum generation of second harmonic as MAX BLUE, the intermediate position closer to the maximum

of generation as INT MAX, the second intermediate position of generation closer to the minimum as INT MIN and finally the lower intensity of the second harmonic corresponding to the position where the BBO has its least generation efficiency is represented as MIN BLUE.

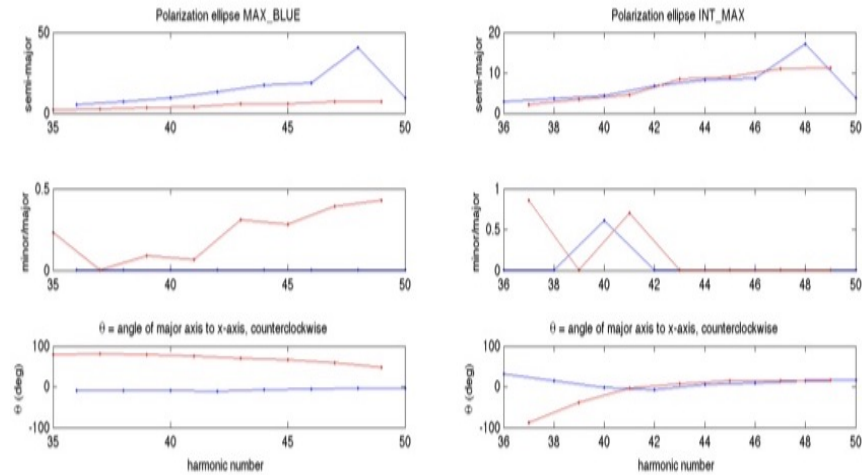


Figure 3.41: Representation of the polarisation ellipse for HHG for maximum generation of second harmonic and intermediate maximum. On the x-axis the harmonic order is portrayed. The red line corresponds to the odd harmonics and the blue line to the even harmonics. The first plot shows the semi-major axis of the ellipse. The second plot the ratio minor/major axis of the ellipse and the last plot the angle to the major axis to the x-axis.

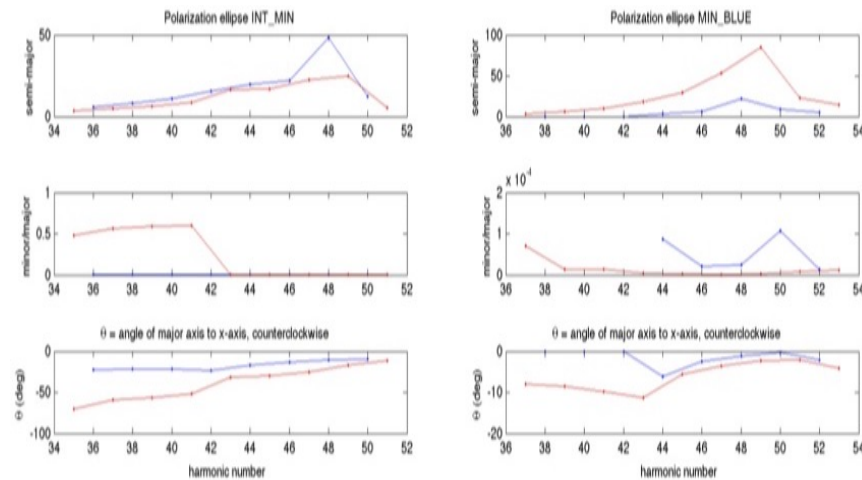


Figure 3.42: Representation of the polarisation ellipse for HHG for intermediate minimum and minimum of the generation of second harmonic. On the x-axis the harmonic order is portrayed. The red line corresponds to the odd harmonics and the blue line to the even harmonics. The first plot shows the semi-major axis of the ellipse. The second plot the ratio minor/major axis of the ellipse and the last plot the angle to the major axis to the x-axis.

This image is plotted as a function of the analyser angle  $\beta$  and covering the

harmonics from 35<sup>th</sup> to 50<sup>th</sup>. In the first image the even harmonics are clearly more intense and its peak seems to be around the analyser position zero even if the intensity still remains important from -50 to 50 degrees. In the first intermediate case the intensity of the even and odd harmonics is mixed no clear harmonics stand out. For the second intermediate minimum case depending on the analyser angle odd or even harmonics stand out and present some degree of ellipticity. The final case shows really intense odd harmonics that seem linear polarised. The change from odd to even is possible when the weak field is detuned slightly from the second harmonic. This is to be expected since the driving laser field is almost only the fundamental.

Applying to the four different cases of blue intensity the graphs presented on the figure 3.41 and 3.42 can be plotted. For each plot the odd and even harmonics were separated in order to better analyse their behaviour.

These plots correspond to the experimental values obtained previously rewritten as a function of the polarisation ellipse since it was shown that the polarisation of the harmonics are essentially elliptic. The first plot of the three series corresponds to the semi-major or  $A/2$  the longest diameter line. It gives the amplitude of the movement. The second plot corresponds to the ratio minor/major or  $B/A$  giving us the degree of ellipticity of the harmonics when equal to 1 both axes have the same intensity thus reflecting a circular polarisation, when equal to zero linear polarisation is to be expected. The third plot is a representation of the  $\theta$  angle of the polarisation ellipse. It can be seen on figure 3.51 that it corresponds to the angle of the major axis or ( $A$ ) to the referential. Under a rotation of the polarisation ellipse  $I$  and  $V$  remain constant but  $L$ ,  $Q$  and  $U$  are affected.

The following plot was obtained for the four cases of generation 3.43. This figure represents the stem plot to be compared with the simulation results of the fundamental and second harmonic field component on each harmonic for each set of data.

From these analyses it can be seen that indeed the ellipticity is present in the harmonics generated no matter the regime. No clear behaviour pattern can be extracted from these plots several abrupt changes are portrayed confirming that the phenomenon of the polarisation of high harmonics is deeper.

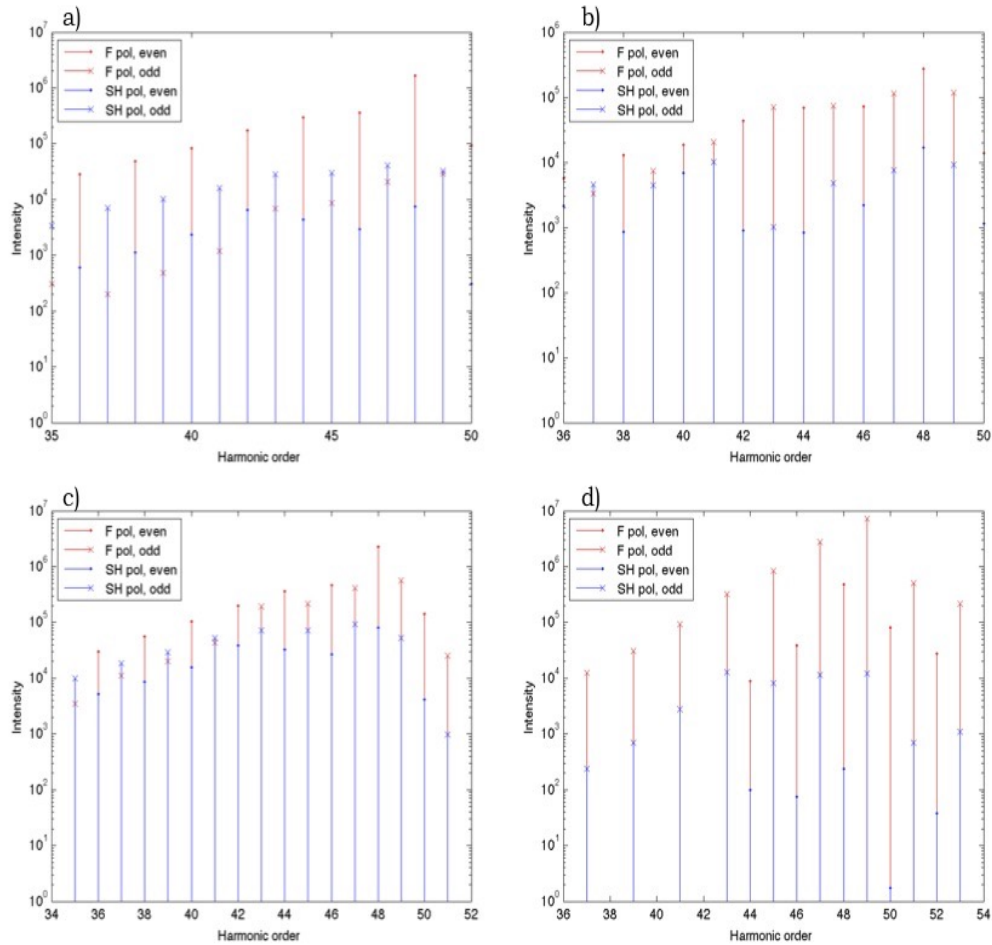


Figure 3.43: Representation of the contributions either from the fundamental field or the second harmonic field on the HHG for maximum generation of second harmonic (a), intermediate maximum (b), intermediate minimum (c) and minimum (d).

In order to begin to understand the physical phenomenon behind the generation of High Harmonics simulations have been performed and will be presented in the next section.

### 3.3 Polarisation simulations

High harmonic generation in a two-colour field presents a great number of parameters that can be varied in order to generate at one's liking. The intensities of both fields, their polarisation, the frequency ratio and relative phase can all be varied and by doing so they can dramatically change the generation in the theoretical

point of view [57].

The approach used in this manuscript is to try to use a polarisation ellipse to explain the polarisation of the orthogonal fields. An example of the polarisation ellipse is given on the figure 3.51.

In the beginning of this chapter it was shown that the single atom description was not sufficient to explain the experimental data. It is convenient in order to establish an agreement between theory and practice to consider the effects of propagation and phase matching of the HH in the macroscopical approach.

The ellipticity of the harmonic pulse is the product of the coherence between the harmonic cut-off and their relative phase [64]. As seen in the beginning of the chapter there are at least two trajectories leading to the same energy but aiming at different angles and delayed in time that contribute to the same harmonic a more profound study is needed in order to understand the phenomenon. According to Lewenstein [56] the harmonic ellipticity is given in terms of the quantum mechanical spreading of the electronic wave packet after ionisation and the features of the classical electron trajectory. Resulting in different quantum paths that contribute to the radiating pole. The perturbation theory predicts a non-zero ellipticity but since the HHG is a strongly non-perturbative phenomenon the results of the perturbation theory can hardly be applied even for a qualitative understanding of the HH ellipticity. The quantum-mechanical theories based on the strong field approximation allows a calculation of the ellipticity value.

In order to establish a connection between the experimental results and theoretical studies a cooperation with the ICFO at Barcelona was established.

### 3.3.1 Strong field approximation - Bauer

The code used in this part is the code is used by Professor Jen's Biegert team at ICFO. A cooperation was put to place in order to try to understand the behaviour of the polarisation of the exiting High Harmonics generated in an orthogonal two colour field. Since the application of the  $\delta^3$  model wasn't accurate in this section we turn to the Strong Field Approximation (SFA) model. It is very much related to the  $\sigma$ -potential of Becker allowing to reach the problem without having to numerically

solve the time-dependent Schrodinger equations. This model has shown good consistency [74] while giving a mechanical description of the HHG [56].

In the SFA some of the bound states electrons tunnels over the potential barrier near the peak of the laser field. Once in the continuum the electron returns to the vicinity of the parent ion described as a chirped plane wave. This plane wave then interacts with the bound state portion of the wavefunction leading to an oscillation that radiates electromagnetic radiation.

A vector potential of the form

$$vA(t) = A_z(t)v e_z + A_x(t)v_x \quad (3.41)$$

where  $z$  corresponds to the fundamental axis and  $x$  corresponds to the second harmonic axis and where  $A_z$  is the amplitude of the fundamental pulse and  $A_x$  the amplitude of the second harmonic pulse are both sinusoidal pulses that can be shifted in phase  $\omega r t$  to each other, with different frequencies, duration etc. The gas used as an input for the simulations was Neon, since it presents a good conversion efficiency for the range of energies that are interesting for this manuscript. The dipole  $d^{(L)}(t)$  is calculated according to the Lewenstein model. The expression developed by P. Mulser and D. Bauer on "High-Power Laser-Matter Interaction" is implemented and extended for polarisation also in x-direction.

Considering that the problem is illustrated as following:

The initial parameters for the generation are a fundamental field, linear polarised with a central wavelength of 815 nm with a peak intensity of  $2.6 \times 10^{15} \text{ W/cm}^2$  and 40 fs pulse duration. The second harmonic pulse that arrives 18.5 fs before the fundamental (as explained in the beginning of the chapter) presents a wavelength of 408 nm at a duration of 42 fs and second harmonic peak intensity of  $2.46 \times 10^{12} \text{ W/cm}^2$ .

The following set of data present variations of the intensity of the fundamental field. That can be changed chirping the generating laser pulse this simulation is presented in figure 3.45.

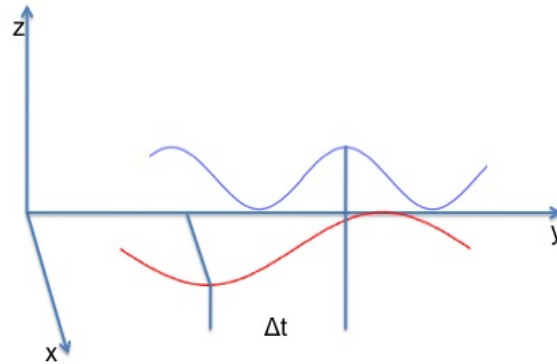


Figure 3.44: Geometry for the SFA simulation studies where the red line corresponds to the fundamental field that is generated over the  $xy$  plane and the blue line corresponds to the second harmonic field that is generated orthogonally (BBO type 1) in the  $zy$  plane.  $\Delta t$  corresponds to the delay time between the two pulses.

It can be seen that the effect of the variation of the intensity of the fundamental field is mainly the intensity of the harmonics generated and the extension of the cut-off no shift is detected between both odd  $z(F)$  or even harmonics  $x(SH)$ .

The variation of the second harmonic wave parameters can be made possible by the interaction of the BBO crystal in the generation parameters. With the increase of the  $I_2$  the ratio  $\beta = I_2/I_f$  also increases, an increase of the plateau region would be expected as explained by the perturbation theory [69]. This effect was also studied and it is presented on figure 3.46.

In this case 3.46 no extension of the plateau effect was perceptible due probably to the low intensities of the cut-off harmonics. This model also filters only some of the electronic trajectories so it can be a result of this limitation. As for the effect of the variation of the second harmonic it can be seen that the harmonics are slightly shifted it looks like there is almost an effect of inversion between the odd and even harmonics. The intensity of the second field is very important to the generation of the harmonics.

The variation of the phase of the second harmonic wave can be induced by the BBO crystal. Frolov *et al* showed the phase dependence of the HHG for Ne in the two-color field. While brugnera *et al* [74] showed that the calculated harmonic signal is very weak around  $0.3\pi$ . Figure 3.47 shows the resulting simulation calculations for our parameters and for various phase values.

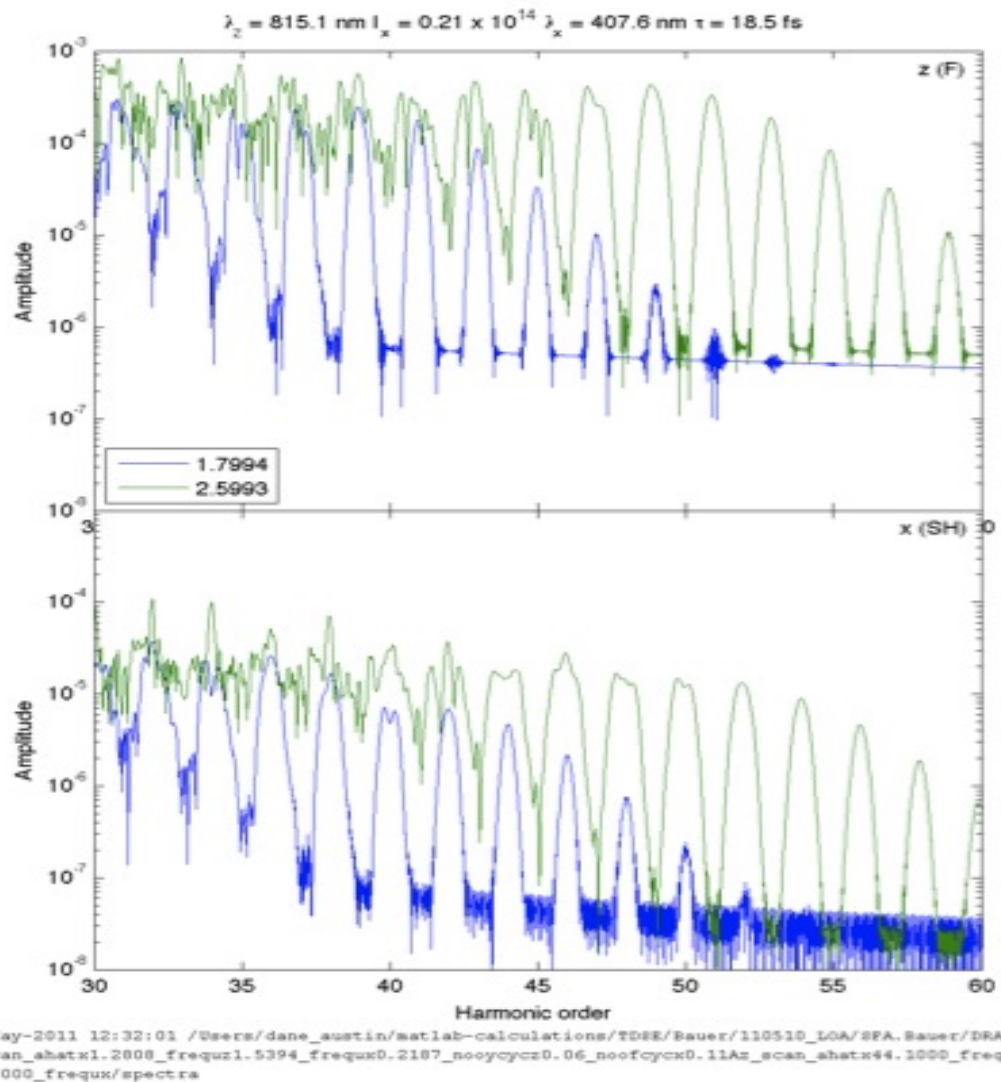


Figure 3.45: Variation of the fundamental field intensity. In this simulation the fundamental wavelength is blocked at 815 nm and the intensity of the field at  $2.6 \times 10^{15} \text{ W/cm}^2$ . The second harmonic field varies its intensity from  $2.1 \times 10^{14} \text{ W/cm}^2$  to  $2.0 \times 10^{14} \text{ W/cm}^2$  and its wavelength from 407 to 412 nm. The pulse duration varies from is 18.5 to 18.7 fs.

In figure 3.47 can be seen that changing the phase the spectra also changes. Firstly the harmonics seem less intense with the increase of the phase, this can be explained by the decrease of superposition between both fields, ending in a lower generation intensity itself. The harmonics shift a little around their optimal value. No conclusions as to the generation of the polarisation of harmonics can be made from this plot. The biggest change so far in the spectra has been the intensity of the second harmonic field. Figure 3.48 shows the effects of varying the second

$$2.60 \times 10^{14} \text{ W/cm}^2 \lambda_z = 815.1 \text{ nm } I_x = 0.2098-0.2102 \times 10^{14} \lambda_x = 407.6-412.0 \text{ nm } \tau = 18.5-18.7 \text{ fs}$$

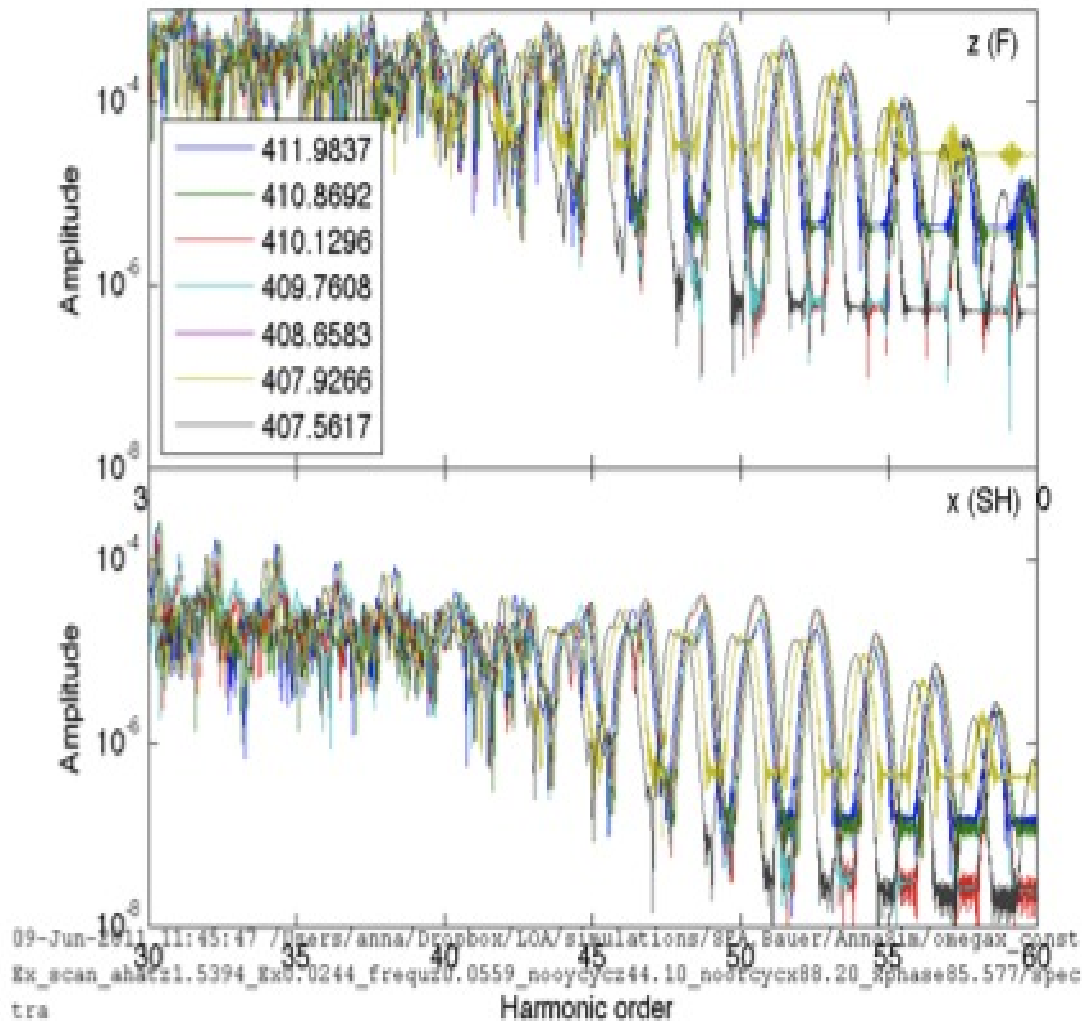
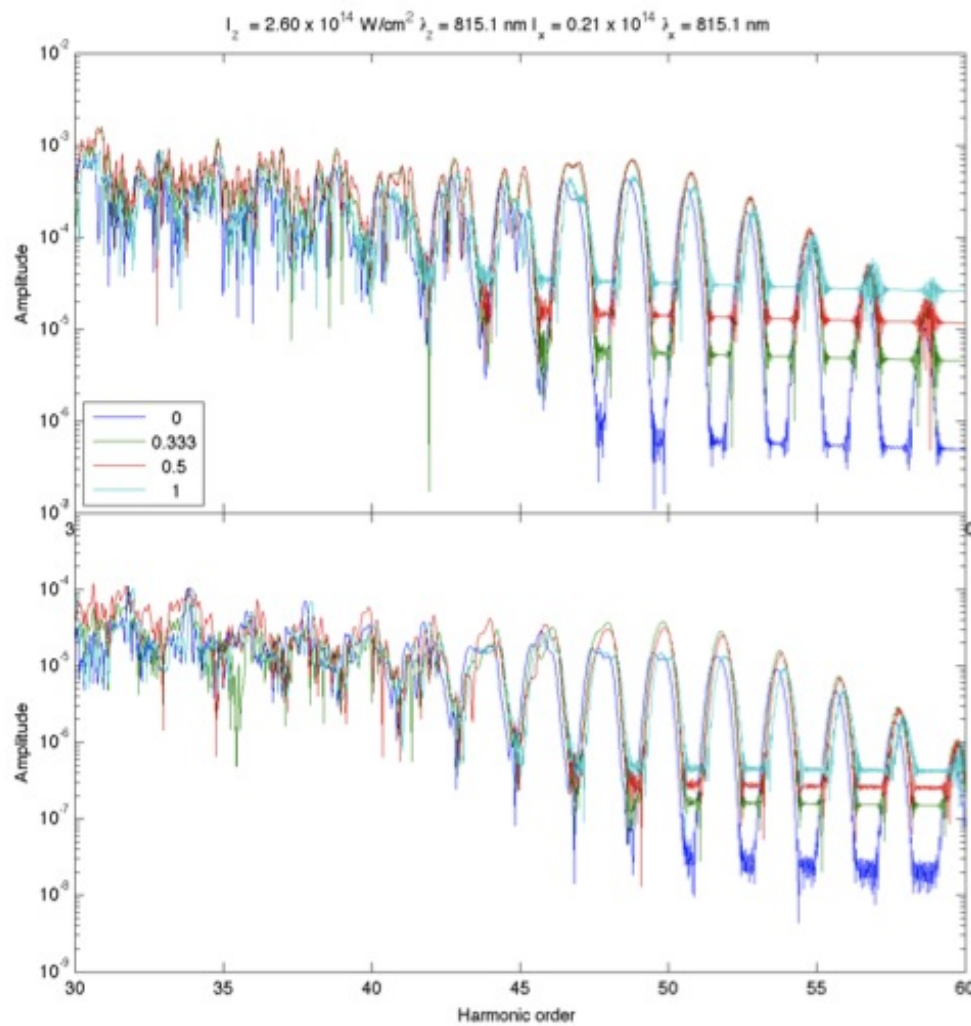


Figure 3.46: Variation of the second harmonic field intensity. In this simulation the fundamental wavelength is blocked at 815 nm and the intensity of the field varies from its peak intensity  $2.6 \times 10^{15} \text{ W/cm}^2$  to  $1.8 \times 10^{15} \text{ W/cm}^2$ . The second harmonic field has stationary parameters: Intensity of  $2.1 \times 10^{14} \text{ W/cm}^2$  and wavelength of 407 nm. The pulse duration is 18.5 fs.

harmonic intensity and adding  $\pi$  to the phase between both fields.

The two plots fig. 3.46 and fig. 3.48 are very similar between them showing no significant interest in the change of the phase between them.

As a final simulation and in order to be able to compare the results for different conditions of generation argon was used as input. Being the most commonly found



11-May-2011 12:18:23 /Users/dane\_austin/matlab-calculations/TDSE/Bauer/110510\_LOA/SPA.Bauer/DRA/xpbase\_scan\_ahatz1.5394\_ahatz0.2187\_frequz0.0559\_frequz0.1118\_noofcyz44.10\_noofcyz88.20/spectra

Figure 3.47: Variation of the HH spectra with the phase. Maintaining all the parameters fixed in this simulation. The phase between the two waves will be varied. In blue the waves have no shift. In green the shift corresponds to 0.3 in red the shift corresponds to 0.5 and in light blue the shift corresponds to 1.

laser for HHG and in order to compare the generation using both systems. The electron binding energy is for Neon of 21.6 eV and for the Argon 15.7 eV. The results are presented in figure 3.49.

As expected the amplitude is higher and the spectra is slightly different, the data window is adjusted to the generation in the Neon. Odd and even harmonics seem to be perfectly aligned with their generating field.

$$2.60 \times 10^{14} \text{ W/cm}^2 \quad \lambda_z = 815.1 \text{ nm} \quad I_x = 0.2098\text{-}0.2102 \times 10^{14} \quad \lambda_x = 407.6\text{-}412.0 \text{ nm} \quad \tau = 19.2\text{-}19.4 \text{ fs}$$

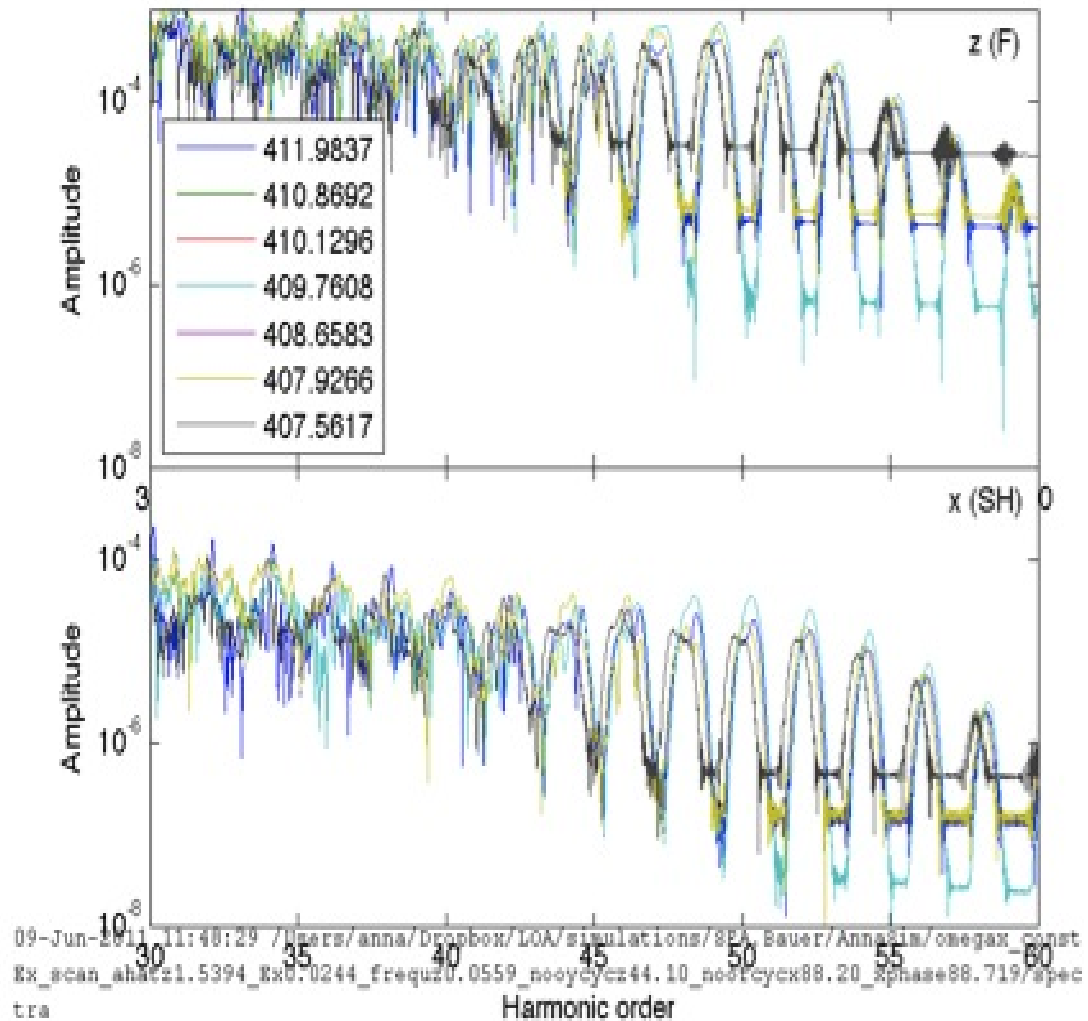


Figure 3.48: Variation of the second harmonic wavelength maintaining a  $\pi$  phase between the fundamental and the second harmonic pulse. The fundamental wavelength is blocked at 815 nm and the intensity of the field at  $2.6 \times 10^{15} \text{ W/cm}^2$ . The second harmonic field varies its intensity from  $2.1 \times 10^{14} \text{ W/cm}^2$  to  $2.0 \times 10^{14} \text{ W/cm}^2$  and its wavelength from 407 to 412 nm. The pulse duration varies from is 19.2 to 19.4 fs.

From this simulation round it can be stated that the initial conditions are not sufficient to explain the problematic.

The experiment clearly shows that in the fundamental polarisation (into which most of the XUV energy is emitted), the harmonics change from odd to even for the strongest second harmonic field. Therefore, either the above analysis is incorrect,

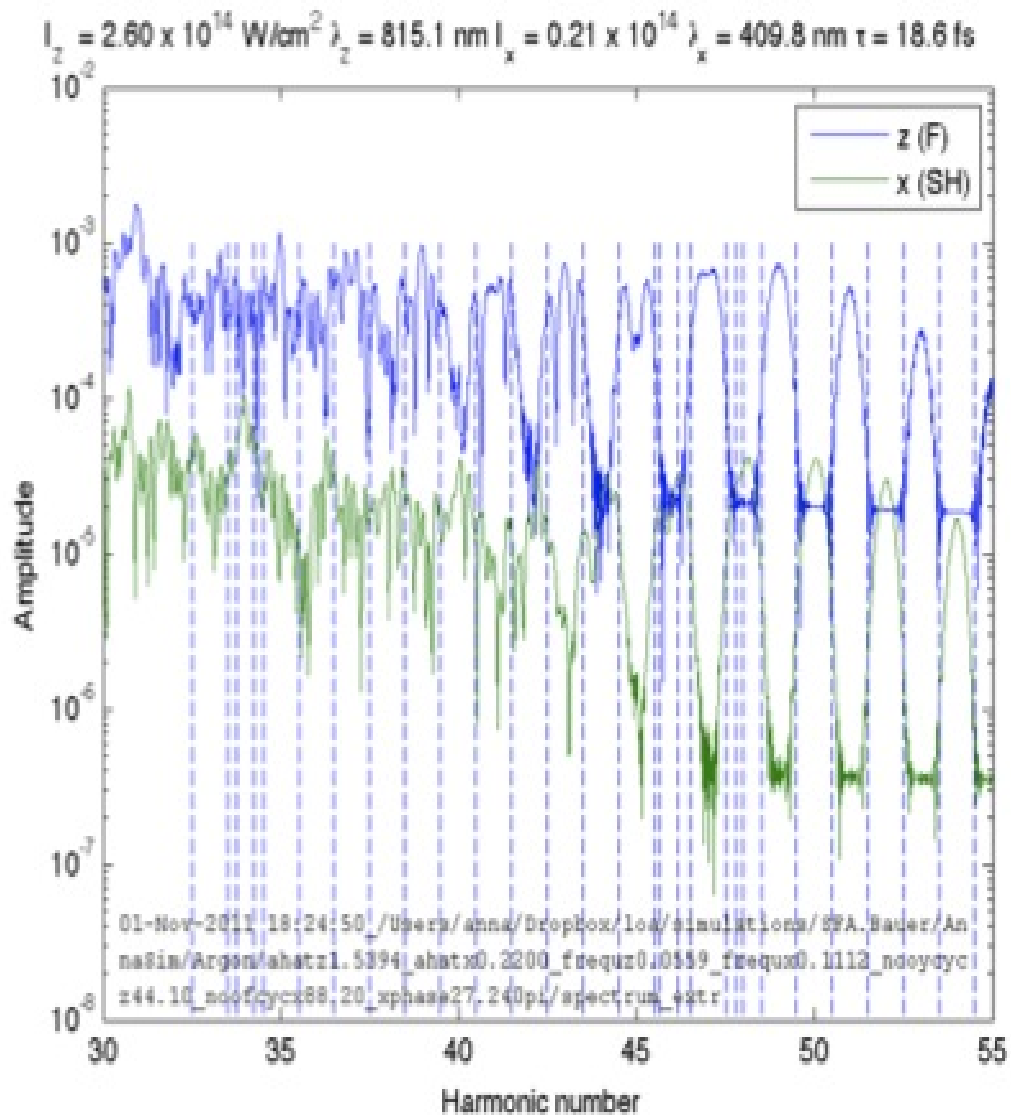


Figure 3.49: Simulation for Argon for both the fundamental pulse and the second harmonic pulse. In this simulation the fundamental wavelength is blocked at 815 nm and the intensity of the field at  $2.6 \times 10^{15} \text{ W/cm}^2$ . The second harmonic field varies its intensity from  $2.1 \times 10^{14} \text{ W/cm}^2$  and its wavelength from 410 nm. The pulse duration is 18.6 fs.

the fields were not orthogonally polarised, or the second harmonic field was strong enough to go beyond the first-order approximation, which the calculations indicate is valid for  $E_w < 0.1E_s$ . In the experiment, the strongest second harmonic fields are about  $E_w$  approximately  $0.3E_s$ .

Further developments have to be made in order to go deeper into the generation process.

### 3.3.2 New theoretical approach

The previous simulations didn't explained the experimental results obtained in the laboratory. The hypothesis of the ellipticity of the harmonics has still to be proved under a theoretical point of view.

A correlation between the fundamental and the second harmonic intensity and polarisation is necessary. The analysis of the phase-matching on the BBO is represented on figure 3.50. This plot represents the effects of keeping the crystal length fixed and varying the phase-mismatch represented by  $\Delta k$ .

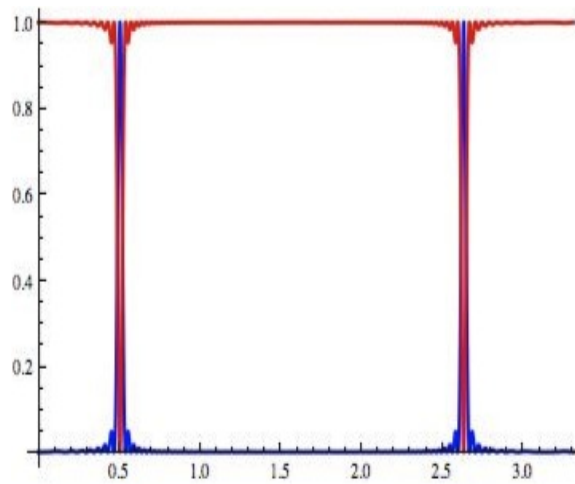


Figure 3.50: Phase-match conditions for a BBO type 1 of  $100\mu m$  as a function of the crystal orientation in radians.

For a  $100\mu m$  BBO the phase-match is reached at 0.5 radians, corresponding to 28.5 degrees. In red in this model is represented the  $\omega$  signal while in blue is represented the  $2\omega$  signal. In our case the field is generated orthogonally since the BBO in use is a type 1.

Considering the following diagram for the  $\omega$  and  $2\omega$  presented on figure 3.51 the generation in the BBO certain observations can be deduced.

In a general case the  $\omega$  field is projected on the ordinary and and a component on the extra-ordinary axis of the crystal. Depending on the incident  $\omega$  field. If the field is linear horizontal such in the figure 3.51 the  $\omega$  field is projected only on the ordinary axis. The refractive index of the extraordinary axis  $n_e$  changes with the orientation (rotation) of the crystal. Meaning that one polarisation component

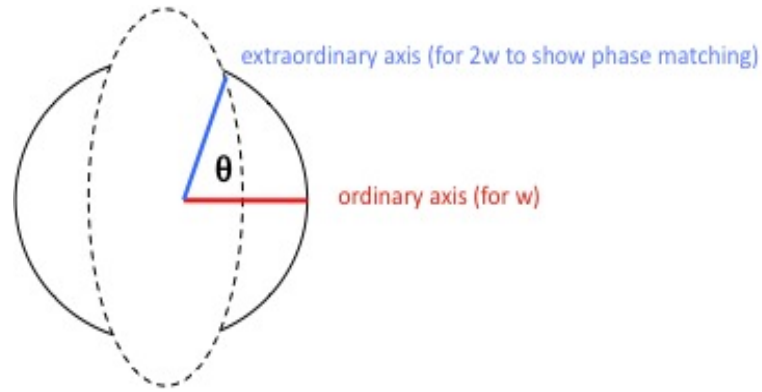


Figure 3.51: Representation of the elliptic polarisation for a linear horizontal polarisation of the incident fundamental field.

of the  $\omega$  field gets delayed in respect to the other polarisation component and the delay depends on the orientation of the crystal. It can be said that the crystal behaves like a waveplate for  $\omega$ , the fundamental frequency.

The delay between the polarisation components is given by:

$$\Delta\varphi = \frac{2\pi}{\lambda}d(n_{slow} - n_{fast}) \quad (3.42)$$

where  $n_{fast}$  depends on the orientation angle.

Considering these effects the intensity and polarisation of the  $\omega$  signal can be correlated to the High Harmonics signal. The harmonics considered are between the harmonic 15 and 37 and have been generated on Argon. The reason for this shift is only due to experimental logistics. However to study the physical phenomenon their use is valid.

Figure 3.52 shows the normalised intensity of the harmonics generated for, in red, the odd harmonics and in blue the even harmonics. The odd harmonics can present until 3 times a higher value. The generation of the harmonics is here portrayed as a function of the BBO efficiency to generate the second harmonic field. While less ellipticity is reached for odd harmonics, even harmonics show signs of ellipticity. Implying that the second harmonic field may have a significant impact on the ellipticity.

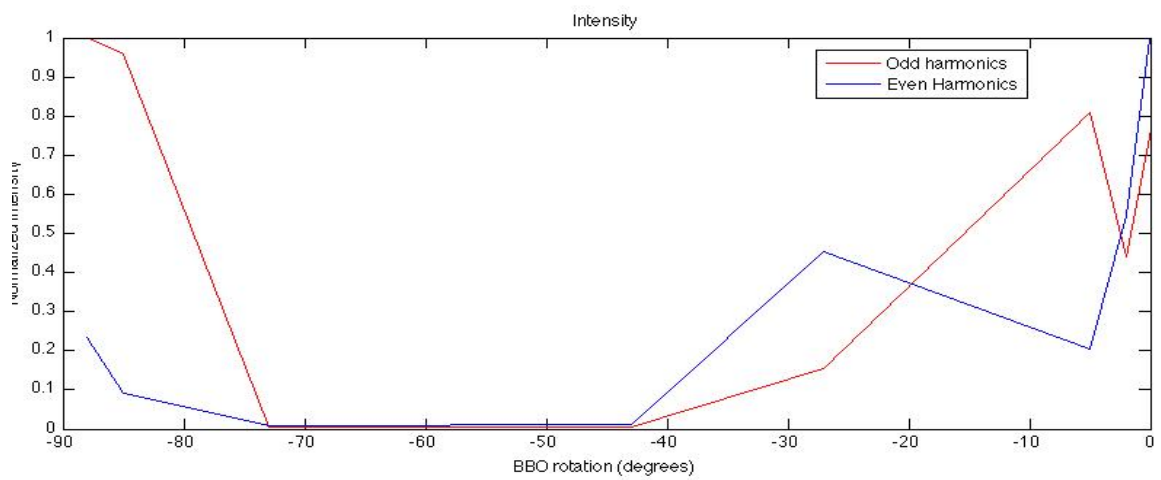


Figure 3.52: Normalised intensity of the even and odd harmonics as a function of the  $100\mu\text{m}$  thickness BBO crystal.

The calculated ellipticity of the  $\omega$  field is presented in order to compare with the ellipticity values retrieved from the measurements. This plot is presented on figure 3.53.

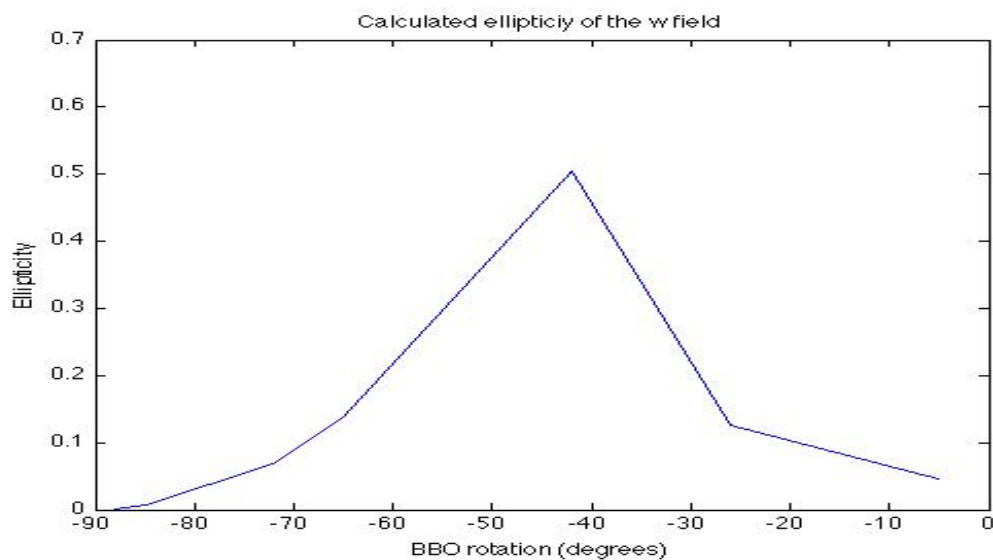


Figure 3.53: Calculated ellipticity of the fundamental field as a function of the  $100\mu\text{m}$  thickness BBO crystal.

From the experimental data it is possible to extract the ellipticity of the High Harmonics generated. Figure 3.54 shows the measured ellipticity as function of the BBO rotation angle.

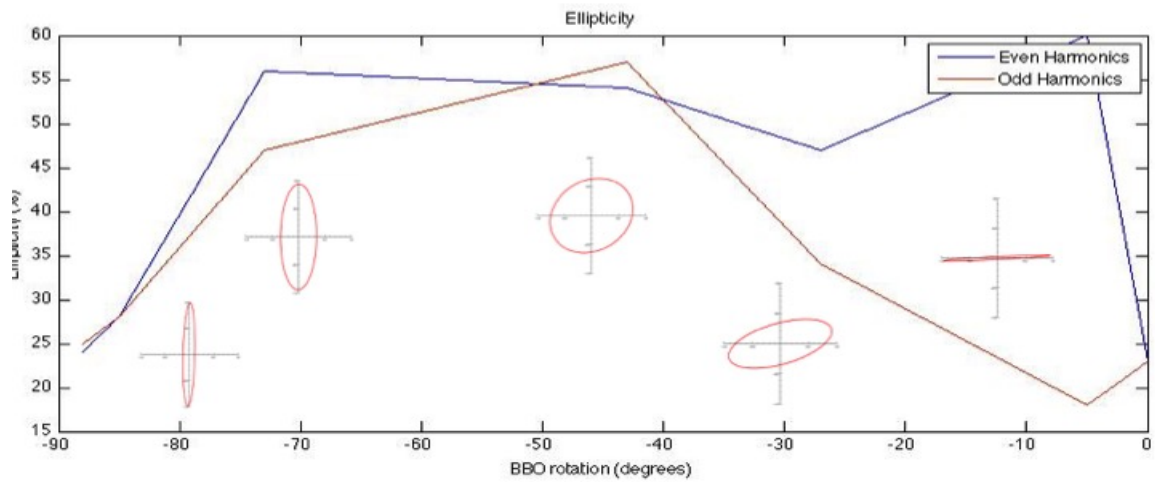


Figure 3.54: Ellipticity of the even (blue) and odd (red) harmonics in function of the BBO rotation. The inlets show the calculated polarisations of the fundamental field as a function of the  $100\mu\text{m}$  thickness BBO crystal.

Once again the odd harmonics are represented in red and the even harmonics are represented in blue. It can be seen that the ellipticity of the measured harmonics is resemblant to the ellipticity of the  $\omega$  field. So a big influence from the BBO induced ellipticity is present in the resulting harmonics.

Calculating the axis of the  $\omega$  polarisation of the  $\omega$  field due to the passage through the BBO gives the following plot, figure 3.55.

Once again it can be seen a big influence of the BBO in the polarisation axis. Comparing the measured axis of polarisation present in figure 3.56.

The behaviour is quite similar. A new hypothesis to be proven can be that the generation of high harmonic on the two colour orthogonal experiments can result of the fundamental field, the second harmonic field a third field combining the previous two. One component that follows the fundamental field, one smaller component that follows the fundamental but weaker field generated during the frequency doubling and one component generated during frequency doubling that is orthogonal and resembling to the second harmonic field.

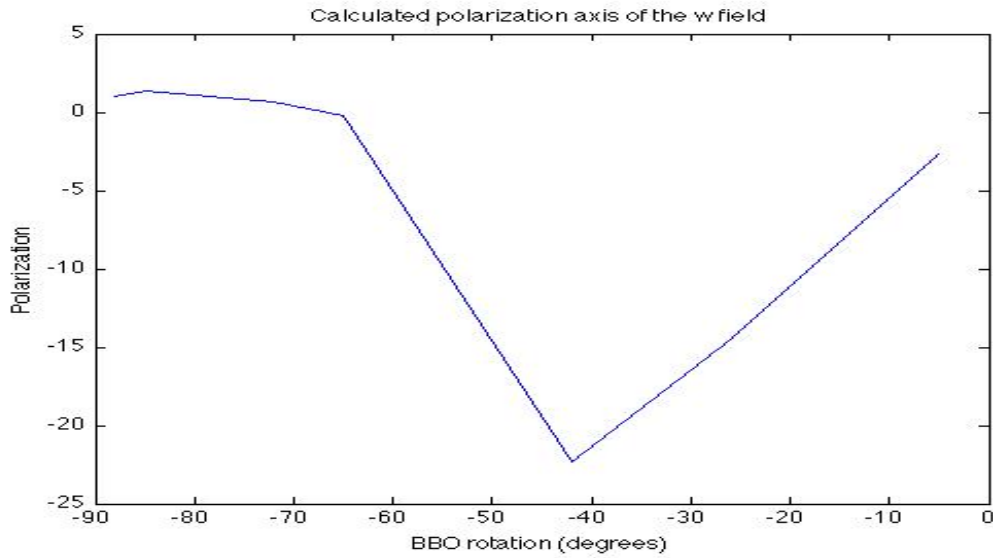


Figure 3.55: Calculated polarisation of the  $\omega$  axis, fundamental field as a function of the  $100\mu\text{m}$  thickness BBO crystal.

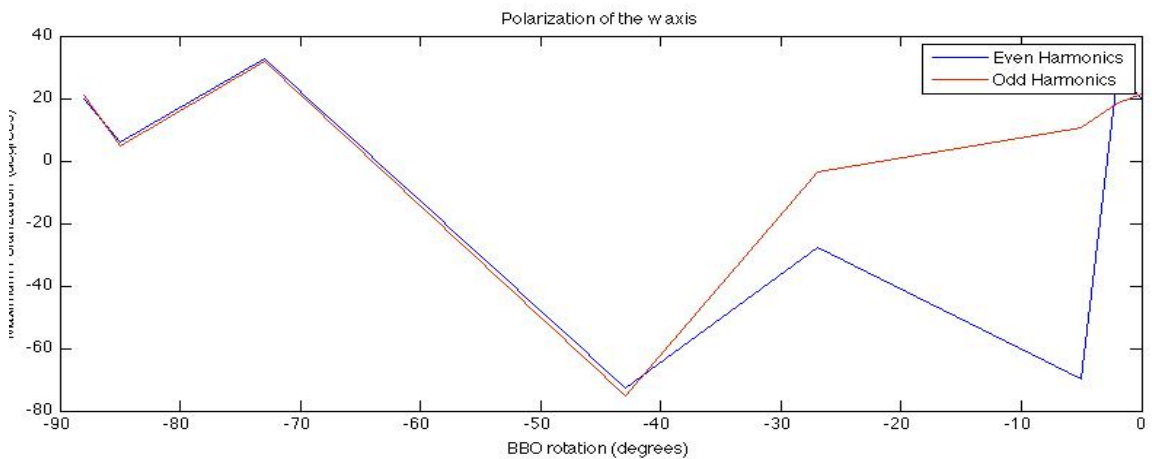


Figure 3.56: Experimental axis  $\omega$  of polarisation as a function of the  $100\mu\text{m}$  thickness BBO crystal.

### 3.4 Conclusions and Perspectives

As a summary of the HHG properties obtained with the table top source located in Laboratoire d'Optique appliquee we have a femtosecond pulse duration fully coherent in a simple system that is intense at short wavelengths and tuneable with

both odd and even harmonics and presents an aberration-free beam in a high repetition rate fundamental laser. However there is a need to improve the stability of the shot-to-shot intensity. Circularly polarised light in the EUV region could be obtained using HHG source and a four mirror circular polariser. A degree of circular polarisation equal or close to 100 % was obtained for harmonics of wavelengths ranging from 18.1 to 26.3 nm with a circular transmission between 2.6 and 4.4 %. It has been shown that bright circularly polarised harmonics could be obtained with this system. It should be emphasised that our setup can be improved at least on two points. First in this report, the polariser was optimised for a precise wavelength. The performance of the polariser for other wavelengths are then suboptimal. Second, our attention was focused on the maximisation of the degree of circular polarisation. A less restrictive criterion, and often more useful for experiment, is the maximisation of the number of circularly polarised photons yielded by the polariser. This criterion implies smaller glancing angles and thus higher reflectivities. Theoretically, circular transmission close to 20 % could be obtained. A polarisation chamber was built on the grant RMASES and tested at SOLEIL and BESSY-II for further experiments.

With these light source, the MCD effect at the absorption M-edge of Fe, Co and Ni (at 23.8, 20.7 and 18.5 nm respectively) can be probed and used to study nanoscale ultrafast magnetic dynamics. For the time being, this type of studies can be conducted at only a few places worldwide. We hope that the use of circular XUV light from HHG sources will open this field of study to a wider community. Other applications will benefit from a circularly polarised coherent XUV light source. First, it can be used in FEL or in laser plasma amplifier as a seed to obtain circularly polarised amplified light. There are other approaches to obtain circularly polarised light with a seeded FEL but for laser plasma amplifier using a circularly polarised seed is the only solution. Another application which could benefit greatly from a circularly polarised HHG source is the nanoscale dynamics of biological systems. Indeed, these systems often show structures that can be image only by circularly polarised light such as chiral domains. It will be possible to observe the dynamic of such structures at the nanoscale level with circularly polarised harmonics. Element specific imaging could even be performed.

Considering the studies of the polarisation in a two colour field there is still room for improvement. To move forward it would be good to have systematic simulation results. In addition to the simulations which attempt to replicate the ex-

perimental conditions, it would be useful to attempt to test the new set-up consisting on the two-colour orthogonal set-up with an elliptical fundamental field added. An interferometer can be done in order to compensate both fundamental and second harmonic wave and therefore superimpose them. The same study could be lead using comparable  $\omega$  and  $2\omega$  energies. Studying HHG for non-monochromatic fields with variable polarisation will provide further clues to the physical mechanism of the cut-off and allow the manipulation of the resulting spectra. Non-collinear polarisation configurations seem to produce mixing signals that are equally or even more intense that the harmonics of linearly polarised monochromatic fields. An example is presented on figure 3.57. The interferometer and the gas cell are represented.

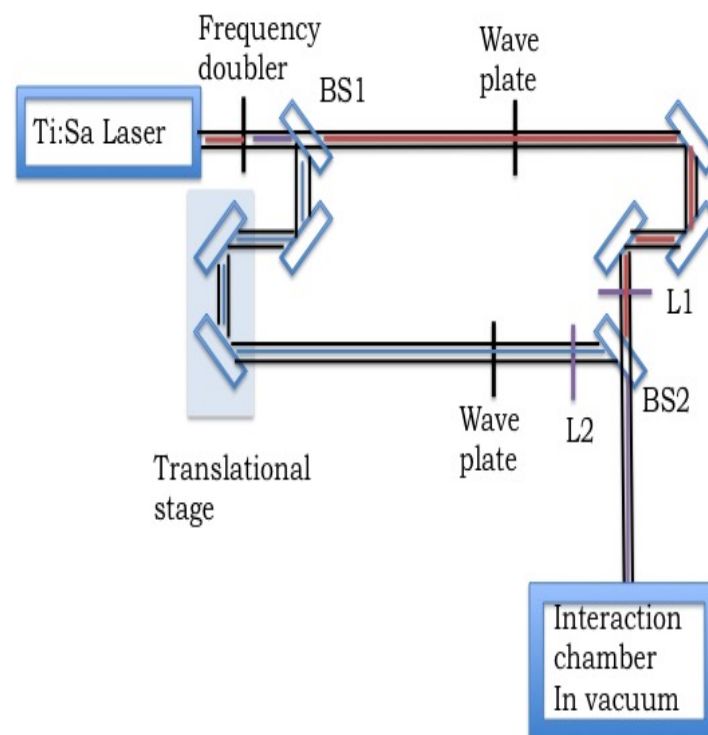


Figure 3.57: Example of a pump-probe experiment that can be used to adjust the delay between both fields and their relative intensity

By varying the relative phase between the generating beam and its harmonic, control over the chirp of attosecond pulses and the enhancement of a portion of the spectrum becomes possible.

Reaching this point on the manuscript a polarisation study on the two colour field HHG is achieved. Comparative theoretical methods were presented with no

exact theory but with a significant improvement in the knowledge of the physical atomic phenomenon.

The goal is to have circular polarised radiation to excite the M edge of the Cobalt and therefore be able to realise magnetic structure imaging. At this point our samples need to be made and characterised as it will be explained in chapter 4.

---

## Preparation and characterisation of samples containing magnetic nanostructures

---

---

### Contents

---

<b>4.1 Optical Activity and Light Polarisation . . . . .</b>	<b>138</b>
4.1.1 Optical rotation . . . . .	139
4.1.2 Circular Dichroism . . . . .	140
4.1.3 Ellipticity . . . . .	146
<b>4.2 Ultrafast demagnetisation . . . . .</b>	<b>146</b>
4.2.1 Magnetic Optical Kerr Effect (MOKE) . . . . .	147
4.2.2 Magnetic Optical (MO) Faraday Effect . . . . .	149
<b>4.3 Sample design . . . . .</b>	<b>152</b>
4.3.1 Reaching the magnetic behaviour information . . . . .	153
<b>4.4 Measurements at BESSY-II . . . . .</b>	<b>155</b>
4.4.1 BESSY-II End Station . . . . .	156
4.4.2 Experimental Method . . . . .	159
4.4.3 Experimental data - Magnetic properties of the sample . . .	161
4.4.4 Conclusions . . . . .	165
<b>4.5 Further developments . . . . .</b>	<b>166</b>

---

Matter and radiation have a peculiar interaction. The world we know macroscopically follows different physical laws from the microscopical which is actuated by quantum mechanisms. Being of harder access the study is rewarding since it encloses the primary behaviour of atoms and his constitutes. One of this manifestations is magnetism. Magnetism is defined as a physical phenomenon that occurs normally in nature in uncharged materials, that is materials not subjected to any external force known as ferromagnetic materials. The global phenomenon is not totally understood and its study engages an advance in our comprehension of fundamental physics.

In the previous chapter I have presented the development of a High Harmonic source of electromagnetic radiation at *Laboratoire d'Optique Appliquée (LOA)*. This fully coherent source delivers soft-X-ray pulses in the femtosecond time-scale and with a light polarisation vector control. The intensity at the optimised short wavelengths from 17 to 41 nanometers, translates into the energy range of 30 to 72 eV. This range is in concordance with the M absorption edges of known ferromagnetic materials such as iron (Fe), Cobalt (Co) and Nickel (Ni). The study of the absorption edges is crucial for the knowledge of the elemental properties and such kind of studies have been performed already at the K and L edges. These electronic shells are predominantly actuated by X-ray radiation and have been studied recently in large facilities such as synchrotrons.

In this chapter I will present a study of the characteristics of the sample and the adjustment of the magnetic nano structures in order to introduce the demagnetisation thematic. A sample will be then prepared at a specialised laboratory (LCPMR) being suitable to exhibit significant magneto-optical behaviours in response to the action of the source developed. It will be analysed both with a large facility and the instrumentation we have developed previously.

## 4.1 Optical Activity and Light Polarisation

Optical activity is a property exhibited by certain media and which consists on the alteration of the light vector when traversing them. This property is observed either for absorption and refraction. For the above referred media different phenomena can be included in this domain, optical rotation, circular dichroism and

ellipticity.

An example of an active medium is a solution of molecules that do not present a plane of symmetry an inversion centre or improper symmetry axes, such a material is known as a *chiral molecule*. Chirality is present in our everyday life in the forms of sugars, amino-acids and most other bio-molecules. They all come in two different forms called enantiomers meaning they are mirror images of one another hence presenting different properties. Figure 4.1 represents these structures.

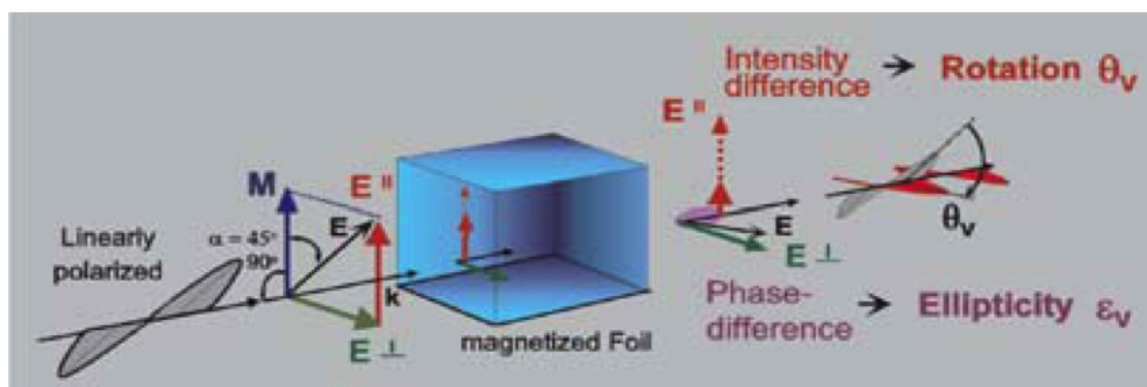


Figure 4.1: Linearly polarised light upon transmission through a sample with magnetic moment perpendicular to the light direction. The phase difference between the electric field components leads to ellipticity; the dichroism in the absorption leads to an intensity difference and thus to rotation of the polarisation plane after the sample [12]

#### 4.1.1 Optical rotation

A monochromatic linearly polarised light beam can be considered as the sum of two circularly polarised electromagnetic waves propagating in the same direction with the same frequency and with an opposite sense of rotation. A media that presents optical activity exhibits a slightly different refractive index for left and right-hand circularly polarised light. Thus since the two components are not absorbed they present different travel speeds through the medium and the resulting wave can be rotated by the insertion of a phase shift between its two components. In the case of a solution of chiral molecules given as example on the last section the rotation angle is proportional to the path length through the medium and the concentration. In the presence of a magnetic field all the molecules present optical activity. Therefore a rotation of the polarisation of the light traversing a medium

actuated by a magnetic force. This Faraday effect is one of the first discoveries of a relation between light and electromagnetism.

### 4.1.2 Circular Dichroism

The other phenomenon falling in the category of optical activity and light polarisation is *circular dichroism (CD)*. It is a measure of absorption of circular polarised light. The electronic absorption spectrum is recorded with left-hand circular and right-hand circular light polarisation which differ slightly from one another. Plotting the difference between the two absorption spectra we obtain the CD spectrum.

#### Circularly Polarised Light

The two forms of circular polarisation of light (left or right) are mirror images of each other. We consider only the electric field component of the electromagnetic wave. If we superimpose (add) two linearly polarised electromagnetic waves with the same amplitude and frequency (wavelength) but where the electric field vector in the one case oscillates in the  $xz$  plane and in the other case it oscillates in the  $yz$  plane and supposing that the waves propagate in the  $z$  direction and if the two waves have a phase shift of exactly one quarter of the wavelength: we obtain a light wave where the resulting electric field vector at any point along the  $z$  direction turns around on a circle either clock-wise or anti-clock-wise. This is why we call this light wave circularly polarised. An example is shown on Figure 4.2

#### Biological Circular Dichroism

Circular dichroism is only observed on chiral molecules. The two forms of chiral molecules, *enantiomers* have the same properties: mass, volume, chemical reactivity however they are not the same. They are optically active. The two forms of circularly polarised light interact slightly differently with a chiral molecule which causes the circular dichroism. A difference in interaction of the two forms of circularly polarised light with an enantiomer of a chiral molecule also causes the optical rotation which was explained above.

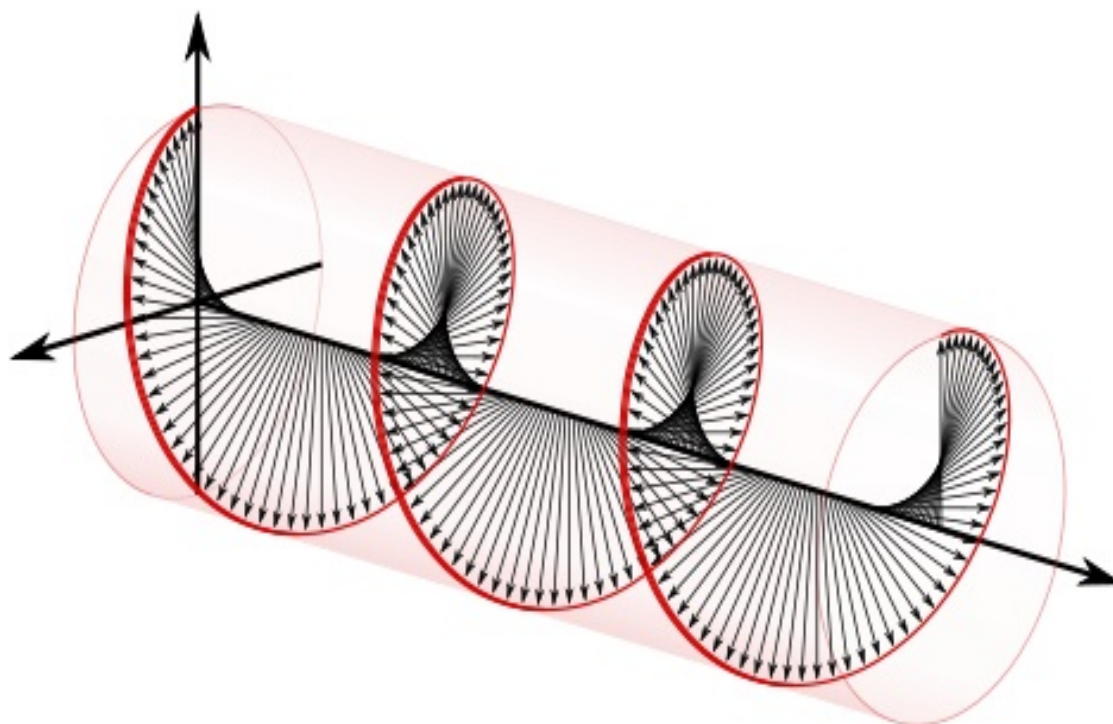


Figure 4.2: Scheme of circular polarised light. [13]

As an example, consider the molecule "Hexahelicene". Its chemical formula is shown below on the left (Hexa because of the 6 six-rings). The molecule adopts a helical shape as shown in the middle, otherwise the atoms at the ends of the molecule would get too close. There are two possible forms: a left-handed helical form as shown below ("M" for "Minus"), or the mirror image which has a right-handed helical shape (not shown. This molecule is named (P)-Hexahelicene, with "P" for "Plus"). Because of its helical shape, the molecule is chiral. It has a very intense CD spectrum shown on Figure 4.3

In green is the experiment and in red is the results of the computation.

The study of DNA being the brick of life is of utmost importance. DNA is by nature a chiral protein. It can adopt different conformations A-DNA, B- DNA and Z-DNA. The distance between two subsequent base pairs along the helical axis is called helical rise (h).The pitch (p) is the length of the helix axis for one complete helix turn. The turn angle per nucleotide or twist angle (t) is given by  $360^\circ /$  number of nucleotides per turn. C2'-endo and C3'-endo are descriptions of sugar conformations. The most frequently occurring nucleic acid model conformations

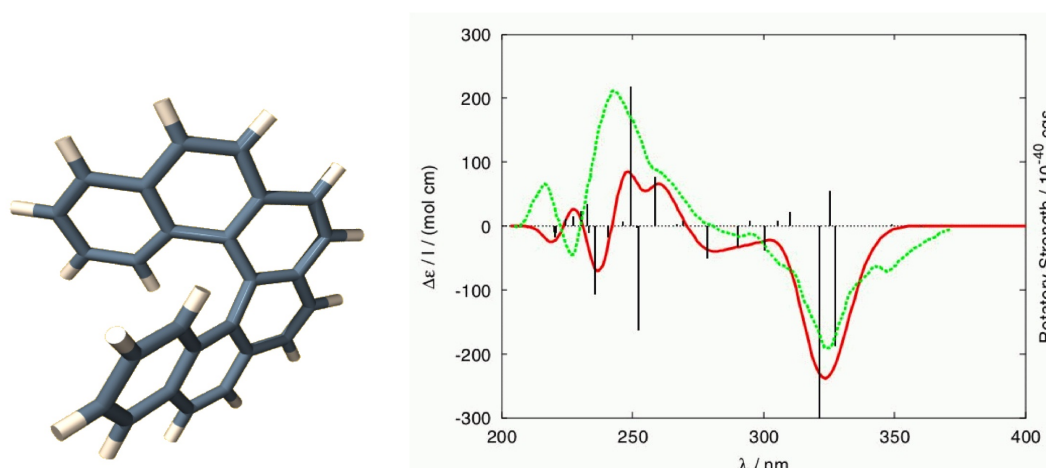


Figure 4.3: Chiral molecule a) (M)-Hexahelicene. b) Circular Dichroism (CD) Spectrum of (M)-Hexahelicene.

are characterised by the following geometrical parameters :

- A-DNA: right-handed helix; sugar pucker: C3'-endo; number of nucleotides per pitch: 11; h: 2.56 ; t:  $+32.7^\circ$ .
- B-DNA: right-handed helix; sugar pucker: C2'-endo; number of nucleotides per pitch: 10; h: 3.38 ; t:  $+36^\circ$  .
- Z-DNA: left-handed helix; G: syn conformation; sugar pucker: C3'-endo; C: anti conformation, sugar pucker: C2' endo; number of nucleotides per pitch:  $6 \times 2$ ; h:  $3.7 \times 2$  ; t=  $-30^\circ \times 2$  (for Z-DNA the repeat unit is the dimer (G-C).

And example is shown of Figure 4.4.

CD spectroscopy is an useful method since it is quick and does not require large amounts of proteins or extensive data processing. However for biological studies many proteins are embedded in membranes in their native state. Solutions containing membrane structures are often strongly scattering meaning that the CD is sometimes measured in thin films. CD gives less specific structural information than X-ray crystallography and protein Nuclear Magnetic Resonance (NMR) spectroscopy. Biological CD will not be studied during this work. This leads us to the next big group that can be sensitive to the polarisation of light: *magnetic materials*.

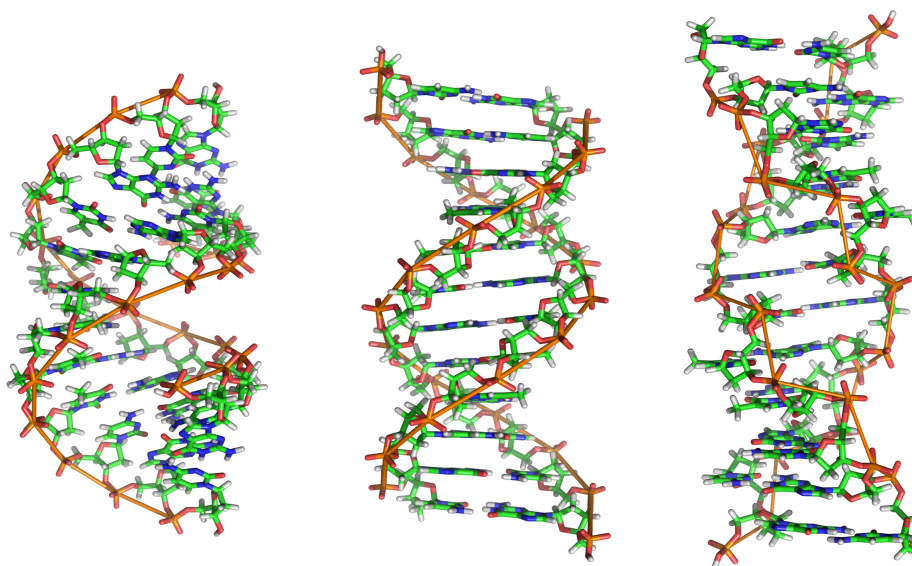


Figure 4.4: DNA configurations a) A-DNA b) B-DNA, right hand c) Z-DNA, left hand.

### Magnetic Circular Dichroism

*Magnetic Circular Dichroism (MCD)* is apparent when in the presence of a magnetic field the difference between the left circularly polarised light and the right circularly polarised light no longer interact equivalently with the absorbing medium as happens in natural CD. Natural CD is due to the molecular stereochemistry while MCD is due to magnetic optical activity that is a property of all matter. During my work I have been focused in this group, studying MCD, more specifically on the X-ray and Soft-x-ray range with various energies and time resolutions.

On the x-ray range we refer to this phenomenon as the *X-ray Magnetic Circular Dichroism (XMCD)*.

XMCD separates spin and angular component of the total magnetic moment in:

$$m_s \approx A - 2B \quad (4.1)$$

$$m_O \approx A + B \quad (4.2)$$

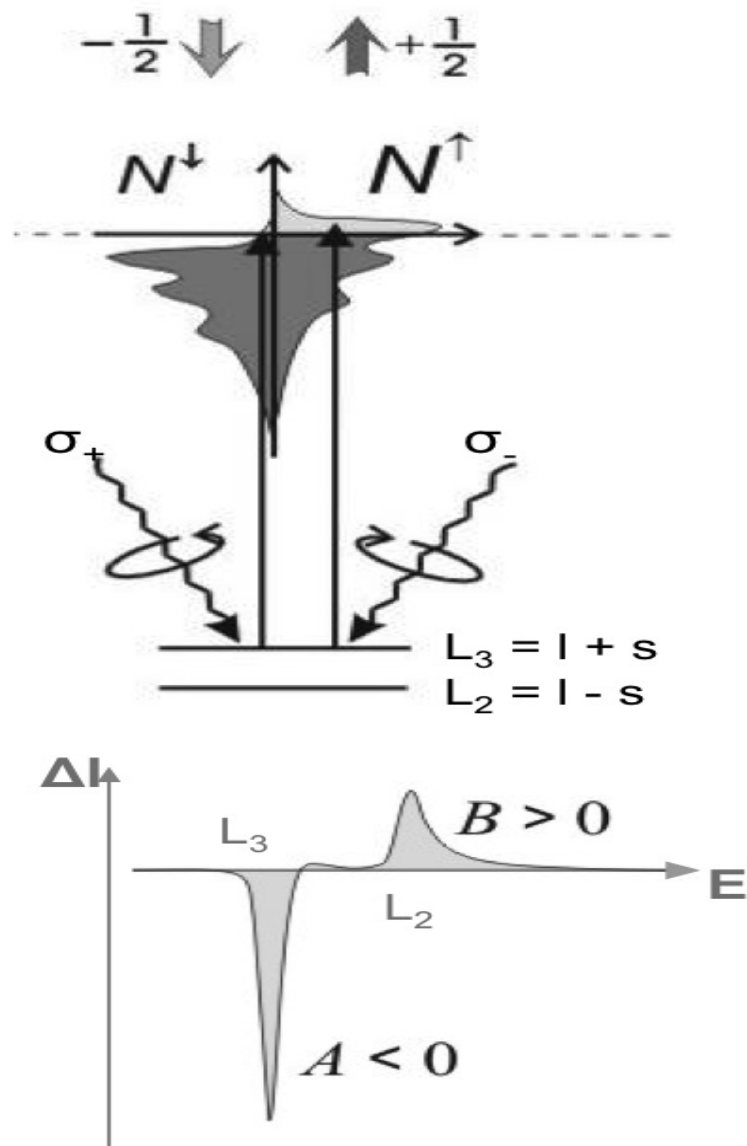


Figure 4.5: Electronic transitions in a conventional L-edge x-ray magnetic circular x-ray dichroism illustrated in a one-electron model. The transitions occur from the spin-orbit split 2p core shell to empty conduction band states. By use of circularly polarised x-rays the spin moment and orbital moment can be determined from linear combinations of the dichroic difference intensities A and B, according to other sum rules [12]

Figure 4.5 shows a representation of the atomic states and transitions for the L edge of a ferromagnetic material. The L-edge for Iron (Fe) is around 710 eV, for Niquel (Ni) is around 850 eV and for Cobalt (Co) is around 778.8 eV. The two main structures are called  $L_3$  (lower energy) and  $L_2$ . The two main peaks are due to the spin-orbit interaction of the 2p core shell and the total intensity of the peaks is proporcional to the number of unoccupied 3d valence states thus yields

quantitatively the total magnetisation. The X-ray absorption process yields a spin-resolved integration thus is spin dependent.  $L_3$  and  $L_2$  have opposite spin orbit coupling.

### Artificial Circular Dichroism

Circular Dichroism is a useful property and it has been used in soft-x-ray optics where the radiation cannot be manipulated with everyday regular optics. Examples of this are Multilayers and thin layers. Where the selectivity to the properties of the layer of interest can be obtained due to the element specificity of x-ray absorption resonances. The related resonant enhancement of the absorption coefficient enhances furthermore the sensitivity to the small quantity of material composing the thin layer. This behaviour is exemplified on figure 4.6.

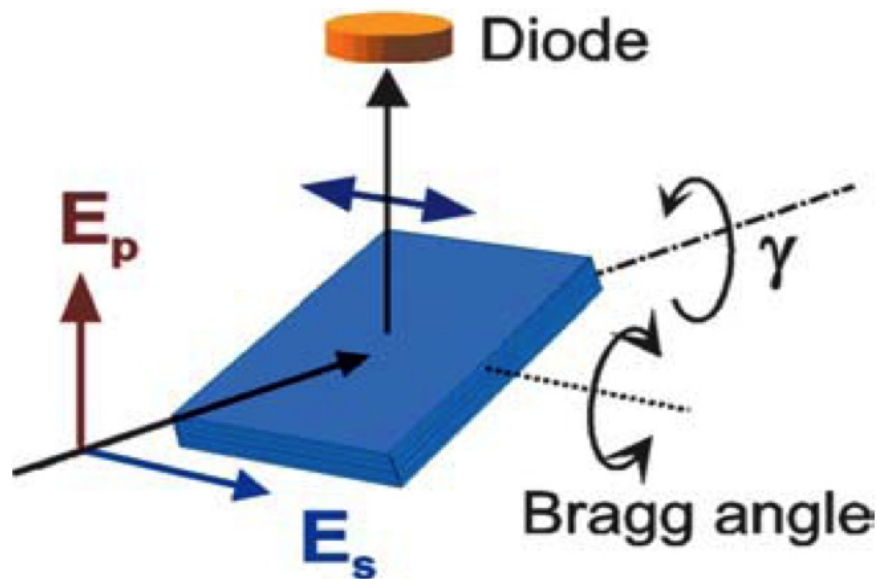


Figure 4.6: Example of a set-up of an X-ray polarisation detector based on a multilayer mirror. The polarisation studies are performed rotating the multilayer and the diode in the light axis, that is around the  $\gamma$  angle. The incidence is set to the Bragg which is close to the Brewster angle. [12]

Circular dichroism was studied during this thesis at LOA and LCLS using multilayers and thin layers produced at Institut d'Optique and LCPMR.

### 4.1.3 Ellipticity

Suppose we investigate optical rotation at a wavelength where the medium absorbs some of the light's intensity. Since a chiral medium absorbs left- and right-hand circularly polarised light differently (the CD effect), the amplitudes of the outgoing two circularly polarised components of the light beam are not equal anymore after they have passed through the absorbing chiral medium. They have a phase shift and a different amplitude. Because the elliptic polarisation results from the different absorption coefficients at that wavelength (or frequency) the amount of ellipticity is directly related to the strength of the circular dichroism. The difference is that the CD is obtained by considering the absorption of left- and right-hand circularly polarised light individually and then taking the difference. Ellipticity can be understood as being the result of doing the experiment with both light polarisations simultaneously (by starting out with linearly polarised light).

## 4.2 Ultrafast demagnetisation

The quest for faster and smaller means to store and process information magnetically prompts the study of elementary magnetisation dynamics. Magnetic storage devices use different patterns of magnetisation by setting the magnetisation vector of the magnetic nanometric domains either up or down [75]. One of the faster ways to reverse the magnetisation is to perform a precessional switching which englobes a external magnetic field applied orthogonally with an opposite direction of the domain magnetisation. The associated torque is used to control the magnetisation precessional motion and the reversal is achieved after several precessional oscillations [14]. A scheme is represented on figure 4.7.

Ultrafast demagnetisation was first discovered in 1996 [4] and it has been ever since a point of debate between the scientific community. Magnetisation phenomena occurring in a femtosecond time scale and in a nanometer length scale are a perfect fit for the femtosecond laser high harmonic generation set-ups. This progress in laser technology gives us the ability to see magnetic domains with better spatial resolution and allows us to follow the temporal evolution.

This states the ground for the *Magnetical-optical effects (MO)* that are know

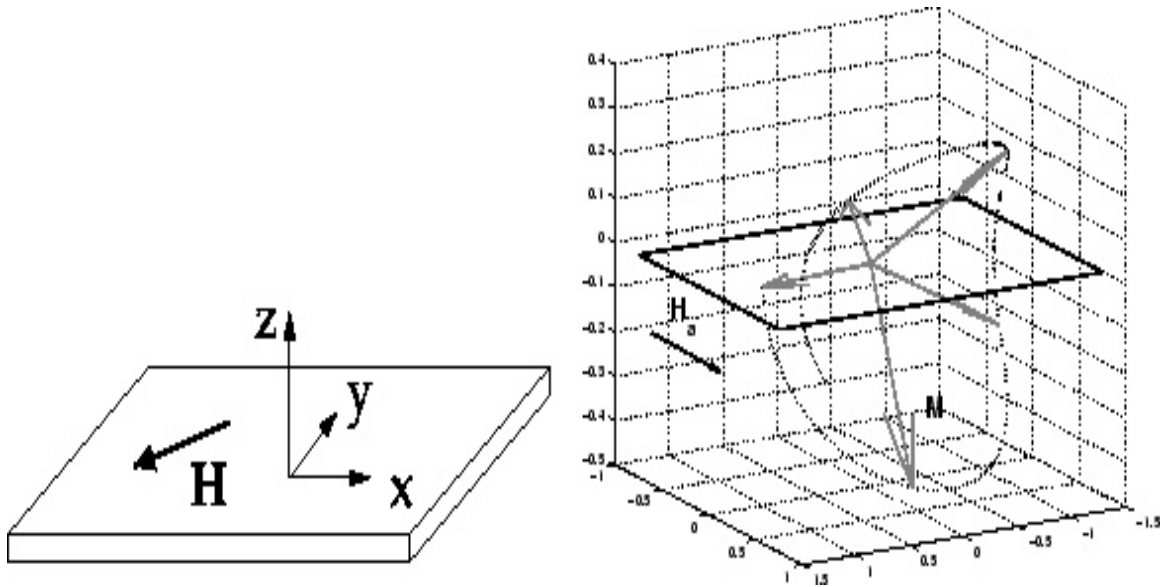


Figure 4.7: Example of precessional motion of magnetisation. [14]

for breaking the time-reversal symmetry and only the propagation of light, not the source of the magnetic field, is considered. MO effects are due to a propagation of an electromagnetic wave through a medium that has been altered by the presence of a quasi-static magnetic field, in this case by left and right elliptical polarisations propagate at different speeds.

Another characteristic of light is that when circularly polarised it has the capability of acting over a magnetic system in a similar way as an external magnetic field applied parallel to the wave vector of light. This is the so called *inverse Faraday effect*. The latter states that static magnetisation is introduced by an oscillating electric field such as an intense laser.

MO effects can be measured in transmission by means of the Faraday effect and in reflection the by means of the magnetical optical Kerr effect (MOKE). Figure 4.8 shows a table with a resume of the magneto-optical techniques. The Faraday effect and the MOKE will be presented on the following sections.

#### 4.2.1 Magnetic Optical Kerr Effect (MOKE)

The change in the polarisation state induced by reflection on a sample under a magnetic field is known as magneto-optical Kerr effect (MOKE) [76] [77] and has

Detection	Magnetic sensitivity	Light Polarisation	Transmission	Absorption	Reflection
Intensity measurement	$\langle M \rangle$	Circular	XMCD		XMRS
		Linear			T-MOKE
	$\langle M^2 \rangle$	Linear	XMLD		XMLD-type reflectometry
Polarisation analysis	$\langle M \rangle$	Linear	Faraday		Kerr L-,P-MOKE
	$\langle M^2 \rangle$	Linear	Voigt		

Figure 4.8: Survey of X-ray magneto-optical spectroscopy techniques, classified according to three criteria: (i) intensity measurement or polarisation analysis, (ii) using linearly or circularly polarised light, and (iii) dependence on magnetisation, i.e. sensitivity to  $M$  or  $M^2$ .

its origin in the modification of the dielectric properties of the material in the presence of a magnetic field. It can be described by a material parameter  $Q$ , the so-called Voigt constant. According to the direction of magnetisation vector with respect to the reflection surface and the plane of incidence, the MOKE can be categorised into three geometries, the polar MOKE, the longitudinal MOKE, and the transversal MOKE. When the magnetisation vector is perpendicular to the reflection surface and parallel to the plane of incidence, the effect is called the polar Kerr effect.

Figure 4.9 shows a scheme of the three types of MOKE geometries.

*L-MOKE*: In the longitudinal effect, the magnetisation vector is parallel to both the reflection surface and the plane of incidence. The longitudinal setup involves light reflected at an angle from the reflection surface and not normal to it, as above in the polar MOKE case. In the same manner, linearly polarised light incident on the surface becomes elliptically polarised, with the change in polarisation directly proportional to the component of magnetisation that is parallel to the reflection surface and parallel to the plane of incidence. This elliptically polarised light to first-order has two perpendicular  $E$  vectors, namely the standard Fresnel amplitude coefficient of reflection  $r$  and the Kerr coefficient  $k$ . The Kerr coefficient is typically much smaller than the coefficient of reflection.

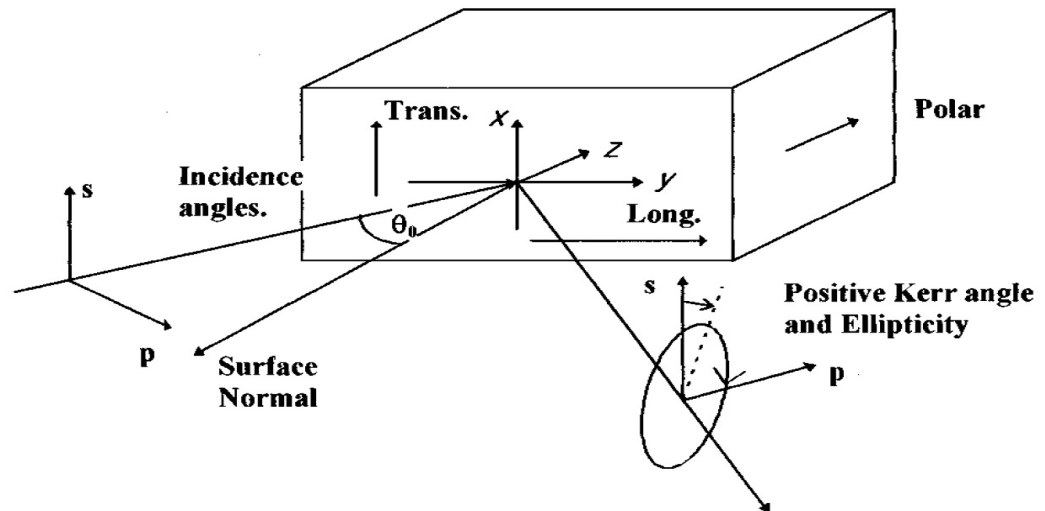


Figure 4.9: Schematic of MOKE geometry. [15]

*T-MOKE*: When the magnetisation is perpendicular to the plane of incidence and parallel to the surface it is said to be in the transverse configuration. In this case, the incident light is also not normal to the reflection surface but instead of measuring the polarity of the light after reflection, the reflectivity  $r$  is measured. This change in reflectivity is proportional to the component of magnetisation that is perpendicular to the plane of incidence and parallel to the surface, as above. If the magnetisation component points to the right of the incident plane, as viewed from the source, then the Kerr vector adds to the Fresnel amplitude vector and the intensity of the reflected light is  $|r + k|^2$ . On the other hand, if the component of magnetisation component points to the left of the incident plane as viewed from the source, the Kerr vector subtracts from the Fresnel amplitude and the reflected intensity is given by  $|r - k|^2$ .

#### 4.2.2 Magnetic Optical (MO) Faraday Effect

If any transparent solid or liquid is placed in a uniform magnetic field and a beam of linear polarised light is passed through it, in the direction parallel to the magnetic lines of force (through holes in the pole shoes of a strong electromagnet), it is found that the transmitted light is still linear polarised, but that the plane of polarisation is rotated by an angle proportional to the intensity of the field. This "optical rotation" is called the *Faraday rotation (or Faraday effect)* and differs in an important respect

from a similar effect, called optical activity, occurring in sugar solutions. In a sugar solution, the optical rotation proceeds in the same direction, whichever way the light is directed. In particular, when a beam is reflected back through the solution it emerges with the same polarisation as it entered before reflection. In the Faraday effect, however, the direction of the optical rotation, as viewed when looking into the beam, is reversed when the light traverses the substance opposite to the magnetic field direction; that is, the rotation can be reversed by either changing the field direction or the light direction. Reflected light, having passed twice through the medium, had its plane of polarisation rotated by twice the angle observed for single transmission. This behaviour is exemplified on figure 4.10.

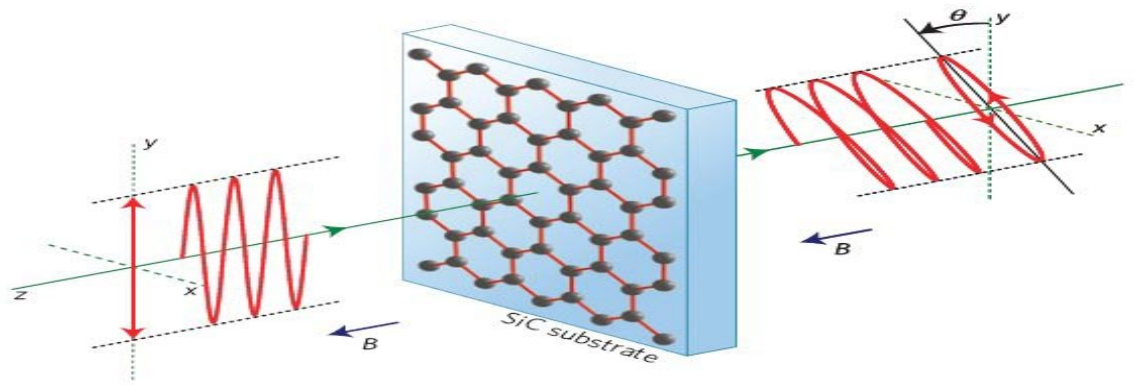


Figure 4.10: Scheme of a system showing Faraday rotation.

The incident linearly polarised light is the result of two polarised waves with opposite ellipticity. When an interaction occurs with a magnetic material the following optical constants can be written as:

$$n_{\pm} = 1 - (\delta_0 \pm \Delta\delta) + i(\beta_0 \pm \Delta\beta) \quad (4.3)$$

Where  $n_{\pm}$  corresponds to parallel/antiparallel orientation of the photon helicity and sample magnetisation,  $\delta_0$  the real dispersive part and the  $\beta_0$  the absorptive imaginary part for linearly polarised light.

The circular dichroism which corresponds to the difference for left and right circularly polarised light can then be written as:

$$\Delta n = n_+ - n_- = -\Delta\delta + i\Delta\beta \quad (4.4)$$

In polar geometry the incident linearly polarised beam can be written as a sum of equal amounts of left and right circular polarised light. The Faraday rotation  $\theta_F$  and the Faraday ellipticity  $\varepsilon_F$  can correlate on the following equation:

$$\left(\frac{1 - \tan \varepsilon_F}{1 + \tan \varepsilon_F}\right) e^{2i\theta_F} = e^{i\omega d_t (n_+ - n_-)/c} \quad (4.5)$$

where  $d_t$  is the transmitted thickness of the sample,  $d_t = d_0$  at normal incidence. The difference between  $n_+$  and  $n_-$  is generally small and gives the influence of the magnetisation.

The intrinsic dichroic material dispersive and absorptive components can be written by:

For an incident linearly polarised beam the ellipticity and the rotation angle of the transmitted light are related directly to the optical constants [12]:

$$\theta_F = (\omega/c)d\Delta\delta \tan \phi_i \quad (4.6)$$

and

$$\tan \varepsilon_F = (2\omega/c)d\Delta\beta \tan \phi_i \quad (4.7)$$

with  $\omega$  the frequency of the light,  $\phi_i$  the angle of grazing incidence and  $d$  the sample thickness.

At this point the Magnetic Optical effects are already covered and a system will be presented in order to be able to study and verify them in the laboratory. This starts with the choice and fabrication of the sample used presented in the following section.

### 4.3 Sample design

With all the magnetic optical effects explained in the last section it is now time to develop the experimental set-up aiming to retrieve this magnetic optical information. In 2004 S. Eisebitt *et al* [62] performed a technique of lensless imaging of magnetic nanostructures using high-resolution x-ray Fourier Transform Holography (FTH) with a sample consisting of a mask and a sample integrated in the same substrate. Figure 4.11 represents the sample structure used in this experimental step. The central element of this structure is a x-ray transparent SiN membrane represented in the figure in a darker shade. A thin magnetic film, is grown on one side of this membrane represented in the figure as the thin layer on the bottom. The x-ray opaque gold film grown on the other side of the membrane is structured using a Focused Ion Beam (FIB) and it is represented in the figure as the top thicker layer.

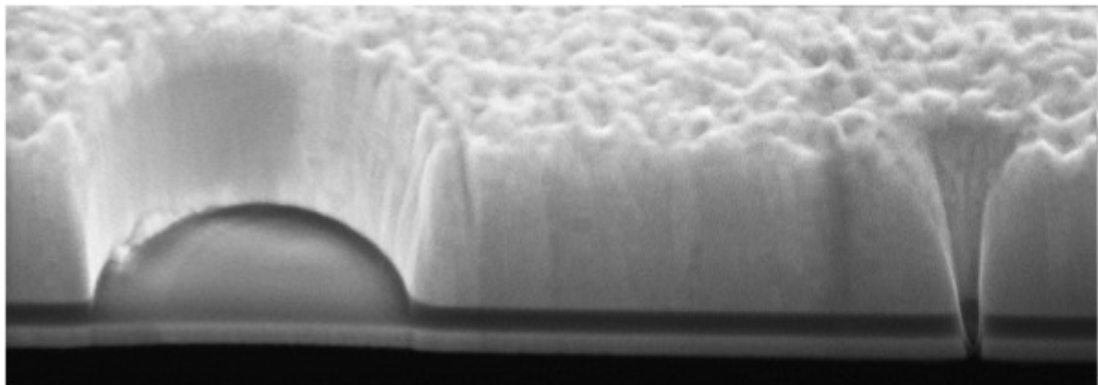


Figure 4.11: SEM image of the integrated mask sample structure patterned with a focused ion beam. This is the final sample structure to be used on further studies. The characterisation studies will only take charge of the magnetic multilayer component.

Since the FIB etches the gold film significantly faster than the SiN membrane selective cuts can be made and the sample can be resized onto a micron-sized aperture into the gold film without penetration of the SiN membrane. An therefore a second sub-micron sized aperture can be cut through the entire mask-sample structure. The first ablation corresponds to the area of the magnetic film that will be used in the experiment. The second one corresponds to the reference hole needed to complete de Fourier Transform Holography technique. In this set-up the reference hole sets the minimum spatial resolution. Therefore the diameter of the reference hole that gives birth to the reference beam should be as small as possible. At the LCPMR a methodology for the fabrication of small apertures can

provide samples with reference hole diameters as small as 20 nm on micron thick gold/SiN/sample multilayer structures.

The lower layer of the Figure 4.11 needs to be examined in order to access the magnetic properties. This is the work presented in this section and performed at the BESSY-II facility. Two magnetic elements are to be accessed, Iron and Cobalt. Their resonance energy at the  $M_{2,3}$  edge is placed at  $\approx 56\text{eV}$  for Fe and  $\approx 59\text{eV}$  for Co. Both elements are to be studied in transmission and reflection.

Four samples are to be characterised.

- sample R19 - Fe on 3nm Aluminium for reflection
- sample T466 - Fe on 3nm Al for transmission
- sample R9 - Co100nm on Al5nm on Si in reflection
- sample T9 - Co40nm one Al5nm on SiN 50 nm

The remaining sample is the standard Gold mesh (Au/Si) and it is labelled as R21. Since the absorption of Au in the  $M_{2,3}$  edge is higher than in the  $L_{2,3}$  edge the thickness has to be of around 100-200 nm. The representation of the sample is shown on figure 4.12

The magnetic multilayer structures prepared used in this manuscript were further used with for two different regimes. The nanosecond-picosecond regime at the synchrotron SOLEIL and FLASH Hamburg and the femtosecond regime at LOA and CEA and LCLS. These experimental data will be presented on chapter 5.

With the first step of sample design achieved let us follow for the characterisation part.

#### 4.3.1 Reaching the magnetic behaviour information

Reaching the  $M_{2,3}$  edge will allow us to have new information of the magnetic behaviour that can be seen using the two different techniques of Kerr Effect and

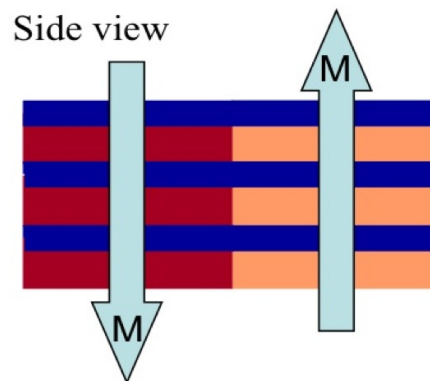


Figure 4.12: Representation of the arrangement of the sample used

the XMCD. This requires a sample with a good magnetic structure where the magnetisation and spin of materials can be measured using a radiation source of around 20nm. For this step the study of the photon energy dependance around the  $M_{2,3}$  edges in scattering based imaging is made by retrieving the real and imaginary part of the material's refractive index that contribute to the scattering cross section. The total photon energy dependance of the image contrast is complex.

Imaging the test samples presented in the last subsection in a synchrotron will enable to characterise qualitatively a part of the switching process. Its final state will be recorded thus allowing to develop the correct equilibrium between the pump power and the magnetic switching. Controlling the pump power and exploring the influence of the variation of the pump pulse on the all-optical switching process can be addressed by this type of facility.

Addressing the study of  $L_{2,3}$  Edges can be done in large facilities such as BESSY-II, SOLEIL and LCLS. Imaging experiments at synchrotron radiation sources enable to correlate image contrast at the  $L_{2,3}$  edges and  $M_{2,3}$  edges. The  $L_{2,3}$  edges allow us to decompose the total magnetic moment in its spin and orbital component, which is not possible at the  $M_{2,3}$  edges due to the smaller spin orbit splitting of this core level.

With its fundamental covering the energy range of the  $L_{2,3}$  edges of the transition metals, the study of ultrafast magnetisation phenomena will certainly play a key role at that source as well.

The main problem of these facilities apart from being large and of difficult

access is the large time resolution.

The absorption of gold is significantly stronger at these energies than around the  $L_{2,3}$  edges. The small, grey filled apertures are cut selectively through the gold layer, stopping at the SiN layer, which protects the magnetic film grown onto the other side of the membrane. This effect can be studied with a nanosecond-picosecond time-resolution in a synchrotron and with a femtosecond time resolution at LOA, however, accessing the  $M_{2,3}$  edges of transition metals.

The x-ray polarisers have to be optimised since the sensitivity to the magnetisation is obtained through circular polarisation. To obtain right or left circularly polarised x-rays from the linearly polarised HHG source we will make use of the same dichroism effect used for imaging of the sample magnetisation. In this study sample characterising on optimised polarisers at BESSY-II is conducted using radiation absorption and reflectivity experiments.

#### 4.4 Measurements at BESSY-II

The time required in the synchrotron facility was used for experiments with synchrotron radiation to characterise resonant polarisers in order to investigate the resonant scattering cross section at the M edges of the 3d transition metals Iron (Fe), Cobalt (Co) and Niquel (Ni). All-optically switched magnetisation imaging of regions during exploration of pump power and duration dependence were also performed.

The aim of the proposed experiment is to measure for Cobalt the real ( $\delta$ ) and imaginary ( $\beta$ ) part of the refractive index ( $n = 1 - \delta + i\beta$ ) as well as their respective magnetic dichroism ( $\delta - \delta$  and  $\delta - \beta$ ) in the photon energy range covering their  $M_{2,3}$  absorption edges. This photon energy range has recently become of interest. While the smaller spin-orbit splitting of the  $M_{2,3}$  edges hampers quantitative analysis of a sample's magnetisation, their magnetic dichroism of around 10 allows nevertheless imaging of static magnetic domain structures and following of their magnetisation dynamics. One shortcoming of currently developed FEL sources for magnetism research is their linear polarisation, while a (high degree of) circular polarisation is desirable for experiments investigating a sample's magnetic

properties. To qualitatively evaluate schemes for modifying the X-ray polarisation in this photon energy range (by absorption, resonant or non-resonant reflection) exact knowledge of the optical parameters is required, which is proposed here to be obtained experimentally. This knowledge will furthermore allow to select the optimal photon energy for experiments, where tuning of the photon energy is rather cumbersome.

The way to measure the index of refraction on materials in the XUV spectral range are based on the reflectivity and absorption of the sample. The method that is mostly used to extract the optical indexes lays down on absorption measurements and the following application of the Kramers-Kronig relations. This is rigorous therefore the measurements of the absorption must be precise. Hence its application to the absorption edges of the materials.

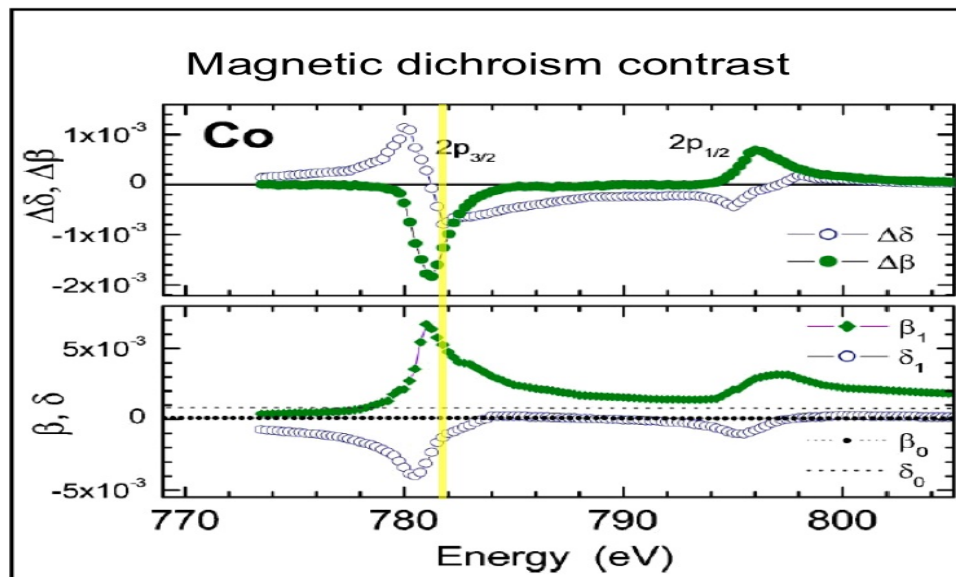


Figure 4.13: L-edge for Cobalt measured at BESSY [12]

#### 4.4.1 BESSY-II End Station

Changes in the state of polarisation occur depending on the effective index of refraction at the surface and the angles involved. At low VUV energies (say below 100 eV) acceptable reflectivity for use in synchrotron radiation beam lines is obtained at relatively steep angles of incidence. However, this causes significant polarisation effects. A typical example is the BESSY UE112 undulator [16] operating in first harmonic between 8 eV and 250 eV. Controlling the photon energy and ellipticity and

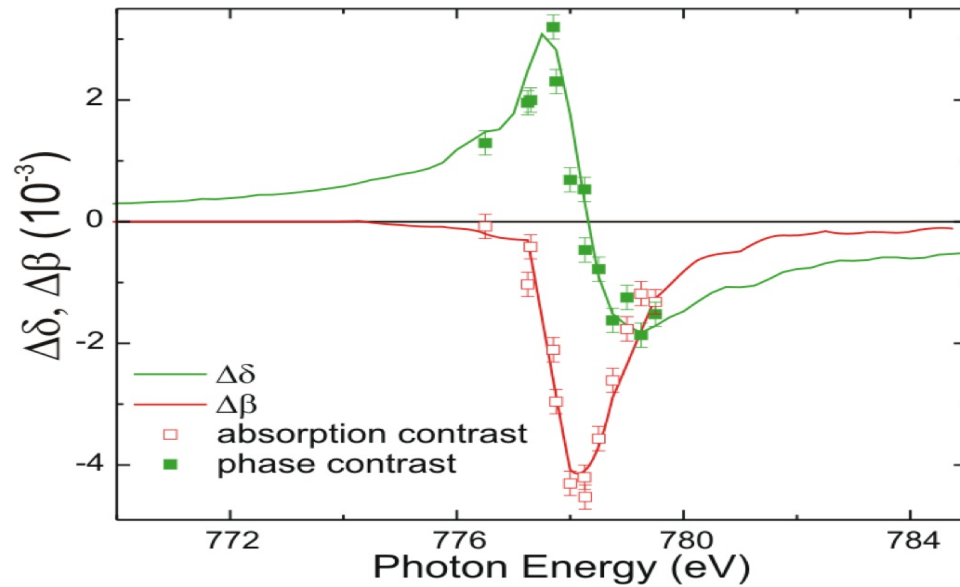


Figure 4.14: Refractive index shown for the L-edge in Cobalt measured at BESSY [12]

inclination of the polarisation ellipse requires three degrees of freedom. APPLE type undulators [16] using permanent magnets allow for shorter periods. The low susceptibility of the magnet material makes linear superposition of fields from different magnets a useful design approximation. APPLE undulators, too, provide the necessary flexibility provided all four rows are independently shiftable by  $s_1$ ,  $s_2$ ,  $s_3$ , and  $s_4$  as in UE112 (not to be mixed up by the Stokes parameters  $S_0$ ,  $S_1$ ,  $S_2$ , and  $S_3$  already introduced on the previous chapter). Shifting two diagonal rows into the same direction (row 3 and 4 in fig.1, parallel shift,  $s_3 = s_4$ ) controls the ellipticity of the polarisation ellipse. Shifting two diagonal rows into opposite directions (row 1 and 2, anti-parallel shift,  $s_1 = -s_2$ ) controls the inclination of the polarisation ellipse. The photon energy is controlled by a simultaneous shift of two rows next to each other with respect to the other two rows (row 1 and 3 with respect to row 2 and 4). However, at BESSY the control of photon energy is achieved by changing the gap, i.e. the separation between row 1 and 3 with respect to row 2 and 4. Linear superposition allows simultaneous and independent control of all three degrees of freedom. Note that in all cases the controls are not orthogonal, i.e. an adjustment of the polarisation of the radiation usually also changes the photon energy.

The UE112-PGM1 Beam end station has the following characteristics:

- Segment 12

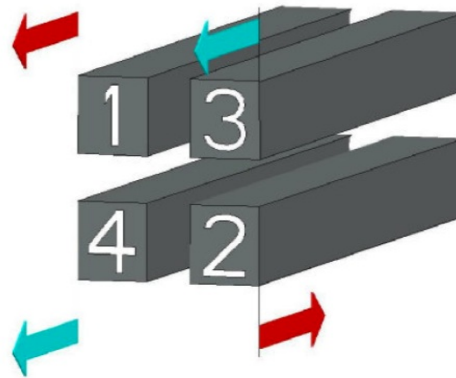


Figure 4.15: APPLE II undulator, schematic. Row 1 and 2 shift in opposite direction (dark arrows, anti-parallel shift,  $s_1 = -s_2$ ) which controls the inclination of the polarisation ellipse. Row 3 and 4 shift in the same direction (light arrows, parallel shift,  $s_3 = s_4$ ) which changes the ellipticity of the polarisation ellipse. [16]

- Location 14.2
- Source UE112
- Monochromator PGM
- Energy Minimum 20 eV
- Energy Maximum 700 eV
- Polarisation VARIABLE
- Flux  $> 10^{13}$  ph/s (20-100eV),  $> 10^{12}$  ph/s (100-300eV) (standard grating)
- Energy resolution 30,000 (10-150eV),  $> 20,000$  (150-350eV) (standard grating)
- Divergence horizontal 1.4 @ 63.5eV mrad
- Divergence vertical 0.5 @ 63.5eV mrad
- Distance Focus/last valve 1190 mm
- Distance Focus from floor level 1396, inclined mm

This characteristics allow the performance of Magneto-optical spectroscopy (in reflection, transmission):

- Resonant Magnetic Scattering (specular and diffuse)

- Intensity spectroscopy: MCD, LMD, Kerr-effect (L, T-MOKE)
- Polarisation spectroscopy: Faraday-, Voigt-effect

#### 4.4.2 Experimental Method

For realising the experiment the BESSY polarimeter was used, which is operated by a member of the BESSY team and which has been used intensively by him and others for characterising the intensity and polarisation of transmitted as well as scattered X-ray beams. The polarimeter is equipped with electro-magnets, which allow in-situ sample magnetisation in any required direction. Thin film samples on silicon wafers as well as SiN membranes will be grown sputtering. The first analysis will be of the XMCD signal for both circular positive and circular negative polarisations. We will start out with XMCD measurements, which will yield the imaginary part ( $\beta$ ) of the refractive index as well as its dichroism ( $\Delta\beta$ ). Although this is in principle a 'standard' measurement, it is experimentally challenging due to the weak strength of the  $M_{2,3}$  absorption resonances. This is also the reason while results from previous measurements [78] are not of sufficient quality for our purpose. Furthermore, this low oscillator strength in combination with the close proximity of the  $M_{2,3}$  edges to the strong valence electron absorption resonances prevents successful application of the Kramers-Kronig relationship, normally used to derive numerically the real part of the refractive index from the measured imaginary part. We will therefore characterise the optical properties of transmitted as well as reflected X-ray beams to obtain the real part ( $\delta$ ) of the refractive index as well as its dichroism.

The experiment was operated in ultra high vacuum ( $1 \times 10^{-8}$ ) and the system used to detect radiation was a GaAsP-diode with Keithley electrometer 617 (6514) controlled by speckle, the computer of the experiment which is a Personal Computer, measurement bus-extension, OS/2-operating system, with the data-acquisition software EMP/2.

On Figure 4.16 the optical layout of the beam line UE112 - PGM1 is represented.

A premonochromator optics: Mirror M1 is placed on the beginning of the line. It is a cylindrical mirror, with horizontal deflection  $2\Theta = 174^\circ$ . M1 is gold coated

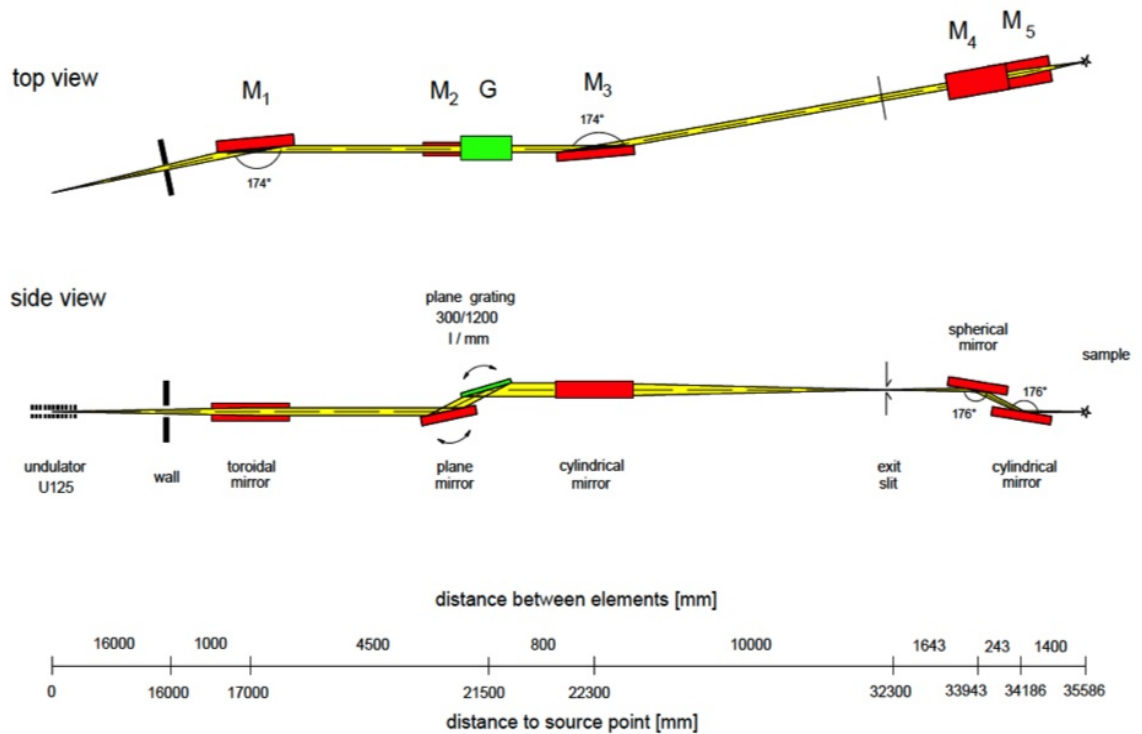


Figure 4.16: Optical layout of the beam line UE112 -PGM1 (schematic).

water cooled and with vertical and horizontal collimation. The monochromator has a variable deflection angle and collimated plane grating. Its optical components are the mirror M<sub>2</sub> and the Gratings G<sub>1-3</sub>. M<sub>2</sub> is a plane mirror with vertical deflection  $2\Theta = 169 - 177^\circ$ , gold coated and water cooled. The gratings are spherical with a vertical deflection  $2\Theta = 169 - 177^\circ$  also gold coated and water cooled. G<sub>1</sub> presents 300 l/mm for the range 15-600 eV. G<sub>2</sub> presents 600 l/mm for the range of 30 - 300 eV. Finally G<sub>3</sub> presents 1200 l/mm for 60-600 eV. An exit slit of 180 microns was placed before the focalising optics. The focalising optics are composed by the Mirror<sub>4</sub> and Mirror<sub>5</sub> in BESSY-II notation and have the following characteristics. Spherical mirror (M<sub>4</sub>), vertical deflection,  $2\Theta = 176^\circ$ , gold coated, vertical demagnification (1:1) of exit slit. Cylindrical mirror (M<sub>5</sub>), horizontal deflection,  $22\Theta = 176^\circ$ , gold coated, horizontal demagnification (12.1:1) of source. At the focus position with an exit slit of 100 microns the spot size obtained has  $92 \times 92 \mu\text{m}^2$  with a divergence at focus position 1.4 mrad (hor.) x 0.5 mrad(ver.) all this data were obtained at an energy of 63.5 eV. The last valve is DN 63 CF window valve and the focus position from last valve is 1190 mm. That means that the distance from the entrance aperture is 540 mm and 120 mm from the reflecting stage. The beam is inclined - going down at a rate of 1mm/430mm.

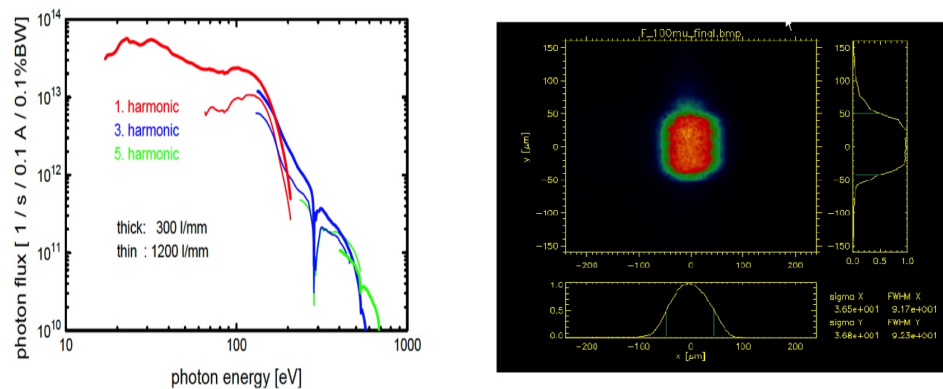


Figure 4.17: Source characteristics. Photon flux at UE112. Focal spot for 100 microns exit slit

In our experiment the focalisation of the beam was done by scanning the small diode D2 placed between the angles of Beta 90 and 270. An aperture of 0.5 mm diameter defined the size of the beam. The horizontal divergence was hence limited by the entrance aperture and the distance of the entrance aperture and it was approximately 0.9 mrad. The front end aperture limits the divergence to 0.11 mrad. Figure 4.17 shows the source characteristics such as the photon flux and the focal spot for a 100 microns exit slit.

#### 4.4.3 Experimental data - Magnetic properties of the sample

In order to stop unwanted radiation two metallic filters were used: Beryllium and aluminium. Both of the elements are fairly transparent for the radiation that we are trying to retrieve from the experiment. Figure 4.18 shows the experimental transmission for both Beryllium and aluminium.

Adding to this data we have the calibration of the system taken at the beginning of each round. For each shot the conditions of the synchrotron radiation are stored in the way we can correlate them more accurately. Figure ?? shows the calibration of the system for the different radiation polarisations used: linear in blue, circular positive in red and circular negative in green.

Placing the Co(40nm)/Al(5nm)/SiN(50nm) sample in the set-up set to transmission the XMCD effect can be seen as presented on figure ??.

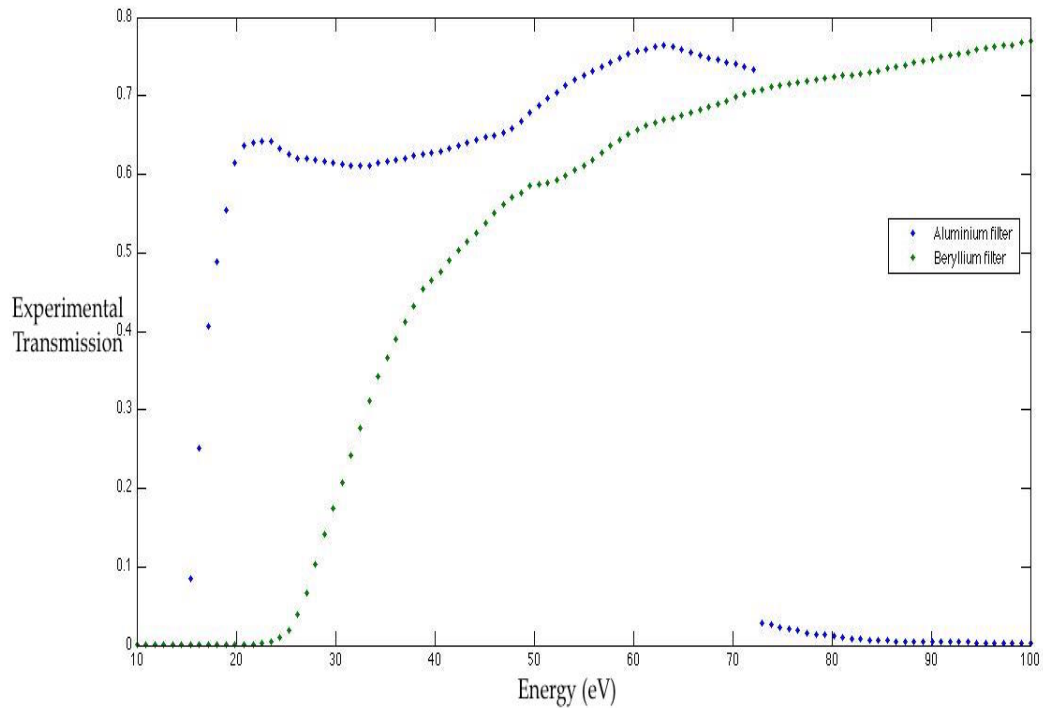


Figure 4.18: Examples of transmission of a foil of 0.2 microns of Aluminium (blue) and a foil of 0.2 microns Beryllium (red)

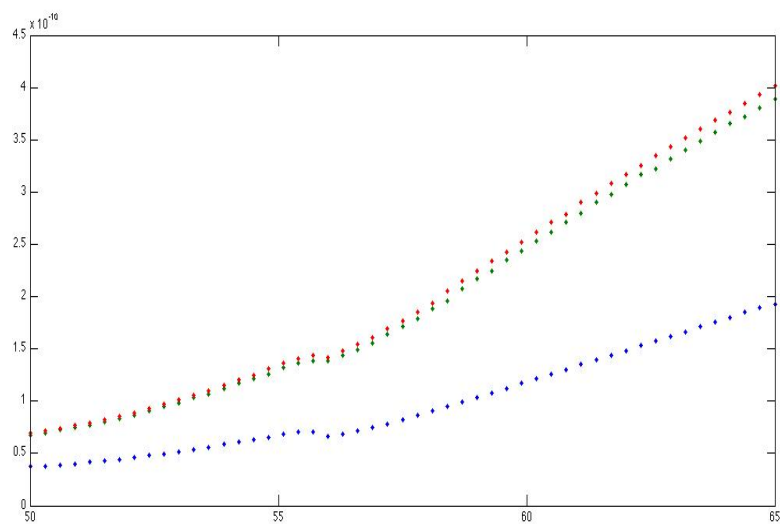


Figure 4.19: Calibration of the system for the different radiation polarisations, Linear (blue), circular positive (red), circular negative (green)

The transmission magnetic optical Kerr effect was also studied and it presented a strong signal. Acquiring the data at 59 eV demagnetisation was observed and

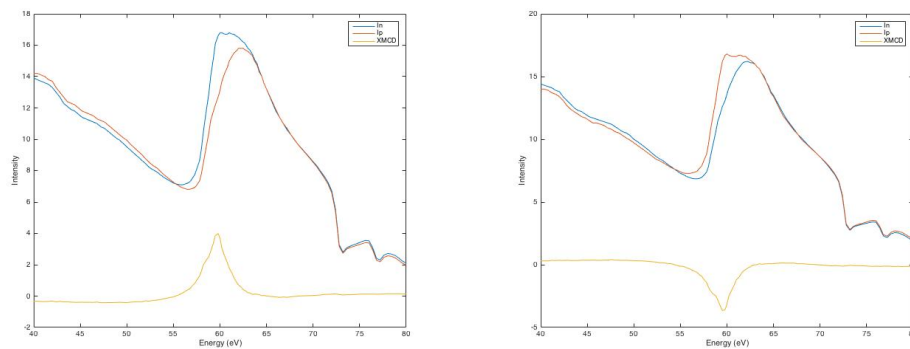


Figure 4.20: XMCD measurements on the Co(40nm)/Al(5nm)/SiN(50nm) sample. The angle of incidence was 30 degrees and the maximum signal can be seen at 60 eV as expected corresponding to the M-edge of Cobalt

it is represented on figure ?? and 4.22 A high demagnetisation of the sample is shown. The measurements were taken using a polar geometry which means that the magnetic vector is perpendicular to the sample.

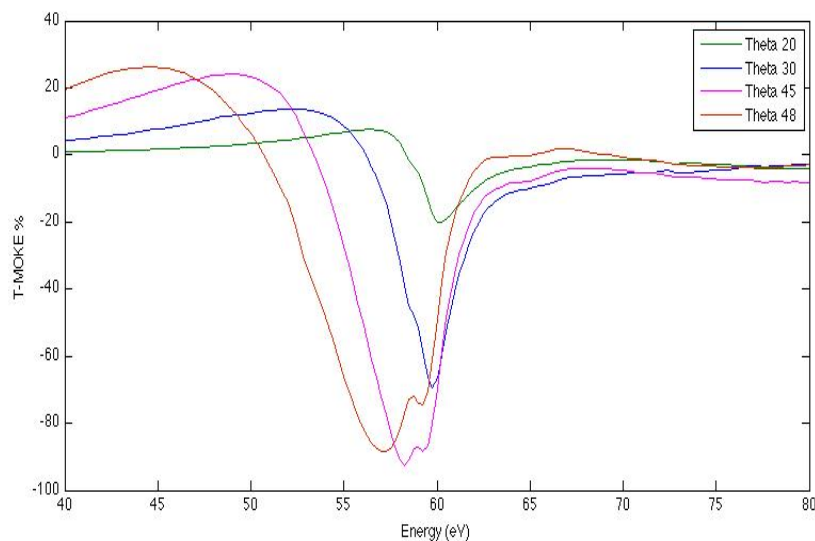


Figure 4.21: Signal in function of the polarisation of the incident beam (from s to p at an energy of 60 eV)

The XMCD effect is strong as expected around the M absorption edge of the Cobalt (60 eV). The measurement was done on transmission using a Co(40nm)/Al(5nm)/SiN(50nm) sample. In XMCD analysis the dichroism is measured. Dichroism is given by the asymmetry parameter  $A$  that is defined as:

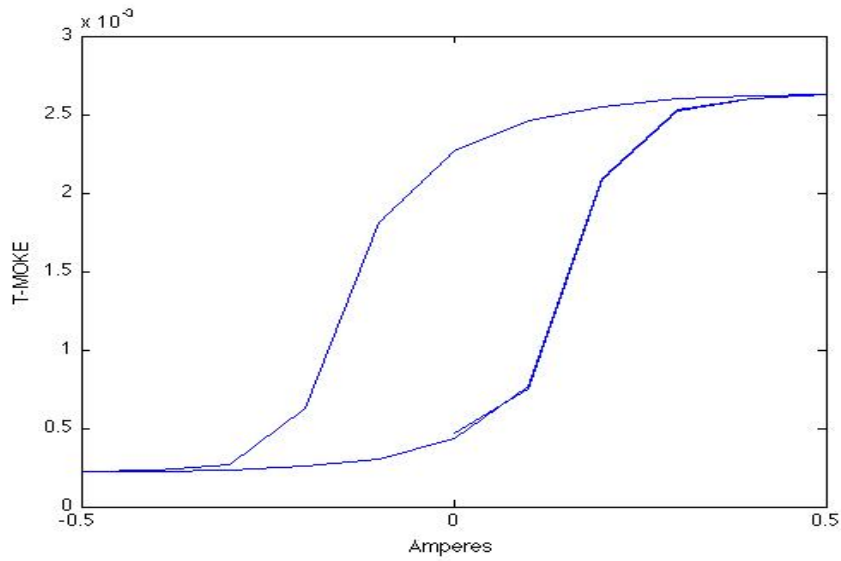


Figure 4.22: Raw data showing the hysteresis on the Co(100nm)/Al(5nm) sample using the T-MOKE geometry.

$$A = (T_+ - T_-)/(T_+ + T_-) \quad (4.8)$$

with  $T_-$  and  $T_+$  the transmission coefficients for left and right handed circular polarised x-rays. This asymmetry parameter is directly proportional to the faraday ellipticity  $\epsilon_F$ . In XMCD experiments the absorptive component ( $\Delta\beta$ ) of the refractive index can be retrieved and the dispersive component ( $\Delta\delta$ ) has to be derived from a Kramers-Kronig transformation.

In Faraday experiments, on the other hand, one measures both dichroic quantities ( $\Delta\delta$  and  $\Delta\beta$ ) in a single experiment with the advantage of using only linearly instead of circularly polarised light.

Therefore the magnetic Optical effects were studied as the the L-MOKE. These effects were not very pronounced especially the L-MOKE 4.23 but with the T-MOKE measurements we could access the demagnetisation of the Cobalt. The sample itself was changed now being a Co(100nm)/Al(5nm) on Si with 4 poles.

Magneto-optical effects are measured in reflection of linearly polarised x-rays. In polar geometry at normal incidence the Kerr rotation  $\theta_K$  and Kerr ellipticity  $\epsilon_K$  are given by:

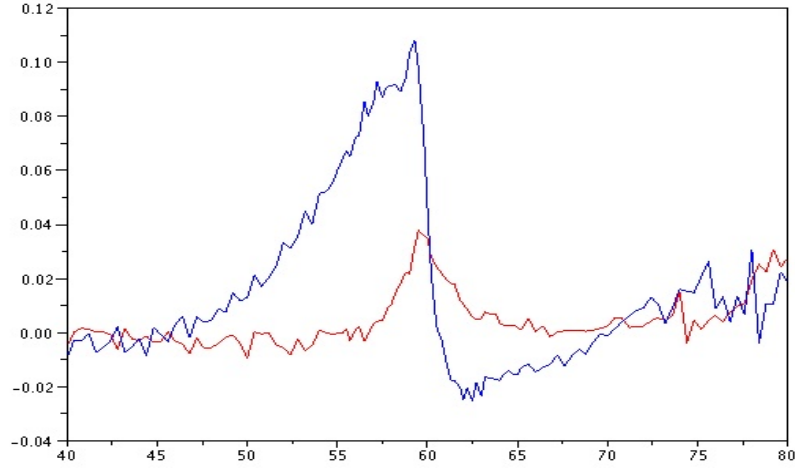


Figure 4.23: Longitudinal MOKE

$$\left(\frac{1 - \tan \varepsilon_K}{1 + \tan \varepsilon_K}\right) e^{2i\theta_K} = \frac{1 + n_-}{1 - n_-} \frac{1 - n_+}{1 + n_+} \quad (4.9)$$

Acquired data was treated dividing the spectra by the response of the system from where the absorption and reflection of the samples were subtracted. Applying the formulas written above we can find the dispersion and the absorption that the sample induced in the incident radiation. The representation is shown on Figure 4.24

#### 4.4.4 Conclusions

The proposed experiment yielded the real and imaginary part of the refractive index of the transition metal Co in the photon energy range of 30-100 eV, which covers the magnetically dichroic M<sub>2,3</sub> absorption resonances of this transition metal. Subsequent analysis of these data provided us to effectively recording high quality data for Co, Ni and other materials relevant for our x-ray laser experiments on ultrafast magnetisation dynamics. These data will serve two purposes. Firstly, they will allow us to optimise schemes for transforming the polarisation of linearly polarised X-ray beams to circular polarisation using resonance phenomena of these materials. Secondly, we will be able to optimise sample design and photon energy

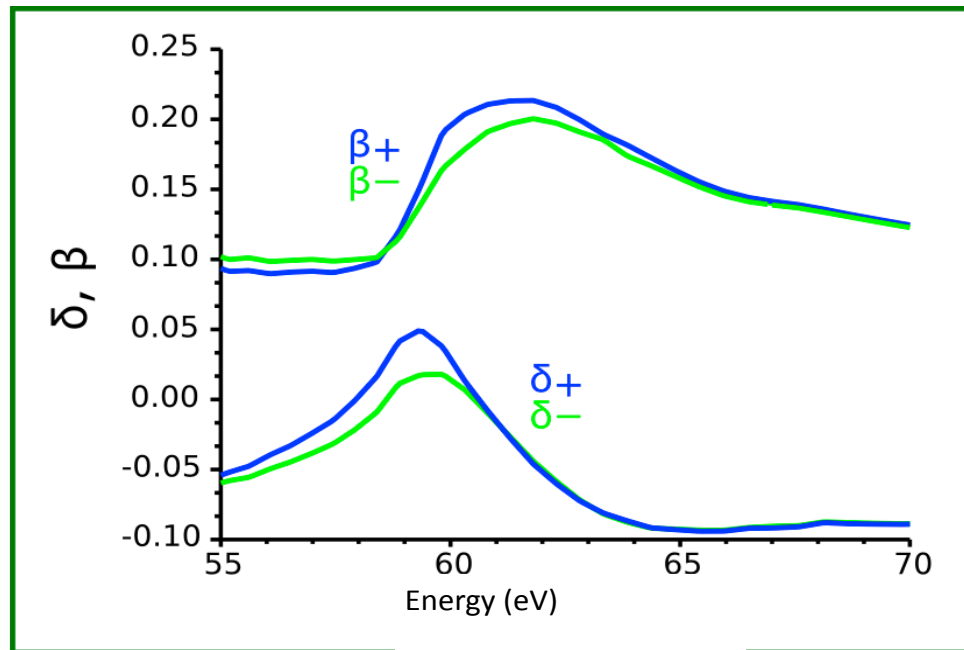


Figure 4.24: Measured dispersive ( $\Delta\beta$ ) and absorptive ( $\Delta\delta$ ) components of the refractive indices for Cobalt

choice for future experiments on ultrafast magnetisation dynamics at FLASH, the currently only operational X-ray Free Electron Laser. Both results will be crucial for experiments at FLASH, where an approach to X-ray Fourier Transform Holography [?] for time resolved imaging of magnetisation dynamics will take place on the femtosecond time scale.

## 4.5 Further developments

The point of the characterisation of the samples is to make the step from the large facility (BESSY-II in the case) to the LOA. Analysing the demagnetisation of the materials requires a high brightness, tuneable X-ray source covering the photon energy range of 30-100 eV with variable polarisation. Insertion devices with variable polarisation are therefore the only possible sources where the here proposed experiment could be realised. At LOA the experiment was also done as the following chapter will present.

Adjusting the parameters we can excite electrons in order to be able to perform table top diffraction and to measure the magnetisation curves

The magnetic nanostructures characterised on this chapter that can be study with our source. This source has been optimised as seen in previous chapters, chapter 2. The goal will be its study on a pump-probe set-up by diffraction and holography (chapter 5).

---

**Imaging of nanomagnetic structures by diffraction and study of the evolution of the demagnetisation**

---

**Contents**

---

<b>5.1 Magnetisation studies at LOA . . . . .</b>	<b>170</b>
5.1.1 Sample preparation . . . . .	170
5.1.2 Development of the tabletop set-up for the ultrafast demagnetisation experiment . . . . .	172
5.1.3 Ultrafast demagnetisation curves . . . . .	177
5.1.4 Comparison between the HHG source and X-FEL . . . . .	181
<b>5.2 Imaging of nanomagnetic structures by diffraction and study of the evolution of the demagnetisation . . . . .</b>	<b>183</b>
<b>5.3 Linac Coherent Light Source - LCLS . . . . .</b>	<b>184</b>
5.3.1 Single-shot magnetisation dynamic experiment at LCLS . . . . .	184
5.3.2 Single-shot diffraction patterns . . . . .	187
5.3.3 Conclusion . . . . .	192

---

Magnetisation phenomena occurring on nanometer length scale and sub-nanosecond time scale are one of the forefront research areas in solid state physics. Scientifically, these phenomena are challenging due to the often complex interplay of interactions spanning a wide range of strength and length scale. In addition, these activities are strongly motivated by the technological desire for ever smaller and ever faster magnetic devices. The realisation of non-volatile magnetic memory is a recent example, which has strongly influenced and vice-versa been strongly influenced by most recent research activities on spin-injection phenomena. The development of novel experimental tools has traditionally paved the way for new discoveries and thus dramatically influenced our scientific understanding. In the context of magnetism scientific discoveries and technological progress has always been influenced by the ability to see magnetic domain structures with higher spatial resolution and to follow its temporal evolution on shorter time scales. For example, magnetic domain structures with atomic resolution can be obtained today by spin polarised scanning transmission microscopy. And femtosecond lasers add ultra-fast time resolution to magneto-optical Kerr effect measurements [4]. Especially powerful are "multi-dimensional" techniques giving access to more than one property of a material. A recent demonstration of this has been when picosecond time resolution was successfully added to x-ray microscopy. This has given us movies showing the temporal evolution of a wide variety of magnetisation dynamics occurring on nanometer length and picosecond time scale. We note that while 15 nm spatial resolution has been demonstrated in x-ray microscopy, the spatial resolution routinely achieved in time-resolved imaging experiments is about 50 to 70 nm. The duration of synchrotron radiation pulses, given by the spatial length of the electron bunches circulating in the storage ring, is about 50 to 100 picoseconds. Schemes like the so-called low-alpha mode and femto-slicing can reduce the x-ray bunch length to picoseconds and even a few hundred femtoseconds, respectively. The inherent drastic reduction in intensity, however, inhibits so far their use for intensity demanding x-ray microscopy techniques. Pushing the time resolution for imaging of magnetisation dynamics from the picosecond to the femtosecond time scale while preserving sub 100 nm spatial resolution is a fascinating challenge. To achieve this we used laser based higher harmonic generation as ultrashort coherent soft x-ray source. Over the past years, the performance of these sources has developed tremendously. Most importantly is the push of the intensity cut-off towards 100 eV allowing to access the M<sub>2,3</sub> edges of transition metals; the achieved increase in longterm stability and fidelity, essential for pump-probe experiments; and the increase in pulse intensity making single shot imaging experiments possi-

ble. Pushing the time resolution down from the pico- to the femtosecond without deterioration of the spatial resolution or dramatic decrease of the available x-ray intensity will allow us to follow magnetisation dynamics on a time scale which has so far not been accessible.

## 5.1 Magnetisation studies at LOA

### 5.1.1 Sample preparation

As stated before the working range will be of the femtosecond and nanometer. At LOA a high harmonic generation source that provides electromagnetic pulses sub-100 nm and 40 fs was already put in place as described on the second chapter.

The HHG source is highly coherent also considering infrared pump-XUV probe experiments, the use of HHG offers jitter-free capability. It is ultrashort, table-top, tunable and more accessible than the FEL. On the down side it provided low flux of radiation. It was been tuned to cover the M-edge of transition metals as shown on figure 5.1.

The transition materials Iron (Fe), Cobalt (Co) and Niquel (Ni) have M-edges in the photon energy of respectively 54eV, 59.5eV and 66.5eV. Analysing figure 5.1 the content of Cobalt will create a bright peak at the energy of 60 eV that will match the absorption  $M_3$ . This will allow to see the magnetic dichroism associated. The sample presents alternating up and down magnetic domains aligned in stripes. When the XUV light reaches the sample diffraction will occur. Since the domains are in the same direction but with opposite magnetic domains the diffraction image will have two bright spots corresponding to the plus and minus first order diffraction peaks. The intensity will be given by  $I(q)$ . The distance to the centre of the image by  $q$ .

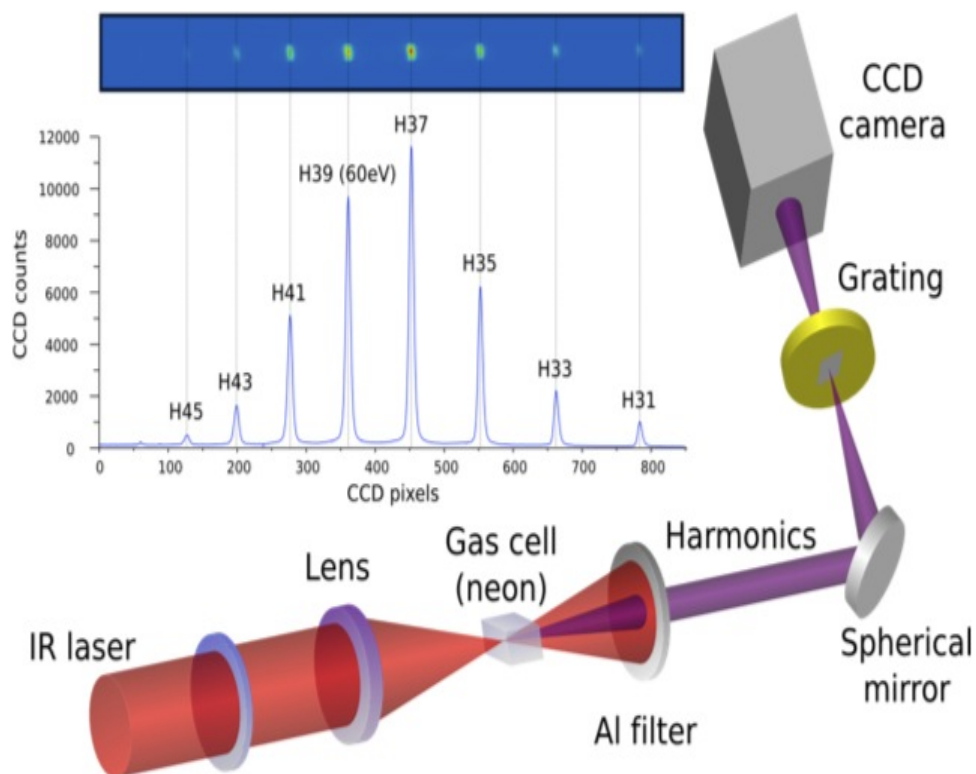


Figure 5.1: Magnetic force micrograph of the magnetic structures of the sample composed by Cobalt and Palladium. The magnetic domains presented are in aligned stripes alternating the up and down magnetic domains. The domains are in the same direction with an out-of-plane magnetisation.

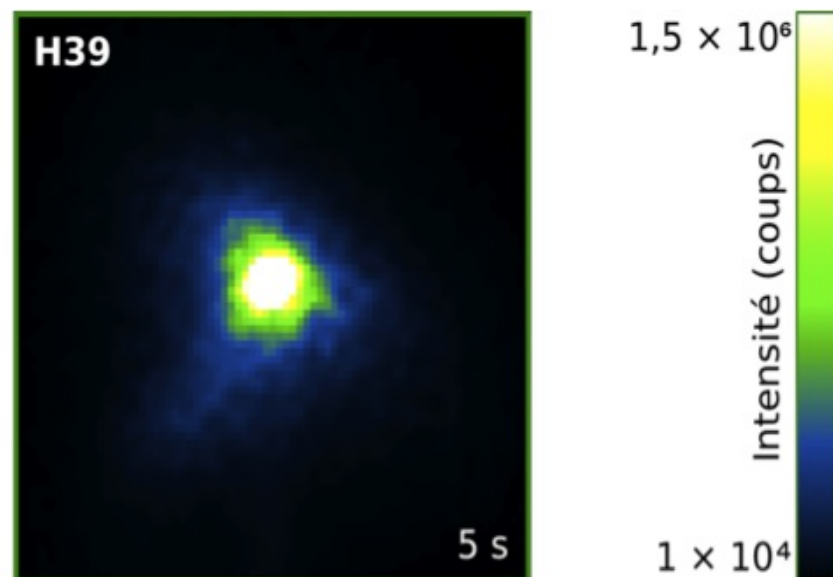


Figure 5.2: Cross-section of the beam spectrally filtered to keep only of the harmonic 39 in Neon corresponding to 60 eV

### 5.1.2 Development of the tabletop set-up for the ultrafast demagnetisation experiment

Ultrafast magnetisation is a result of the excitation of a sample by an intense femtosecond infrared laser pulse. This phenomena is not yet properly understood. The knowledge of magnetic domains magnetisation has been limited by the available radiation sources. The processes that make the macroscopically observed ultrafast demagnetisation phenomenon to be recorded require nanometer range and femtosecond resolution. Such processes are the transfer of angular momentum between electrons, spins and lattice and take place in nanometric length scale [4].

A high harmonic source can reach this goal and allow the visualisation for the first time of the demagnetisation itself. In order to do so a pump-probe experiment has been set. The pump will consist of the HHG tuned on to the M edge of the sample this will give rise to an XMCD effect persists and to magnetic scattering even when using linearly polarised harmonics. The pump will consist of a small fraction of an intense infrared laser pulse that drives the HHG process triggering the demagnetisation dynamics. These two beams will be directed onto a thin film exhibiting a nanometric domain structure. Figure 5.3 represents a scheme of the set-up.

This set-up will have a good spatial resolution and due to the fact that pump and probe originate from the same laser pulse the set-up is jitter free. As a result the demagnetisation dynamics can be recorded with a time resolution of 40 fs which is a breakthrough.

The pump-probe set-up is based on the Ti:sapphire laser (815 nm), delivering 5 mJ, 40 fs (FWHM), linearly polarised (horizontal) pulses at 1 kHz, presented before and on the previous section. Each pulse is split into a stronger part and a weaker part (pump) the ratio: 90% - 10 % using a beam splitter. The strong part is focused into a gas cell filled with neon (35 mbar) to generate high harmonics (probe) by non linear interaction between the laser and the gas. The pump beam goes through a delay line (step size of 3 fs) and is focused (focal spot of  $150\mu\text{m}$  in diameter) to excite the sample. The fluence of the pump beam can be adjusted and the size of the focal spot ensures an uniform illumination across one membrane. The delay line can be seen on figure 5.4.

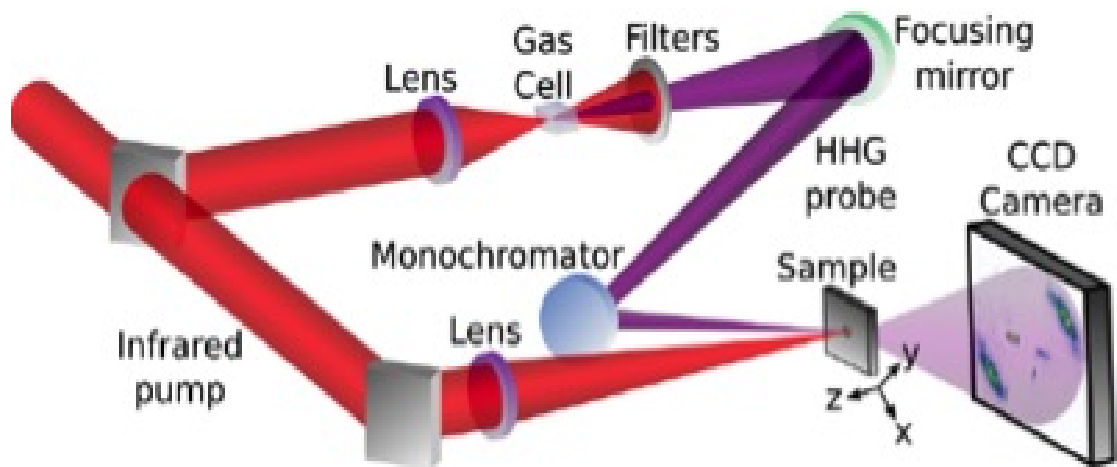


Figure 5.3: Pump probe setup. An intense IR laser pulse is split by a beam splitter resulting on a pump beam and a probe beam. The probe beam is focused by a lens onto a gas cell resulting in high harmonic generation. The IR is filtered and the remaining beam is reflected on a focusing mirror onto a monochromator onto the sample. The pump is directed onto the sample and focused by means of a lens. A CCD camera records the data.

The sample used will be a multilayer film  $[\text{Co}(0,4 \text{ nm})/\text{Pd}(0,6 \text{ nm})]_{30}/\text{Al}(30 \text{ nm})/\text{Si}_3\text{N}_4(30 \text{ nm})$  the multilayer is deposited by magnetron sputtering on a 30 nm thin  $\text{Si}_3\text{N}_4$  multi-membranes (squares of 50 microns by 50 microns) chip. The 30 nm Al layer is used to enhance heat dissipation and to avoid oxidation a 2 nm thick cap layer was added. The sample is demagnetised so as to present an aligned stripe domain state with an in-plane oscillating magnetic field. This structure of aligned stripes acts as a diffraction grating for the resonant soft X-rays ending in plus or minus first order diffraction peaks. A scheme of the sample is presented on the figure 5.5.

The temporal evolution of the scattering pattern thus reveals the evolution of the magnetic domain structure on the nanometer length scale during the demagnetisation process. The achievable spatial resolution is in principle only limited by the wavelength employed and magnetic domains as small as 60 nm are easily detected.

The sample and CCD are placed inside the third chamber as shown on figure 5.6.



Figure 5.4: Image of pump-probe set-up at salle orange. The intense IR beam is split in two at the beginning of the table. The non covered beam is the pump and the probe will be in vacuum. When the probe beam crosses the first chamber containing the gas cell harmonics are generated here portrayed in light blue. The IR will be filtered by a metallic filter and the probe will be mainly XUV radiation.

The harmonic light elastically scattered by the magnetic domain structure of the sample is collected by a PI-MTE CCD camera (Princeton Instrument) located 4 cm behind the sample and protected from any infrared light by an aluminium filter. This foil is supported by an Ni mesh which appears as a grid on the scattering patterns. The CCD pixels have been binned 4 by 4 yielding a pixel size of 54. The time resolution of this experiment is less than 45 fs (FWHM), which is set predominantly by the infrared pulse duration (40 fs). This happens because the harmonic pulses are shorter and it is a jitter-free set-up.

The CCD camera will record the scattered intensity  $I(q)$  that is proportional to  $|S(q)|^2$  with  $q$  the wave vector transfer and  $S(q)$  the Fourier transform of the

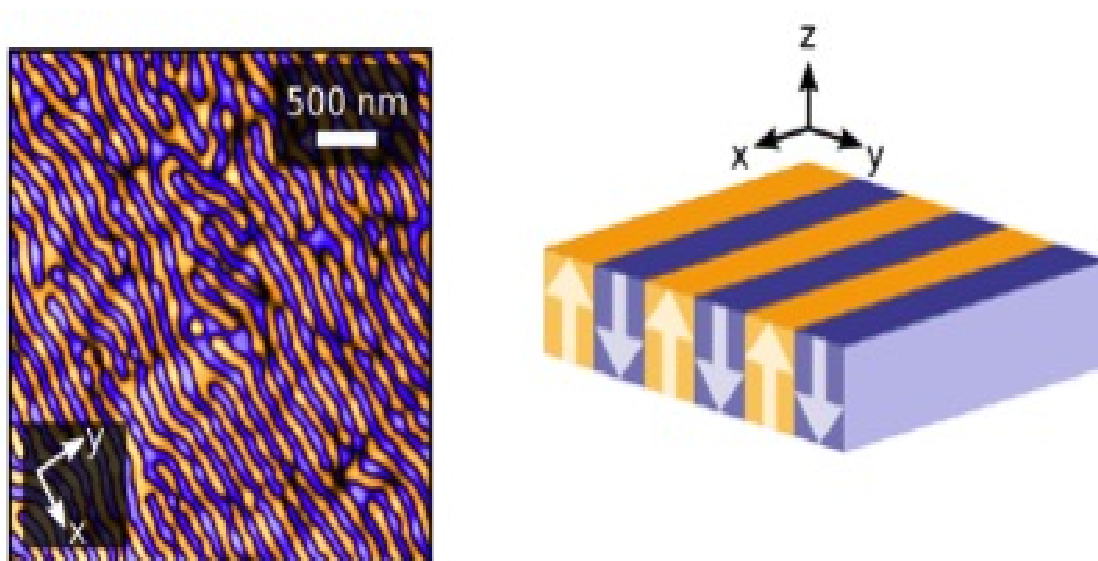


Figure 5.5: Set-up of HHG at LOA tuned to cover the M-edge of transition metals.

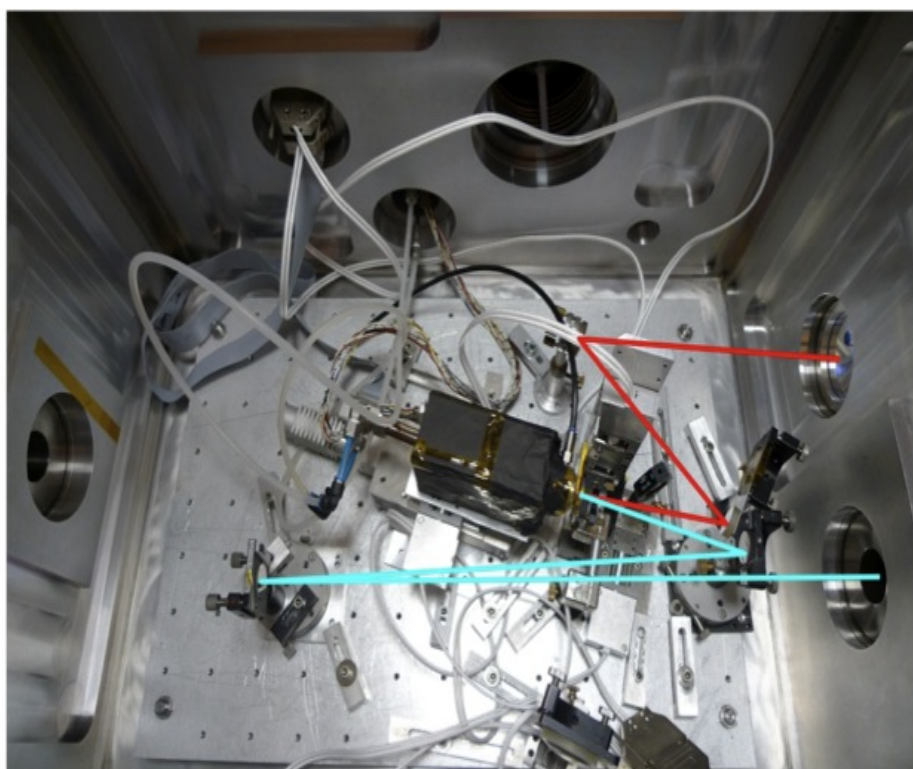


Figure 5.6: Interior of the interaction chamber. The probe of XUV radiation is portrayed in light blue. The pump of IR radiation is portrayed in red.

magnetic domain structure [79]. The changes during the timescale of the scattering pattern will reveal the evolution of the magnetic domain structure during the demagnetisation process.

The distance between the sample and the CCD, the pixel size and the wavelength of the radiation allows to convert the data into the wave vector transfer  $q$  given in  $\text{nm}^{-1}$ . Applying a pseudo-Voigt profile will fit the data and allow to sum up the intensities of each pixel on both scattering spots. The integrated intensity is then found and it will be proportional to the square of the magnetisation. The HHG can vary in intensity around 2% for a time span of 50s.

The direct XUV radiation is blocked by a beam-stop and the resulting image shows only the scattering pattern due to the magnetic domains with the same radius,  $r$ , in relation to the centre of the image. The radius can be retrieved knowing the distance between the CCD and the sample,  $D=40$  mm, the size of the pixel, 0.054 mm and the wavelength of the light,  $\lambda = 20.7\text{nm}$ . The wave-vector transfer  $q$  in  $\text{mm}^{-1}$  is given by:

$$q = \frac{4\pi}{\lambda} \sin \frac{1}{2} \arctan \frac{0.054r}{D} \quad (5.1)$$

The data is fitted by the following equation:

$$F(t) = G(t)xH(t)(K1[1 - \exp(-t/tth)] \exp(-t/ts - ph) + K2[1 - \exp(-t/ts - ph)]) \quad (5.2)$$

where  $G(t)$  is the Gaussian function,  $H(t)$  is the Heavyside function and  $\tau_{th}$  and  $\tau_{s-ph}$  are respectively the thermalisation time and the relaxation time from spins to other degrees of freedom. This fit neglects the cooling down of the lattice system, which occurs on the nanosecond time scale and is thus of no relevance on the time scale studied here.

The film average transmission is constant during the experiment so the magnetisation at the magnetic domain level can be retrieved for each delay. The magnetic scattering showing the domain size is portrayed on figure [? ].

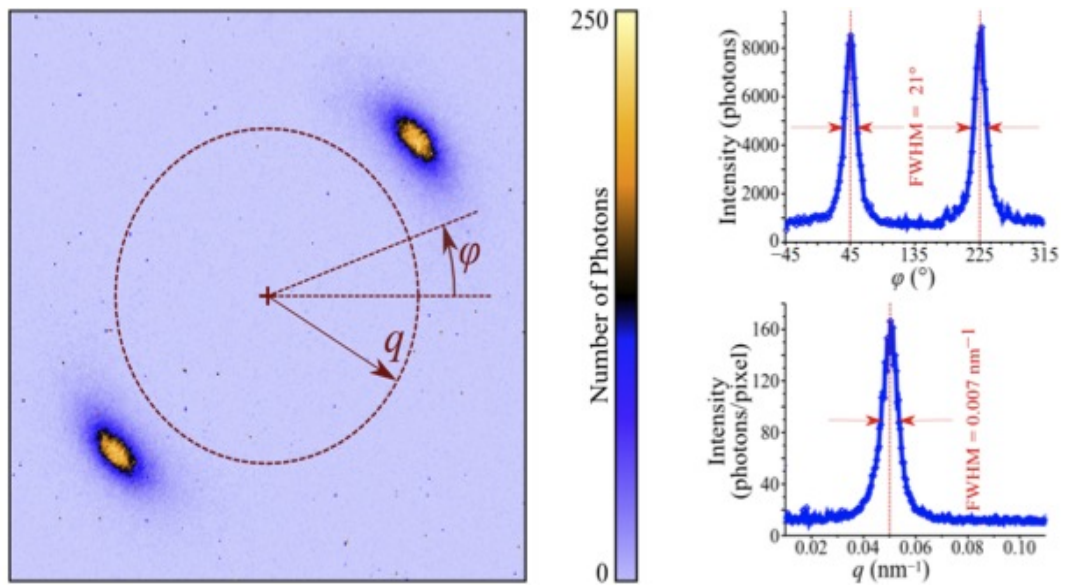


Figure 5.7: Magnetic scattering and domain size

### 5.1.3 Ultrafast demagnetisation curves

In order to establish the demagnetisation of the sample resonant magnetic scattering patterns were acquired with different time delays and pump fluences. The patterns seen in figure ?? reminds the patterns obtained from incoherent small angle x-ray scattering even if a coherent HHG source was used. The speckles due to the coherence are too small since the area illuminated was very large yielding incoherent-like scattering patterns. The beam stop blocked the scattering of the soft X-rays creating a shadow of completely removed radiation. The integration time necessary to have a clear scattering pattern was of 250 s while to attain demagnetisation 50s sufficed.

Figure 5.8 shows the resonant magnetic scattering patterns and radial integration of the intensity. It shows two clear opposite bright regions which confirms that the magnetic structure of the sample consists on aligned magnetic domains, one up another down. With time there is a clear image of the magnetic demagnetisation fading away. On the bottom the integrated radial intensity for pump fluence of  $7.5 \text{ mJ/cm}^2$ . The data were fitted by the pseudo-Voighth profile. There is a clear centre at  $0.04 \text{ nm}^{-1}$  that translated onto  $80 \text{ nm}$  being consistent with the given size of the magnetic domains.

The magnetisation of the sample can be attained by the integrated intensity of

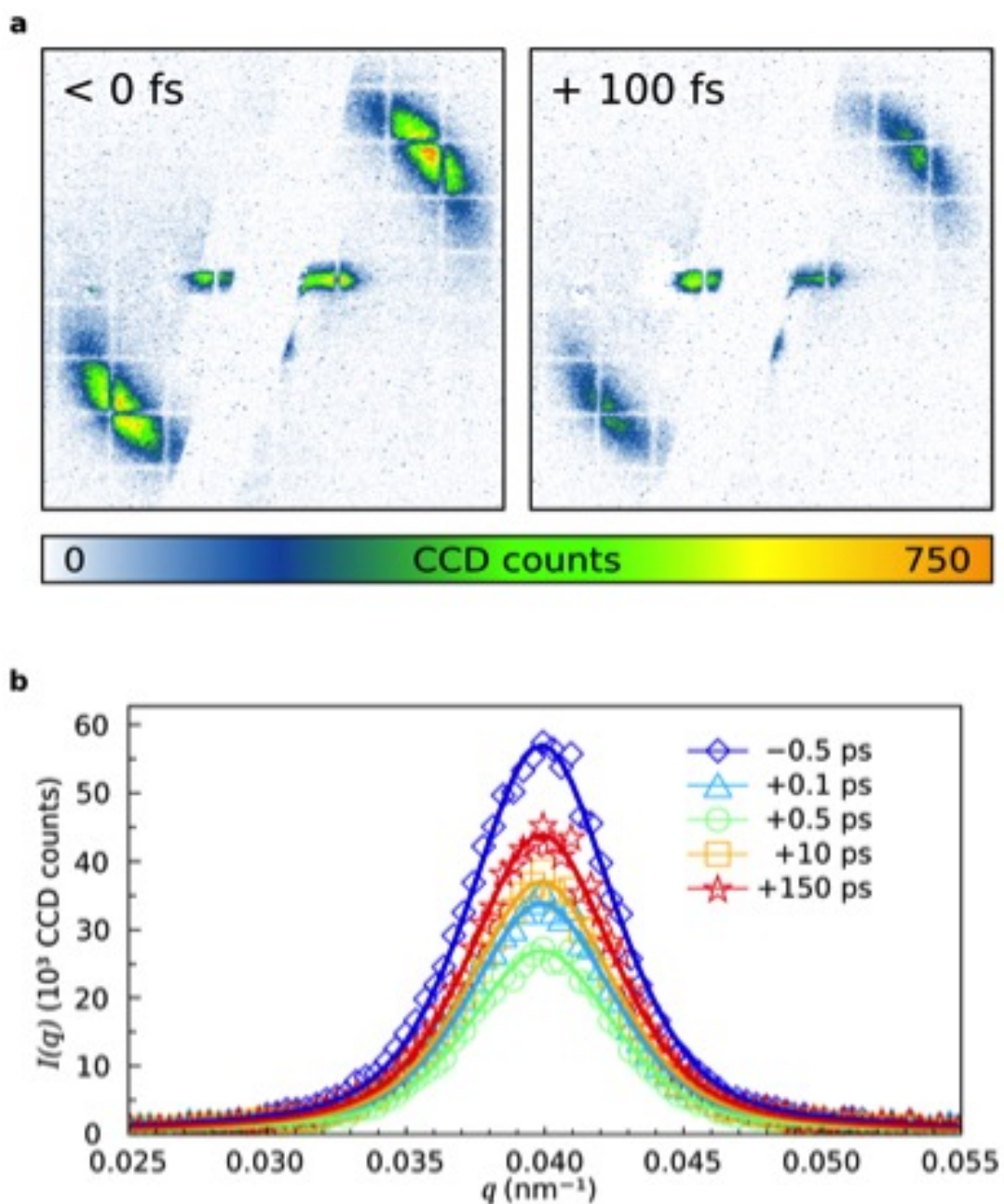


Figure 5.8: Resonant magnetic scattering patterns and radial integration of the intensity

the diffraction. Considering that there are two alignments, the up (+) and down (-) the transmission can be represented by  $t_+$  and  $t_-$ . The diffracted intensity of the first order is then given by:

$$I \propto |t_+ - t_-|^2 \quad (5.3)$$

with

$$t_{\pm} = \exp\frac{2\pi i d n_{\pm}}{\lambda} \quad (5.4)$$

where

$$n_{\pm} = 1 - (\delta \pm \Delta\delta) + i(\beta \pm \Delta\beta) \quad (5.5)$$

$n_{\pm}$  being the optical index of up (+) and down (-) magnetic domains,  $d$  the thickness of the film and  $\lambda$  the wavelength of the radiation. This last expression leads to the reason of proportionality between  $I$  and  $T(\Delta\delta^2 + \Delta\beta^2)$   $T$  being the average transmission of the magnetic domain structure. The magnetic domain structure is approximated to a square grating. Since  $\Delta\delta$  and  $\Delta\beta$  are proportional to the magnetisation  $M$  the proportionality reason is found:

$$I \propto TM^2 \quad (5.6)$$

Varying the time delay of the pump and its fluence the following curves were fitted and are represented at the figure 5.9.

The behaviour of the curves is similar. From here the thermalisation factor can be attained and it points onto the 90-110 fs with an error of  $+/- 20$  fs. Long scans were also performed to try to determine the spin-phonon relaxation. Using the highest possible pump fluence the thermalisation was found to be around 100 fs with a demagnetisation of 44%. On figure 5.9 we have reproduced the raw diffraction pattern acquired before pumping the magnetic system and 100 fs later. It is interesting to remark that apart of the loss of intensity the general structure remains unchanged. This means that in average the nano-domains are not modified significantly by the IR laser. To verify this hypothesis we superimposed the intensity plots along the +1 diffraction for different delays ranging from -0.5 ps (i.e. before the pump arrival) up to +150 ps. The position of the peak, the shape and

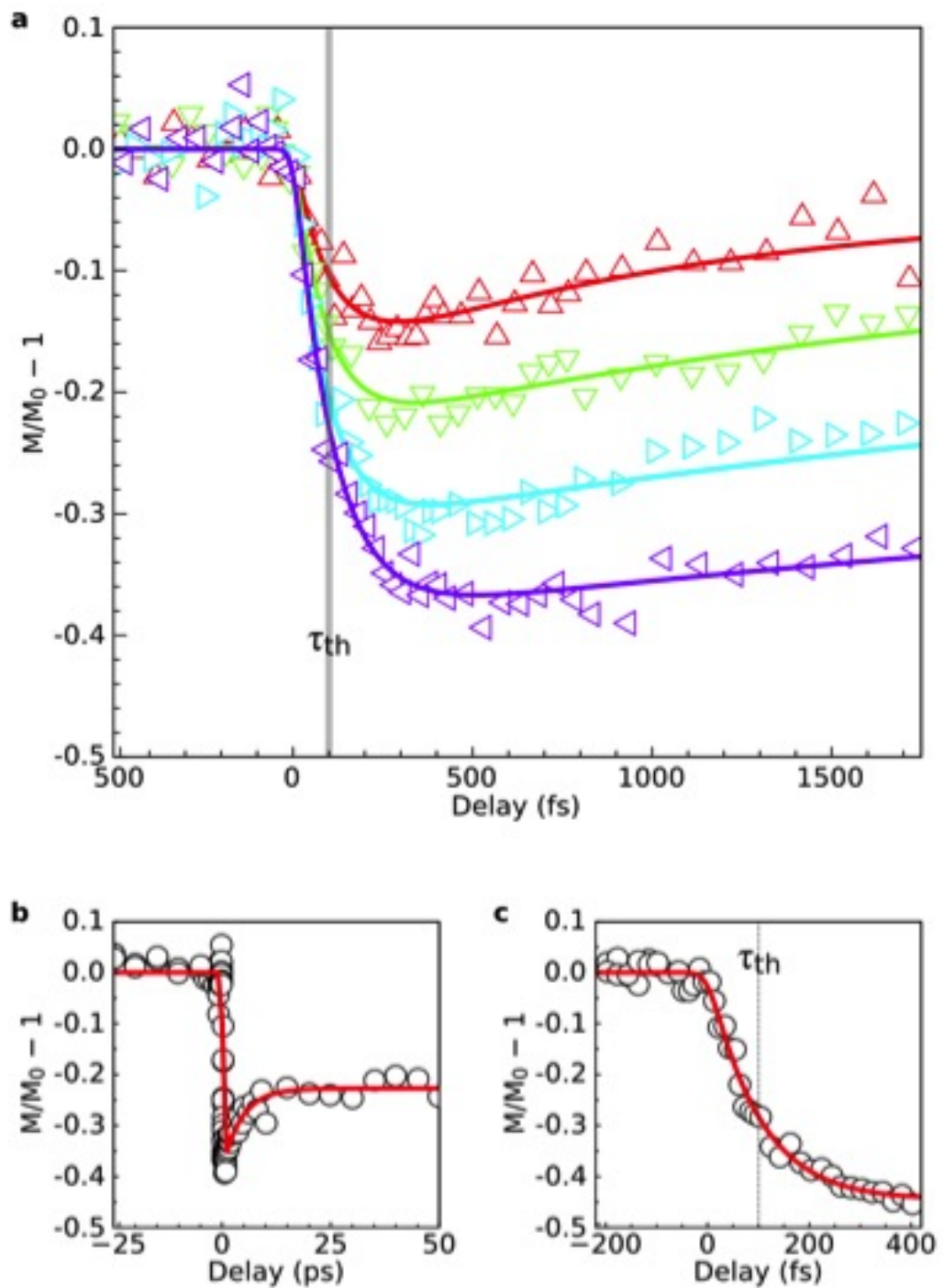


Figure 5.9: Demagnetisation curve obtained at salle orange (LOA). For a fluence given in  $\text{mJ}/\text{cm}^2$  of 4 (represented in red), 6 (represented in green), 7.5 (represented in cyan) and 9 (represented in purple).

the width of the diffraction lobes are exactly the same confirming our finding. We may observe a slight remagnetisation for long durations ( $>1$  ps) after the excitation. It is thus consistent with the use of a kHz laser that implies that magnetism fully recovers between two shots.

#### 5.1.4 Comparison between the HHG source and X-FEL

The X-FEL offers is a brilliant source compared to HHG which has as a major set back the lack of photon power. On the other hand HHG sources have the advantage of offering a smaller pulse of around 40 fs as seen in the previous sections and chapters. For more accurate time resolutions having a pump and a probe from the same laser it is a big advantage since the jitter is inexistent. Being table top makes it a more accessible source.

In order to keep the temporal resolution low there a femto-slicing source at BESSY-II attained the following results for a sample of CoPd(15 nm)/Cu(20 nm)/Si<sub>3</sub>N<sub>4</sub>(200 nm). A time resolved XMCD measure was performed by Boeglin [4] with the following results. Figure 5.10 shows the thermalisation times for Cobalt L-edge employing X-ray magnetic circular dichroism (XMCD) absorption spectroscopy. This technique employs the same resonant magnetic effect as the experiment done at LOA.

With the HHG the thermalisation time was of around 120 fs while the XMCD thermalisation time was of around 280 fs.

The layers where of approximately the same thickness so differences between the structure of the samples can be discarded. The photon energy was also different since with the HHG we aimed for the M-edge and at BESSY-II the L-edge was aimed. It would be unreasonable to expect that inferior photon energies give shorter relaxation times. The presence of a nanometric magnetic domain structure can be the origin of the observed faster thermalisation time [80]. According to Malinowski on a magnetic bilayer, spaced by a thin non-magnetic conductive layer, the demagnetisation appears to be faster for an antiparallel orientation of the magnetisation directions in the two layers. The laser induced demagnetisation process could be sped up by direct transfer of spin angular momentum between the two magnetic layers. A direct transfer of spin angular momentum between

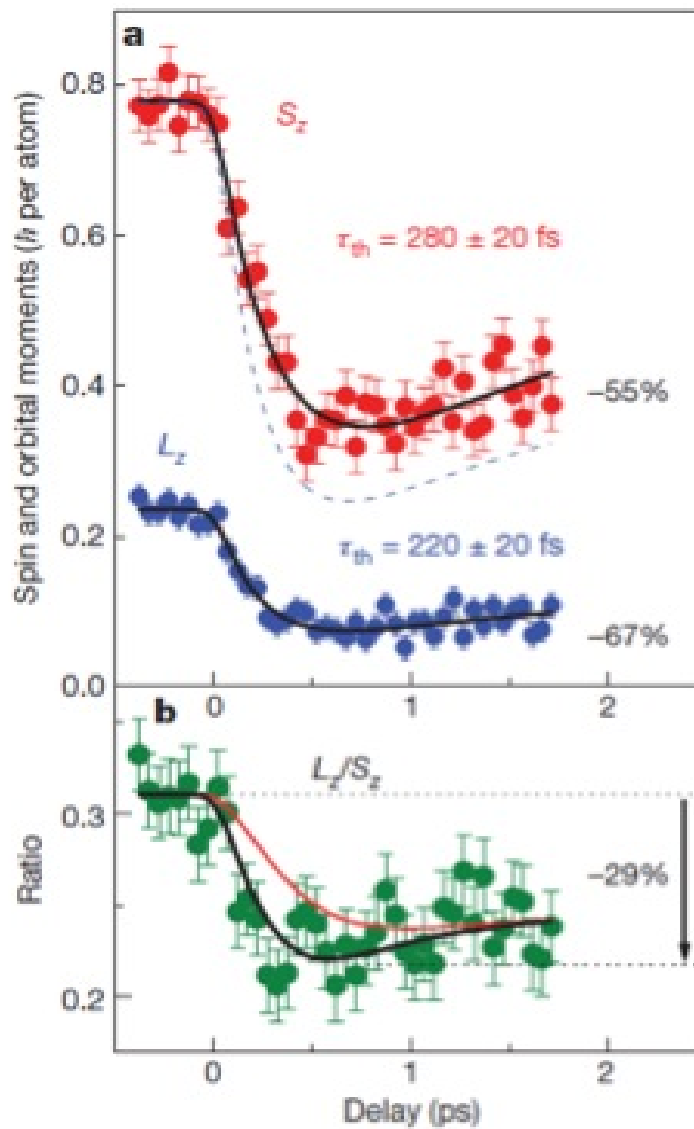


Figure 5.10: Femto-slicing measurements at BESSY-II [17]

neighbouring domains would then lead to an acceleration of the demagnetisation process. The efficiency depending of the number of hot electrons (carriers) the speed will depend on the specific properties of the junctions. This can lead to an early stage of ultrafast demagnetisation.

## 5.2 Imaging of nanomagnetic structures by diffraction and study of the evolution of the demagnetisation

Electronic structures as well as their intrinsic interactions define the functionality and the macroscopic properties of matter [81]. Reaching the scale of atoms, charges and spin motion opens a window to understand how exactly the dynamics of these electronic and magnetic nanostructures combine and give birth to the material, whether it is inanimate or biological.

Reaching the transient states of materials and monitoring them can open the door to understand its properties and its real-space structure. On the last section a table top HHG source optimised to deliver femtosecond pulses on a nanoscale on the range of 60 eV all in a table top set-up was explained. This particular experiment allowed the study of the M-edge of Cobalt. However groundbreaking the results shown on the last section have been in terms of imaging and temporal resolution, low fluence remains a limitation of the technique. On this perspective XFELs can provide the needed photon flux at a femtosecond X-ray pulse on a nanoscale.

X-Ray diffraction techniques have been used to image materials but the stochastic and deterministic ultrafast, nanoscale dynamics is yet to be fully understood and characterised. Recording and monitoring all the steps of the demagnetisation process will lead to an understanding and consequent use of these states on numerous applications.

The goal of this section is to reach the pertinent scale of atoms, charges and spin motions and record it on a single-shot. Single-shot X-ray imaging provides an insight on the underlying organisation of transient states and its evolution.

On this optic and in order to complete the dynamic magnetisation studies resolved so far a new facility was used which provides high fluence and a femtosecond x-ray pulse on a nanoscale - the Linac Coherent Light Source (LCLS) - part of the SLAC (Stanford, USA).

## 5.3 Linac Coherent Light Source - LCLS

The Linac Coherent Light Source or LCLS for short is a linear accelerator that delivers a linear polarised pulse. The LCLS is designed to produce 300 femtosecond long radiation pulses at the wavelength of 1.5 with 9 GW peak power [82]. It can be matched to the L-edges of transition metals however with a 5 orders of magnitude smaller fluence when it comes to resonant x-ray spectroholography [81].

The brilliance of this source it is still very high compared to the HHG sources in use today and it can lead to severe damages on the sample. Radiation can destroy matter macroscopic sample destruction has been shown by Einsenbit [62] and can modify the atomic structure. It has been shown that short femtosecond pulses ( $<70$  fs) allows to capture the structural information before the alterations manifest [2], [1]. However there are two phenomena that are faster than the electronic movement due to the Coulomb forces which are the photoabsorption and photoionization, auger decay and subsequent eletron cascades [81] these are set in a few femtoseconds. Single-shot in this time scale is vital and allow us to infer about the speed limits of the changes and repeatability.

The experimental approach at LCLS will be of conducting time resolved resonant scattering experiments. Although coherent x-ray scattering can yield spatial frequency information imaging is necessary to recover the complete real-space structure. A resonant magnetic small angle X-ray scattering using both multiple and aiming the single X-ray pulse and a snapshot imaging by Fourier Transform Holography. The experiments were carried out at the SXR beam line at the LCLS and the beam line 13.3 at SSRL using the Resonant Coherent Imaging (RCI) end station.

### 5.3.1 Single-shot magnetisation dynamic experiment at LCLS

The resonant x-ray spectroholography combined with sample spatial multiplexing results on a fluence threshold of  $5mJ/cm^2$  corresponding to  $4 \times 10^5 photons/\mu m^2$ , after which an image can be retrieved. The damage threshold, after which the sample suffers irreparable damage through heating is found to be around the  $25mJ/cm^2$ . This means that the image can be retrieved without irreversible changes

due to heating on the range  $5 - 25 \text{ mJ/cm}^2$  allowing to repeat the experiments on the same condition since it won't destroy the sample. This will be vital when combining pum-probe techniques in order to make a movie of excited state dynamics using a sequence of snapshots.

The sample used was based on Cobalt since it has been the element studied throughout this thesis. The sample consisted on sputter-deposited multilayers  $Ta_{1.5 \text{ nm}}Pd_{3 \text{ nm}}(Co_{0.5 \text{ nm}}/Pd_{0.7 \text{ nm}})_{40}Pd_{2 \text{ nm}}$  on  $Si_3N_4$  membrane that have been studied extensively as a candidate system for perpendicular recording media. To the holographic study an integrated holographic mask is used to record the individual diffraction patterns. An 800 nm thick Au film opaque to soft x rays, is sputtered on the back side of the membrane. This set-up is shown on figure ???. The picture represents on (a) the 15-reference gold holographic mask taken during a scanning electronic microscopy exam and the aperture and the references can be recognised. The sample aperture diameter is  $1.45 \mu\text{m}$  and the references are 100 nm in diameter. Each of which will produce a snapshot of the sample. On (b) the set-up for recording of the hologram is represented. The hologram is recorded on far field and a beam blocker of tungsten carbide is used to block the direct beam to preserve the CCD. The LCLS pulse is tuned to the Co  $L_3$  edge at the corresponding energy of 778.8 eV and the spin orientation of the ferromagnetic domain is resolved via x-ray magnetic circular dichroism effect. On (c) a reconstructed image of the initial magnetic domains obtained using circularly polarised x-ray pulses with white and black regions corresponding to 100-150 wide domains with opposite out-of-plane magnetisation directions. The corresponding fluence was inferior to  $2 \text{ mJ/cm}^2$ .

To tune the energy X-ray pulses up to 1.87 mJ are sent on a monochromator to select the photon energy corresponding to the Co  $L_3$  edge with an energy resolution of 0.5 eV. To be able to use the dichroic effect the incident pulse has to be circularly polarised with the help of a 40 nm in-plan-e-magnetised Co magnetic thin film polariser. The unfocused monochromatic beam is therefore sent through the polarizer at 60 degrees to the incident x rays, producing up to  $10^9$  photons per pulse with 58% circular polarization.

The large beam spot size at the polarizer results in a low energy density ( $< 1 \text{ mJ/cm}^2$ ) and the magnetization of the polarizer film remains fixed by a permanent magnet. Focusing the beam with bendable Kirkpatrick-Baez mirrors on the sample

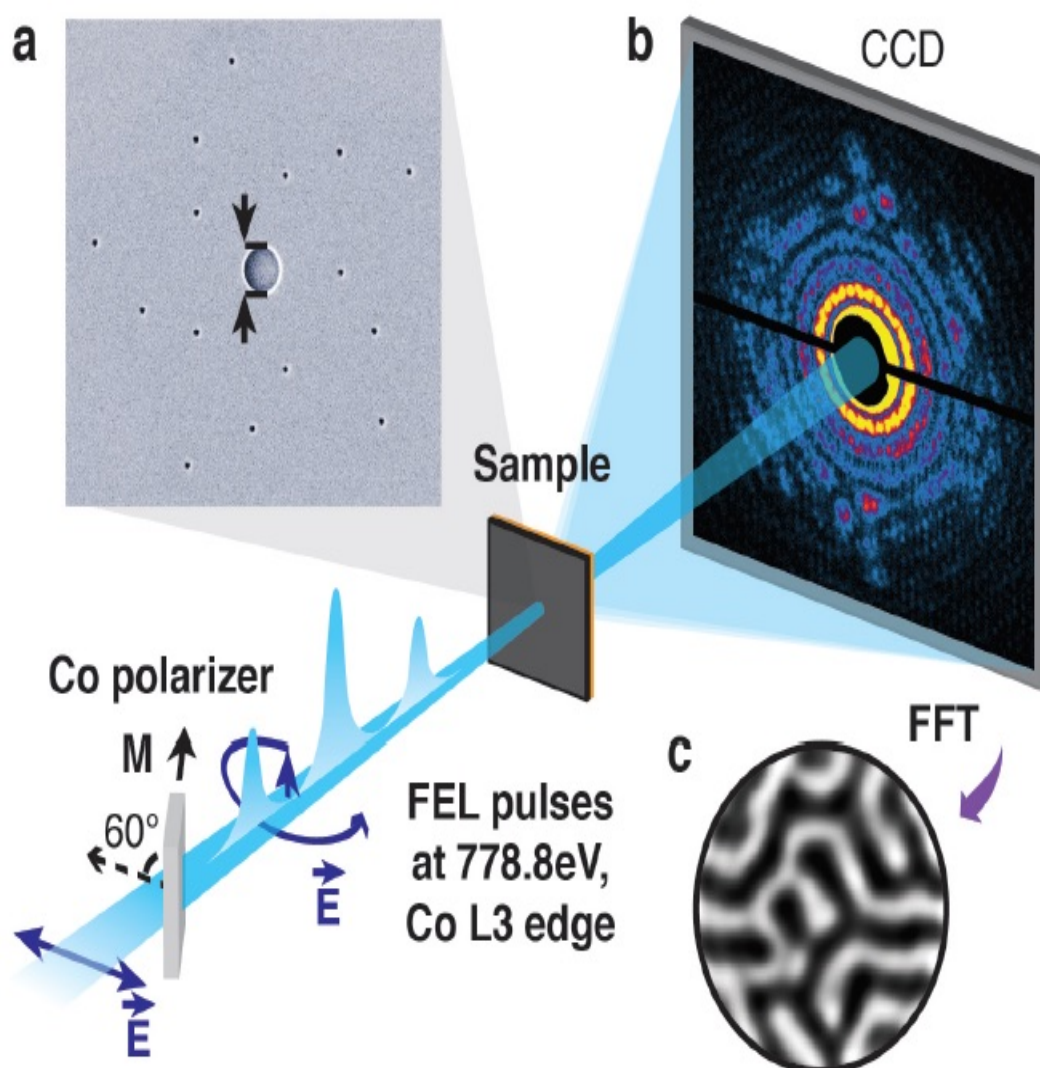


Figure 5.11: Experimental set-up (a) 15-reference gold holography mask. Aperture and references, (b) Spectro-holography: A CCD camera located 490 nm with a numerical aperture of 0.028 records in the far field, (c) reconstruction of the initial magnetic states.

will result on a spot size of 10 by  $30\mu\text{m}$ . The x-ray holograms are recorded on a CCD detector with  $2048 \times 2048$  pixels of  $13.5 \times 13.5\mu\text{m}^2$  mounted on a translational stage to adjust the sample-detector distance.

The maximum momentum transfer of  $0.111\text{nm}^{-1}$  for a wavelength 1.59 nanometers corresponding to an energy of 778.8 eV or in this case the Co  $L_3$  edge is found at 490 nm on the translational stage of the CCD and a numerical aperture of 0.0282

is chosen. The holographic mask contains multiple reference holes as the phase information is encoded by the sample-reference interference, a single Fourier inversion of the diffraction pattern recovers the real space image. Initial domain patterns are reconstructed from many low-fluence x-ray pulses. Subsequently, a series of single-shot images are collected with 80 and 360 femtosecond x-ray pulses at higher fluences.

### 5.3.2 Single-shot diffraction patterns

Here we demonstrate single-shot imaging of the spin-resolved electronic structure of the 3d valence shell in a nanoscale-ordered magnetic film. For 80 femtosecond pulses, no manifestation of damage is observed during the pulse. For the longer 360 femtosecond pulses, demagnetisation due to the thermalisation of electrons and subsequent equilibration with the spin reservoir and the lattice is observed during the pulse.

Figure ?? represents a single-shot diffraction pattern derived of a 80 femtosecond pulse. Due to the incidence of circularly polarised x-rays a pattern appears due to charge-magnetic interference (CMI) from both the sample and the interference waves where the resonant charge and magnetic scattering contrasts are proportional to the vacancies and the spin splitting of the 3d valence states, respectively. The 5-reference sample contains  $1.5 \times 10^5$  detected photons and the scale corresponding to the photon count per pixel. To the corners corresponds a momentum transfer of  $0.054 \text{ nm}^{-1}$ . The strategic placement of the references allows to have space separation of the complex autocorrelation after the Fourier inversion. Each reference generates an independent reconstruction - a pair of radially opposite complex object-reference conjugates in the autocorrelation. The centre corresponds to the self-correlation of the object and the references. The final averaged reconstruction with a 10%-90% resolution of 80 nm. The resolution is limited by the reference size.

Some autocorrelations seem more defined than others and this is due to uneven beam profile and beam position jitter that make that not all the references may be illuminated equally during a pulse, resulting in different image qualities. The reconstructions without a sufficient signal-to-noise-ratio (SNR) are then discarded during averaging. The summation over all independent reconstructions

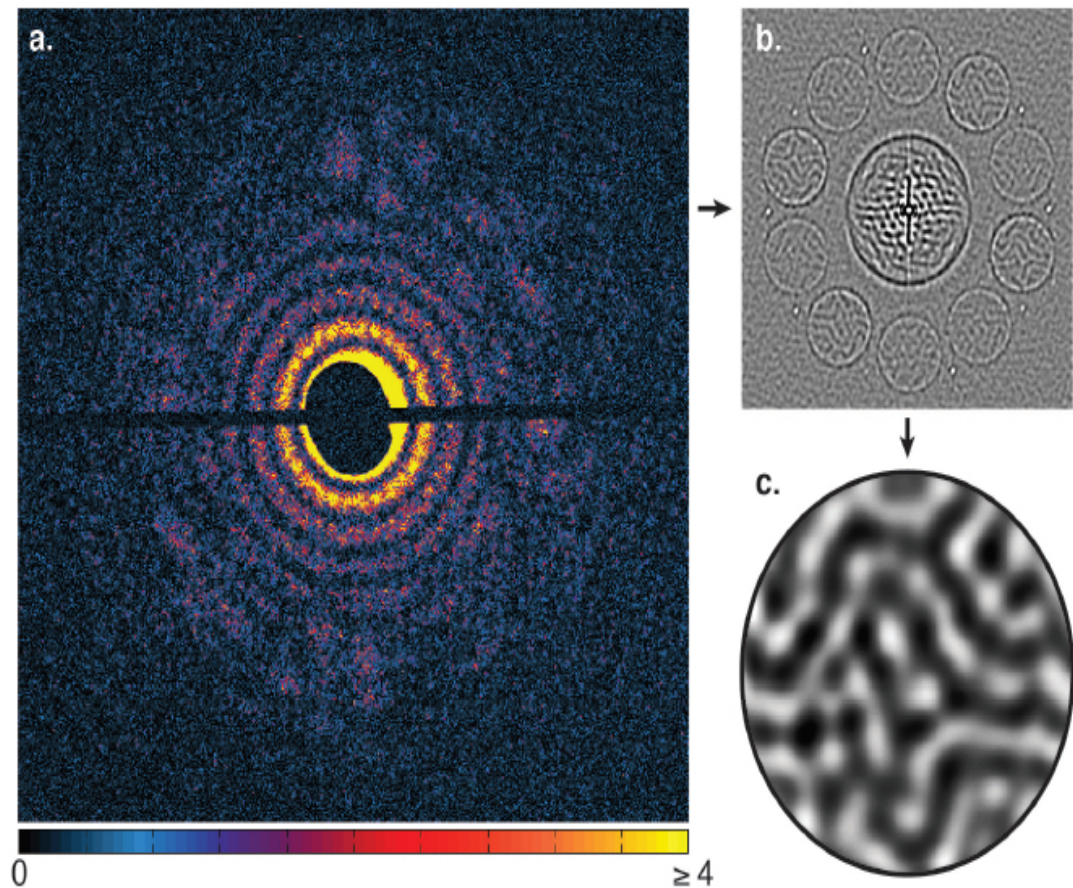


Figure 5.12: (a) Single shot reconstruction of the nanoscale ferromagnetic ordering with a 80 femtosecond pulse, (b) and (c), the strategic placement of the references produces well-separated images of the spin-resolved electronic structure in the autocorrelation after the Fourier inversion.

significantly improves the image quality, enhancing the SNR by up to a factor of 4 for 15 references. The imaging threshold of  $5mJ/cm^2$  was attained for the set-up provided and due to the stochastic intensity jitter at LCLS reconstructions were achieved for approximately half of the x-ray pulses used.

To have a significant insight of the structure induced x-ray modifications shouldn't appear on the probe pulse. Considering a fluence of  $20mJ/cm^2$  approximately 1 in 1000 Co atoms absorbs a photon [81]. As stated before Auger decays are in the order of the few femtoseconds and the core holes on the L shells decay at 99%. When Auger electrons generate a cascade of secondary electrons in the sample with a typical collision rate of  $1/femtosecond$  transferring 3d electrons to the continuum and electronic damage takes place. The 100 femtosecond demagnetisation

time can be then explained due to the distribution of energy of 0.8 eV per atom (average) over all atomic sites. This phenomena gives birth within several tens of femtoseconds to a hot electron gas in the valence band that thermalises. When thermalisation occurs the energy and angular momentum are transferred on the order of the 150-300 femtoseconds to the spin and under the 0.5 picoseconds to phonons systems leading to ultrafast demagnetisation and heating of the lattice.

Analysing Charge-magnetic interference (CMI) intensity during the pulse gives us a damage as a function of the fluence. Figure 5.13 shows the plot considering both a pulse of 80 femtoseconds and a pulse of 360 femtoseconds.

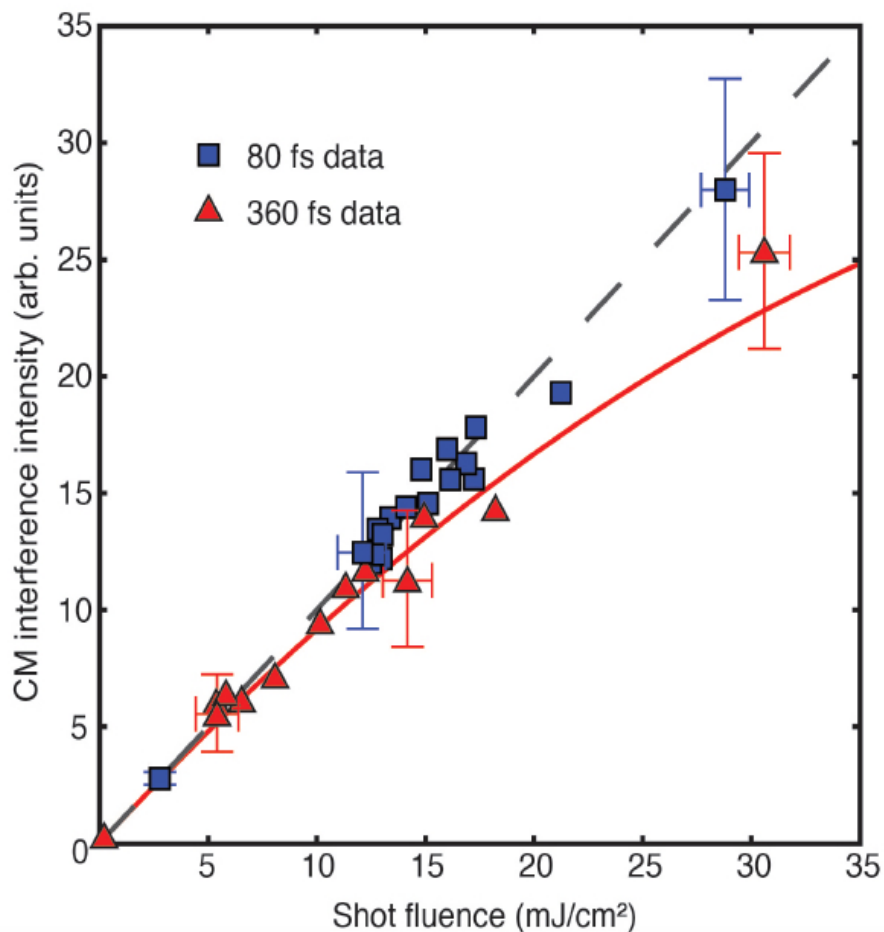


Figure 5.13: Shot fluence

The CMI intensities are found by comparing the CMI contrast from the reconstructions. The normalization of the single-shot diffraction patterns is based on the photon intensity per snapshot relative to the low fluence reconstruction of the starting domain state. As the pulse increases in intensity data started to get discarded

due to the significant alteration of the sample. On the first case scenario, the 80 femtosecond pulses the CMI intensity presents a proportional trendline up to a fluence value of  $28\text{mJ}/\text{cm}^2$ . It can be concluded by this result that the sample state remains significantly the same during the pulse. The pulse durations refer to electron bunch length measurements and may be considerably shorter as suggested by the electronic response of atoms to intense x-ray beams.

On the second case, the duration of the pulse on the 360 femtosecond the CMI intensity decreases with the increase of fluence and a linear trendline is no longer viable. This can be a result of the above mentioned demagnetisation triggered by the secondary-electron cascades. The deposition of energy by the x-ray laser can also trigger this response by providing energy easily absorbed by the sample.

The conclusion that can be taken from this plot 5.13 is that the pulse must be shorter than 80 femtoseconds to prevent secondary demagnetisation processes. The ultrafast demagnetisation process can be calculated easily due to the sample demagnetisation decreases linearly with increasing frequency until the sample is completely demagnetised at a threshold fluence. The reported values for this ultrafast demagnetisation are on the order of the 280 femtoseconds according to [17]. Dividing the 360 femtosecond pulses to 10 femtosecond slices and propagating it through the sample leads to a integrated CMI intensity over the pulse.

A movie of ultrafast processes can then be possible using the small pulse frames. One of the requirements for this technique is that the sequential single shot is non destructive and that the sample is able to reboot before the next shot.

On 5.14 the feasibility of sequential single-shot is presented for 360 femtosecond pulses. On (a) the blue markers represent pulses above the statistical threshold of  $5\text{mJ}/\text{cm}^2$  and the red marker represents the pulse with enough fluence to produce damage in the structure. The grey markers indicate pulses below the imaging threshold of  $5\text{mJ}/\text{cm}^2$ . All the shots have associated error bars due to shot noise. On the (c) and (d) line cuts show good agreement of the domain patterns shot to shot. Back to back snapshots produce highly correlated (75%) images as seen on (b), (c), (d) and (e). Minor lateral fluctuations of the domain borders near the damage threshold of  $25\text{mJ}/\text{cm}^2$  are visible. At the Co L3 absorption edge, the Co/Pd multilayers absorb 83% of the photons with 70% of the total energy deposited in Cobalt.

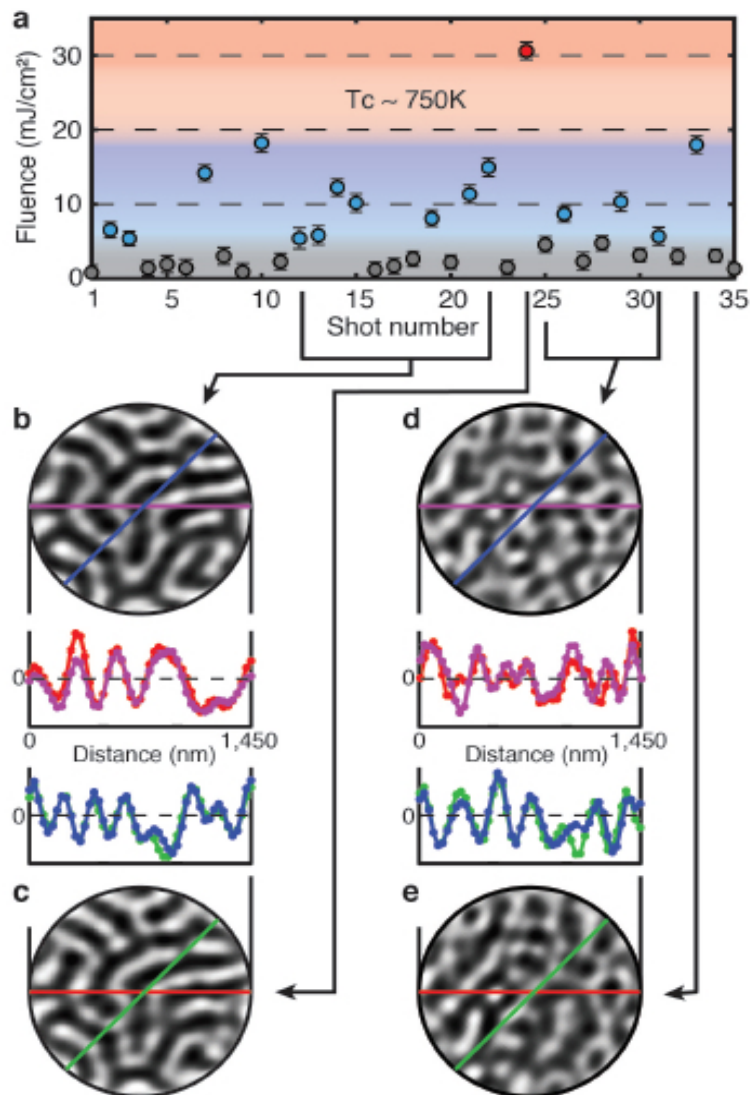


Figure 5.14: Fluence thresholds on single-shot images with 360 femtosecond pulses (a) fluence plot for a single-shot sequence, (b)-(c) average reconstruction from the shots 12 to 23 and reconstruction of the shot 24, (d)-(e) average reconstruction from the shots 25 to 31 and reconstruction of the shot 33

At the damage threshold the average temperature of the sample is around 1100K and heat transfer phenomena occurs, above  $25\text{mJ}/\text{cm}^2$  temperatures above the Curie temperature are reached and the sample forms a new domain pattern upon cooling due to irreversible thermal damage. On (d) and (e) the altered nanoscale periodicity suggests irreversible thermal damage caused by interstitial diffusion across *Co/Pd* interfaces and subsequent anisotropy softening. The key to nondestructive sequential imaging is to utilize the regime between the minimum imaging and the thermal damage thresholds.

### 5.3.3 Conclusion

Highly efficient single-shot imaging of the spin-resolved electronic structure has been tested with precise results. The strong interaction of intense x-rays with electronic systems was proved to cause damage on the spin structure but it can be avoided using time range pulses inferior to 80 femtoseconds. Enhancements in resolution can be achieved at higher fluences with smaller x-ray focuses at the expense of sample destruction, and by using holography techniques such as uniformly redundant arrays and differential holographic imaging.

The demonstrated feasibility of nondestructive sequential single-shot imaging provides a very attractive tool for the time-resolved study of nanoscale femtosecond dynamics.

## Conclusion and perspectives

The goal of this thesis was based on the development of a tabletop imaging system in three dimensions in the XUV range with polarisation control of the electromagnetic ultra-short pulses and with nanometric resolution for visualizing magnetic systems. This system was built to allow the exploration of the demagnetisation processes in a time-scale and with a resolution never reached before.

High harmonic generation for its relatively easy control of the characteristics of the emitted XUV radiation has proven to be a reliable source with an exceptional spatial quality beam in this range. It is highly collimated, coherent, close to the diffraction limit, and has a regular and uniform spatial profile. This makes the source perfect for imaging experiments or holography, and generally for the optics field in the XUV. The good wave front of the beam also offers a very good ability to focus, to dimensions close to the diffraction limit, and the illumination obtained should allow a study of laser-matter interaction in this spectral region relatively untapped.

It is nevertheless clear that this source, although mature for use in a diverse range of applications, was currently relatively limited in terms of power. In line with the latest achievements a two-colour field scheme was put in place to increase its conversion efficiency and produce a higher photon count. Simulations were put in place to understand further this non-linear process and increase the knowledge of the high harmonic generation. In this case however the parameters are too wide and various models can apply so the result was a small step further and there is still room for improvements.

In order to access the demagnetisation process the absorption edges of mag-

netic metals were targeted and in particular the M-edge of Cobalt. This unprecedented choice of working on the M-edge at 58.9 eV instead of the L-edge near 900 eV has been a big challenge forced by the lack of high harmonic generation emitting at such high energies.

To attain good dichroic contrast a circularly polarised XUV beam is as well required. This is a major advance since most of the available XUV sources have polarisation control together with the other light parameters and so the polarisation degree was not easily accessed. So in this work the development and mount of this system with the purpose of measuring the polarisation was conceived and simulations were conducted in order to verify the experimental results. Large-scale facilities already have the ability to control the polarisation of the released beam however it was the first time that the polarisation set-up was put in place with a table-top source.

The new system has been tested and it is in use. However, the measurement of the exact polarisation degree and the discrimination between unpolarised and circular polarisation has to be improved in order to access the experimental conditions more exactly. Also an interferometer can be put in place in order to optimise independently both fundamental and second harmonic beams. The energies can be matched and therefore the system can be more adjustable and precise since non-collinear polarisation tend to produce mixing signals allowing to precisely measure them.

The Cobalt samples were then used for the purpose of imaging its magnetic nanostructures by magnetic diffraction and in order to perform a magnetisation study. The experiments done at BESSY-II to characterise the sample yielded the real and imaginary part of the refractive index of the transition metal Co in the photon energy range of 30-100 eV, which covers the magnetically dichroic M<sub>2,3</sub> absorption resonances of this transition metal and validated their dichroic qualities. Therefore the samples were taken to be used at the LOA. We first demonstrated that coherent diffraction of magnetic nanosystems (Co) is possible using a high harmonic generation source linearly polarised. Then we have developed a pump-probe setup in order to measure the ultrafast demagnetisation of Co magnetic layers. We measured the to-date fastest demagnetisation time of 80 fs. Since the low HHG flow at LOA required 100,000 HHG flashes to acquire a single image, we used the same sample but at LCLS where a single flash enabled to acquire an

image. We verified that in average the magnetic domains come back to their initial states and structures after demagnetisation (on a few ns) validating the use of HHG. However, we also observed that locally very few domains do not retrieve their exact structure. Single-shot and multiple-shot images are thus complementary.

Having set the HHG beamline with linear or circular polarisation and having demonstrated its usefulness on femtomagnetism experiments, we believe that scientists from outside LOA (like the LCPMR team) will continue to actively use the beamline for many new researches.

## Optical Coherence

---

---

Historically the first meaning given to the coherence of an optical field was his ability to produce interference. Currently it is considered as the set of correlation properties of the optical field. For practical reasons, there are often temporal coherence (or longitudinal), the spatial coherence (or transverse) and polarization coherence not discussed here. It will be assumed in a scalar approximation the field  $U$  emitted by a source consisting of a plurality of transmitters.

### Definition

The problem is whether there is a relationship between the field at two points  $A$  and  $B$  different at two different instants  $t_1$  and  $t_2$ . It is impossible to follow the erratic fluctuations of the emitted field by all non-synchronous transmitters that constitute the source. The field will be described as a random process and it is defined in this context the correlation function of the field, given by its covariance

$$\Gamma_{AB}(t_1, t_2) = E [ U_A(t_1) U_B^*(t_2) ] \quad (\text{A.1})$$

Under the assumption of a stationary process (statistical properties invariant over time) and ergodic (average time on a large number of realizations is equal to the time average statistics) this function is written:

$$\Gamma_{AB}(\tau) = \langle U_A(t) U_B^*(t + \tau) \rangle \quad (\text{A.2})$$

where  $\tau = t_1 - t_2$ . It is introduced then the degree of normalized mutual coherence:

$$\gamma_{AB}(\tau) = \frac{\Gamma_{AB}(\tau)}{\sqrt{\Gamma_{AA}(0)\Gamma_{BB}(0)}} = \frac{\Gamma_{AB}(\tau)}{\sqrt{I_A I_B}} \quad (\text{A.3})$$

with  $I_A$  (resp.  $I_B$ ) the mean intensity in  $A$  (resp.  $B$ ). The case  $\gamma_{AB} = 1$  corresponds to a total coherence and the case  $\gamma_{AB}$  to incoherence.

The degree of spatial coherence can be therefore defined between two points  $A$  and  $B$  at a given instant  $\gamma_{AB}(0)$  and the degree of temporal coherence in a point  $A$  given  $\gamma_{AA}(\tau)$ :

$$\gamma_{AB}(0) = \frac{\Gamma_{AB}(0)}{\sqrt{I_A I_B}} \quad \text{Spatial coherence} \quad (\text{A.4})$$

$$\gamma_{AA}(\tau) = \frac{\Gamma_{AA}(\tau)}{I_A} \quad \text{Temporal coherence} \quad (\text{A.5})$$

### The Zernike van Cittert theorem for spatial coherence

The spatial coherence of a source is the ability of different fields emitted by this source points to interfere with each other. Therefore there is a need to characterise the phase correlation of the fields emitted by each point of the source. A quasi-monochromatic point source will be completely coherent in terms of the spatial coherence. It can be said then that if the viewing distance of the source is large enough this source can be considered punctual and will be seen as coherent. We then speak abusively of the coherence of the radiation emitted by the source. We can calculate the degree of coherence between two distinct points  $\mathbf{P}_1$  and  $\mathbf{P}_2$  of a plane located at a distance  $D$  of the incoherent source, and show that if  $D$  is large compared to the spatial extent of the source it is given by the Fourier transform of the intensity distribution of the source:

$$|\Gamma(\mathbf{R}_1, \mathbf{R}_2)| = \left| \frac{\iint_S I(\mathbf{r}) e^{i2\pi \frac{\mathbf{R}_2 - \mathbf{R}_1}{\lambda D} \cdot \mathbf{r}} d\mathbf{r}}{\iint_S I(\mathbf{r}) d\mathbf{r}} \right| \simeq \frac{\left| \tilde{I} \left( \frac{\mathbf{P}_2 - \mathbf{P}_1}{\lambda D} \right) \right|}{I_{source}} \quad (\text{A.6})$$

in the case where  $|\mathbf{R}_1|$  and  $|\mathbf{R}_2|$  represent the distances between  $P_1$  and  $P_2$  and the current point of the source  $\mathbf{r}$  are large compared to  $|\mathbf{r}|$ . This results constitutes the Zernike-van Cittert theorem and shows that a quasi-monochromatic source of non-zero spatial extent radiates a coherent part.

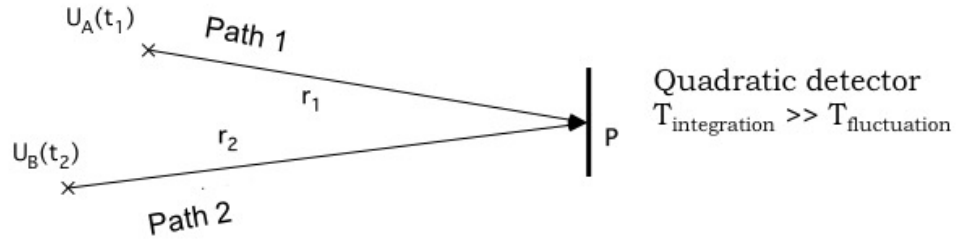


Figure A.1: Coherence and interferences

### Measurement of the coherence and the particular case of the Young slits for spatial coherence

Lets us consider the two arm interferometer presented in Fig. A.1 and a quasi-monochromatic source  $k = 2\pi/\bar{\lambda}$ . The intensity recieved by the detector in a a point  $P$  is written by:

$$I_P = \left\langle \left| U_A \left( t - \frac{r_1}{c} \right) e^{ikr_1} + U_B \left( t - \frac{r_2}{c} \right) e^{ikr_2} \right|^2 \right\rangle \quad (\text{A.7})$$

It can be shown that:

$$I_P = I_A + I_B + 2\Re e \left[ \Gamma_{AB}(\tau) e^{ik(r_1-r_2)} \right] \quad (\text{A.8})$$

then making  $\Gamma_{AB}(\tau) = |\Gamma_{AB}(\tau)| e^{i\Phi_{AB}(\tau)}$ :

$$I_P = 2\bar{I} \left[ 1 + 2|\gamma_{AB}(\tau)| \cos \left( \frac{2\pi}{\lambda} \delta_P + \Phi_{AB}(\tau) \right) \right] \quad (\text{A.9})$$

with  $\tau \simeq t_1 - t_2$ ,  $\delta_P = r_1 - r_2$ ,  $\Phi_{AB} = \frac{2\pi c \tau}{\bar{\lambda}}$  and  $\bar{I}$  the mean value of the interferogram. The contrast of the obtained fringes is then given by the absolute value of the normalised coherence degree.

The method most widely used for measuring the spatial coherence of a source at least in the XUV range is the Young interferometry with a double slit system of variable spacing. This set-up is presented on Fig. A.2. This is an interferometer with a wavefront division composed of two parallel slits in an orthogonal plane to the direction of propagation of the beam. According to the Huygens-Fresnel principle the two secondary waves created by the slits have the same phase as the points corresponding to the incident wave. The diffraction in the direction

perpendicular to the slits permits the recovery of these two secondary waves and thus the appearance of an interference field if they are mutually coherent.

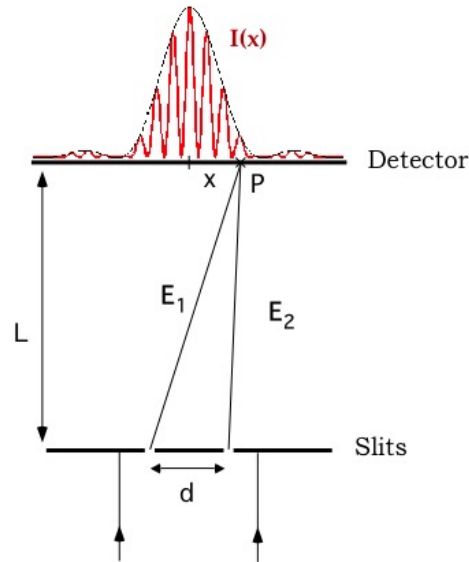


Figure A.2: Principle of the Young slits experiment

The field created by one slit  $F$  with width  $e$  is written as a function of its initial phase as  $\Psi_F E(F) = E_F \sin(\omega t + \Psi_F) \Pi\left(\frac{x}{e}\right)$ . Consider a point  $P$  situated on the detector placed on the orthogonal plane to the slit plane at a  $L$  distance from them. The field received by this point is the sum of the two fields created by each slit. It can be said hypothetically that the fields have the same amplitude  $E_0$  (for an incident beam centred in between the slits) and the same initial phase (coherent wave):

The field created by a slit  $F$  of width  $e$  is written in function of its initial phase  $\Psi_F E(F) = E_F \sin(\omega t + \Psi_F) \Pi\left(\frac{x}{e}\right)$  where  $\Pi$  is the function. Consider a point  $P$  located on the detector placed in the orthogonal to the plane of the slots and at a distance  $L$  of these ones. The field received by this point is the sum of two fields created by each slit and it is assumed that these fields have the same amplitude  $E_0$  for an incident beam centred on the slots and the same initial phase coherent wave is written as:

$$E(P) = E_0 \sin(\omega t) \text{sinc}\left(\frac{\pi e}{\lambda L} x\right) + E_0 \sin(\omega t - \Delta\varphi) \text{sinc}\left(\frac{\pi e}{\lambda L} x\right) \quad (\text{A.10})$$

if we are in the case of the Fraunhofer diffraction  $L \gg e$ . The phase-shift  $\Delta\varphi$  is due to the fact that these two waves have followed a different optical path before

arriving to the point  $P$ . This phase shift is written in function of the difference between the optical paths of each wave and the difference of path traversed  $\delta(x)$  and on the case where the distance between the slits and the detector is large in comparison to the spacing of the slits  $d$ :

$$\Delta\varphi = \frac{2\pi\delta(x)}{\lambda} \simeq \frac{2\pi d}{\lambda L}x \quad \text{si} \quad L \gg d \quad (\text{A.11})$$

The intensity in  $P(x)$  is written:

$$I(x) = I_0 \cos^2\left(\frac{\pi d}{\lambda L}x\right) \text{sinc}\left(\frac{\pi e}{\lambda L}x\right) \quad (\text{A.12})$$

We observe then on the detector an alternation of dark fringes ( $\Delta\varphi = (2n + 1)\pi$ ) and brilliant fringes ( $\Delta\varphi = 2n\pi$ ) wrapped by a sinus function due to the diffraction by the width of the slit.

The magnitude allowing to measure the coherence between the emitted waves by the slits is the contrast of the fringes that is defined by:

$$V = \frac{I_{max} - I_{min}}{I_{max} + I_{min}} \quad (\text{A.13})$$

The measurement of the visibility of the fringes gives directly the degree of mutual coherence between the waves therefore of the source.

## Fourier transform, convolution and correlation: notations and useful properties

---

For square-integrable functions  $g(x)$  and  $f(x)$  on the following applications are applied:

Fourier Transform:

$$\mathcal{F}\{g(x)\}_{x \rightarrow k} = G(k) = \frac{1}{\sqrt{2\pi}} \int_{-\infty}^{\infty} g(x) e^{-ikx} dx \quad (\text{B.1})$$

With the reciprocal relation:

$$g(x) \stackrel{\mathcal{F}}{\Leftrightarrow} G(k) \quad (\text{B.2})$$

$$g^*(-x) \text{ transform : } g^*(-x) \stackrel{\mathcal{F}}{\Leftrightarrow} G^*(k) \quad (\text{B.3})$$

Homothety:

$$g(ax) \stackrel{\mathcal{F}}{\Leftrightarrow} \frac{1}{|a|} G\left(\frac{k}{a}\right) \quad (2.4)$$

Definition of the convolution product:

$$f(x) * g(x) = \int_{-\infty}^{\infty} f(x') g(x - x') dx' \quad (2.5)$$

Property of derivative of the convolution product:

$$\frac{d}{dx}[f(x) * g(x)] = g(x) * \frac{d}{dx}[f(x)] = f(x) * \frac{d}{dx}[g(x)] \quad (2.6)$$

Definition of the correlation product:

$$[f \otimes g](x) = \int_{-\infty}^{\infty} f^*(x') g(x' + x) dx' = \int_{-\infty}^{\infty} f^*(x' - x) g(x') dx' \quad (2.7)$$

Relation between the convolution product and the correlation product:

$$f^*(-x) * g(x) = [f \otimes g](x) \quad (2.8)$$

Derivative of the correlation product:

$$\frac{d}{dx}[f(x) \otimes g(x)] = (-1)\left(\frac{d}{dx}[f(x)]\right) \otimes g(x) = f(x) \otimes \frac{d}{dx}[g(x)] \quad (2.9)$$

Autocorrelation product:

$$[f \otimes f](x) = f^*(-x) * f(x) \quad (2.10)$$

The autocorrelation product is Hermitian.

The correlation product is commutative and associative but the correlation product is not:

$$f^*(-x) * g(x) = [f \otimes g](x) \quad (2.11)$$

is different than

$$f(x) * g^*(-x) = [g * f](x) \quad (2.12)$$

The autocorrelation product is commutative.

Fourier relations convoluted:

$$f(x) * g(x) \stackrel{\mathcal{F}}{\Leftrightarrow} F^*(k)G(k) \quad (2.13)$$

Since

$$[f \otimes g] = f^*(-x) * g(x) \stackrel{\mathcal{F}}{\Leftrightarrow} F^*(k)G(k) \quad (2.14)$$

## ABSTRACT

A utilização de raios X é essencial para obter resoluções espaciais na ordem das dezenas de nanómetros. A duração destes flashes vai desde as dezenas de femtosegundos ( $1 \text{ fs} = 10^{-15} \text{ s}$ ) até à centena de attosegundos ( $1 \text{ as} = 10^{-18} \text{ s}$ ). Durante esse intervalo de tempo os nano-objectos não têm tempo de evoluir, assegurando imagens precisas do seu estado. Excitando nano-objectos entre dois flashes de radiação X é possível traçar a sua evolução temporal e desta forma obter um "filme" da mesma após uma excitação. Esta informação é extremamente importante pois irá permitir a identificação de estados estruturais intermediários de nano-objectos conhecidos como os mais importantes para entender o seu poder reactivo.

Este género de estudos está apenas a começar mundialmente devido ao surgimento muito recente de fontes de radiação X suficientemente breves e intensas que permitem produzir este tipo de imagens. A fonte de referência é o laser dito a electrões livres (FEL) do qual apenas existem três exemplares em todo o mundo, na Alemanha, nos EUA e no Japão. O baixo número de exemplares vem do custo extremamente elevado deste aparelho. Desde há alguns anos que tem vindo a ser demonstrado no Laboratoire d'Optique Appliquée (LOA) que os lasers podem produzir radiação X suficientemente intensa e na ordem dos femtosegundos para obter imagens de nano-objectos com resoluções espaciais e temporais equivalentes às obtidas com os FELs.

Esta tese foi construída em torno de três fases: a produção de uma fonte de raios-X polarizada circularmente; a implementação de um novo e mais eficaz sistema de imagem e o teste de amostras de nano-objectos cujo intervalo de alteração após excitação se situa em redor dos 100 fs. Estes estudos foram conduzidos no LOA, Linac Coherent Light Source (LCLS), Chemical Physics Laboratory Matter and Radiation (LCPMR) e no Commissariat à l'énergie atomique CEA Saclay durante os primeiros anos desta dissertação. Estas colaborações permitiam desenvolver uma grande expertise em imagem nanométrica baseada na nova tecnologia desenvolvida ao longo deste trabalho.

Numa primeira instância procedeu-se à optimização de uma fonte XUV em redor dos 20 nm por interação laser-matéria para obter um sinal forte e coerente com uma duração na ordem dos femtosegundos. Para isso foi desenvolvido um

set-up explorando o fenómeno da geração de harmónicas de ordem elevada permitindo a maleabilidade dos parâmetros de geração da radiação. Estes 20 nm ou 60 eV correspondem a uma linha de absorção do cobalto (M-edge), sendo escolhida por apresentar um bom contraste dicróico. Como parâmetros de geração, foram otimizados o comprimento da célula de gás, a pressão, o foco do laser IR e o tipo de gás. O chirp do laser foi ligeiramente modificado, uma vez que tem um efeito no comprimento de onda da harmónica gerada a fim de melhor ajustar o comprimento de onda da harmónica ao M-edge do Cobalto. Usando esta configuração otimizada a 20 nm, um esquema óptico de duas cores foi implementado para aumentar a eficiência de conversão, pois a formação de imagem requer uma elevada contagem de fótons.

Com a fonte desenvolvida o passo seguinte é o estudo da polarização das harmónicas de ordem elevada geradas num campo ortogonal de duas cores. O objetivo geral é de compreender o processo de formação e estudo da polarização da radiação HHG de maneira a replicá-lo e desta forma poder aceder a aplicações só actualmente disponíveis em grandes estruturas (sincrotrão, LCLS). Para controlar a polarização um sistema de detecção da polarização em radiação XUV foi concebido, o que experimentalmente representa um avanço para fontes compactas. Foram realizadas simulações a fim de encontrar um modelo para verificar os resultados experimentais.

O passo seguinte é a caracterização por XMCD e efeitos óptico-magnéticos dos nano-objects. Este estudo foi realizado no BESSY II em Berlim onde as características dicróicas foram verificadas a fim de ter um termo de comparação para uma experiência posterior utilizando a nossa fonte. Diversos estudos foram realizados em SOLEIL, FLASH e BESSY II, em torno de outros fechos de camada iónica (L-edge, M-edge) o que permite conhecer a resposta dos materiais e nos da uma base sólida de comparação.

Foi efectuado um estudo de magnetização em função do tempo das nano-estruturas magnéticas preparadas depois de serem excitadas por radiação laser. Este estudo foi realizado em duas gamas de comprimentos de onda: os X-duros, num laser de raios X em Stanford, o LCLS (L-edge); e nos XUV utilizando a nossa fonte otimizada a 20 nm (M-edge). No LCLS foram efectuadas imagens por difração magnética e holografia com o objetivo de monitorizar a evolução das nanoestruturas magnéticas e tirar imagens instantâneas e desta maneira se

poder verificar a evolução comportamento magnético com grande resolução temporal. Por último um set-up pump-probe de difração magnética foi construído no LOA a fim de permitir o estudo da evolução da magnetização das nano-estruturas magnéticas numa configuração compacta acrescentando mais informação sobre a dinâmica, graças a uma resolução temporal mais precisa.

**Keywords:** Laser; Plasma; Geração de Harmónicas de Ordem Elevada; Radiação XUV; Holografia XUV; Desmagnetização.

# ABSTRACT

L'utilisation des rayons X est indispensable pour obtenir la résolution spatiale de la dizaine de nanomètres. La durée de ces flashes va de la dizaine de femtosecondes ( $1 \text{ fs} = 10^{-15} \text{ s}$ ) à la centaine d'attosecondes ( $1 \text{ as} = 10^{-18} \text{ s}$ ). Durant ce laps de temps, les nano-objets n'ont pas le temps d'évoluer, assurant l'obtention d'une image précise. En excitant les nano-objets entre deux flashes de rayons X, il est alors possible de suivre son évolution temporelle et ainsi de réaliser un 'film' de son évolution suite à une excitation. Cette information est extrêmement importante car elle permettra d'identifier les états structuraux intermédiaires des nano-objets qui sont connus comme étant les plus importants pour comprendre leur pouvoir réactionnel.

Ce genre d'étude vient uniquement de débiter dans le monde en raison de l'apparition très récente des sources de rayons X suffisamment brèves et intenses pour réaliser ce genre d'images. La source de référence est un laser dit à 'électrons libres' (LEL) dont il existe trois exemplaires au monde, en Allemagne, aux USA et au Japon. Le faible nombre d'exemplaires provient du coût extrêmement élevé de cette machine. Depuis plusieurs années, nous avons montré au Laboratoire d'Optique Appliquée (LOA) que les lasers pouvaient produire un rayonnement X femtoseconde et suffisamment intense pour réaliser des images de nano-objets avec des résolutions spatiales et temporelles équivalentes à celles obtenues avec LEL.

La présente thèse a été construite autour de trois phases : réalisation d'une source de rayons X polarisés circulairement, réalisation d'un nouveau système plus performant d'imagerie, et test sur des échantillons possédants des nano-structures dont la vitesse d'évolution après excitation est prévue aux environs de 100 fs. Ces études ont eu lieu au LOA, Linac Coherent Light Source (LCLS), Laboratoire de Chimie-Physique Matière et Rayonnement (LCPMR) et le Commissariat à l'énergie atomique (CEA) de Saclay pendant les deux premières années de thèse. Les collaborations ont permis d'acquérir une forte expertise en imagerie nanométrique basée sur la nouvelle technique que nous avons développée.

Dans le premier cas nous avons procédé à l'optimisation d'une source XUV environ 20 nm d'interaction laser-matière pour un signal fort et cohérent avec une

durée de l'ordre de femtosecondes. Pour cela on a développé un set-up exploitant le phénomène de génération d'harmoniques d'ordre élevé permettant une génération malléable du rayonnement. Ces 20 nm ou 60 eV correspondent au seuil d'absorption du cobalt (M-edge), en étant choisi pour avoir un bon contraste dichroïque. En tant que paramètres de génération ont été optimisés: la longueur de la cellule de gaz, la pression, le foyer du laser infrarouge et le type de gaz. Le chirp du laser a été légèrement modifié, puisqu'il a un effet sur la longueur d'onde de l'harmonique générée afin d'ajuster la longueur d'onde de l'harmonique au M-edge du Cobalt. En utilisant cette configuration optimisée à 20 nm, un schéma optique de deux couleurs a été mis en oeuvre pour augmenter l'efficacité de conversion car la formation d'image nécessite d'un comptage élevé de photons.

Avec la source développée l'étape suivante consiste à étudier la polarisation des harmoniques d'ordre élevé générés dans un champ orthogonal à deux couleurs. L'objectif global est de comprendre le processus de formation et d'étudier la polarisation du rayonnement HHG afin de le reproduire et être en mesure d'accéder aux applications actuellement disponibles uniquement dans les grandes installations (synchrotron, LCLS). Pour contrôler la polarisation un système de détection de polarisation du rayonnement XUV a été conçu, ce qui représente une avance expérimentale pour les sources compactes. Des simulations ont été effectuées pour trouver un modèle capable de vérifier les résultats expérimentaux.

La prochaine étape est la caractérisation par XMCD et effets magnéto-optiques des nano-objets. Cette étude a été réalisée à BESSY II à Berlin, où les caractéristiques dichroïques ont été révélés pour avoir une référence pour une expérience plus tard en utilisant notre source avec les nano-objets. Plusieurs études ont été réalisées à SOLEIL, FLASH et BESSY II, autour d'autres fermetures de couches d'ions (L-edge, M-edge) qui permettent de connaître la réponse des matériaux et nous donne une base solide pour comparaison.

Une étude de l'aimantation en fonction du temps des nanostructures magnétiques préparées après excitation par un rayonnement laser a été effectuée. Cette étude a été menée dans deux gammes de longueurs d'onde: le X-dur, un rayon laser à Stanford le LCLS (L-edge); et les XUV utilisant notre source optimisée de 20 nm (M-edge). À LCLS images par diffraction magnétique et holographie ont été faites afin de suivre l'évolution des nanostructures magnétiques et de prendre des clichés. Cette mesure vérifie l'évolution du comportement magnétique avec une

haute résolution temporelle.

Enfin un set-up pompe-sonde de diffraction magnétique à été construit au LOA afin de permettre l'étude de l'évolution de l'aimantation de nanostructures magnétiques dans une configuration compacte en ajoutant des informations sur la dynamique, grâce à une résolution temporelle plus précise.

**Keywords:** Laser; Plasma; Generation d'Harmoniques d'ordres élevés; Radiation XUV; Holographie XUV; Demagnetisation.

## Bibliography

- [1] Chapman H.N. et al. Femtosecond diffractive imaging with a soft-x-ray free-electron laser. *Nat Phys*, 2(12):839, 2006.
- [2] Neutze R. et al. Potential for biomolecular imaging with femtosecond x-ray pulses. *Nature*, 406(6797):752, 2000.
- [3] A-S. Morlens. *Applications en optique XUV de la phase temporelle et spatiale des harmoniques d'ordres élevés: des miroirs chirpés à l'holographie*. PhD thesis, École Polytechnique, 2007.
- [4] Beaurepaire E. et al. Ultrafast spin dynamics in ferromagnetic nickel. *Phys. Rev. Lett.*, 76:4250-4253, 1996.
- [5] Kazamias S. et al. High order harmonic generation optimization with an apertured laser beam. *Phys. Rev. L*, 90:193901, 2003.
- [6] Constant E. et al. Optimizing high harmonic generation in absorbing gases: Model and experiment. *Phys. Rev. Lett.*, 82(8):1668, 1999.
- [7] Lambert G. et al. An optimized khz two-colour high harmonic source for seeding free-electron lasers and plasma-based soft x-ray lasers. *New J. Phys.*, 11:083033, 2009.
- [8] Kim I. et al. Highly efficient high-harmonic generation in an orthogonally polarized two-color laser field. *Phys. Rev. Lett.*, 94:243901, 2005.
- [9] Kim I. et al. Generation of submicrojoule high harmonics using a long gas jet in a two-color laser field. *Appl. Phys. Lett.*, 92:021125, 2008.
- [10] Lambert G., Tissandier F., Gautier J., Hauri C., Ph. Zeitoun, Valentin C., Marchenko T., J-Ph. Goddet, Ribière M., Sardinha A., Fajardo, M. Hamouda F., Maynard G., Rey G., and Sebban S. Aberration-free high-harmonic source generated with a two-colour field. *EPL*, 89:24001, 2010.

- [11] Kim C. and Nam C. Selection of an electron path of high order harmonic generation in a two-color femtosecond laser field. *J. Phys. B: At. Mol. Opt. Phys.*, 39:3199–3209, 2006.
- [12] Mertins H. C et al. Magneto-optical polarization spectroscopy with soft x-rays. *Appl. Phys. A*, 80:1011D1020, 2005.
- [13]
- [14]
- [15] [http://bostechltd.com/magneto\\_optic\\_effect](http://bostechltd.com/magneto_optic_effect).
- [16] Bahrdt J. et al. Apple undulator for petra iii. *Proc.*, EPAC08:2219, 2008.
- [17] Boeglin C. et al. Distinguishing the ultrafast dynamics of spin and orbital moments in solids. *Nature*, 465:458–461, 2010.
- [18] Brabec Th. and Krausz F. Nonlinear optical pulse propagation in the single cycle regime. *Phys. Rev. Lett.*, 78:3282–3285, 1997.
- [19] Quéré F., Itatani J., Yudin G.L., and Corkum P.B. Attosecond spectral shearing interferometry. *Phys. Rev. Lett.*, 90:073902, 2003.
- [20] Miao J. et al. High resolution 3d x-ray diffraction microscopy. *Physical Review Letters*, 89(8):088303, 2002.
- [21] Sandberg R. L. et al. Lensless diffractive imaging using tabletop coherent high-harmonic soft-x-ray beams. *Phys. Rev. Lett.*, 99:098103, 2007.
- [22] Chapman H.N. et al. Femtosecond time-delay x-ray holography. *Nature*, 44(7154):676–679, 2007.
- [23] Emma P. et al. First lasing and operation of an angstrom-wavelength free-electron laser. *Nat. Photon.*, 4:641–647, 2010.
- [24] Schwarz A. S. The European X-ray free electron laser project at DESY. In *Proceedings of FEL 2004*, 2004.
- [25] Shintake T. Status of Japanese XFEL project and SCSS Test Accelerator. In *Proceedings of FEL 2006, BESSY, Berlin, Germany*, 2006.
- [26] Motz H. Application of the radiation from fast electron beams. *J. Appl. Phys.*, 22:527–535, 1951.

- [27] Motz H., Thon, and W. Whitehurst R. N. Experiments on radiation by fast electron beams. *J. Appl. Phys.*, 24:826–833, 1953.
- [28] Madey J. M. J. Stimulated emission of bremsstrahlung in a periodic magnetic field. *J. Appl. Phys.*, 42:1906, 1971.
- [29] Deacon D. A. G. et al. First operation of a free-electron laser. *Phys. Rev. Lett.*, 38:892–894, 1977.
- [30] Kim K. J. and M. Xie. Self-amplified spontaneous emission for short wavelength coherent radiation. *Nucl. Instrum. Methods A*, 331:359, 1993.
- [31] Tiedtke K. et al. The soft x-ray free-electron laser FLASH at DESY: beamlines, diagnostics and end-stations. *New J. Phys.*, 11:023029, 2009.
- [32] Ronsivalle C. et al. The SPARC project: a high-brightness electron beam source at LNF to drive a SASE-FEL experiment. *Nucl. Instrum. Methods A*, 507:345–349, 2003.
- [33] Lambert G. et al. Injection of harmonics generated in gas in a free-electron laser providing intense and coherent extreme-ultraviolet light. *Nat. Phys.*, 4:296–300, 2008.
- [34] Strickland D. and Mourou G. Compression of amplified chirped optical pulses. *Opt. Comm*, 56:219, 1985.
- [35] Miao J. et al. Extending the methodology of x-ray crystallography to allow imaging of micrometre-sized non-crystalline specimens. *Nature*, 400:342–344, 1999.
- [36] Spence J. C. H. et al. Coherence and sampling requirements for diffractive imaging. *Ultramicroscopy*, 101:149–152, 2004.
- [37] Gabor D. A new microscopic principle. *Nature*, 161(4098):777–778, 1948.
- [38] Goodman J. W. Digital image formation from electronically detected holograms. *Appl. Phys. Lett.*, 11:77–79, 1967.
- [39] Kronrod MA. et al. Reconstruction of holograms with computer. *Sov. Phys.-Tech Phys. USA*, 17:333–334, 1972.
- [40] Onural L. and Ozgen M. Extraction of three-dimensional object-location information directly from in-line holograms using wigner analysis. *Journal of the Optical Society of America A*, 9:252–260, 1992.

- [41] Schnars U. Direct recording of holograms via ccd-target and numerical reconstruction. *Appl. Opt.*, 33:179–181, 1994.
- [42] Rogers G. L. Gabor diffraction microscopy. the hologram as a generalized zone-plate. *Nature*, 166:236, 1950.
- [43] Attwood D. *Soft X-rays and Extreme Ultraviolet Radiation: Principles and applications*. Cambridge University Press, 1999.
- [44] Genoud G. et al. Xuv digital in-line holography using high-order harmonics. *Appl. Phys. B*, 90:533–538, 2008.
- [45] Goodman J.W. *Introduction to Fourier optics*. Roberts Co., 2005.
- [46] McNulty I. et al. High-resolution imaging by fourier transform x-ray holography. *Science*, 256(5059):1009–1012, 1992.
- [47] Ravasio A. et al. Single-shot diffractive imaging with a table-top femtosecond soft x-ray laser-harmonics source. *Phys. Rev. Lett.*, 103:028104, 2009.
- [48] Paulus G. et al. Measurement of the phase of few-cycle laser pulses. *Phys. Rev. Lett.*, 91:253004, 2003.
- [49] Seres J. et al. Laser technology : sources of coherent kiloelectronvolt x-rays. *Nature*, 433(7026):596, 2005.
- [50] Krause J. L. et al. High-order harmonic generation from atoms and ions in the high intensity regime. *Phys. Rev. Lett.*, 68(24):3535, 1992.
- [51] Corkum P. B. et al. Plasma perspective on strong field multiphoton ionization. *Phys. Rev. Lett.*, 71:1994–1997, 1993.
- [52] Keldish V. et al. Ionization in the field of a strong electromagnetic wave. *Soviet Physics jetp*, 20:5, 1965.
- [53] Lee D. et al. Coherent control of high-order harmonics with chirped femtosecond laser pulses. *Phys. Rev. Lett.*, 87:243902, 2001.
- [54] Mauritsson J. et al. Measurement and control of the frequency chirp rate of high-order harmonic pulses. *Phys. Rev. A*, 70:021801, 2004.
- [55] Eichmann H. et al. Polarization-dependent high-order two-color mixing. *Phys. Rev. A*, 51(5):3414, 1995.

- [56] Lewenstein M. et al. Theory of high-harmonic generation by low-frequency laser fields. *Phys. Rev. A*, 49(3):2117, 1994.
- [57] Long S. and McIver J. Polarization-dependent high-order two-color mixing. *Phys. Rev. A*, 51(5):3414, 1995.
- [58] Kim C. M. et al. Generation of a strong attosecond pulse train with an orthogonally polarized two-color laser field. *Phys. Rev. A*, 72:033817, 2005.
- [59] Mercere. P. et al. Hartmann wave-front measurement at 13.4 nm with  $\lambda/120$  accuracy. *Opt. Lett.*, 28(17):1534D1537, 2003.
- [60] Gautier J. et al. Optimization of the wave-front of high-order harmonics. *Eur. Phys. J. D*, 48(3):459D463, 2008.
- [61] Kazamias S. et al. High order harmonic generation optimization with an apertured laser beam. *Eur. Phys. J. D*, 21:353, 2002.
- [62] Einsele S et al. Lensless imaging of magnetic nanostructures by x-ray spectroholography. *nature*, 432:885, 2004.
- [63] Depresseux S et al. Demonstration of a circularly polarized plasma-based soft-x-ray laser. *Phys. Rev. Lett.*
- [64] Ruiz C. et al. Control of the polarization of attosecond pulses using a two-color field. *New J. Phys*, 11:113045, 2009.
- [65] Dudovich N. et al. Measuring and controlling the birth of attosecond xuv pulses. *Nature Phys*, 2:781 – 786, 2006.
- [66] Milosevic D., Becker W., and Kopold R. Generation of circularly polarized high-order harmonics by two-color coplanar field mixing. *Phys. Rev. A*, 61:063403, 2000.
- [67] Allaria E et al. Control of the polarisation of a vacuum-ultraviolet high-gain, free-electron laser. *PRX*.
- [68] Zeng Z. et al. Tunable high-order harmonic generation and the role of the folded quantum path. *Phys. Rev. A*, 77:023416, 2008.
- [69] Frolov M. V. et al. Analytic description of high-order harmonic generation by atoms in a two-color laser field. *Phys. Rev. A*, 81:063407, 2010.
- [70] Antoine P. et al. Theory of high-order harmonic generation by an elliptically polarized laser field. *Phys. Rev. A*, 53:1725, 1996.

- [71] Westerveld W. et al. Production and measurement of circular polarization in the vuv. *Appl. optics*, 24:2256–2262, 1985.
- [72] Hochst H. et al. Multiple-reflection phase shifter: Available alternative to generate circular-polarized synchrotron radiation. *Nuclear Instruments and Methods in Physics Research Section A: Accelerators, Spectrometers, Detectors and Associated Equipment*, 347:107–114, 1994.
- [73] Windt D. et al. Imd software for modelling the optical properties of multilayer films. *Computers in Physics*, 12:360, 1998.
- [74] Brugnera L. et al. Enhancement of high harmonics generated by field steering of electrons in a two-color orthogonally polarized laser field. *Opt. Lett.*, 35:(32)3994–3996, 2010.
- [75] Stanciu C. D. et al. All-optical magnetic recording with circularly polarized light. *Phys. Rev. Lett.*, 99:047601, 2007.
- [76] Sugano S. and Kojima N. *Magneto-optics*. Springer, 1999.
- [77] Zvezdin A. K. and Kotov V. A. *Modern Magneto-optics and Magneto-optical Materials*. Institute of Physics Pub., 1997.
- [78] Valencia S. et al. Faraday rotation spectra at shallow core levels: 3p edges of fe, co, and ni. *New Journal of Physics*, 8:254, 2006.
- [79] Gutt C. et al. Resonant magnetic scattering with soft x-ray pulses from a free-electron laser operation at 1.59 nm. *prb*.
- [80] Malinowski et al. Control of speed and efficiency of ultrafast demagnetisation by direct transfer of spin angular momentum. *Nat Phys*.
- [81] Wang et al. Femtosecond single-shot imaging of nanoscale ferromagnetic order in co/pd multilayers using resonant x-ray holography. *PRL*, 108:267403, 2012.
- [82] <http://www-ssrl.slac.stanford.edu/lcls/technotes/lcls-tn-99-6.pdf>.

**Titre : Imagerie en trois dimensions de nano-objets en l'éclairant par une succession de flashes ultra-brefs de rayons X**

**Mots clés :** *Laser* ; Génération d'Harmoniques d'ordres élevés ; Radiation XUV ; Holographie XUV ; Demagnetisation

**Résumé :** L'utilisation des rayons X est indispensable pour obtenir la résolution spatiale de la dizaine de nanomètres. La durée de ces flashes va de la dizaine de femtosecondes ( $1 \text{ fs} = 10^{-15} \text{ s}$ ) à la centaine d'attosecondes ( $1 \text{ as} = 10^{-18} \text{ s}$ ). Durant ce laps de temps, les nano-objets n'ont pas le temps d'évoluer, assurant l'obtention d'une image précise. En excitant les nano-objets entre deux flashes de rayons X, il est alors possible de suivre son évolution temporelle et ainsi de réaliser un 'film' de son évolution suite à une excitation.

La présente thèse a été construite autour de trois phases: réalisation d'une source de rayons X polarisés circulairement, réalisation d'un nouveau système plus performant d'imagerie, et test sur des échantillons possédants des nano-structures dont la vitesse d'évolution après excitation est prévue aux environs de 100 fs. Ces études ont eu lieu au LOA, Linac Coherent Light Source (LCLS), Laboratoire de Chimie-Physique Matière et Rayonnement (LCPMR) et le Commissariat à l'énergie atomique (CEA) de Saclay pendant les deux premières années de thèse.

**Title : Three-dimensional imaging of the nano-objects by illuminating a succession of ultra-short x-ray flashes**

**Keywords :** *Laser* ; High Harmonic Generation ; XUV Radiation ; XUV Holography ; Demagnetisation

**Abstract :** The use of X-rays is essential to attain the spatial resolution of the tens of nanometers. The duration of these flashes will be in the range of tens of femtoseconds ( $1 \text{ fs} = 10^{-15} \text{ s}$ ) to hundreds of attoseconds ( $1 \text{ as} = 10^{-18} \text{ s}$ ). During this time, the nano-objects do not have time to develop, ensuring accurate imaging of its state. By exciting the nano-objects between two X-ray flashes, it is possible to trace the time evolution and so achieve a "film" of its evolution after excitation.

This thesis was built around three phases: production of a source of X-rays circularly polarised, implementation of a new more efficient imaging system and the test of samples with the possessing nano-structures whose rate of change after excitation is expected to be around 100 fs. These studies were conducted at LOA, Linac Coherent Light Source (LCLS), Chemical Physics Laboratory, Matter and Radiation (LCPMR) and Commissariat à l'énergie atomique (CEA) Saclay in the first two years of dissertation.

